Analysis of thermoelectric properties in arsenic-based structures using DFT

Alban d'Harcourt

PhD

University of York
Department of Physics

December 2022

Abstract

Thermoelectric materials are useful tools for energy conversion that are becoming increasingly ubiquitous in the modern world thanks to their reliability, their autonomy and their compact nature. Their primary limitation is usually their relatively low efficiency, which struggles to be competitive with other energy conversion systems.

This thesis focuses on the computational analysis of semiconductors with complex Fermi surfaces in order to identify properties that may be beneficial to thermoelectric function. In doing so, it attempts to refine a methodology built on first principles calculations so as to realistically evaluate the characteristics of highly anisotropic crystals, in a field where this approach has traditionally been applied to isotropic materials.

Despite the goal specified of thermoelectricity, the properties studied included electrical transport properties that may be of interest in multiple other fields of material research. As such, a priority throughout this body of work is to test the strengths, versatility and limitations of a new methodology while applying it on computationally challenging materials.

These are the different phases of As_2Te_3 and As_2S_3, along with doped and alloyed variants. These materials have, as of the time of writing, been subject to relatively little computational research despite key similarities to well-known thermoelectrics.

As a result, a variety of key behaviours have been identified in correlation to thermoelectric function, and promising figure of merit values have been predicted for As_2Te_3. While less promising overall, As_2S_3 has also shown that it can offer some interesting thermoelectric characteristics if specifically selected for, while revealing some of the computational and theoretical limitations of our models.

Our method was effective for materials that are very computationally challenging and physically anisotropic, and involved steps that for the most part were quite systematic. This suggests that it may be possible to incorporate its use into a high-throughput evaluation of computationally cheaper materials for thermoelectric optimization.

Contents

List of Figures

List of Tables

Declarations

I declare that the work presented in this thesis, except where otherwise stated, is based on my own research and has not been submitted previously for a degree in this or any other university.

Signed

Alban d'Harcourt

Acknowledgements

I would like to thank my supervisors Matt Probert and Phil Hasnip for all the support and advice given throughout my time working on this body of work. Without their help and their patience, it would have been impossible to get this far.

I would also like to thank students and postdocs from the condensed matter dynamics group, both in N/102 and C/106, who have provided so much in terms of advice, camaraderie and tea breaks. This pleasant office environment has added a lot to my time as a PhD student.

Finally, I would like to thank my family, who have been so supportive throughout my time as a student.

Chapter 1

Introduction

1.1 Thermoelectric materials

1.1.1 The thermoelectric effect

When a hot material is placed against a cold material, a thermal gradient is created between the two. Heat will then flow across this gradient in order to achieve thermal equilibrium. The transfer of thermal energy can occur via two processes.

In electrical insulators, the dominant process is lattice thermal conduction. This describes the transference of heat in the form of propagating vibrations of the atoms that constitute the material.

In electrical conductors, the dominant process is the flow of thermally excited electrons from the hot material to the cold material, and less thermally excited electrons from the cold material to the hot material.

A thermoelectric is a semiconductor that acts as a converter between electrical and thermal energy. It can convert thermal gradients into electrical currents by harnessing the electron flow across them. This flow can then be wired into a complete circuit to produce a usable electrical current, see figure 1.1.

Conversely, the application of an electrical potential across a thermoelectric material results in the transfer of thermal electrons, leading to the creation of thermal gradients. If put in an electrical circuit, this selective current produces the transfer of heat across the material, cooling one extremity of the thermoelectric while heating the other.

Based on these properties, a thermoelectric device can be used to generate electricity from any material that is either above or below their environmental temperature, thus producing a thermal gradient. It can also be connected to a power supply to transfer heat between an object and its environment, thus either behaving as a heater or a cooler. Alternatively, it can be used to regulate and maintain a set thermal gradient

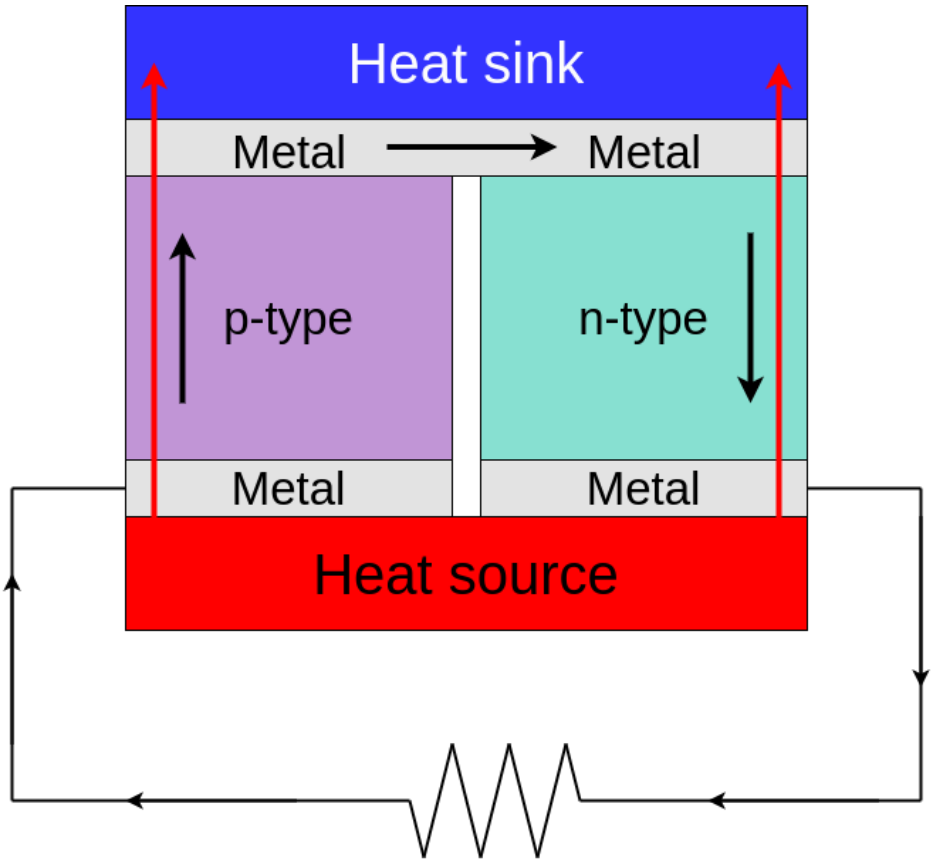

Figure 1.1: Thermoelectric generator, constructed out of two thermoelectric semiconductors operating in opposite directions so as to generate a voltage across a wire. The current is shown in black arrows and the thermal flow in red arrows.

between two physical systems, preventing them from achieving thermal equilibrium.

1.1.2 Thermoelectric structures

Thermoelectric materials can harness the flow of charge carriers travelling either in the same or the opposite direction to the heat flow. These two categories are called p-type and n-type thermoelectrics respectively. By connecting one of each type together into a loop between a hot material and a cold material, one can create a thermoelectric module. In this module, both thermoelectric types complement each other to convert a single temperature difference into a current.

This design can be extended into a series of p- and n-type thermoelectrics connecting back and forth between two materials of different temperatures. This allows a stacking of the potential difference across the circuit as a result of the thermal gradient. However, this comes at the cost of an ever increasing electrical resistance with each length of thermoelectric material.

By extending this design in two dimensions and making use of parallel series to mitigate the impact of compounding resistances, it is possible to produce a thermoelectric

weave covering a surface. This allows for a thermoelectric interface to be used to separate two materials, or a material from its environment. Such an interface can then be used to capture thermal energy or maintain thermal differences with minimal loss, depending on the efficiency of the thermoelectric device.

A thermoelectric effect can also be produced by joining two conductors with different conducting properties to isolate specific thermal electron ranges. This is known as a thermocouple, and is typically both inexpensive and compact due to its simple design. However, thermocouples tend to have lower thermoelectric efficiencies than thermoelectric materials, limiting their applicability. They are typically used as cheap and precise thermal sensors.

1.2 Historical background

1.2.1 Seebeck effect

An early observation of the apparent production of electricity as a result of thermal differences was made by Alessandro Volta in 1794 [1][2]. At the time, he experimented on electricity by completing circuits with frog parts so as to produce an observable reaction. The finding was that by subjecting conductors with uneven physical properties such as coarse iron wires to substantial differences in temperature, in this case cold and boiling water respectively, he could occasionally observe a current running across the metal.

By replicating this experiment with other more uniform conducting materials and finding that it failed when the metal was manufactured in a more uniform manner, he was able to conclude that both the thermal difference and the uneven nature of the wires were necessary to produce the effect. It also allowed him to ensure that he was not accidentally creating a galvanic cell. However, due to the early state of the field of research in electricity, the discovery of a new source of electromotive force (or emf) did not become commonly known.

It wouldn't be until 1821 that thermoelectromotive forces would become established thanks to Thomas Seebeck [3]. He did so by connecting a copper wire to both ends of a plate made of bismuth, and looping it around a compass. By then heating the plate, he found that the needle of the compass would be deflected, demonstrating the creation of a magnetic field, see figure 1.2.

He would first present it in the form of thermo-magnetism, appearing hesitant to assume that the magnetic field was the result of an electric current. It would however be accepted by 1923 [5] that he had produced an electric circuit, which would for the first time be referred to in print as "thermo-electric".

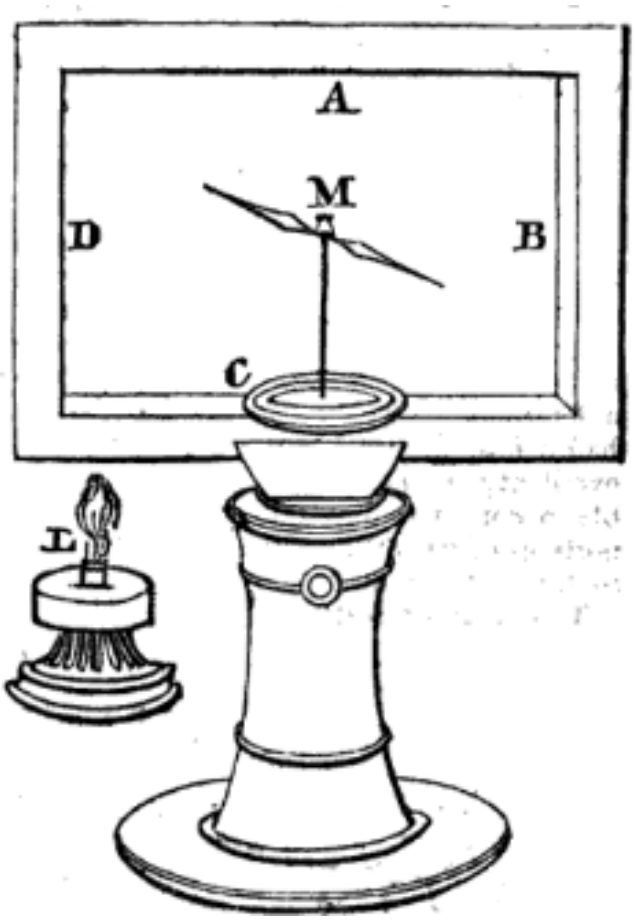

Figure 1.2: The experiment through which Seebeck observed thermoelectric behaviour. Figure from [4].

Seebeck would be known to experiment with this effect on a number of materials, including zinc antimonide, lead sulfide, cobalt arsenide [6]. This work would be resumed in earnest nearly a century later, when Werner Haken would start analysing a broader range of materials, with special focus on non-metals belonging to the carbon group, pnictogens and chalcogens [7].

Throughout the studies of various materials, it was found that each thermocouple appeared to have a proportionality constant relating the size of a temperature difference to the electromotive force they would produce as a result. In 1851, Gustav Magnus would determine that this proportionality did not depend on the thermal distribution [8], but merely on the ratio between an applied voltage ΔV and a difference in temperature driving said voltage ΔT, such that:

$$S = -\frac{\Delta V}{\Delta T} \tag{1.1}$$

This constant S, which would be named thermopower, or the Seebeck coefficient, allowed for the controlled use of thermocouples by merely knowing the temperature on either end.

1.2.2 Peltier effect

The reciprocal observation of thermal flow induced by an electrical current was made by Jean Peltier in 1834 [9]. This experiment was done by creating a thermocouple made of copper and zinc, and submitting it to a variable current produced with a galvanic cell. He then connected a thermometer to the extremities of the thermocouple to identify the variations in temperature.

Upon this discovery, he went about trying to answer six questions. These included: Determining whether the effect occurred regardless of the intensity of the current, whether it could be observed across the length of the components, how it was affected by the length of the thermocouple, whether it was impacted by changing materials, whether it was impacted by varying the setup with liquid conductors or the use of soldering, and which materials were most effective at inducing the thermal transfer.

As such, he found that the thermal transport occurred continuously with the current intensity as it varied, but that the temperatures appeared to gather near the extremities of the thermocouple instead of varying homogeneously across the setup. By observing that longer thermocouples and wider thermocouple surfaces did not impact the amount of thermal energy transferred when answering his third question, he deduced that it was correlated to the intensity of the current by a proportionality constant, which he then measured.

In the process of attempting to answer his last three questions, he then found that by changing the component materials of the thermocouple or the direction of the current, he ended up with variations both in the magnitude and direction of the thermal flow. As such, he found that by coupling different materials, he could obtain transfers of heat of varying intensity, and either in the same or opposite direction to the electrical current. The effectiveness of each thermocouple could thus be described with a term that would be referred to as the Peltier coefficient, that related the intensity of the current to the thermal gradient produced.

1.2.3 Thomson effect

William Thomson would observe in the 1850s the effect by which a single conductor, when subjected to both a thermal gradient and an electrical current, could manifest something akin to the Seebeck effect along its length [10].

This could be done by heating a single conductor, such as a copper bar, at its center while applying a current across it. The result would be that the copper bar would absorb heat along the length where the temperature increased in the direction of the current, and release it along the length where the temperature decreased in the direction of the current. This effect would also depend on the material, occurring to

a lesser extent in iron, and not occurring at all in lead.

Thomson found that the heat absorbed or produced was determined by the thermal gradient across the material, its current density, and a material specific coefficient that would be known as the Thomson coefficient. Thomson would then offer a series of relations between the Seebeck, Peltier and Thomson coefficients, and temperature, suggesting that they all were describing a single physical phenomenon [11].

The advantage of the Thomson coefficient is that unlike Seebeck and Peltier coefficients, it could be directly measured in a single material without the use of thermocouples, demonstrating that individual materials could have inherent thermoelectric properties. Additionally, while the Seebeck coefficient had the most applicable physical significance, the Thomson coefficient could, if measured over a broad temperature range, be used to derive the other two.

More generally, Thomson's observations serve to demonstrate the versatility of thermoelectricity, that individual materials can be used to convert both electrical currents into thermal gradients and thermal gradients into electrical currents, either in the same or in opposite directions to each other.

Additionally, the Thomson relations point at the thermal dependence of the thermoelectric coefficients. Thermoelectric materials when subjected to thermal differences will adjust their behaviour accordingly, making them powerful tools for automated thermal regulation, allowing for extremely sensitive and accurate forms of heating or refrigeration.

1.3 Uses and applications

1.3.1 Thermoelectric generation

1.3.1.1 Automotive generation

Automotive thermoelectric generators (or ATEGs) can be used to convert waste heat from vehicles such as cars or trucks into electricity. This is significant, as close to 40% of the thermal energy produced by burning fuel is lost through fuel exhaust [12], leading to high thermal gradients of several hundred kelvin located along the exhaust pipes, see figure 1.3.

As a result, ATEGs are designed to capture that energy to power on-board electrical systems, thus reducing the need for electric generation and improving fuel efficiency. Such devices have been the subject of research by multiple automobile brands, showing that it should be possible to reduce fuel costs by around 4% [14][15][16][17].

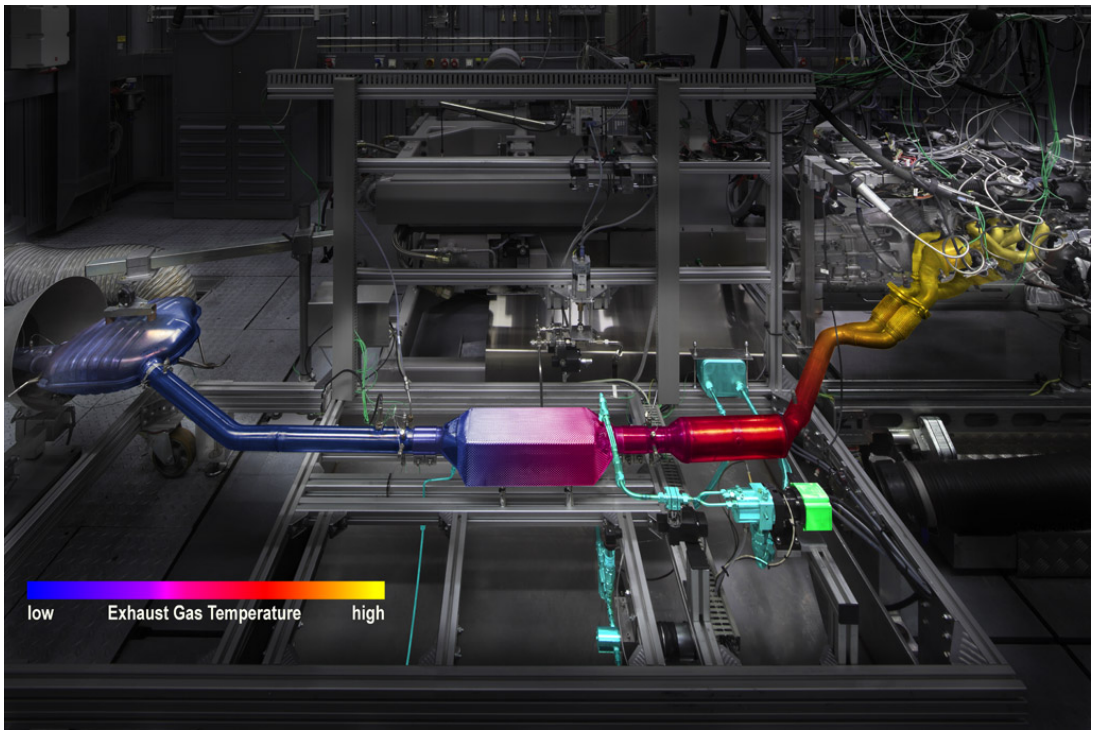

Figure 1.3: Depiction of a thermoelectric device, designed to be set up on the exhaust pipe of a BMW 5-Series car [13].

One part of the challenge lies in the cost of the thermoelectric material, which needs to be relatively efficient to be effective over the limited surface area available. Additionally, the thermal range that it is subjected to from the engine may vary substantially depending on use, requiring it to be effective over a broad range of temperatures.

Despite this, it has been predicted that fuel consumption could be decreased by up to 10% when utilizing the car radiator as a heat exchanger for the thermoelectric generator [18]. Reciprocally, the cold side of the thermoelectric can be put in contact with a coolant from the radiator as opposed to air to keep its function more constant, at the cost of increasing the load on the radiator.

The concept of converting waste heat into electrical energy to be used for hybrid vehicle functionality has also shown promise, albeit with a greater focus on the need for efficient conversion, considering the greater demand for electrical power [19]. This has even resulted in the development of various models to predict efficiency [20], one of which predicted 2% fuel savings for heavy goods materials using already existing technologies [21].

All of these applications can cause additional engineering challenges, however. For example, the use of a heat exchange system through which the exhaust must pass can cause a loss in velocity, impacting engine performance unless accounted for, such as by downsizing the muffler.

However, other issues, such as added weight to the exhaust manifold, have not

proven to be as much of an issue. The compactness and longevity of thermoelectric generators appears to result in minimal impact on the broader function of vehicles.

1.3.1.2 Waste body heat

Waste body heat is a potential source of energy that can be harnessed with thermoelectric generators. However, the thermal difference that can be produced is relatively small, at around 13 K, meaning that the power produced is quite low, typically measured in μW. Despite these restrictions, it can still be harnessed to power wearable devices for medical or fitness purposes [22][23].

Self-sustaining thermoelectric devices can also be used in biomedical implants, such as pacemakers [24]. Advances have even included the development of a pacemaker with a very low voltage startup process that avoids the need for batteries within the system entirely [25].

This reduces the volume of certain such implants by up to 60%, and can circumvent the costly process of having to re-access the device to replace power sources, which in the case of pacemakers will occur around once a decade [26]. It can also reduce the likelihood of issues related to the power source malfunctioning or overheating.

1.3.1.3 Spacecraft power generation

A historically significant application of thermoelectric generators is the radioisotope thermoelectric generators (or RTGs) used on a variety of spacecraft, including Voyager 1 [27]. The RTGs on Voyager 1 convert the decay heat from Plutonium-238 oxide spheres into electrical power, still acting as the primary power supply for the craft many decades later. As a result, other isotopes have been the subject of research for similarly designed nuclear battery-thermocouple systems

NASA alone has reportedly used RTGs to power over twenty space systems [28], demonstrating the extreme versatility, longevity and resilience of thermoelectric generators. This is in part due to their lack of macroscopic moving parts and consistent behavior, even when subjected to high accelerations or variations of the gravitational forces applied to them.

1.3.1.4 Aircraft

An aircraft using any form of turboprop, turbofan or turboshaft engines will naturally produce substantial thermal gradients as a result of its function. As a result, the use of thermoelectric generators can be a promising venue for autonomous energy

harvesting, assuming that an appropriate gradient can be maintained using a passive cooling solution [29].

This allows for the reduced need for batteries and capacitors, when electrical power is passively generated from the mechanical function of the aircraft. This can then be used alongside solar panels to decrease the load on engines required for electrical power production, thus increasing fuel efficiency.

Fuel efficiency gains on aircraft aren't as substantial as on cars or trucks due to the higher relative fuel consumption during travel. However, their usage favours modular construction of large aircraft [30], allowing sections with low energy requirements to be powered autonomously, reducing the need for cabling, which reduces the mass of the aircraft, improving fuel efficiency.

Additionally, this simplification in overall design combined with the reliability of the device reduces the need for aircraft maintenance. By measuring their power production, thermoelectric materials have also been used as localised thermal sensors in aircraft, allowing said aircraft to maintain an autonomous and self-regulating wireless network for maintenance-related information.

1.3.2 Peltier cooling

1.3.2.1 Biomedical cooling

Peltier coolers can be used to construct thermoelectric refrigerators that are both compact and extremely consistent as they do not rely on mechanical components or a compressor cycle [31]. As a result, while they have seen use as domestic appliances for preserving food, they are more commonly used as medical devices for preserving medical resources.

Indeed, their ability to maintain reliably set temperatures with a high level of accuracy when combined with a processing unit as part of a compact unit means that they can be used to easily transport biological compounds such as blood cells, vaccines, and other drugs and biological products. As such, this facilitates the mobility of emergency resources both to other facilities and for use in on-site medical emergencies.

A larger scale version of this setup can be implemented in connection to the thermal regulation of spacecraft [32]. This is not only advantageous due to the light, compact, reliable and accurate properties of thermoelectric coolers, but also because they are silent. Continuous noise pollution must be minimized in spacecraft intended for extended use, and thus noise-producing valve-based cooling systems are generally avoided where possible.

1.3.2.2 Microprocessors

Modern microprocessors often see their performance being impacted by a thermal bottleneck, as the production of highly localised thermal energy pushes them far above optimal temperatures, especially when they are overclocking. While heat sinks can mitigate the problem and the use of fans and water-cooling can be very effective, Peltier coolers can offer a more targeted solution [33].

By placing the Peltier cooler in close contact with the microprocessor, it can serve a form of electronically driven thermal conduction of heat away from the chip. When combined with other cooling systems to act upon the opposite side of the thermoelectric device, it can effectively draw the heat out of the microprocessor so as to keep it well below ambient temperatures. While this setup is easy to regulate so as to avoid excess energy consumption and apply appropriate cooling, it also involves a number of challenges.

Firstly, thermoelectric devices still lack in efficiency and will by design not have a particularly high thermal conductivity. As a result, the energy consumption remains high and the cooling is more appropriate for maintaining sub-ambient temperatures than for combating continuous overheating.

Secondly, the highly localised thermal variation produced by the thermoelectric device may lead to various surfaces acting as dehumidifiers, causing condensation to form on or around the microprocessor. As a result, the design needs to be carefully adjusted and environmental factors need to be accounted for, such as air humidity.

1.3.2.3 Dehumidifiers

Peltier coolers are also used in dehumidifiers for their compact nature and their quietness when compared to ones with mechanical compressors [34]. They function by simply applying a localised cooling upon a surface to incur condensation, but due to their limited power efficiency, they are typically used in smaller devices.

It has however been shown that they can effectively be used for livestock purposes as their quietness, longevity and resilience make them more appropriate for use than mechanical dehumidifiers in harsher environments.

1.3.3 Thermal regulation

1.3.3.1 Isolated solar panel systems

A hybrid approach using both the Seebeck effect and the Peltier effect has been developed in the form of solar panel cooling devices [35]. This is a solid-state device

that generates electric power through the Seebeck effect in the form of a thermal solar panel, which is then used to power a Peltier cooling system.

One advantage of this system is that it is partially self-regulating, as the power supplying the cooling system increases and decreases depending on the thermal energy externally available. This can be used in combination with photovoltaic cells to power a spatially separate Peltier cooling device [36], which can serve as a useful cooling system for food and vaccines in remote areas without access to reliable energy grids.

Another application of solar-based thermoelectric power generation and conversion has also been researched in the form of desalinating stills [37]. These stills rely on a high thermal difference between the evaporating and condensing components to distill water, desalinating it in the process. By attaching thermoelectric generators to photo-voltaic cells and converting the resulting current into thermal gradients within the still, it is possible to significantly increase the aqueous throughput of the device.

1.3.3.2 Thermal sensors

A common application of the thermoelectric effect is in the form of thermal measurements. Here, high efficiency is not a concern, allowing for the use of a cheap and compact thermocouple to measure temperatures over a broad range [38].

Industrial use of thermocouples is varied, covering thermal regulation of kilns, furnaces, water heaters and other systems subject to thermal variation and in need of regulation. As a result, they are commonly used in the steel industry, gas appliances, industrial power production and chemical processing plants.

While cheap and interchangeable, thermocouples subjected to extreme temperatures may age, leading to errors in measurement that may be specific to the range they have been subjected to, making re-calibration in a different environment impractical [39]. Additionally, they have limited accuracy, often being unable to measure temperature to an uncertainty of less than one kelvin.

Thermocouples are also used as vacuum gauges [40], as the temperature measured at a junction is a function of the thermal conductivity of the gas, which itself is a function of its pressure.

1.4 Thermoelectric material selection

1.4.1 Core criteria

Determining the effectiveness of a thermoelectric material can be done by evaluating its efficiency in converting electrical energy into thermal energy via the Seebeck effect. This efficiency is described in the theory section with equation 2.1, as determined by a dimensionless factor known as the figure of merit. The higher the figure of merit, the higher the efficiency.

The significance of this figure of merit is based on its constituent properties, which are the electrical conductivity, the Seebeck coefficient, the average temperature and the thermal conductivity. Materials with a higher electrical conductivity will more readily allow the induction of an electrical current, thus increasing its affinity for thermoelectric behaviour.

Reciprocally, a high thermal conductivity will more easily allow the material to approach a state of thermal homogeneity, decreasing the thermal gradient that can be maintained across the material. This component can have such an impact that it is the primary target of certain material selection methods [41].

The Seebeck coefficient is the component with the greatest impact on the figure of merit, as it defines the voltage driving the electromotive force produced as a result of the thermal gradient. The higher the Seebeck coefficient, the greater the electric potential difference across the material with respect to temperature.

Finally the average temperature itself increases the figure of merit through multiple physical effects. For one, it broadens the energetic distribution of thermal electrons, incorporating a larger range into the materials' thermoelectric behaviour and increasing their thermoelectric flow, similar to how increasing electrical conductivity improves thermoelectric efficiency.

The thermal conductivity of solids as a result of lattice vibrations will also tend to decrease when temperature is increased, reducing its negative impact on thermoelectric function. Additionally, the Seebeck coefficient is temperature dependent, and will tend to increase with temperature in most materials.

As such, we can conclude that to improve the thermoelectric efficiency of a material, we may look at increasing its Seebeck coefficient and electrical conductivity, decreasing its thermal conductivity, and increasing the average temperature at which we wish to have it operate.

However, while thermoelectric devices are typically used at temperatures commonly seen in industrial processes of up to 500K, these are also the temperatures at which they must compete with other more efficient forms of conversion between thermal and

electrical forms of energy. These circumstances may not capitalise on their strengths, such as their compact nature and long shelf lives.

As such, the practical potential for comparatively efficient devices operating at room temperatures of around 300K may be much higher, and balancing efficiency against applicability must also be considered when selecting a thermoelectric material.

1.4.2 Material properties

Considering the properties preferred in a thermoelectric can help to determine which materials and structures are more likely to show effective thermoelectric function.

Many of the thermoelectrics that have shown promise so far have been compounds of at least two elements, often consisting of one element from either the carbon group or pnictogen groups, and one from the chalcogen groups. One of the main reasons for this is likely to lie in the electronic structures in these elements producing thermally sensitive semiconductors.

The material in question needs to demonstrate electron state distributions that favour the conduction of thermal electrons in one spatial direction with respect to the opposite direction, when the material is subjected to a thermal gradient. As these criteria cannot be directly observed before analysis, it may be useful that we be able to approximate the adherence to this criteria with relatively cheap preliminary calculations.

On the matter of thermal conductivity, the scattering of lattice vibrations is paramount. One way of doing this is to include multiple elements of widely varying masses, meaning a general preference for selecting elements that are on different rows of the periodic table.

Another source of lattice vibration scattering can come from the inherent presence of narrow gaps within the material structure governed by van der Waals forces. As these are weaker than ionic or covalent bonds within lattices, they may serve as an impedance to the transfer of lattice vibrations.

This commonly occurs in the two-dimensional form of layers within the material, but can also manifest in the form of materials forming strands or more complex interlocking structures connected by van der Waals forces. Materials with layers or other such structures that include multiple atoms or ions within their thickness may effectively lead to anharmonic movement scattering multiple ranges of lattice vibrations.

The manufacturing process of the material may also impact the thermal conductivity, such as the creation of point defects when manufacturing alloys [42][43]. These are occurrences of elements being misplaced within the lattice leading to sites being occupied by the wrong element, known as antisite defects, sites not being occupied and leaving a gap in the lattice, known as vacancy defects, and even elements being

trapped between lattice sites, known as interstitial defects.

The presence of either vacancy defects or antisite defects, where the atom is of a substantially different mass relative to its placement in the lattice, can lead to anharmonic interaction with lattice vibrations, scattering them. Interstitial defects can have a similar impact as a result of their placement, but are high energy defects that rarely occur unless there is a large difference in size between the atoms within the lattice.

Defects will tend to naturally occur in all manufacturing processes, although their prevalence may vary depending on the manufacturing method. Traditional alloying techniques rely on cooling the material to allow the lattice structure to form. Faster cooling will typically lead to a higher number of defects being produced. The number of defects may also be artificially increased by doping the material with certain elements, although this may also impact the electronic structure depending on their number of valence electrons.

The formation of crystal structures via nucleation may lead to a polycrystalline material. In this situation, the crystallites, or grains, may form uneven structures at their contact points, referred to as grain boundaries. Such grain boundaries can effectively scatter lattice vibrations that would otherwise travel unimpeded across an idealised material.

Smaller grains can lead to a higher density of grain boundaries, up to a point where their size can be sufficient to become the primary factor in lattice vibration scattering, known as the small grain limit. However, the deformations that they apply to the lattice may end up also scattering travelling electrons and render the electronic properties needed for thermoelectric function less effective.

Another potential way of scattering lattice vibrations may be the purposeful creation of nanostructures. These are nanoscopic features added to the material to fulfill certain functions. One example would be the creation of columns along the surface of the material, with their proportions determined so as to allow them to vibrate at selected frequencies. By doing this, these nanostructures can capture certain lattice vibration modes, thus preventing them from effectively travelling across the lattice.

That being said, the analysis of nanostructures would require models that include large numbers of atoms or ions, and account for material surfaces. All of these would greatly increase the scale and computational cost of our simulations. As such, this avenue of research was not explored considering the already substantial cost of the calculations required without it.

1.4.3 Other criteria

While both the choice of alloy and manufacturing process may determine the effectiveness of a thermoelectric material, these are not necessarily our only criteria when

evaluating it.

For one thing, the cost of the material must be taken into account. To start off, we can find approximate values for the price of the individual components. For example, Bi_2Te_3 is a highly efficient thermoelectric alloy, but is composed of relatively valuable elements, with bismuth being valued at around 14.02 US dollars (or USD) per kilogram, and tellurium being valued at around 139.99 USD per kilogram [44].

Additionally, while evaluating the cost of manufacture is difficult, it may be worth noting the prevalence of elements in semiconductor manufacture, as that will inform us on the infrastructure available for transport and manufacture were a thermoelectric found to be of interest. This may also be impacted by the issue of toxicity, as toxic elements may conceivably require certain precautions be taken during manufacture.

Additionally, while the presence of a toxic element within a stable crystal alloy may not necessarily pose a health risk, it might lend itself to limited commercial interest due to public concern, limiting its applicability. While these factors should perhaps not define our research, awareness of these issues is nonetheless necessary.

Reciprocally, while the applicability of elements such as lead, arsenic or polonium could be limited due to their toxicity, it is also worth mentioning that materials that are subjected to limited research for this very reason may end up being suitable candidates for study, if only due to the limited work that may have been done on them so far.

In fact, as computational simulations give us the ability to predict the properties of materials that have not yet undergone substantial review, it may be preferable to look for materials and structures that have not been thoroughly studied as of yet. This plays to the strengths of computational work and reinforces the relevance of our work to the current state of thermoelectric material research.

Finally, it is necessary to determine whether our structures are stable or meta-stable and, if it is the latter, we must then determine their lifetimes. Indeed, while being meta-stable does not necessarily limit the applicability of a material, it may be a problem if its lifetime is too short to be reasonably used as part of a thermoelectric device.

1.5 Objectives

While this thesis is fundamentally a study of a particular set of thermoelectric materials, it is focused not only on producing data, but also on making its findings transferable and relevant for future work in the field. As such, its primary objectives are as follows:

- Develop a rigorous and versatile method for analysing all thermoelectric properties of a material, with particular focus on accounting for electron-phonon coupling.
- Implement this method on a challenging material in order to produce a detailed

analysis of said materials while identifying the limitations of the method
- Attempt to refine the method and define its primary sources of error with respect to our materials, while expanding the set of materials studied
- Identify within the data key material properties that are more easily evaluated than the final results, and relevant when considering thermoelectric efficiency

Through these objectives, we have planned to produce new and relevant data while proposing a methodology which may be transferable and applicable in cases of future higher-throughput studies beyond the scope of this thesis.

Chapter 2

Theory

2.1 The thermoelectric effect

2.1.1 Thermoelectric flow

Let us consider the Fermi-Dirac distributions of electrons in two materials, one described as hot and the other as cold. For the sake of simplicity, we will imagine the cold one as converging towards zero kelvin. As such, we now can observe all of the

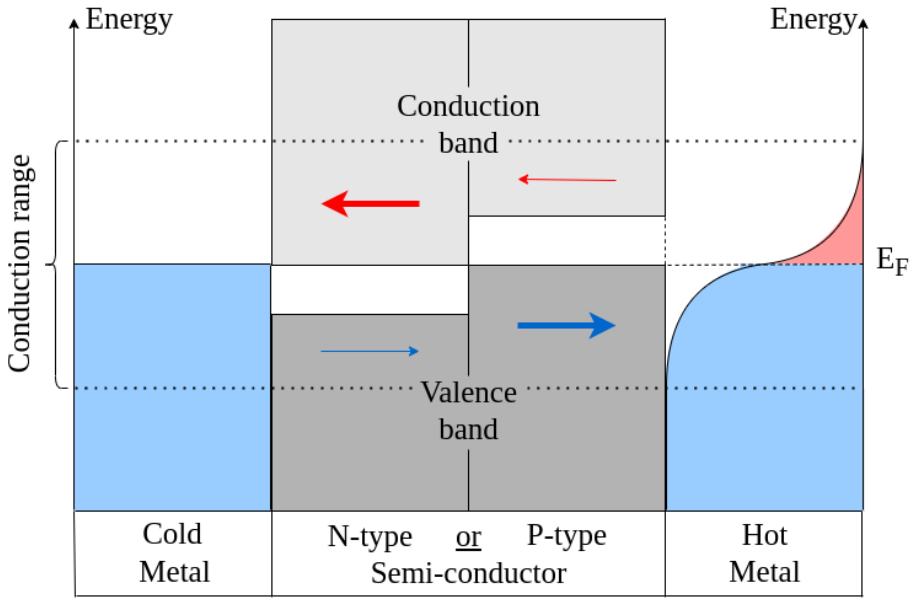

Figure 2.1: A visual aid to thermoelectric devices. On the left and right, we have simplified Fermi-Dirac distributions of a cold and hot metal respectively, plotted vertically with respect to energy. In the middle, we have the available bands of two possible semiconductors, also plotted vertically with respect to energy, including a space for the band gap. From the arrows representing electron flows above and below the Fermi energy, we would expect to observe hot-to-cold and cold-to-hot net thermoelectric currents for the n- and p-type semiconductors respectively.

states beneath the Fermi level in the cold material as filled, and all those above it as empty, see figure 2.1.

When put in contact with a hot material, with an appropriately smeared Fermi-Dirac distribution, one can expect two separate electron flows to occur. The electrons above the Fermi level in the hot material will spread over to the cold material to fill the available electron states. And reciprocally, the electrons beneath the Fermi level in the cold material will transfer over to and occupy the unoccupied electron states in the hot material. These two electron flows would typically cancel each other out, mitigating any possibility of a usable electrical current forming.

A thermoelectric device can be seen as a semiconductor with a carefully shaped band gap, such that conduction is almost exclusively allowed across either the valence band or the conduction band of the semiconductor, but not both. When placed between the two materials, it would effectively allow electron flow in only one direction, thus preventing them from cancelling each other out.

Reciprocally, if an electrical potential is applied to such a thermoelectric device in thermal equilibrium, one would expect only the electrons either above or below the Fermi level to start travelling. This unidirectional transport of thermally selected electrons would then artificially disrupt thermal equilibrium across the material, effectively causing thermal transport across it.

2.1.2 Thermoelectric effectiveness

2.1.2.1 Thermoelectric figure of merit

The efficiency of such a device can thus be determined as a measure of how much of the thermal transport between the hot and cold sources is converted into a total effective electrical current. The maximum such efficiency η_{max} can be calculated using equation 2.1:

$$\eta_{max} = \frac{T_{hot} - T_{cold}}{T_{hot}} \frac{\sqrt{1+Z\overline{T}}-1}{\sqrt{1+Z\overline{T}}+\frac{T_{cold}}{T_{hot}}} \tag{2.1}$$

where T_{hot}, T_{cold} and $\overline{T}$ are the temperature of the hot end, that of the cold end, and the average temperature across the device respectively. Here, $Z\overline{T}$ is a dimensionless figure of merit such that the efficiency η_{max} increases with $Z\overline{T}$, which will simply be referred to as ZT moving forwards:

$$ZT = \frac{\sigma S^2 T}{\kappa_e + \kappa_l}, \tag{2.2}$$

where we find that ZT is dependent on the electrical conductivity σ, the Seebeck

coefficient S, the electron component of the thermal conductivity κ_e and the lattice component of the thermal conductivity κ_l.

The Seebeck coefficient, being the only squared component, is the most important component of ZT, and describes the electrical potential caused by the asymmetry of the density of states across the Fermi level with respect to temperature. As such it is measured in volts per kelvin.

Thermal conductivity is also significant, as the total thermal conductivity κ_T such that $\kappa_T = \kappa_e + \kappa_l$ is directly inversely proportional to ZT. This is linked to the inherent proportionality between σ and κ_e, as a higher lattice component κ_l will lead to a lesser electron transport contribution to maintaining the thermal gradient.

This relationship between the electrical conductivity and the electron thermal conductivity is underlined by the Wiedermann-Franz law, see equation 2.3, which describes the ratio as equal to the temperature T times a proportionality constant L known as the Lorenz number.

$$\frac{\kappa_e}{\sigma} = LT \tag{2.3}$$

Unfortunately, this empirical law is not exact in practice, meaning that the effective Lorenz number can vary substantially depending on conductors and temperatures, and even more so in semiconductors. As such, we cannot accurately use it to solve for ZT.

The thermal conductivity κ_T also plays a secondary role in maintaining a thermal gradient in thermoelectric devices. A high κ_T will cause the thermal gradient to be distributed across other materials in the system, whereas a low κ_T constrains more of the gradient within the thermoelectric bulk.

2.1.2.2 Thermoelectric power factor

A secondary component useful in measuring the effectiveness of a thermoelectric material is called the power factor, defined in equation 2.4. It determines the amount of power produced per meter of thermoelectric device per temperature squared. As such, it determines the amount of energy that a thermoelectric device can produce based on its electronic throughput and asymmetry.

$$P = \sigma S^2 \tag{2.4}$$

This can be useful, as a high efficiency may not be of much value if the material is barely able to conduct electricity. However, it is very rarely the limiting factor in power production, meaning that ZT is typically a better standard to use when evaluating

the thermoelectric ability of a material, as it tends to be the primary limiting factor to thermoelectric power production.

2.2 Density functional theory

2.2.1 Overview

Density functional theory (or DFT) is a computational technique used to simulate many-body systems, including crystalline structures studied in condensed matter physics. It was originally formulated in 1964 [45] as the principle that a functional of electron density, defined below, could be used to calculate the ground-state energy of a system.

This approach applies the Born-Oppenheimer approximation [46], which dictates that as the motion of electrons is much faster than that of nuclei, due to the large difference in their respective masses, one can view the wave function of a system of electrons and nuclei as the product of their respective but separate wave functions. Physically, this is the equivalent to seeing nuclei as non-moving objects applying a potential to rapidly moving electrons.

As the nuclear wave function is highly localized, the semi-classical approximation is applied, wherein the nuclei are treated as classical point particles. As a result, the principle focus of the simulation is the calculation of the electron wave function, which is diffuse due to the particles' low mass in a system considered time-independent. These electrons, however, can be seen as all interacting with each other, making the problem scale rapidly as the number of electrons increases.

In order to solve this computational challenge, one can apply the Hohenberg-Kohn theorems, which were developed in 1964. These rely on knowing the many-body electron density, which is a measure of the probability of the presence of electrons within an infinitely small volume at any one location, such that the electron density ρ at $\mathbf{r}$ in a system of N electrons is of the form:

$$\rho(\mathbf{r}) = N \int \prod_{l=2}^{N} d\mathbf{r}_l |\Psi(\mathbf{r}_1, \mathbf{r}_2, ..., \mathbf{r}_N)|^2 \tag{2.5}$$

where Ψ is the many-electron wavefunction of the system.

The Hohenberg-Kohn theorems tell us that the ground state properties of a system of interacting particles can be derived directly from its ground state particle density. This relationship can be formalised through a description of the ground state energy E as a functional of the ground state density of the system ρ, and is described as:

$$E[\rho] = T[\rho] + V[\rho] + V_{ext}[\rho] \tag{2.6}$$

where $T[\rho]$ is the kinetic energy functional, $V[\rho]$ is the internal potential energy functional and $V_{ext}[\rho]$ is the external potential energy functional. However, although the existence of this functional was proven by Hohenberg and Kohn, its actual form was unknown. A means of determining or approximating this unknown functional was required before it could be used for practical calculations.

A subsequent ansatz was introduced by Kohn and Sham in 1965. It proposes that the exact ground state density of a system of interacting particles can be represented by that of a system of non-interacting particles subjected to an effective potential. Hence, a functional such as that introduced by the Hohenberg-Kohn theorems can be implemented for the ground state density of this new system in order to calculate ground state properties. These concepts, developed through the Hohenberg-Kohn theorems and the Kohn-Sham ansatz form the basis for density functional theory. With this single-particle viewpoint, the electron density can now be written as:

$$\rho(\mathbf{r}) = \sum_{l=1}^{N} |\psi_l(\mathbf{r})|^2, \tag{2.7}$$

where ψ_l is a single-particle wavefunction for electron l. Thus, for a system of N electrons, we can convert the problem of solving the Schrödinger equation for N bodies to that of solving N equations, each assuming an additional potential applied to a single body. These single-body Schrödinger-like equations apply to single-particle wavefunctions ψ_l, and are known as Kohn-Sham equations, of the form:

$$\left\{ -\frac{\hbar^2}{2m}\nabla^2 + V_0(\mathbf{r}) \right\} \psi_l(\mathbf{r}) = E_l \psi_l(\mathbf{r}), \tag{2.8}$$

where V_0 is a local effective potential, known as the Kohn-Sham potential, calculated from:

$$V_0 = V_{ext} + V_H + V_{xc}, \tag{2.9}$$

where V_{ext} is the external potential acting on the system, V_H is the classical Coulomb potential arising from a charge density distribution $\rho(r)$ between interacting particles, and V_{xc} is the exchange-correlation potential, accounting for exchange and correlation interactions between particles.

Solving these equations allows the computational cost of the simulation to scale much more efficiently with the number of electrons, assuming a known exchange-correlation potential across the system. It is even theoretically possible for it to approach linear scaling under ideal circumstances, although this is rarely feasible in practice. However,

we do not know the exact exchange-correlation potential V_{xc}, meaning that it must then be approximated at sampling points across the system. This spatially dependent fictitious potential can be calculated as a functional of electron density.

The different eigenvalues E_l can be plotted with respect to energy range. However, it's worth noting that for N electrons in a non-spin polarized system, one expects E_l to solve to $N/2$ different solutions, such that n eigenvalues can accommodate $2n$ electrons under the Pauli Exclusion principle, with both a spin-up and spin-down electron for each.

2.2.2 Automating DFT calculations

One of the primary uses of DFT is the simulation of unknown materials from quantum mechanical principles. This involves solving the electron density functional for a Kohn-Sham potential. This gives us an energy and set of properties for the system.

However, as the wave function (and hence also the density) of the ground state is not initially known, it is necessary to make an initial guess of the Kohn-Sham potential for which the energy and density are then calculated and the resulting Kohn-Sham potential recalculated. This potential can then be used to recalculate the density and hence the energy, and see if it has changed substantially. Based on the direction and the amplitude of the energy change, this process can then be repeated to further explore the energy landscape of the system until the change in energy is within an acceptable tolerance. This new minima gives the ground state of the material within said precision.

The use of this self-consistent loop to explore the variation of a system's energy and discover its ground state is known as the self-consistent field (or SCF) method. There are various software packages that involve the use of DFT to complete SCF cycles in an efficient and computationally parallelised manner, including CASTEP [47], VASP [48] and Quantum Espresso [49].

2.2.3 Crystal structures

Practically expanding the use of DFT from a system consisting of a few dozen electrons to a macroscopic system would increase the scale of the calculation by many orders of magnitude. However, many solids have a crystalline structure with periodically arranged nuclei. This means that the effective electron densities and related potentials are also periodic.

Bloch's theorem [50] dictates that in a periodic potential the electron density is periodic, and the corresponding wavefunction can be described in terms of a phase factor times a periodic function, written as [42][51]:

$$\psi_k(\boldsymbol{r}) = e^{i\boldsymbol{k}\cdot\boldsymbol{r}} u_k(\boldsymbol{r}) \tag{2.10}$$

where $\psi_k(\boldsymbol{r})$ is the wavefunction, $\boldsymbol{k}$ is a wave vector, $e^{i\boldsymbol{k}\cdot\boldsymbol{r}}$ is a phase factor and $u_k(\boldsymbol{r})$ is a periodic function. Here the periodic function shares the periodicity of the lattice, which occurs both in real and reciprocal space, meaning that we can calculate the properties of a single primitive cell, called a Brillouin zone when represented in reciprocal space, and correctly determine those of a perfect macroscopic crystal structure as a result.

Through the implementation of a periodic boundary condition, we can describe the periodic function in terms of wave vectors $\mathbf{G}$ such that $e^{i\mathbf{G}\cdot\mathbf{r}}$ has the periodicity of the real-space cell. This allows for the decomposition of the periodic function $u_{kl}(\boldsymbol{r})$ using a basis set of plane waves $e^{i\mathbf{G}\cdot\mathbf{r}}$, such that:

$$u_k(\boldsymbol{r}) = \sum_{\mathbf{G}} c_{Gk} e^{i\boldsymbol{G}\cdot\boldsymbol{r}} \tag{2.11}$$

where c_{Gk} are complex coefficients. This leads to a new expression for the wavefunction:

$$\psi_k(\boldsymbol{r}) = \sum_{\mathbf{G}} c_{Gk} e^{i(\boldsymbol{G}+\boldsymbol{k})\cdot\boldsymbol{r}} \tag{2.12}$$

As corresponding waves, known as plane waves, have wavelengths that must fit within the real space cell, the set of allowed $\mathbf{G}$ must be multiples of a minimum nonzero $\mathbf{G}_{min}$ corresponding to the longest allowed wavelength. However, as $|\mathbf{G}|$ increases, the c_{Gk} term tends towards zero, allowing for truncation of the infinite summation within an acceptable tolerance. If we consider the wave vector G_{max} at which point the error due to this truncation is deemed sufficiently small, it is convenient to define a corresponding kinetic energy term E_{cutoff} via the dispersion relation:

$$E_{\text{cutoff}} = \frac{\hbar^2 |\boldsymbol{G}_{max}+\boldsymbol{k}|^2}{2m} \tag{2.13}$$

where m is the electron mass. This term is the cut-off energy, which defines the set of wave vectors we include in a calculation. In practical calculations it is important to ensure the properties of interest have converged with respect to increasing this cut-off energy.

It should be noted that the number of basis states in the plane-wave basis set is discrete and changes discontinuously with the cut-off energy. This is because the number of allowed states is determined by adding multiples of the smallest wave vector $\mathbf{G}_{min}$ that can fit within the boundary set by $|\mathbf{G}_{max}|$. Thus, by increasing the cut-off energy, and by extension $\mathbf{G}_{max}$, one may observe a step-wise increase in the number of states. If the cut-off energy is low, then this will have consequences for the computed total

energy and stress, although the resultant errors can be approximately corrected [52].

2.2.4 Pseudo-potentials

A key component to managing the scale of an electron-dependent system is the separation of outer electron states from core states. The latter can be seen as electron states trapped within atomic or ionic structures by the nuclei which they both interact with and screen, reducing the effective potential that they apply on electrons outside that range. As such, it may be appropriate to treat core electrons and their nuclei as a single effective core of electrostatic charge with a localised wave function.

This allows us to further reduce the scope of our Kohn-Sham equations to valence electrons primarily, but also means that their behaviour has to be redefined relative to their interaction with this large electrostatic core. In this version of the model, the valence electrons are subject to a single fictitious potential (or pseudo-potential) applied by the core, and could therefore be described by a fictitious wave function.

The wave function that is being described may tend to oscillate substantially within the core region, but is only of significance to the larger DFT model when influencing the outer valence electrons. Hence the fictitious wave function need only accurately describe the system outside of the core region for a radius $r > R_{inner}$ where R_{inner} is the radius separating the core region from the valence electrons.

As fewer oscillations are required of the fictitious wave function, it is smoother and requires fewer plane waves to represent it. Thus a lower cut-off energy is required for the plane wave basis set [53].

The resulting pseudo-potential is then nonphysical within the core, but effectively realistic when applied to valence electrons, resulting in a pseudo-wavefunction that is appropriate for use in DFT, see figure 2.2.

2.2.5 Exchange-Correlation functionals

2.2.5.1 Local functionals

There exist multiple functionals that have been developed to approximate the exchange-correlation functional. One of the earliest ones is the local density approximation (or LDA) [55], which calculates the exchange-correlation energy as a function of the electron density, see equation 2.14. This is a relatively straight-forward approach that has proven successful for predicting Fermi levels and band structures (introduced in section 2.3.1) in semiconductors [56], and is known to be quite computationally cheap.

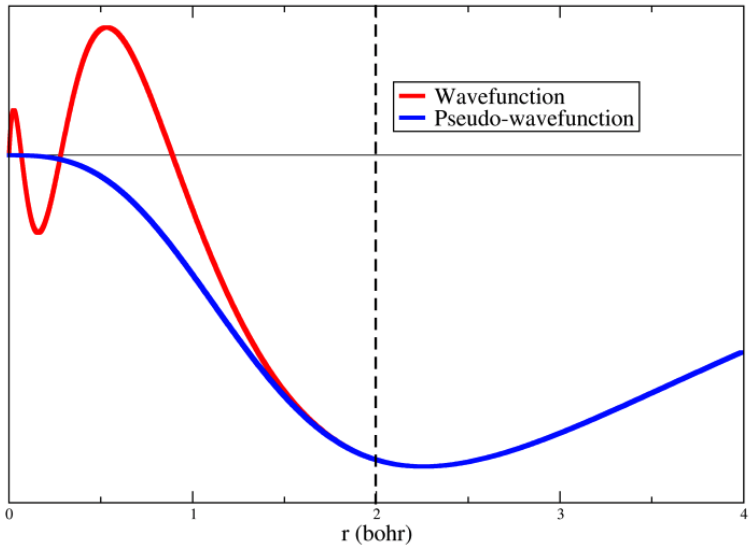

Figure 2.2: An example of a pseudo-wavefunction produced with the aid of a pseudo-potential to emulate the results of an intended wavefunction. The reduced number of oscillations represented within the core allows for an effectively smaller cut-off energy required [54].

$$V_{xc}[\rho](\mathbf{r}) = \frac{\delta E_{xc}[\rho](\mathbf{r})}{\delta \rho(\mathbf{r})}$$
$$E_{xc}^{LDA}(\rho(\mathbf{r})) = \int \rho(\mathbf{r}) E_{\rho,xc}^{LDA}(\rho(\mathbf{r}))d\mathbf{r} \tag{2.14}$$

where E_{xc} is the exchange correlation energy functional, dependent on the electron density ρ at position $\mathbf{r}$, and E_ρ is exchange-correlation energy density. This approach can over-bind materials and underestimate the electronic band gap [57; 58]. It also ignores the long range correlations that lead to van der Waals forces. Despite that, LDA tends to naturally weakly bind distant structures in a way that can mimic an effective van der Waals force.

2.2.5.2 Semi-local functionals

Another type of functional that has become prevalent in the field is the generalised gradient approximation (or GGA) [59], which also accounts for the gradient in the electron density as a derivative at each point, see equation 2.15. As a result, the exchange-correlation energy is not calculated solely based on the electron density at each point, making the GGA a semi-local functional.

$$E_{xc}^{GGA}[\rho(\mathbf{r})] = \int \rho(\mathbf{r}) E_{\rho,xc}^{GGA}[\rho(\mathbf{r}), \nabla\rho(\mathbf{r})]d\mathbf{r} \tag{2.15}$$

This more sophisticated method can give more realistic descriptions of systems with substantial electron density gradients, such as molecular structures, and does not substantially add to the computational cost of the LDA method. It also negates part

of the binding found in the LDA, requiring the additional manual inclusion of van der Waals forces.

However, the semi-local nature of the calculation of the gradient means that it produces zero-value derivative discontinuities [60; 61]. As a result it does not accurately model the non-zero discontinuities in the electron population at the band gap, and tends to underestimate it as a result. More sophisticated derivative models may increase the sensitivity across the discontinuity in electron density, but will likely still be susceptible to underestimating band gaps nonetheless.

More recently, another type of functional has started to be used, known as a meta-GGA, which makes use of the Laplacian of electron density, see equation 2.16, to offer a more advanced description of the exchange-correlation interaction [62; 63].

$$E_{xc}^{meta-GGA}[\rho(\mathbf{r})] = \int \rho(\mathbf{r}) E_{xc}^{meta-GGA}[\rho(\mathbf{r}), \boldsymbol{\nabla}\rho(\mathbf{r}), \nabla^2\rho(\mathbf{r})] d\mathbf{r} \tag{2.16}$$

These functionals may give a better description of electronic structures than LDAs or GGAs, but also prove more computationally expensive, and may not necessarily be implemented yet in all DFT software packages due to their recent nature. Additionally, despite no longer being entirely local, they do not effectively account for van der Waals interactions.

Using the Laplacian of electron density appears to be the natural next step considering the progression between LDAs and GGAs.

However, in practice, meta-GGAs do not typically use the Laplacian of density, but instead use the Laplacian of the occupied orbitals as an analogue. It is then defined, for the sake of numerical stability, in terms of the orbital kinetic energy density ζ such that [64]:

$$\zeta(\mathbf{r}) = \frac{1}{2} \sum_{l=1}^{N} |\nabla \phi_l(\mathbf{r})|^2 \tag{2.17}$$

where ϕ_l represents the occupied orbitals, allowing for this expression to be reinterpreted as:

$$\zeta(\mathbf{r}) = \frac{1}{2} \sum_{l}^{occupied} |\nabla \psi_l(\mathbf{r})|^2 \tag{2.18}$$

The advantage of using ζ is that it can then be used when optimizing the functional.

Indeed, it is possible to define the single-orbit limit ζ_W and electron gas limit ζ_U, see equation 2.19.

$$\zeta_W(\mathbf{r}) = \frac{|\nabla\rho(\mathbf{r})|^2}{8\rho(\mathbf{r})}$$
$$\zeta_U(\mathbf{r}) = \frac{3}{10}(3\pi^2)^{2/3}\rho^{5/3}(\mathbf{r}) \tag{2.19}$$

We can now define an indicator α that acts as a comparison between our ζ and its defined limits, see equation 2.20. This indicator will then allow us to predict the presence of single orbitals signifying covalent bonds if $\alpha = 0$, slowly varying electron densities suggesting metallic bonds if $\alpha \approx 1$, or overlapping closed shells if $\alpha \gg 1$, where:

$$\alpha = \frac{\zeta - \zeta_W}{\zeta_U} \tag{2.20}$$

The results of this approach have been found to be promising [65]. However, it is important to note that just as GGAs are effectively corrections of LDAs, so are meta-GGAs corrections of GGAs. Thus, with each attempt to go one step further in improving our model by adding further derivatives to our exchange-correlation interaction equation, we must expect an accelerating increase in computational cost.

2.2.5.3 Non-local functionals

It is possible to use a hybrid approach to exchange-correlation functionals which combines the exchange interaction from the Hartree-Fock method [66] with an electron density dependent functional [67]. The Hartree-Fock method approximates a many-body wave function in the form of a single determinant of its constituent spin-orbitals.

As the individual electrons are merely subject to an average non-local potential, correlation interactions between electrons are ignored by this method. This hybrid functional can help correct errors in the electronic structure including the underestimation of band gaps, but at the higher computational cost of applying the Hartree-Fock method while still having to include a DFT functional like a GGA or LDA.

2.2.6 Sampling parameters

When using a plane wave basis set within periodic boundary conditions, DFT implementations become primarily dependent on two sampling parameters: sampling points in reciprocal space (or k-space) and the plane wave basis set cut-off, known as the k-points and cut-off energy respectively.

The sampling of k-points needs to be sufficiently dense to accurately describe the electron density and potential, and thus find the ground state energy. In order to evaluate these terms across the Brillouin zone, k-points can be arranged into a grid. As the spacing of the sampling points is fixed for a given quality of sampling, the

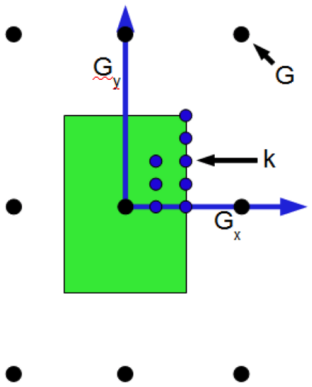

Figure 2.3: An example of a two dimensional single-atom primitive cell being sampled with a minimal number of k-points based on symmetry, leading to the appearance of an irreducible wedge of sampling points [54].

number of points is therefore proportional to the size of the Brillouin zone, and as a result inversely proportional to that of the unit cell.

It may not always be necessary to directly sample every k-point. If there are symmetries in the real space unit cell, then symmetry-equivalent k-points can be assumed to provide equivalent results, reducing the number that need to be explicitly sampled within the grid.

In some cases, this can be compounded over multiple occurrences of line or point symmetry to reduce the sampling to that of a small but irreducible wedge-like shape of the Brillouin zone, see figure 2.3.

Due to symmetry, it may not always be the case that two k-point grids of different densities require a different number of k-points to be sampled. For example, a grid with an odd number N of k-points sampled along one axis would require k-points centered upon the axis to be sampled. However, a grid with an even number N+1 of k-points sampled along said axis would not include k-points centered upon said axis, leading to an equal number of k-points needing to be sampled in both cases.

The cut-off energy of the plane-wave basis set must be determined separately, and may vary substantially depending on the depth of the electron energy wells and radius of the core electrons within the crystal's constituent atoms. Greater and more varied changes in electron state energies across the material can only be realistically simulated with broader sampling of the basis set.

Softer pseudo-potentials may mitigate this effect by reducing the plane wave sampling that would otherwise be used to describe the wave function within core electron shells.

2.3 Band theory

2.3.1 Overview

As mentioned in section 2.2.4, the inner (core) electron orbitals of atoms in a crystal lattice are highly localized and do not overlap with those of other atoms or ions within the lattice. This means that they do not hybridize and instead remain discrete energy levels.

We can solve for the energy levels of non-core electron orbitals by substituting the Bloch form equation 2.10 of the electron wave function into the Schrödinger equation such that [42]:

$$\hat{H}_{\mathbf{k}} u_{\mathbf{k}l}(\mathbf{r}) = \left(\frac{\hbar^2}{2m} \left(\frac{1}{i} \nabla + \mathbf{k} \right)^2 + V(\mathbf{r}) \right) u_{\mathbf{k}l}(\mathbf{r}) = E_{\mathbf{k}l} u_{\mathbf{k}l}(\mathbf{r}) \tag{2.21}$$

where both the potential $U(r)$ and the Bloch function $u_{\mathbf{k}l}(r)$ have the periodicity of the lattice. As the wave vector $\mathbf{k}$ appears as a parameter in the Hamiltonian, each energy eigenvalue varies continuously with $\mathbf{k}$.

Hence we can describe the energy $E_l(\mathbf{k})$ of the lth electron in a lattice as a set of $\frac{L}{2}$ continuous functions that share the periodicity of the lattice, called bands, where L is the number of electrons in the system. This is referred to as a band structure, in which l serves as an index denoting each energy eigenvalue, referred to as an electron energy band.

The Fermi level E_F at zero temperature in a unit cell with L electrons can then be defined as the energy at which the total number of occupied states below E_F is equal to L. The density of states $g(E)$ is the number of electronic states per unit interval of energy, at energy E, and is of the form[42]:

$$g(E) = \sum_l g_l(E), \tag{2.22}$$

where $g_l(E)$ is the density of states of the lth band, and is given by:

$$g_l(E) = \int \frac{d\mathbf{k}}{8\pi^3} \delta(E - E_l(\mathbf{k})). \tag{2.23}$$

However, at non-zero temperatures, the thermal excitation of electrons leads to fractional occupation of electron energy levels above the Fermi level, and fractional emptying of energy levels below the Fermi level, described by a thermally excited form $N(E)$ of the density of states, such that:

$$N(E) = g(E) f(E), \tag{2.24}$$

where we make the approximation that the underlying density of states $g(E)$ is unchanged by the thermal excitation, and $f(E)$ is the Fermi-Dirac distribution function, defined as:

$$f(E) = \frac{1}{e^{\frac{E-E_F}{k_B T}} + 1}, \tag{2.25}$$

where k_B is the Boltzmann constant and T is temperature .

If the difference in energy between the lowest energy unoccupied band and the highest energy occupied band is non-zero, this is referred to as a band gap. Materials that do not have band gaps are typically referred to as conductors, while those with band gaps are typically referred to as insulators.

Semiconductors are materials with narrow band gaps which can nonetheless conduct electrons under certain conditions, such as when sufficiently thermally excited, compressed, doped, and so on. For example, conduction via thermal excitation will occur at temperatures for which $k_B T$ is comparable to the band gap.

The key features of a material's electronic properties can usually be identified by finely sampling the bands in reciprocal space along paths connecting the high symmetry points of the material's Brillouin zone. This allows us to produce a plot of the full range of band energies available across a three-dimensional space, which is the electronic band structure. Electronic band structures are useful for mapping out band maxima and minima, identifying semiconductor band gaps and visualising band curvature in reciprocal space.

In contrast to band-structure calculations, to compute the density of states, one must perform an accurate sampling of the whole Brillouin Zone, typically via sufficiently dense uniform grid sampling. These two tools are complementary. Densities of states provide the overall distribution of energies across the cell, displaying changes in the density of electron states with energy, which are important terms in calculating the transport properties of said electrons, as will be shown in sections 2.5 and 2.6. This is especially true when considering the Seebeck coefficient, which is effectively a measure of the asymmetry in the density of states across the Fermi level.

2.3.2 Applications

It is possible to begin calculating electronic transport properties based on the dispersion of their bands. Thus we can use them to solve the Boltzmann Transport Equation, covered in section 2.5, or use the curvature of a band with respect to energy to identify the effective mass of an electron. These allow us to understand the movement of valence electrons within the material.

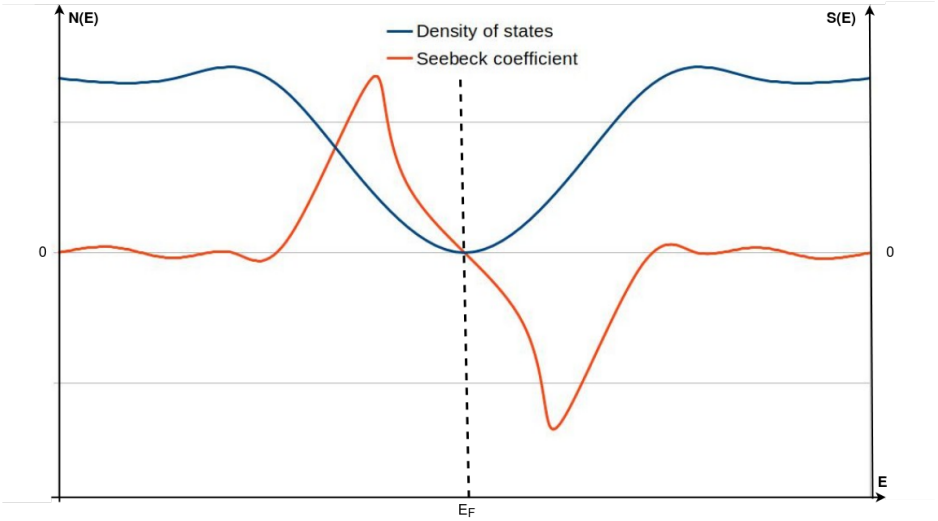

Figure 2.4: Schematic of the Seebeck coefficient $S(E)$ and the density of states $N(E)$ with respect to energy E. The value of the Seebeck coefficient appears to vary proportionally to the average gradient of the DOS across the neighbouring thermal smearing range at each point.

The Seebeck effect is the process by which an asymmetry between thermal electron states above and below the Fermi level drives the charge carriers along a potential created by the thermal gradient. Hence, the amplitude of this effect is correlated to the rate of change of the density of electron states (or DOS) within a k_BT thermal smearing range of the Fermi level as sketched in figure 2.4, and is called the Seebeck Coefficient S, which is defined as:

$$S = -\frac{\Delta V}{\Delta T} \tag{2.26}$$

where ΔV is the change in electrical potential caused by the change in temperature ΔT through the Seebeck effect. The Seebeck coefficient can also be calculated from the Boltzmann Transport Equation (BTE), using equation 2.57, as explained in section 2.5.

Evaluating the Seebeck Coefficient directly from the DOS using the BTE therefore requires a fine sampling across a k_BT range of either the valence band maximum (VBM) or the conduction band minimum (CBM). However, it is also possible to evaluate it across a broader range of electron energies to produce a continuous energy-dependent plot, mapping out peaks and troughs that could be reached via doping in order to optimize thermoelectric efficiency.

Comparing the band structure and the DOS allows us to accurately measure the size of band gaps, and identify whether or not the valence band maximum (or VBM) and conduction band minimum (or CBM) are located at the same k-point . If they are, then the band gap is direct, meaning that electrons merely need to absorb or emit a photon to cross it. If not, then the band gap is indirect, meaning that crossing the band gap requires that the electron be scattered between them via a phononic displacement

and either emit or absorb a photon.

The impact of thermal dependencies can also be accounted for by thermally smearing the electron states in the DOS using either an approximate Gaussian distribution, or a more physically exact Fermi-Dirac distribution. This allows us to track all of the thermal variations in the DOS as a result of varying temperature, typically including the reduction of both band gaps and band energy gradients.

2.3.3 Limitations

Our application of band theory relies on certain simplistic assumptions about our materials. One of them is that our system is infinitely sized which, when considering the difference in scale between our primitive cells and macroscopic devices, has minimal impact beyond the fact that we are ignoring interactions along surfaces and junctions with other materials.

However, we also assume that the material is perfectly homogeneous, which is highly unlikely to be true. A typical manufactured material would include a small percentage of interstitial or substitutive impurities which would have limited electronic impact but may interfere with lattice vibrations, impacting the thermal conductivity.

More importantly, unless the material is manufactured with expensive nano-engineering techniques like the application of single-atom layers, we can expect the formation of grain boundaries. These are likely to scatter both electrons and phonons, thus negatively impacting both forms of conductivity.

Additionally, our approach so far has functioned on the assumption that electrons only interact with the periodic potentials within the lattice. This does not account for electron-electron scattering, which will have to be accounted for later when solving the Boltzmann Transport Equation for electrons.

Similarly, we have not accounted for the impact of electron-phonon scattering on electron transport. This will need to be evaluated separately using deformation potential theory.

2.4 Lattice thermal properties

2.4.1 Phonons

In a typical semiconductor, the dominant type of thermal transport occurs in the form of lattice vibrations. These vibrations can be modelled in the form of quantum mechanical quasi-particles known as phonons, which are described in terms of their

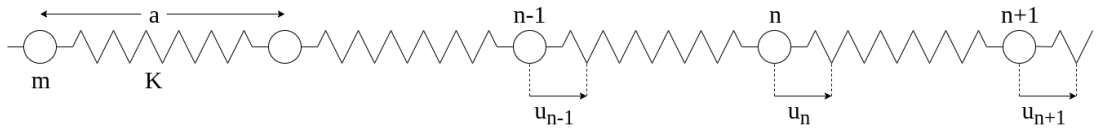

Figure 2.5: Diagram of displacements u along a one dimensional string of identical atoms with mass m and connected by a spring constant K with equilibrium separation a, being applied at and around the nth position.

uniform modes of vibration, or phonon modes. This way, we can calculate lattice vibrations travelling through a lattice in terms of a superposition of phonon modes.

To do so, we must first look at the sum of forces applied to an atom as the forces applied to it by its nearest neighbours. In a one-dimensional string of identical atoms whose inter-atomic forces are treated as springs with a spring constant K, we can derive the equation of motion by combining Newton's second law of motion and Hooke's law [68]:

$$m\frac{d^2u_n}{dt^2} = K(u_{n+1} + u_{n-1} - 2u_n) \tag{2.27}$$

where u_n is a displacement from equilibrium, as shown in figure 2.5, applied to an atom n with mass m such that:

$$u_n = r_n - R_n \tag{2.28}$$

where r_n is the current position of the atom and R_n is its equilibrium position. Equation 2.27 can be solved for displacement, giving us a travelling wave:

$$u_n(t) = \tilde{u}_n e^{i(qx - \omega_q t)} \tag{2.29}$$

where $\tilde{u}_n$ is the amplitude of motion of the nth atom, q is the wavenumber, t is time, ω_q is the angular frequency, and x is the atomic position, such that $x = na$ where a is the inter-atomic distance. From this solution we find the phononic dispersion relation:

$$\omega_q = 2\sqrt{\frac{K}{M}}\left|sin\left(\frac{qa}{2}\right)\right| \tag{2.30}$$

which gives us ω_{max} for $q = \frac{\pi}{a}$ as shown in figure 2.6. This solution can be expanded to a three-dimensional problem by replacing the wavenumber q with a wavevector $\mathbf{q}$, leading to the possibility of a dispersion plot of $\omega_{\mathbf{q}}$ with respect to $\mathbf{q}$ within a cell.

However, to expand to a three-dimensional problem, we need to frame it in terms of three-dimensional unit cells, whose origins are defined with $\mathbf{R}_a$, where $a = (a_1, a_2, a_3)$, labels the cells along three orthogonal directions. These unit cells include atoms labelled with κ, and whose positions are defined relative to the origin of their unit cell, such that:

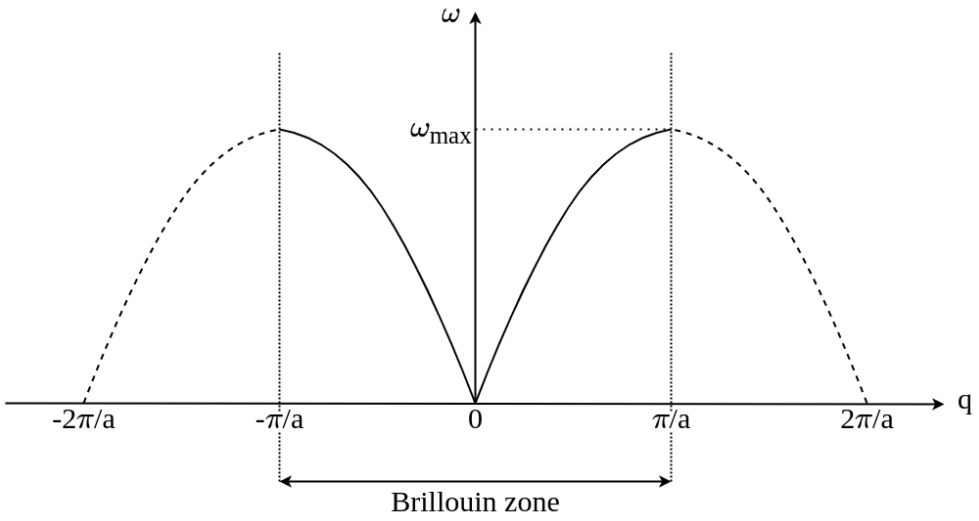

Figure 2.6: Phonon dispersion plot for a 1D chain of identical atoms separated by a distance a. The region between $-\pi/a$ and π/a is the periodic unit cell in reciprocal space, or Brillouin zone.

$$\mathbf{R}_a = a_1\mathbf{a}_1 + a_2\mathbf{a}_2 + a_3\mathbf{a}_3 \tag{2.31}$$

$$\mathbf{R}_{\kappa,a} = \mathbf{R}_a + \mathbf{R}_\kappa \tag{2.32}$$

We can now describe the displacement of an atom in a three-dimensional harmonic system with respect to its displaced position $\mathbf{r}_{\kappa,a}$ and equilibrium position $\mathbf{R}_{\kappa,a}$. From here we perform a displacement-dependent Taylor series expansion of the total potential energy E_{pot} of the crystal:

$$E_{pot} = E^0_{pot} + \sum_{\kappa,a} \frac{\partial E_{pot}}{\partial \mathbf{u}_{\kappa,\alpha,a}} \cdot \mathbf{u}_{\kappa,\alpha,a} + \frac{1}{2}\sum_{\kappa,a}\sum_{\kappa',a'} \mathbf{u}_{\kappa,\alpha,a} \cdot \frac{\partial^2 E_{pot}}{\partial \mathbf{u}_{\kappa,\alpha,a}\partial \mathbf{u}_{\kappa',\alpha',a'}} \cdot \mathbf{u}_{\kappa',\alpha',a'} + \ldots \tag{2.33}$$

where E^0_{pot} is the energy at equilibrium (i.e. zero displacement) and $\mathbf{u}_{\kappa,\alpha}$ is the displacement of an atom κ in the α direction. As forces are zero at equilibrium, we know that the first order derivative must also be 0. The second order derivative accounts for the impact of the displacement of one atom in terms of the force experienced by another atom at equilibrium, and thus includes the effects of some interatomic interactions.

For small displacements, we may assume that higher-order terms can be neglected. Solving the Taylor series expansion of the potential energy using only terms up to second order is called the harmonic approximation. This approximation can only work because it assumes that, as the displacements are small relative to inter-atomic spacing, the second order term is dominant over the higher order ones. The second order term is the matrix of harmonic force constants Φ within the system, of the form:

$$\Phi^{\kappa',\alpha',a'}_{\kappa,\alpha,a} = \frac{\partial^2 E_{pot}}{\partial u_{\kappa,\alpha,a}\partial u_{\kappa',\alpha',a'}} = -\frac{\partial F_{u_{\kappa,\alpha,a}}}{\partial u_{\kappa',\alpha',a'}} \tag{2.34}$$

which is equivalent to the derivative of the force on the atom at $u_{\kappa,\alpha,a}$ with respect to a displacement of a second atom at $u_{\kappa',\alpha',a'}$. The Fourier transform of this quantity is given by:

$$D^{k,k'}_{\alpha,\alpha'}(\mathbf{q}) = \frac{1}{\sqrt{M_\kappa M_{\kappa'}}} \sum_a \sum_{a'} \Phi^{\kappa',\alpha',a'}_{\kappa,\alpha,a} e^{-i\mathbf{q}\cdot\mathbf{R}_a} \tag{2.35}$$

where $\mathbf{q}$ is a displacement wavevector, and the resulting object D is called the dynamical matrix. Along with the 3d analogue of equation 2.29, this can be substituted into Newton's second law, which gives the eigenvalue equation:

$$\omega^2_{q,v} \tilde{u}_{q,v} = D(q) \tilde{u}_{q,v} \tag{2.36}$$

where $\tilde{u}_{q,v}$ are the mass weighted phonon eigenvectors. As a result, we can calculate phonon modes as eigenvectors of the dynamical matrix $D^{k,k'}_{\alpha,\alpha'}(\mathbf{q})$. However, it is important to note that this is a matrix of separable equations of motion for each of 3N phonons for a primitive cell containing N atoms. In other words, each phonon is independent of the other phonons, and so there are no phonon-phonon interactions at this level of truncation of the Taylor expansion.

In an ideal semiconductor (without defects, grain boundaries etc), the scattering of phonons is usually dominated by phonon-phonon interactions, which we have shown to be neglected in the harmonic approximation. We have also neglected electron-phonon interactions (see section 2.6), and so at this level of approximation a phonon emitted across an ideal semiconductor could theoretically travel an infinite distance at a constant velocity, which is clearly unrealistic and would lead to a large overestimate for phonon thermal conductivity. Thus, even for a pristine material our approach needs to account for the anharmonic components of lattice vibrations, in order to compute the phonon lifetimes, and hence a reasonable thermal conductivity.

Just as the second order term is dominant in the harmonic Taylor expansion, we expect that the third order term is the dominant anharmonic term. This means that it can be approximated as the sole non-harmonic term and the determining factor of phonon-phonon scattering frequencies.

2.4.2 Force constant calculations

2.4.2.1 Finite displacement

The force constants of our material can be defined as the proportionality constants relating the displacement of atoms to the forces that they induce, as described by Hooke's law. As such, we can attempt to evaluate them directly by applying finite displacements in either direction along an axis to atoms within the cell, so as to find

the resulting variation in inter-atomic forces, see equation 2.37:

$$-\frac{dF}{du_{\kappa,\alpha}} = -\left(\frac{F^{+}_{\kappa,\alpha} - F^{-}_{\kappa,\alpha}}{2u}\right) \approx \frac{d^2E}{du_{\kappa,\alpha}du_{\kappa',\alpha'}} \tag{2.37}$$

where $F^{+}_{\kappa,\alpha}$ and $F^{-}_{\kappa,\alpha}$ are the forces applied to atoms at $\boldsymbol{r}_{\kappa,\alpha}$ in the positive and negative directions of displacement along our axis. As displacements are periodic within the periodic boundary conditions, we can only directly compute Γ-point phonons with this method. It also has the advantage of being applicable for the calculation of higher order terms of our Taylor series, by combining displacements, so as to evaluate scattering effect.

In practice, this method requires the construction of a supercell containing multiple primitive cells in order to simulate relative displacements at non-zero **q** [69]. While this leads to more computationally expensive calculations when simulating longer range effects, due to the cubic scaling of calculation time with supercell size, recent developments have shown that the use of non-diagonal supercells may help to minimize the size of supercells required[70].

However, cell periodicity also means that the range over which a displacement applies a significant difference in force could result in unwanted overlapping interactions caused by the displacement. We can determine a range such that beyond it, the force constants have decayed to the point as to make the impact of displacement effectively insignificant. Thus, any cell chosen to be twice the size of said range will not incur its overlap as a result of periodicity.

2.4.2.2 Density Functional Perturbation Theory

Alternatively, it is possible to apply perturbation theory [71; 72] to the small amplitude linear response λ to our atomic displacement, by expanding it into a power series, see equation 2.38. Here, we look at a property X with respect to our response, where the zeroth order term $X^{(0)}$ is the property at equilibrium, with $\lambda^n X^{(n)}$ being the nth order corrections. As λ is considered to be small, we can approximate the non-equilibrium contribution as being equal to the first order term in the Taylor expansion:

$$X(\lambda) = X^{(0)} + \lambda X^{(1)} + \frac{\lambda^2 X^{(2)}}{2} \ldots \tag{2.38}$$

In our case, X can refer to the electron orbitals $\phi(\lambda)$ or energy $E(\lambda)$ calculated from our Kohn-Sham equations, or the electron density $n(\lambda)$ or potential $V(\lambda)$. In this series, the expansion coefficient of our properties is defined as:

$$X^{(n)} = \frac{1}{n!}\frac{d^n X}{d\lambda^n}\bigg|_{\lambda=0} \tag{2.39}$$

By fitting the terms impacted by a phononic perturbation into the Sternheimer equation, see eq. 2.40, we find the relation of our $X^{(1)}$ terms to equilibrium properties. As the first order terms are interdependent, we can solve the Sternheimer equation using a self-consistent loop via electron density mixing, similar to our SCF cycles for finding the ground state:

$$\left(H^{(0)}-E_l^{(0)}\right)\left|\psi_l^{(1)}\right\rangle=-V^{(1)}\left|\psi_l^{(0)}\right\rangle \tag{2.40}$$

where $H^{(0)}$ is the unperturbed Kohn-Sham Hamiltonian (as described in equation 2.8), $E_l^{(0)}$ is the unperturbed energy eigenvalue of band l, $\psi_l^{(0)}$ is the unperturbed wavefunction for band l, $\psi_l^{(1)}$ is the first-order change in said wavefunction, and $V^{(1)}$ is the first order change in the Kohn-Sham potential.

This approach does not require that the phonons be necessarily calculated at the Γ-point, and unlike the finite displacement method, does not require the use of a large cell to avoid the overlapping of interatomic forces due to displacement. Instead, the cut-off range of the inter-atomic forces is determined by the sampling density over which the wave function is effectively being perturbed. As a result, such a process is significantly less numerically intensive than the finite displacement method.

2.5 Boltzmann transport theory

2.5.1 The Boltzmann transport equation

To evaluate the transport properties of electrons and phonons, one can solve the Bolzmann transport equation [73; 74; 75; 76], or BTE, see equation 2.41. This equation describes the rate of change in the probabilistic distribution of a large number of particles or quasi-particles in terms of three types of interaction: that with an external applied force, their statistical described diffusion, and their scattering with each other.

$$\frac{df_k}{dt}=\left.\frac{\delta f_k}{\delta t}\right|_{force}+\left.\frac{\delta f_k}{\delta t}\right|_{diff}+\left.\frac{\delta f_k}{\delta t}\right|_{coll} \tag{2.41}$$

The three types of interaction listed above can be found in the three respective terms listed in the equation. This equation must be solved in $6n$ dimensions to account for both the position and momentum of n particles in all three spatial dimensions.

In the case of an external force F applied to the system over a time t, one would expect a change in the position r and the crystal momentum $\boldsymbol{k}$ of an average particle with mass m such that $\Delta r=(\boldsymbol{k}/m)\Delta t$ and $\Delta\boldsymbol{k}=\boldsymbol{F}\Delta t$. We can describe this effect relative to F such that:

$$\left.\frac{\delta f_k}{\delta t}\right|_{force} = \boldsymbol{F} \cdot \frac{\delta f_k}{\delta \boldsymbol{k}} \tag{2.42}$$

The effect of diffusion can be described relative to a particle located at r and travelling at velocity v_k such that its position after Δt is $\boldsymbol{r}+\boldsymbol{v}_k\Delta t$. As such, it can be written as:

$$\left.\frac{\delta f_k}{\delta t}\right|_{diff} = -\frac{\delta f_k}{\delta \boldsymbol{r}} \cdot \boldsymbol{v}_k \tag{2.43}$$

In the case of a system in a state of equilibrium, one would expect the change in the probabilistic distribution to be equal to zero. As such, it is possible in such a situation to define the collision term relative to the two others:

$$\left.\frac{\delta f_k}{\delta t}\right|_{coll} = \boldsymbol{F} \cdot \frac{\delta f_k}{\delta \boldsymbol{k}} - \frac{\delta f_k}{\delta \boldsymbol{r}} \cdot \boldsymbol{v}_k \tag{2.44}$$

While the exact form of the collision term in a state of non-equilibrium is not known, we can now attempt to evaluate the impact on scattering of entering such a state relative to our state of equilibrium.

2.5.2 Application to electron bands

In the case of the electronic BTE, it is relatively straightforward to fill in the external force component, as it is a direct result of the electromagnetic forces, see equation 2.45.

$$\left.\frac{\delta f_k}{\delta t}\right|_{force} = -\frac{e}{\hbar}\left[\boldsymbol{E} + \frac{\boldsymbol{v}_k \times \boldsymbol{B}}{c}\right] \cdot \frac{\delta f_k}{\delta \boldsymbol{k}} \tag{2.45}$$

where e is the electron charge, $\hbar$ is the reduced Planck constant, $\boldsymbol{E}$ is the electric field, $\boldsymbol{v}_k$ is the electron velocity, $\boldsymbol{B}$ is the magnetic field and c is the speed of light. While we do not yet know the scattering term, we can give an analytical description of the transition probability for an electron moving from state k to k', based on a transition rate calculated from Fermi's Golden rule:

$$P_k^{k'} d\boldsymbol{k}' = f_k(1-f_{k'})Q_k^{k'} d\boldsymbol{k}' \tag{2.46}$$

where $Q_k^{k'}$ is the intrinsic transition rate, and is equal to $Q_{k'}^{k}$. We can describe the scattering term when travelling back and forth between the two states as the difference between $P_k^{k'}$ and $P_{k'}^{k}$, such that:

$$\left.\frac{\delta f_k}{\delta t}\right|_{coll} = \int \left(P_k^{k'} - P_{k'}^{k}\right) d\boldsymbol{k}' = \int (f_k - f_{k'}) Q_k^{k'} d\boldsymbol{k}' \tag{2.47}$$

As the equilibrium distribution is constant with respect to time, and we are only interested in phenomena occurring when outside of equilibrium, we can subtract the

equilibrium component $f_{\boldsymbol{k}}^0$ from both states. This allows us to make the relaxation time approximation, where we assume that scattering merely drives non-equilibrium systems back to equilibrium [77]. This means that the rate at which a system returns to equilibrium is proportional to its deviation from equilibrium.

$$\left.\frac{\delta f_k}{\delta t}\right|_{coll} = \int \left[\left(f_k - f_k^0\right) - \left(f_{k'} - f_{k'}^0\right)\right] Q_k^{k'} d\boldsymbol{k}' \approx \frac{f_k - f_k^0}{\tau_k} \tag{2.48}$$

where τ_k is the mean free time between scattering events, also known as the relaxation time. This last part is known as the relaxation time approximation, in which scattering events are assumed to be relaxations events from f_k to f_k^0, which are on average separated by a time τ_k.

Now, to evaluate the electron transport behaviour with respect to the distribution function f_k, we can begin by imagining an electric field applied to an isotropic system along the x-axis, such that its electric current density $\boldsymbol{j}$ takes the form [78]:

$$\boldsymbol{j} = \frac{-e}{8\pi^3} \int \boldsymbol{v}_k f_k d^3\boldsymbol{k} \tag{2.49}$$

where f_k can be described in terms of an equilibrium distribution, to which a perturbation is added in the form of an electric field, such that:

$$f_k \approx f_k^0 + \tau_k \frac{e}{\hbar} E_x \frac{\delta f_k^0}{\delta k_x} \tag{2.50}$$

where E_x is the electric field along x. However, it should be noted that there is no electric current, and therefore no electric current density, in a system with no applied electric potential, meaning that:

$$\int \boldsymbol{v}_k f_k^0 d^3\boldsymbol{k} = 0 \tag{2.51}$$

As a result we can reduce our current density along x to

$$j_x = -\frac{e^2}{8\pi^3} E_x \int v_{k_x}^2 \tau_{k_x} \frac{\delta f_k^0}{\delta E} d^3\boldsymbol{k} \tag{2.52}$$

where E is the electron energy. We can convert our direction specific electric current density j_x to transport distribution $\sigma(E,T)$, where T is temperature, via the relation $\sigma(E,T) = j_x/E_x$. If we then generalise it with respect to directions, we obtain the form:

$$\sigma(E,T) = \tau_k \frac{1}{8\pi^3} \int \boldsymbol{v} \times \boldsymbol{v} \delta(E - E_k) d^3\boldsymbol{k} \tag{2.53}$$

We can now use this function to evaluate the moments of generalized transport coefficients $\mathcal{L}^\alpha$ [79].

$$\alpha = 0,1,2...$$
$$\mathcal{L}^{(\alpha)} = e^2 \int \sigma(E,T)(E-E_F)^{\alpha} \left(\frac{-\delta f_k^{(0)}}{\delta E} \right) dE \tag{2.54}$$

We can then reconstruct a generalised form for electric current density in terms of η, as well as for the electron heat current q:

$$\begin{aligned} j &= \mathcal{L}^{(0)} \boldsymbol{E} + \frac{\mathcal{L}^{(1)}}{qT}(-\nabla T) \\ q &= \frac{\mathcal{L}^{(1)}}{q} \boldsymbol{E} + \frac{\mathcal{L}^{(2)}}{q^2 T}(-\nabla T) \end{aligned} \tag{2.55}$$

By applying additional boundary conditions, we can then obtain the electrical conductivity σ, the Seebeck coefficient S, and the electron contribution to the thermal conductivity κ_e.

$$\sigma = \mathcal{L}^{(0)} = \int \sigma(E) \left(-\frac{\delta f_k^0}{\delta E} \right) dE \tag{2.56}$$

which is found by setting the temperature gradient to zero.

$$S = \frac{1}{eT} \frac{\mathcal{L}^{(1)}}{\mathcal{L}^{(0)}} = \frac{1}{eT} \frac{\int \sigma(E)(E-E_F)\left(-\frac{\delta f_k^0}{\delta E} \right) dE}{\int \sigma(E)\left(-\frac{\delta f_k^0}{\delta E} \right) dE} \tag{2.57}$$

which is the relation between $\boldsymbol{E}$ and ∇T at $j = 0$.

$$\kappa_0 = \frac{\mathcal{L}^{(2)}}{e^2 T} = \int \sigma(E)(E-E_F)^2 \left(-\frac{\delta f_k^0}{\delta E} \right) dE \tag{2.58}$$

which requires by definition that $j \neq 0$. However, as it is always measured at $j = 0$, we must implement $\boldsymbol{E} = S\nabla T$ in the equation for heat flux in equation 2.55 [80]. This results in a new value for the electron thermal conductivity:

$$\kappa_e = \kappa_0 - S^2 \sigma T \tag{2.59}$$

2.5.3 Application to phonons

A similar solution to the BTE can be implemented for phonons, in which we assume the existence of a distribution function $f_{\boldsymbol{q}}$ for phonons $\boldsymbol{q}$ with respect to time and position[68]. As phonons do not have the equivalent to an external electric field force like electrons, our equation only has a diffusion term and a scattering term. For a temperature gradient ∇T causing a variation in temperature T with respect to

position, we can describe the diffusion rate as shown in equation 2.60.

$$\left.\frac{\delta f_{\boldsymbol{q}}}{\delta t}\right|_{diff} = -\boldsymbol{v}(\boldsymbol{q})\cdot\nabla T\frac{\delta f_{\boldsymbol{q}}}{\delta T} \tag{2.60}$$

where $\boldsymbol{v}(\boldsymbol{q})$ is the velocity of the phonon $\boldsymbol{q}$. The total rate of change of our distribution function must be zero in the steady state of heat flow, meaning that the diffusion and scattering terms must balance in the linearised form of the phonon Boltzmann transport equation.

By, once again, defining the transition probability $P_{\boldsymbol{q}}^{\boldsymbol{q}'}$ in terms of the intrinsic transition rate $Q_{\boldsymbol{q}}^{\boldsymbol{q}'}$ we can describe the scattering term of the BTE in terms of the probabilities of scattering from $\boldsymbol{q}$ to $\boldsymbol{q}'$ and from $\boldsymbol{q}'$ to $\boldsymbol{q}$. This allows us to rewrite our linearised Boltzmann transport equation as:

$$-\left.\frac{\delta f_{\boldsymbol{q}}}{\delta t}\right|_{scatt} = \boldsymbol{v}(\boldsymbol{q})\cdot\nabla T\frac{\delta f_{\boldsymbol{q}}^0}{\delta T} \tag{2.61}$$

where f_q^0 is the phonon distribution at thermal equilibrium, which does not change with time. We can then use the macroscopic expression for the transition probability Q with respect to the lattice thermal conductivity κ to calculate the lattice thermal conductivity tensor, see equation 2.62.

$$\kappa_{latt}^{ij} = -\frac{Q^i\cdot\nabla T^j}{|\nabla T|^2} = \frac{1}{N_0\Omega|\nabla T|^2}\sum_{\boldsymbol{q}}\hbar\omega_{\boldsymbol{q}}\psi_{\boldsymbol{q}}f_{\boldsymbol{q}}^0\left(f_{\boldsymbol{q}}^0+1\right)\boldsymbol{v}^i(\boldsymbol{q})\cdot\nabla T^j \tag{2.62}$$

where Ω is the unit cell volume, N_0 is the number of number of sampling points across our cell, $\omega_{\boldsymbol{q}}$ is the phonon frequency, $\psi_{\boldsymbol{q}}$ is a measure of the deviation from thermal equilibrium distribution for our phonon $\boldsymbol{q}$, and i and j denote Cartesian coordinates. Accounting for $\psi_{\boldsymbol{q}}$ is challenging, but we can assume that the norm of ∇T is small enough that we can derive $f_{\boldsymbol{q}}$ as being linearly dependent on ∇T [81]. This allows us use the relaxation time approximation (or RTA) for phonons, as defined in section 2.5.2, and rewrite our equation for our lattice thermal conductivity such that:

$$-\left.\frac{\delta f_{\boldsymbol{q}}}{\delta t}\right|_{scatt} \approx \frac{f_{\boldsymbol{q}}-f_{\boldsymbol{q}}^0}{\tau_{\boldsymbol{q}}} \tag{2.63}$$

$$\kappa_{latt}^{ij} = \frac{1}{N_0\Omega k_B T^2}\sum_{\boldsymbol{q}}(\hbar\omega_{\boldsymbol{q}})^2 f_{\boldsymbol{q}}^0\left(f_{\boldsymbol{q}}^0+1\right)\boldsymbol{v}^i(\boldsymbol{q})\boldsymbol{F}_{\boldsymbol{q}}^j \tag{2.64}$$

$$\boldsymbol{F}_{\boldsymbol{q}}^i = \tau_{\boldsymbol{q}}^i\left(\boldsymbol{v}_{\boldsymbol{q}}^i+\Delta_{\boldsymbol{q}}^i\right) \tag{2.65}$$

where $\tau_{\boldsymbol{q}}$ is the phonon-phonon relaxation time of a phonon $\boldsymbol{q}$, and $\Delta_{\boldsymbol{q}}$ is a measure of how much the phonon distribution, and by extension its associated heat current, deviates from the RTA prediction. As the phonon-phonon relaxation time is dominated by

two- and three-phonon scattering events, which decay quicker with respect to distance, it can be modelled and calculated directly unlike that for electron-electron scattering.

Thus the relaxation time $\tau_{\boldsymbol{q}}^0$ associated with these events is measured by evaluating the second and third order transition rates based on Fermi's Golden rule. While these can be determined from second and third order force constants, only the second order terms are implemented as DFPT calculations, requiring the use of a finite step approach using perturbed supercells to calculate the third order terms. The phonon density of states can then be evaluated from the second order term, while the corrective terms allowing for calculation of a corrected conductivity come from the third order term.

In the case where we assume that grain boundaries have become the dominant source of scattering for phonons, we can redefine our phonon relaxation time as one entirely dependent on grain boundaries. This is called the small-grain limit, and requires the substitution of a new $\boldsymbol{F}_{\boldsymbol{q}}^i$ term, such that:

$$\tilde{\kappa}_{SG}^{ij} = \frac{1}{N_0 \Omega k_B T^2} \sum_{\boldsymbol{q}} \left(\hbar \omega_{\boldsymbol{q}}\right)^2 f_{\boldsymbol{q}}^0 \left(f_{\boldsymbol{q}}^0 + 1\right) \frac{v^i(\boldsymbol{q}) v^j(\boldsymbol{q})}{|\boldsymbol{v}(\boldsymbol{q})|} \tag{2.66}$$

where $\tilde{\kappa}_{SG}^{ij}$ is the proportionality tensor of the lattice thermal conductivity. This term gives us conductivity with respect to a given mean free path defined by the size of the grain, assuming that said mean free path is sufficiently small to dominate phonon-phonon scattering.

2.6 Electron-phonon relaxation times

2.6.1 Deriving the relaxation time

Our approach so far has involved evaluating the properties of electrons and phonons separately, without accounting for their interactions. However, in order to correct our electron transport properties with respect to electron-phonon coupling, we do so by using deformation potential theory, proposed by Bardeen and Shockley [82] and later revised for anisotropic matierals by Herring and Vogt [83].

We are also relying on the assumption that the difference in effective mass between the lattice vibrations and electrons is such that we can treat the impact of electron-phonon scattering on phonons as negligible, and thus ignore its impact on lattice thermal conductivity. However, the impact on electron transport terms is significant, and is therefore determined by evaluating the electron-phonon scattering time, also known as the relaxation time.

A short relaxation time is equivalent to a high electron-phonon scattering frequency, limiting their ability to travel and by extension reducing the electrical conductivity

and electron thermal conductivity. As these transport terms decrease, the relative impact of the lattice thermal conductivity increases as a denominator in equation 2.2 for ZT, thus decreasing ZT. Similarly, as the power factor is proportional to electrical conductivity, it decreases proportionally with the electron-phonon relaxation time.

One way to derive the electron-phonon relaxation time is by starting from a phononic displacement, as in equation 2.29.

$$u_{n,\boldsymbol{q}}(x,t) = \tilde{u}_{n,\boldsymbol{q}} e^{i(\boldsymbol{q}x - \omega_{\boldsymbol{q}} t)} \tag{2.67}$$

where $u_{n,\boldsymbol{q}}$(x,t) is the atomic displacement by a longitudinal acoustic (LA) phonon, where $\tilde{u}_{n,\boldsymbol{q}}$ is its amplitude, $\boldsymbol{q}$ is the wavevector, x is the atomic position, $\omega_{\boldsymbol{q}}$ is the angular frequency, and t is time.

If we assume that the wavelength is much greater than $r \approx 10^{-9}$ meters, then we are operating in the long wavelength limit where $q \ll 1/a$ for an atomic spacing a. We can now calculate the strain ε from a displacement a, such that:

$$\begin{aligned} \varepsilon_{\boldsymbol{q}}(x) &= \lim_{a \to 0} \frac{u_{n,\boldsymbol{q}}(x+a,t) - u_{n,\boldsymbol{q}}(x,t)}{a} \\ \implies \varepsilon_{\boldsymbol{q}}(x) &= i\boldsymbol{q} u_{n,\boldsymbol{q}}(x,t) \end{aligned} \tag{2.68}$$

As we are solely looking at phonon scattering from the perspective of fast moving electrons, we can define a time-independent perturbation Hamiltonian relative to the strain $\varepsilon_{\boldsymbol{q}}$ through a proportionality factor which we will call the deformation potential $D_{\boldsymbol{q}}$.

$$H = iD_{\boldsymbol{q}} \boldsymbol{q} \tilde{u}_{n,\boldsymbol{q}} e^{i\boldsymbol{q}x} \tag{2.69}$$

We can then solve the Hamiltonian for a displacement from $\boldsymbol{k}'$ to $\boldsymbol{k}$ such that $\boldsymbol{k} + \boldsymbol{q} = \boldsymbol{k}'$.

$$\left|H_{\boldsymbol{q}}\right| = \frac{D_{\boldsymbol{q}} \boldsymbol{q} \tilde{u}_{n,\boldsymbol{q}}}{V} \left| \int_V e^{i(\boldsymbol{k} - \boldsymbol{k}' + \boldsymbol{q})x} d^3x \right| \approx D_{\boldsymbol{q}} \boldsymbol{q} \tilde{u}_{n,\boldsymbol{q}} \tag{2.70}$$

where we can give a definition of $\tilde{u}_{n,q}$ as:

$$\tilde{u}^2_{n,\boldsymbol{q}} = \frac{\hbar}{2\omega_{\boldsymbol{q}} \rho V} l \tag{2.71}$$

and h is the Planck constant, $\omega_{\boldsymbol{q}}$ is the angular frequency of the LA phonon, ρ is the mass density of the material, V is the displaced volume, and l accounts for the number of atoms displaced by the phonon. As we are operating in the long wavelength limit and thus $l \gg 1$, we have

$$l \approx \frac{k_B T}{\hbar \omega_{\boldsymbol{q}}} \tag{2.72}$$

where k_B is the Boltzmann constant. We can now use the dispersion relation to

redefine our Hamiltonian.

$$|H_q| = \frac{D_q}{v_q}\left(\frac{k_B T}{2\rho V}\right)^{1/2} \tag{2.73}$$

where v_q is the phonon velocity, which when calculated for acoustic phonon modes is the sound velocity. We then apply Fermi's golden rule to define our transition rate $W_{kk'}$ between the states k and k' [84]:

$$W_{kk'} = \frac{2\pi}{\hbar}\sum_q |H_q|^2\left[G_q\delta\left(E_k - E_{k'} + \omega_q\right) + \left(G_q + 1\right)\delta\left(E_k - E_{k'} - \omega_q\right)\right] \tag{2.74}$$

where E is the energy as a function of state k or k' and G_q is the equilibrium distribution of phonons, as given by a Bose Einstein distribution. We can now evaluate the relaxation time τ_k in terms of the transition rate:

$$\frac{1}{\tau_k} = \sum_{k'} W_{kk'}[1 - cos\theta_{kk'}] \tag{2.75}$$

where $\theta_{kk'}$ is the scattering angle between k and k'. For temperatures of a few hundred kelvin, $\hbar\omega_q \ll k_B T$, which means that $N_q \gg 1$. This allows us to approximate the relaxation time as:

$$\frac{1}{\tau_k} = \frac{\pi D_q^2 k_B T}{\hbar v_q^2 \rho V} N(E) \tag{2.76}$$

where $N(\varepsilon)$ is the number of electron states at energy ε. This is commonly described by the Sommerfeld model as:

$$N(\varepsilon) = \frac{\sqrt{2}m^{3/2}}{\pi^2\hbar^3}E^{1/2} \tag{2.77}$$

However, it should be noted that the free-electron model assumes that there are allowed energy values from 0 to ∞, including at the Fermi energy [85]. This gives us:

$$\frac{1}{\tau} = \frac{\sqrt{2}D^2 m^{3/2} k_B T}{\pi\hbar^4 v_s^2 \rho V}E^{1/2} \tag{2.78}$$

If we then average the relaxation time over energy and reinterpret the sound velocity and mass density in terms of the longitudinal elastic constants c_{ii}, we obtain:

$$\frac{1}{\tau} = \frac{3D^2 m^{3/2}(k_B T)^{3/2}}{2\sqrt{2\pi}\hbar^4 c_{ii}}. \tag{2.79}$$

It is important to note the loss of energy dependency between equation 2.76 and equation 2.79, as the latter assumes an average over energy. This may result in significant error if there is significant variation in the asymmetry across the energy of

states within the range that is studied. Additionally, this approximation relies heavily on the Sommerfeld (or free-electron) model, which assumes that electron states are allowed for all energies, and that the interactions between ions and valence electrons are very weak. This is mostly true in the case of metals, but significantly less so in the case of semi-conductors, whose Fermi energies lie in a band gap. As a result, results coming from this solution may be numerically unstable for non-physical reasons.

However such a compromise is still common in the field, descending from the analytic workaround that was necessary at the time when Bardeen and Shockley published their initial paper on deformation potential theory. The ability to directly evaluate the density of electron states around the Fermi energy through density functional theory, while accounting for the impact of the thermal smearing of electrons, means that the value of $N(E)$ has now become obtainable.

We will look at the traditional approach to evaluating the energy independent version of τ, as well as propose an energy dependent method used for greater versatility in situations where effective masses can be difficult to approach, and to account for energy dependence. As such, the rest of this section will focus on the calculation of the terms found in equations 2.76 and 2.79.

2.6.2 The deformation potential

One challenge involved in evaluating the impact of electron-phonon coupling on electron conductivity is defining the actual effect that a perturbation of the lattice has on the electrons within it.

A solution to this problem was developed by Bardeen and Shockley [82], which involved viewing lattice vibrations as static deformations of the material due to the relative speed of electrons. The varying nature of these deformations would result in a slight variation of the effective periodic potential of the lattice. Over short distances this potential would appear to vary linearly.

This varying potential due to deformation, known as the deformation potential which was incorporated in equation 2.69, would then impact the conductivity of the thermal electrons of interest, which are those at the VBM and CBM. As such, that is where the deformation potential must be measured. It can be formulated as described in equation 2.80:

$$D_{ij} = \frac{dE^{BE}}{d\varepsilon_{ij}} \tag{2.80}$$

where D_{ij} is the deformation potential, i and j are its lattice indices, E_{ij}^{BE} are the band extrema, which is to say the valence band maximum and conduction band minimum,

and ε_{ij} is a strain of a lattice vector defined by ij. We can then define this strain as in equation 2.81, where α_{ij}^{S} and α_{ij}^{0} are the deformed and equilibrium lattice vector components respectively, and $\delta_{ij} \ll \alpha_{ij}^{0}$.

$$\varepsilon_{ij} = \frac{\alpha_{ij}^{S} - \alpha_{ij}^{0}}{\alpha_{ij}^{0}} \tag{2.81}$$

Deformation potentials can be separated into longitudinal deformation potentials, for $i = j$, and shear deformation potentials, for $i \neq j$. In isotropic and mildly anisotropic materials, it is likely that $|\delta_{ij}|$ may be the same for all values of i and j. However, highly anisotropic materials may substantially vary the width of the linear region of their deformation potentials for different directions.

2.6.3 The effective mass approach

2.6.3.1 Effective mass calculations

One key component of evaluating the mobility of electrons in a lattice is accounting for their difference in motion when compared to particles in a vacuum. These differences result from their interaction with the periodic potential across the material and defining them can be challenging. One way to simplify this problem is to view it as a variation of the apparent mass of the electron, known as its effective mass m^*, which is typically described in terms of the electron rest mass m_e.

To derive it, one can start by looking at the kinetic energy of the electron in a vacuum.

$$E = \frac{\hbar^2 k^2}{2m_e} \tag{2.82}$$

From here we can calculate the acceleration a of the electron when subjected to a force F by taking it as the time derivative of the velocity $\frac{1}{\hbar}\frac{dE}{dk}$.

$$a = \frac{dv}{dt} = \frac{d}{dt}\left(\frac{1}{\hbar}\frac{dE}{dk}\right) = \left(\frac{1}{\hbar}\right)^2 \frac{d^2E}{dk^2}\frac{d(\hbar k)}{dt} \tag{2.83}$$

We can also define said force F in terms of the work done dE and the velocity.

$$F = \left(\frac{1}{\hbar}\frac{dE}{dk}\right)^{-1}\frac{dE}{dk}\frac{dk}{dt} = \frac{d(\hbar k)}{dt} \tag{2.84}$$

From here we can find that the effective mass as a result of the force applied F.

$$\frac{1}{m^*} = \frac{a}{F} = \frac{1}{\hbar^2}\frac{d^2E}{dk^2} \tag{2.85}$$

where we find that the effective mass of an electron can be found as the second order

derivative of the electron energy with respect to position. However this derivative is dependent on the axis in which it is measured, and so should result in different relaxation times depending on direction of travel.

However, we want to average them over three orthogonal axes x, y and z in order to obtain the effective mass m^*_{cond} of the total carrier density for the sake of calculating the conductivity, which could thus be directly applied to the DOS. As these are dependent on parabola that may vary in width and thus stencil size depending on the axis of measurement, we can calculate an effective mass from their average curvature.

$$m^*_{cond} = 3\left[\frac{1}{m^*_x}+\frac{1}{m^*_y}+\frac{1}{m^*_z}\right]^{-1} \tag{2.86}$$

2.6.3.2 Elastic constants

The original approach to deformation potential theory by Bardeen and Shockley [82] stated that the mobility of electrons and holes was primarily determined by their scattering on acoustic lattice vibrations and lattice defects, such as impurities. This allowed them to make the assumption that an electron in relatively pure material would only ever scatter against acoustic phonons of comparable wavelength, as described classically. This is due to thermal electrons having wavelengths that are substantially longer than the lattice constant.

To describe these lattice vibrations, the materials' resistance to thermal deformation needed to be accounted for, and this was done by evaluating its elastic constants c_{ij}. Specifically, Bardeen and Shockley chose to focus on longitudinal vibrations on the basis that they would be dominant, which narrows the elastic constants of interest to c_{ii}.

They then described them for different directions of propagation within a cubic crystal based on the assumed knowledge of c_{11}, c_{12} and c_{44}, see equation 2.88. These particular constants are selected in the case of a cubic lattice as c_{11} is the constant for axial compression, c_{12} that for dilation on compression along an orthogonal axis, and c_{44} is the constant for shear strain. Thus in an isotropic cubic system we find:

$$\begin{aligned} c_{11} &= c_{22} = c_{33} \\ \upsilon &= c_{44} = c_{55} = c_{66} \\ K &= (c_{11}+2c_{12})/3 \end{aligned} \tag{2.87}$$

where υ is the shear modulus and K is the bulk modulus.

These directions of propagation were selected on the basis that in isotropic systems, the three possible polarisations consist of one longitudinal mode and two transverse modes. In a cubic crystal, the same is then assumed for waves propagating in the (100),

(110) and (111) directions, which lie along symmetry axes. Transport in other directions can then be given in terms of a mixing of longitudinal and transverse polarisations.

$$\begin{aligned} (100)\ \ c_{ii} &= c_{11} \\ (110)\ \ c_{ii} &= \frac{1}{2}(c_{11}+c_{12}+2c_{44}) \\ (111)\ \ c_{ii} &= \frac{1}{3}(c_{11}+c_{12}+4c_{44}) \end{aligned} \tag{2.88}$$

This approach treats (100) and (111) as extremes between which waves will find themselves in all other directions of propagation. Variations in the values of c_{ii} are considered small for isotropic or near-isotropic materials, limiting the source of error.

Vogt and Herring [83] undertook a more adaptive method to account for limited anisotropy, offering a table of longitudinal and transverse phonon contributions in calculating the squared matrix element for scattering, accounting for both the direction of phonon propagation and that of charge carrier incidence. This relied on the use of an indicator term c^* to evaluate the elastic anisotropy of the material, see equation 2.89. By using this term as a corrective coefficient, they were able to produce generalised forms for the components of the elastic constant matrix.

$$c^* = c_{11} - c_{12} - 2c_{44} \tag{2.89}$$

This approach allowed for an approximation of the anisotropic properties of a cell by calculating an azimuthal average of sampling points, like those in a Lebedev grid [86]. This came at the cost of increased analytical complexity and would be difficult to adapt to non-cubic systems using a generalised method.

However, these approaches were developed to solve the challenge of identifying the elastic constants of unit cells within a material that could only be tested experimentally at a macroscopic scale. If one can apply longitudinal deformations directly to a unit cell, such as through a set of DFT calculations, it is possible to directly measure the elastic constants, both from the longitudinal and shear, merely by expanding lattice parameters along x_{ij}, where $i = j$ for the Young modulus, and $i \neq j$ for the shear modulus. In such a situation, one can can calculatue the elastic constants from:

$$\Xi_{ij} = c_{ijkl}\varepsilon_{kl} \tag{2.90}$$

where Ξ_{ij} are the stresses, that are derivatives of energy, correlated to the strains ε_{kl} that caused them, through the fourth order tensor of elastic constants c_{ijkl}. assuming that the system was at its ground state before displacement, and that the amplitude of displacement does not exceed the parabolic energy region around the ground state.

One may expect individual atoms in a deforming cell to travel towards the lowest

local energy states with respect to the deformed lattice parameters. Hence, ensuring that those states are determined and implemented for each deformation may be necessary to avoid overestimating the elastic constants.

2.6.4 The electron density of states approach

2.6.4.1 Sound velocity

As described in equation 2.76, it is possible to evaluate an energy-dependent relaxation time for electron-phonon scattering. This requires a value for the sound velocity within the material, and a physically accurate depiction of the DOS.

The sound velocity, which is effectively the group velocity of propagation of phonons, can be calculated using the acoustic phononic dispersion relation, as shown in equation 2.91. As such, it can be evaluated as the gradient of dispersion from the Γ-point along the dispersion curve.

$$v_g = \frac{\partial \omega}{\partial k} \tag{2.91}$$

Due to the three dimensional nature of our materials, we must also account for the differences in velocity between the longitudinal and transverse group velocities, which split into three branches in our dispersion curves. Longitudinal phonons tend to travel substantially faster than transverse ones, making them easier to identify, and have a dominant impact upon the relaxation time. As such, we may want to approximate the longitudinal phonon group velocity as the sound velocity for our purposes, as opposed to using an average with an unknown weighting.

Alternatively, it may be possible to use experimental values of the sound velocity, as it is relatively easy to find for many materials, and phonon calculations of multiple phonon sampling points within close proximity to ensure an accurate and linear dispersion may be quite computationally expensive.

2.6.4.2 Thermally smeared electron density of states

To evaluate the electron-phonon relaxation time across a range of energies, we need a well-sampled electron DOS to give us a detailed picture of the band gap and band edges. However, as equation 2.76 describes τ in a temperature-dependent form, we also need to account for temperature dependence in our DOS.

Our default DOS calculations approximate the ground state of our system, which accounts for the hybridisation of electron orbitals due the Pauli exclusion principle, but does not account for the thermal excitation which would cause further smearing

of the electron states. This can be approximated with a Gaussian distribution, but is best calculated using the Fermi-Dirac distribution itself, as written in equation 2.92.

$$f = \frac{1}{e^{(E_k - E_F)/(k_B T)} + 1} \tag{2.92}$$

where $f(k)$ is the average number of electrons in a state k, E_k is the energy of an electron at that state and E_F is the Fermi level, which is assumed to be in the middle of the band gap. This formula is only valid on the condition in which adding a single electron would not significantly change the position of the Fermi level, which our periodic lattice satisfies.

This formula can be translated to a band of continuous energy states in the form of an identically formulated Fermi function $F(E)$. This function can then be multiplied by the degeneracy $g(E)$ at energy E, which is merely the DOS value at that point, to give a thermally corrected density of states $N(E)$, as expressed in equation 2.93.

$$N(E) = \frac{g(E)}{e^{(E - E_F)/(k_B T)} + 1} \tag{2.93}$$

This gives the electronic term for the electron-phonon relaxation time correction, accounting for the thermal smearing of electrons. In principle, this should allow for the estimation of electron-phonon relaxation times at any energy and along any direction, assuming we also have the deformation potential and sound velocity, as per equation 2.76. However, this assumes perfect knowledge of the combined deformation potential contributions of each smeared band within a $k_B T$ energy range of the Fermi level, as described by equation 2.92, and along every direction.

Chapter 3

Methods

3.1 General Workflow

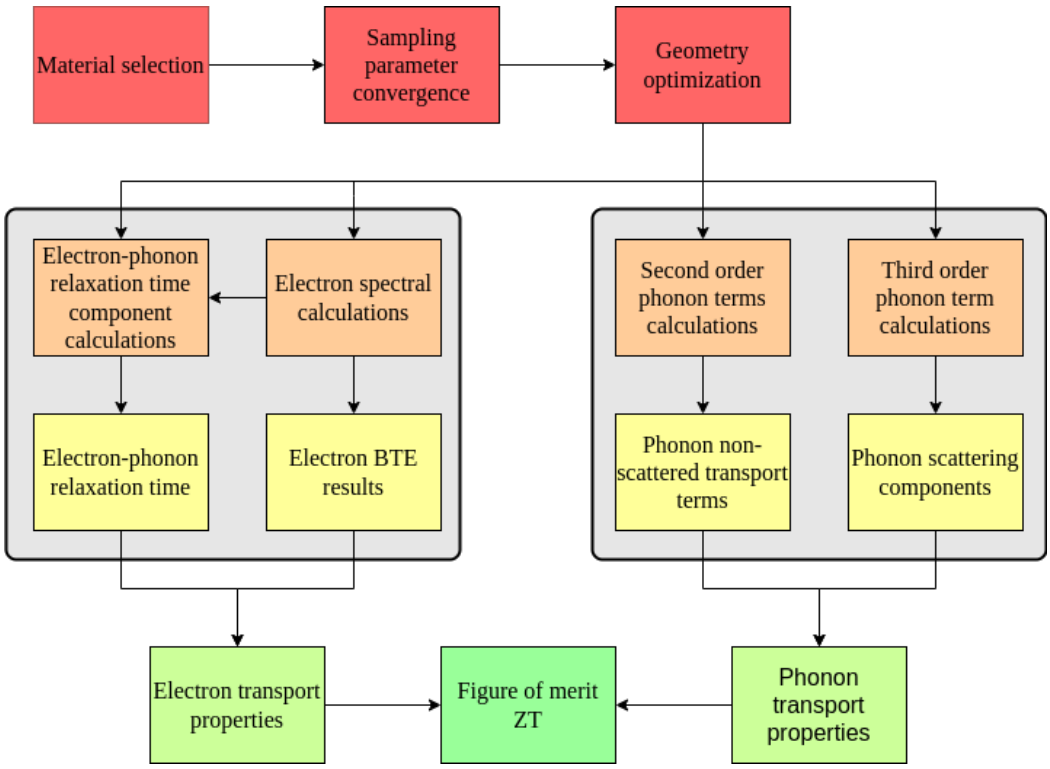

Figure 3.1: Workflow using the thermally smeared density of states approach. Here we see that the calculations are split into two sections. On the left, we evaluate the electron-phonon coupling terms and density of states used to evaluate the electron-phonon relaxation time and the derivation of the uncorrected electron components by solving the electron Boltzmann transport equation. These are then combined to produce the correct electrical conductivity, the corrected electron thermal conductivity and the Seebeck coefficient. On the right, we see the separate calculation of the second and third order phonon terms that are then combined to solve the phonon Boltzmann transport equation and derive the lattice thermal conductivity.

We depend on a structured workflow to study our individual compounds. This is

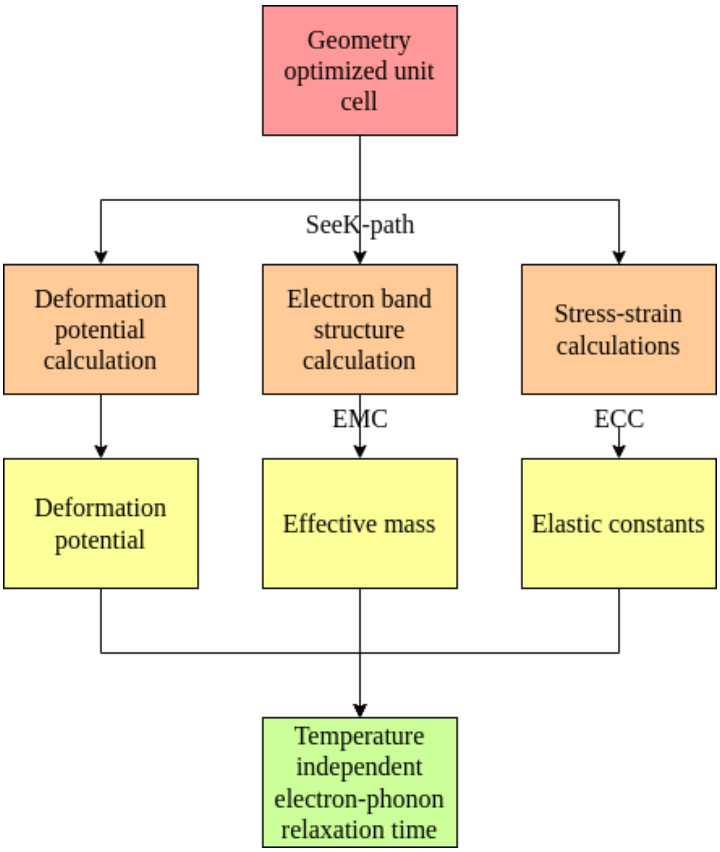

Figure 3.2: Workflow for calculating the relaxation time using the effective mass and elastic constants.

done by first selecting a material and obtaining its crystal structure from a database [87], after which we converge our sampling parameters, optimize its geometry for further calculations, and then take a branching approach to calculate its individual electronic and phononic properties. These culminate in the estimation of each term necessary for solving the equation for the figure of merit ZT.

This workflow also has two variations, as the electronic component depends upon the electron-phonon relaxation time, which can be evaluated either by using the elastic constants and effective mass, or by using a thermally smeared density of states and sound velocity.

While both approaches attempt to estimate the relaxation time, only the latter approach allows for a thermally dependent relaxation time to be calculated. Due to this, and also its greater versatility, the second approach was considered preferable for most of the compounds studied.

Despite the impact of using a thermally averaged value of the relaxation time, both methods were applied on the α-phase of As_2Te_3 to determine whether or not they could be found to produce consistent results.

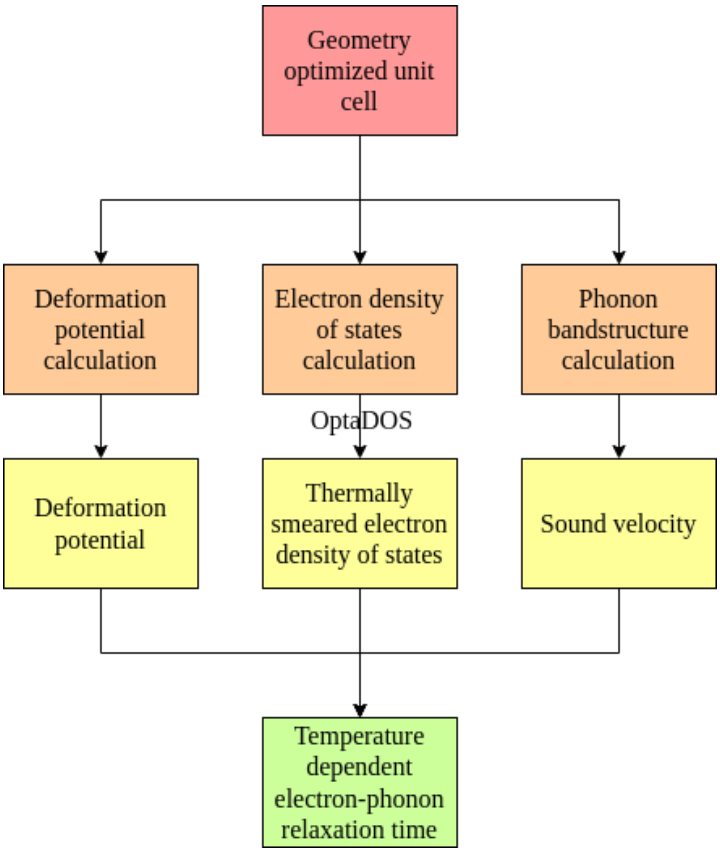

Figure 3.3: Workflow for calculating the relaxation time using the thermally smeared density of states approach.

3.2 Initial material selection

Considering the patterns found in effective thermoelectric materials so far, a preliminary look at potentially thermoelectric compounds can be performed by using the periodic table as a support. Here we find that alloys made of elements in the carbon or pnictogen groups and in the chalcogen groups appear to show promise in their electronic structures.

Additionally, the combination of atoms with large differences in mass appears to be effective for scattering phonons, thus reducing the thermal conductivity of the material. As a result, it may be preferable to construct alloys with elements from different rows of the periodic table.

A more in-depth approach may be the application of predictive algorithms using machine learning to utilize the screening of large numbers of compounds in identifying the potential presence of properties that are beneficial to thermoelectric function.

One such example was a random forest software called Citrination [88], which was trained using the data from 25000 compounds. It uses a coefficient based predictive system to identify how likely various properties may be to support thermoelectric flow. The focus of this structure is on the Seebeck coefficient, the electronic resistivity,

the thermal conductivity, and the band gap. Machine learning has also been used to attempt to predict and develop promising structures based on genetic algorithms [89].

By inputting known compounds with varying thermoelectric efficiencies, such as Si on the lower end or Bi_2Te_3 on the higher end, we find that its predictions give us a general idea of their applicability. It appears to show that Si has poor electrical and thermal conductivities, fitting its limited use in bulk as a thermally sensitive semiconductor, while Bi_2Te_3 is predicted to offer effective power factor components, fitting known studies of the material [90].

It is important, however, to account for the relatively high importance of the Seebeck coefficient component, which requires fine sampling of the Brillouin zone to identify its peaks. This seems to present a challenge for tools like Citrination, which appears to show a limited range of values for its Seebeck coefficient predictions, along with some amount of instability.

Such tools can still prove useful when screening known structures that have been subjected to limited study. This allows us to deconstruct our screening of material properties in terms of component terms, which can then be compared to early calculation results to identify if the predicted properties appear realistic.

3.3 Initial calculation parameters

3.3.1 Initial DFT parameters

As mentioned in section 2.2.6, two sampling parameters that must be used to accurately calculate the electron density during a DFT calculation are the k-point grid and the cut-off energy for the basis set of wave vectors G. As a reminder of equation 2.12, the wave function can be described as:

$$\psi_{kl}(\mathbf{r}) = \sum_{\mathbf{G}} c_{Gkl} e^{i(\mathbf{G}+\mathbf{k})\cdot\mathbf{r}} \tag{3.1}$$

and the electron densities $\rho(\mathbf{r})$ calculated via DFT can be described for a three-dimensional material as described in equation 2.7:

$$\rho(\mathbf{r}) = \sum_{l=1}^{N} |\psi_l(\mathbf{r})|^2. \tag{3.2}$$

Hence, as the basis set is truncated and the k-points calculated are finite, the accuracy of these summative approximations improve with higher k-point grid densities and cut-off energies. However, increasing either the number of k-points on the sampling grid or the number of G-vectors in the basis set will lead to higher computational

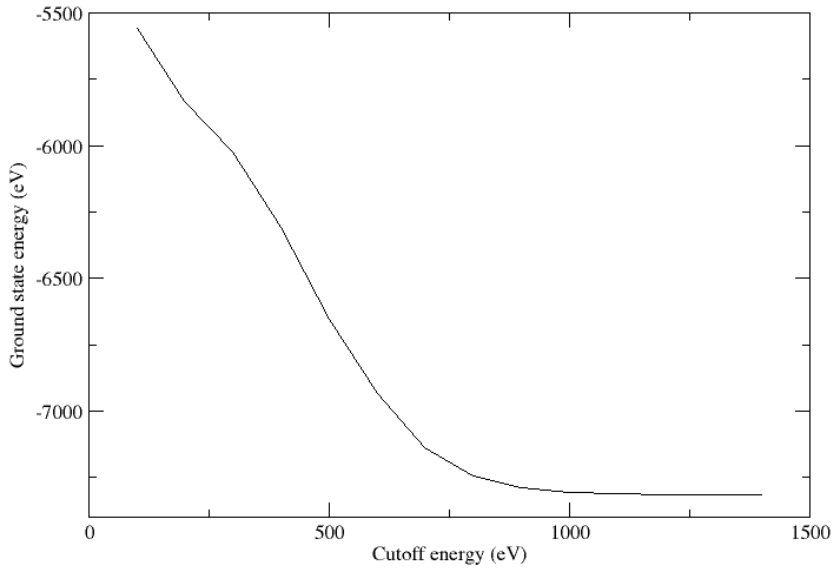

Figure 3.4: Example of a parameter convergence plot for the cut-off energy of As_2Te_3.

cost. Hence the goal should be to minimise these parameters while still producing results within a predetermined acceptable error range. The targeted output selected as a measure of convergence in this body of work was the total energy of the unit cell, for which the acceptable tolerance was set to no more than 1 meV per atom.

One method for this is known as iterative convergence, a process by which a single-point energy calculation is repeated while iteratively increasing the sampling parameters. For example, if a calculation is repeated over a sequence of n different evenly spaced cut-off energies, then we know that it is converged at n if $E_n - E_{n+m}$, where m is a natural number, is lesser or equal than the acceptable error range. As the effect of the change in the sampling parameter between successive iterations grows smaller and smaller, performing $n+1$ iterations is often sufficient to identify the value of n for which the sampling parameter gives a converged output answer. However, as there are sometimes discontinuities in E as n increases, especially in the case of the cut-off energy, it is safer to perform $n+3$ or more iterations to ensure that convergence within the targeted range does indeed occur at n.

Examples of iterative cut-off energy and k-point convergence results are included in figures 3.4 and 3.5 respectively.

3.3.1.1 K-point sampling

The k-point grid is generally assumed to have the same number of dimensions as the material modelled, and to require the same sampling density in all dimensions

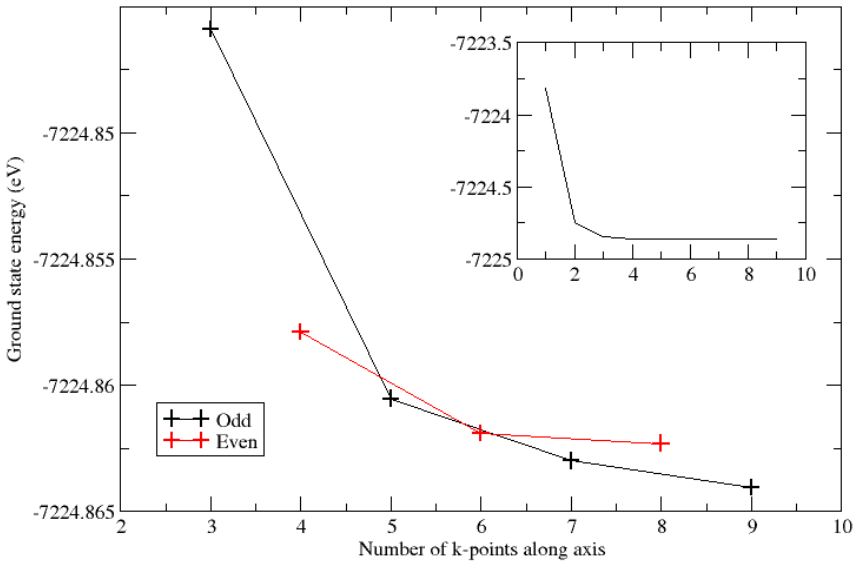

Figure 3.5: Example of a parameter convergence plot for the k-point grid of the β-phase of As_2Te_3. The sampling density required was found to be the same along each axis for this primitive cell, which is elongated along the xyz direction but otherwise highly symmetrical, so the unit given as the number of k-points along the axis in this figure applies to all three axes of the unit cell. The even and odd numbers of k-points are colour coded to highlight the difference in their convergences. This is due to the even grid not having been offset in this example to sample the Γ-point, demonstrating its significant impact on the final energy. The inset figure shows a broader range of convergence starting at a single k-point.

for isotropic cells. In order to ensure consistency in the calculated energy values, some k-point grids may need to be offset in order to always place a k-point at the Gamma-point of the cell. It is essential not to over-converge in order to not waste computational resources. For k-point grids in three dimensional isotropic cells, any number of extra k-points p added to the optimally converged number n will lead to a difference in the number of points sampled equal to $(n+p)^3-n^3$.

Symmetry in a unit cell allows for a reduction in the number of points sampled, as many are equivalent under said symmetry. Repeatedly reducing a sampling grid via symmetry operations reveals a wedge shaped segment of the Brillouin zone that contains the minimum number of k-points that need to be sampled in order to extrapolate the properties of the material. This may be referred to as an irreducible wedge.

However, this reduction in the number of k-points sampled via symmetry operations may further exacerbate the relative impact of over-convergence, as demonstrated in figure 3.6. This is because the step-wise nature of increasing sampling can, when accounting for symmetry equivalencies, lead to a disproportionate increase in com-

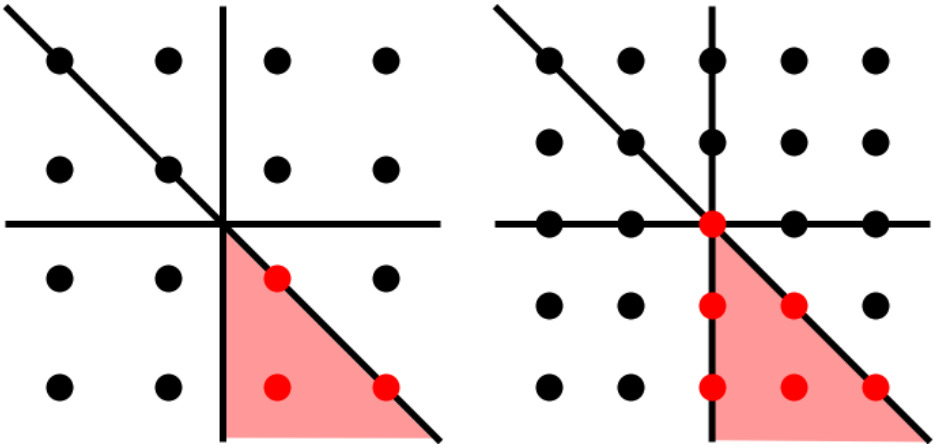

Figure 3.6: Examples of 4 by 4 and 5 by 5 grids reduced to sampling wedges, coloured in light red, through three reflection symmetry operations (across horizontal, vertical and diagonal axes). The sampled points (in bright red) are the ones that are either inside or along the sides of the wedge. It is worth pointing out that a mere shift from 4 to 5 k-points along each axis of this 2-dimensional example still resulted in an effective doubling of the sampling required once symmetry operations are applied.

putational cost.

3.3.1.2 Plane-wave sampling

The cut-off energy is a one dimensional convergence parameter that is greatly impacted by the pseudopotentials selected. Ultrasoft pseudopotentials typically require much lower cut-off energies than norm-conserving ones. However, ultrasoft pseudopotentials may introduce plateaux and sudden steps in the variation of the ground state energy as the cut-off energy increases, requiring higher numbers of convergence iterations than is expected to ensure that convergence conditions were satisfied.

While ultrasoft pseudopotentials were occasionally used during test calculations, the results presented in this thesis were all done with norm-conserving pseudopotentials. This was decided as the former were not implemented for perturbation calculations in CASTEP, which are used to obtain the phonons, and all results needed to be produced using consistent DFT parameters.

It may be worth noting that while DFT calculations can be distributed over multiple cores (or parallelised) for either of these sampling parameters, G-vector parallelisation is generally less efficient than k-point parallelisation, especially when parallelising over less than 1000 G-vectors per core. As such, the number of G-vectors being sampled when there are few k-points can act as a bottleneck for parallelising DFT calculations efficiently.

3.3.2 Initial calculations

3.3.2.1 Singlepoint calculation

Singlepoint energy calculations involve evaluating the system energy based on a set electron density, after which the density is altered in a manner that is predicted to reduce the energy. During each step, the current and previous densities are mixed and the energy is re-evaluated to identify whether convergence has been reached. This self-consistent loop is repeated until the system energy has converged to within a set tolerance, typically one microelectronvolt per atom.

This process is performed at the start of each calculation, from geometry optimizations, to spectral or phonon calculations, as they use the resulting electron density as their basis. It is also used as the tool by which parameter convergence is performed, both for the cut-off energy and the k-point sampling.

Fortunately, being the simplest available type of DFT calculation, it is relatively cheap, and as a result can be used as a quick preliminary calculation to compare energies between different phases, which is useful when testing unknown configurations. Additionally, the CASTEP software allows one to produce a ”checkpoint” file which stores that data produced during a calculation, such that it can generally be reused in other calculations using the same unit cell and convergence parameters so as to reduce computational expense.

Singlepoint calculations are also an iteratively repeated component of many other processes, including the evaluation of each geometry in geometry optimisations and the energy calculation of perturbed supercells in finite step phonon calculations. It is also the dominant source of computational cost when evaluating the deformation potential of materials, although these need only be performed at the VBM and CBM, making them comparatively cheap.

Finally, the progression of the energy during the self consistent loop can occasionally serve as a marker of instability if it fails to converge or makes use of a large number of irregular steps. As such, singlepoint energy calculations can inform us of errors included in the cell, unlikely configurations or unrealistic applications of deformations or perturbations.

3.3.2.2 Geometry optimisation

The process of geometry optimisation is aimed at adjusting the configuration of atoms and lattice parameters so as to match a ground state optimum. This is necessary as the optimised geometry may vary slightly when comparing DFT results to experimental ones, or when changing between pseudopotentials or exchange-correlation functionals.

Example input files for a geometry optimization of one of the materials studied in the results chapters are included in appendix A.

The process begins with a singlepoint calculation so as to find the energy of the system, after which an algorithm displaces them, and the singlepoint calculation is repeated. This process continues until the energy of the system reaches a minimum matching the ground state configuration.

The displacement is determined by a mathematical search for the point at which internal forces converge to zero, which is also the first order derivative of the system energy with respect to its position vector. The curvature of this function is determined by a matrix of second-order partial derivatives of energy, known as a Hessian.

This way, the Hessian is used to determine a difference in the vector position that is predicted to reduce the energy. Once the new energy has been calculated and compared to the previous one, the process can either be stopped if the energy has been converged to within an uncertainty of under one meV per electron, or a new set of positions can be generated.

The number of iterations can increase depending on the sensitivity of the functional used and variation from optimum, or even never realistically achieve convergence within an allotted time if the cell is unstable or too far from its optimised geometry. As such, geometry optimisations can be used to screen for serious errors or problems with either the atomic configuration or the lattice parameters.

A non-relaxed crystal structure may not always offer obviously incorrect data, but the additional uncertainty may be difficult to determine. It can also produce inconsistent values when calculating the deformation potential and elastic constants, and lead to instability during phonon calculations.

The LBFGS algorithm [91] was used as the geometry optimisation algorithm in our CASTEP calculations, and is a low-memory version of the BFGS algorithm [92], named after Broyden, Fletcher, Goldfarb and Shanno. It can optimize for both zero stress and force, allowing it to adjust both lattice parameters and atomic coordinates simultaneously. It also differs from the BFGS by storing a reduced number of inverse Hessian updates, meaning that its memory requirements scale linearly instead of as a function of the square of the system size.

3.4 Electronic properties without phonon scattering

3.4.1 Electronic DFT calculations

To find the electronic properties of a periodic system, one may first calculate its electron states, using equation 2.21:

$$\hat{H}_{\mathbf{k}} u_{\mathbf{k}l}(\mathbf{r}) = \left(\frac{\hbar^2}{2m} \left(\frac{1}{i} \nabla + \mathbf{k} \right)^2 + V(\mathbf{r}) \right) u_{\mathbf{k}l}(\mathbf{r}) = E_{\mathbf{k}l} u_{\mathbf{k}l}(\mathbf{r}) \tag{3.3}$$

3.4.1.1 Band structure

Our objective is to evaluate the electronic energy eigenvalues, or bands, E_{kn} for each electron indexed by n in our lattice, periodic in k. The plot of all n continuous E_{kn} functions with respect to the Brillouin zone is known as a bandstructure, and is used to describe key electronic features across the periodic unit cell.

In order to finely sample relevant features, an effective stratagem can be to plot a sampling path connecting local points that are copied onto themselves by a high number of different symmetry operations, also known as high-symmetry points. Thus by sampling the shortest possible path connecting these points, it is assumed that the bands sampled are representative via symmetry of a much more detailed sampling of the periodic cell with a minimal number of calculations of E_{kn}. An effective third-party tool for predicting high-symmetry points in a unit cell based on its symmetry, and the shortest path connecting them, is SeeK-path [93].

Thus the bandstructure is a two-dimensional plot of n bands E_{kn} with respect to the length of the entire path along high-symmetry points in a three-dimensional material. Within it, one finds a distinct apparent difference between electron energy levels representing core electrons and valence electrons.

The core electrons are trapped within a strong potential well, meaning that we can consider them to effectively have no momentum. As such, their localised nature in real space converts to a constant energy level across k-space, showing up as flat bands in a band structure. This makes computing them much easier.

Conversely, an electron moving freely in space can be considered to have no potential energy, leading to a dominant kinetic energy term. As such, we can describe variations in the electron wavefunction across space in terms of square of its lattice vector, leading to an expected quadratic description of the bands. As such, we generally expect to find parabola featuring across the high energy periodic bands in our structures.

These parabolic structures allow for easier identification of the band maximas and minimas, which we expect to find along the symmetry points. However, band cross-over points may be ambiguous and difficult to identify, even when assuming parabolic formations.

As the results for each spectral sampling point is derived from the wavefunction found

in the original ground state calculation, there is no computational inter-dependency. This means that each spectral sampling can be evaluated separately, with efficiently scaled parallelisation methods.

3.4.1.2 Density of states

While band structures are an effective visual tool and allow for the evaluation of features along specific bands, such as for deformation potential or effective mass calculations, the actual electron transition probabilities depend on the number of available electron states themselves. To determine this, we need a more rigorous, uniform sampling of the entire Brillouin zone, in the form of a three dimensional grid to sample the overall density of eigenvalues $E_{\mathbf{k}n}$ with respect to electron energy across the unit cell, as described in section 2.3.1:

$$g(E_{\mathbf{k}l}) = \sum_{l} \int \frac{d\mathbf{k}}{8\pi^3} \delta(E - E_{\mathbf{k}l}) \tag{3.4}$$

However, similarly to conventional k-point sampling, the higher density spectral k-point grid can also utilise crystal symmetry to reduce effective sampling. This allows for a relatively computationally cheap approach to evaluating the shapes of electron energy levels, including the Fermi surface for example.

Density of states calculations can also benefit from post-processing software such as OptaDOS [94], which can improve the results by applying an adaptive Gaussian broadening to the Brillouin zone integration [95], adjusting the broadening width based on the local energy band gradient. This allows for more physically significant results, which benefit from a high sampling of the Brillouin zone.

As spectral calculations rely on an initial ground state wavefunction calculation, the resulting density of states is effectively that of a material with a temperature converging towards absolute zero. Further Gaussian broadening methods can be applied in OptaDOS to approximate the impact of thermal smearing applied to electron states as a result of temperature. However, more physically accurate results can be produced by editing OptaDOS to replace its Gaussian broadening approach with a formula for Fermi-Dirac thermal electron smearing.

3.4.2 Solving the BTE

3.4.2.1 Interpolation

The automated solving of the BTE is done with the BoltzTraP2 package, which performs its own preliminary fine interpolation of the spectral calculation results it uses

as an input. This is essential for producing a detailed description of the charge carrier transition rates, and is determined with a single parameter, defining the number of points sampled per point included in the input file.

This process is also used to format an input file for the future calculations. As such, we must be cautious about implementing additional interpolation methods on the resulting output, as this may lead over-interpolation of data and by extension the generation of noise in the data.

3.4.2.2 Integration

The core process used by BoltzTraP2 is the integration step, during which it integrates over the charge velocities to calculate the transport distribution and thus derive the electrical conductivity, electron thermal conductivity and Seebeck coefficient. This must be done individually for each selected temperature, although the results may become inaccurate when approaching the materials' Debye temperature.

Additionally it is also possible to manually adjust the number of bins used to sample the energy of the material, effectively adding another way to interpolate results. This may be necessary when approximating the Seebeck coefficient, as it is of most interest at its maxima and minima. These can manifest as very sharp and narrow peaks, which need to be identified and sampled as close to their tip as possible.

The ideal sampling that would be required to find a good estimation using DFT may be computationally intensive, to the point that interpolation is the only option. Otherwise, the Seebeck coefficients' sharp increase and decrease may be partially rounded off by the limited sampling.

A useful tool available in BoltzTrap2 is the scissor function which allows the band gap to be adjusted in size. This can serve to implement adjusted estimates for the band gap in situations where first principles approaches may have produced suspected errors. These artificially implemented values can come from higher quality calculations performed with more sophisticated and expensive exchange-correlation functional, non ab initio calculations, or experimental results.

This point in the methodological process can also serve as a point to reevaluate current progress, as while both the electrical conductivity and electron thermal conductivity produced will require correction, the Seebeck coefficient will already have a final result at relatively low computational cost. As such, and considering its impact on the figure of merit, it gives a good early indication of the materials' likelihood to act as an efficient thermoelectric over a variety of temperatures and electronic doping levels.

3.5 Effective mass dependent relaxation times

We have identified two approaches to evaluating the relaxation time τ in section 2.6.1. As such, we will first look at the methods that can be used to calculate the components of equation 2.79. The components of interest are the deformation potential, the effective electron mass and the elastic constants.

3.5.1 Deformation potential

As mentioned in section 2.6.2, the deformation potential D_{ij} can be described as:

$$D_{ij} = \frac{dE^{BE}}{d\varepsilon_{ij}} \tag{3.5}$$

Where E^{BE} represents band extrema on either side of the band gap, which are the valence band maximum (or VBM) and the conduction band minimum (or CBM), and ε_{ij} is a single strain. In practical terms, this requires identifying the respective band numbers and positions in reciprocal space. In the case of a direct semiconductor, the coordinates in reciprocal space will be the same for both.

In order to estimate the deformation potential, a finite difference calculation is implemented by applying single-strain deformations Δ_{ij} to the materials, and calculating the resulting shift in E^{BE} within the linear region. One can evaluate the effect of opposing deformations, such as both contractions and expansions, in order to reduce the apparent error caused by the linear approximation.

To ensure that the scale of the deformation is within a linear region, one can repeat the process iteratively while decreasing the magnitude of deformation in order to achieve convergence, as shown in figure 3.7. However, over-convergence can lead to such small deformation steps that the error margin in calculating the electron band energy becomes dominant.

In most cases, it was found that a 0.5% or 1% deformation was an appropriate compromise between numerical tolerance and remaining in the linear regime of deformation. One concern, however, is the possible shift in the location of VBMs and CBMs within the lattice as a result of deformations. However, checking for this behaviour in all cases would require the calculation of full bandstructure calculations for each and every deformation, which would significantly increase computational cost. As such, the locations of the band extrema were assumed to remain approximately static during the deformations.

This was found to be an essential simplification of the computational problem, as these calculations are direction-specific measurements, meaning that an anisotropic

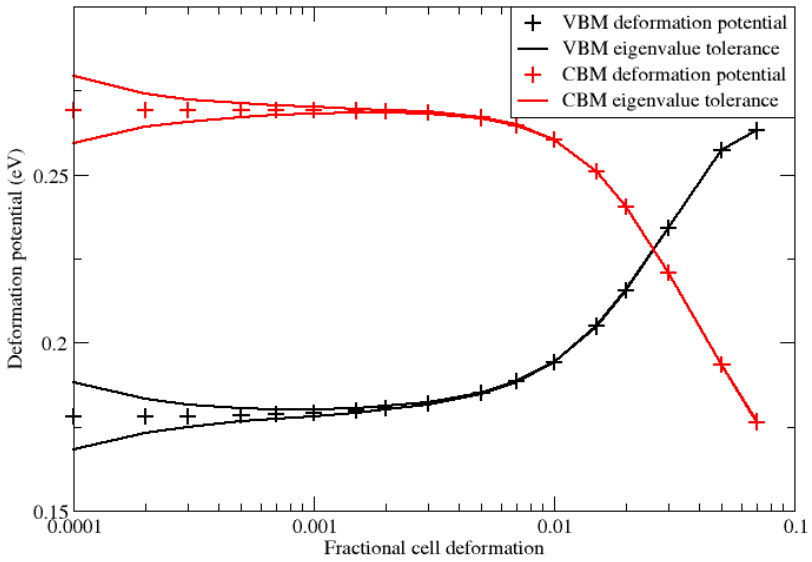

Figure 3.7: Example of a deformation potential linear region convergence of the β-phase of As_2Te_3. Convergence in this case occurs as the deformation size gets smaller (right to left in this figure). However, the impact of the numerical error expands at low deformation ranges when the resulting change in band energy approaches the scale of the tolerance in band energy values. The VBM and CBM in this material are particularly sensitive to deformation size, leading to deformation potential convergence at an unusually low deformation size.

material requires the measurements to be repeated along multiples directions, and while performing both longitudinal and shear deformations, in order to construct a deformation potential tensor. It is however important to ensure that the scale of deformation remains within the linear regime in each direction as, for example, a layered material may react very differently to deformations along or normal to its layers.

3.5.2 Effective electron mass

As derived in 2.6.3.1, we can find that the effective mass m^* is of the form:

$$\frac{1}{m^*} = \frac{1}{\hbar^2}\frac{d^2E}{dk^2} \tag{3.6}$$

such that in order to calculate it along the parabolic region of a band, it is also possible to use a finite difference approach to calculate it. In this case we sample the band within a parabolic region in reciprocal space and fit a second order polynomial to it to solve equation 3.6. While merely using a 3-point stencil across the band is sufficient to evaluate an ideal parabola, a 5-point stencil was used instead to improve results

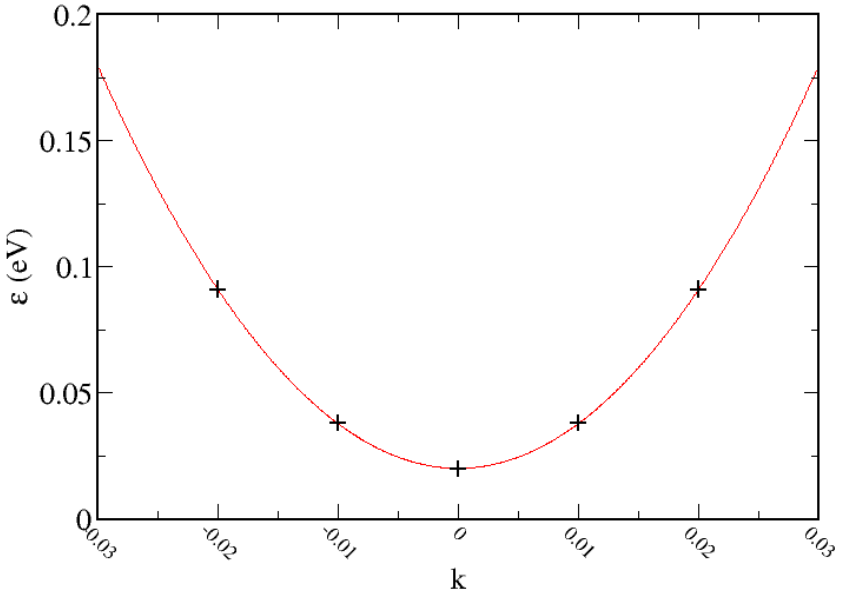

Figure 3.8: Example of a parabolic band curve fitting for the α-phase of As_2Te_3. The black signs represent the 5-stencil sampling of the conduction band minimum with respect to k, plotted here in fractional coordinates of the Brillouin zone, while the red line is a 4^{th} term polynomial function fitted to the sample.

by eliminating possible third and fourth order components.

Proper fitting in this case requires the use of a stencil that is similar in width to the parabola. Too large a stencil will contribute noise from non-parabolic components, while too small a stencil will amplify the impact of stochastic errors from the DFT band calculations, especially if the region sampled becomes narrow enough to appear linear.

A manual comparison of the fitting to the original band structure results is recommended in most cases to account for potential asymmetry in the fitted parabola, bands crossing, or non-parabolic behaviour. The implementation was done with the help of a software package, the Effective Mass Calculator (or EMC) [96], to efficiently generate the stencil spacing and evaluate the effective mass in all directions, using a single DFT bandstructure calculation.

3.5.3 Elastic constants

The individual elastic constant terms are found, as described in section 2.6.3.2, to be of the form:

$$\Xi_{ij} = c_{ijkl}\varepsilon_{kl} \tag{3.7}$$

which are calculated by iteratively applying strains for all non-symmetrically equivalent combinations of i and j, and measuring the resulting stress tensors. The CASTEP software package can directly output stress in cells that are strained, removing the need to calculate said derivative manually. As the length of the cell l_{ij} is already known, solving equation 3.7 once the linear region is sampled becomes trivial.

In order to implement this finite difference calculation, the software package Elastic Constants Calculator (or ECC) [97] is used to generate cells with deformed lattice parameters. With the lattice parameters fixed, the cell geometry is then optimized in order to relax the position of its elements, and the remaining stress used by another script from the ECC to compute the elastic constants.

This process is performed for each strain to form a rank four tensor of distinct components, outputted in the form of a rank two Voigt matrix. As such, sampling this many elastic constant terms requires a large number of geometry optimization calculations, which in the case of α-phase As_2Te_3 was 24, typically making elastic constant calculations the most computationally expensive element to calculate when estimating the electron-phonon relaxation time.

3.6 State dependent relaxation times

3.6.1 Fine sampling of the DOS

The evaluation of the density of states component of the energy-dependent relaxation time requires a very finely sampled spectral calculation to capture any fine features present near the band gap.

As such, while the preliminary singlepoint calculation is typically quite cheap, the grid density of spectral k-points needs to be extremely high. Taking the example of the β-phase of As_2Te_3, it may be necessary to calculate over 10^6 spectral k-points.

The scale of this calculation can be facilitated by the use of symmetry where possible, and is relatively efficient to parallelise over large numbers of cores once the singlepoint calculation has been completed. However, CASTEP does not currently support the creation or usage of ”checkpoint” files during spectral calculations.

As a result, it can be challenging to prepare each calculation so as to complete them within a single run. This will depend upon the maximum job time allocatable on the device used, typically 24 or 48 hours depending on the supercomputing cluster.

Part of the reason why this fine sampling needs to be so fine is to minimize error as a result of the irregular sampling distribution that comes from solving the BTE. These results are higher in density nearer the Fermi energy, and decrease non-linearly as

the energy varies in either direction. As this variation in sampling density changes for each BTE solution, it is not practical to attempt to match the sampling one-for-one with equivalent energy relaxation time values.

The most versatile solution to this is to over-sample the correcting relaxation time with respect to energy so as to be able to match any BTE result with a nearest-energy value for the relaxation time. If done correctly, the error introduced should not be significant as the BTE result density acts as the limiting factor.

3.6.2 Application of electron thermal smearing

To produce a thermally variant relaxation time, it is essential to account for the temperature-dependence of our density of states. This can be applied directly to our zero-temperature DOS results by considering the thermal smearing that would be applied to the individual electrons.

As such, we can use OptaDOS [94] to perform a two-step process. In the first step, it produces an improved density of states by integrating the results over the Brillouin zone, using adaptive Gaussian broadening to extrapolate a better sampling. In the second step, the same Gaussian distribution is then applied with a fixed standard deviation defined by the thermal electron energy E_T at each temperature. In the case of room temperature, this energy is approximately 25 meV.

$$\bar{n}_l = \frac{1}{e^{(E-E_F)/k_BT}+1} \tag{3.8}$$

This approach is a mere approximation however, and could be improved via the use of a Fermi-Dirac distribution function, see equation 3.8. This would allow for a theoretically exact distribution based on a comparison of the variation from the Fermi energy ($E-E_F$) to the thermal energy (k_BT). Here, E is the electron energy, E_F is the Fermi energy, k_B is the Boltzmann constant and T is the temperature of the system.

3.6.3 Sound velocity

As discussed in section 2.6.4.1, the sound velocity v_g can be described as:

$$v_g = \frac{\partial \omega}{\partial k} \tag{3.9}$$

which can be approximated in terms of a small variation $\Delta\omega$ in the acoustic phonon band around the Γ-point with respect to the corresponding variation in position in reciprocal space Δk. As such, one can calculate the sound velocity by sampling the dispersion curve near the gamma point and implementing a finite difference

calculation within the linear region.

Multiple sampling points are recommended to ensure linearity, and it may be necessary to apply this process in all orthogonal directions in order to describe the anisotropy of the sound velocity within the material. One typically expects the longitudinal acoustic mode to be the fastest mode and so it can usually be identified as having the steepest slope within the linear region.

3.7 Phonon transport properties

3.7.1 DFPT calculations

During a phonon calculation using density functional perturbation theory, or DFPT, the sampling of the Brillouin zone is performed using phononic q-points. These are calculated individually by iteratively applying perturbations to the cell and then performing single-point calculations of the perturbed cell. Once all perturbations have been evaluated for one q-point, another is selected and the process is repeated.

The application of perturbations may lead to loss of symmetry, leading to a higher number of k-points needing to be sampled in the perturbed calculations. However, as this loss of symmetry may vary from one perturbation to the next or from one q-point to the next, parallelising according to k-points may be challenging.

While the preliminary single-point calculation of the unperturbed cell serves as an idealised case for k-point parallelisation, it may be preferable to observe parallelisation efficiencies for the first few q-points so as to adapt the number of cores used moving forwards. This is especially applicable when there is a visible trend for a certain k-point sampling being used across multiple perturbed calculations, suggesting that certain symmetry breaks are more likely. However such trends may not necessarily be consistent across the calculation.

Additionally, it is more prudent to account for the number of plane waves available for G-vector parallelisation, so as to ensure that parallelisation efficiencies remain reasonable in cases where an unusually high number of symmetries are broken. This is important as DFPT calculations with many q-points can involve many hundreds of single-point calculations with varying numbers of k-points needing to be sampled, leading to a substantial computational challenge, despite the lack of necessity for supercell calculations as with the finite displacement method.

3.7.2 3rd order force constants

As DFPT calculations available in CASTEP do not support the calculation of third order phonon terms, it is necessary to do this using supercells. This requires the production of many similar supercells with individually simulated phononic components in the form of displaced atoms, done with a program called ShengBTE [81]. These are then evaluated individually using expensive single-point calculations, and the results are processed to produce third order phonon terms.

As the expansion to supercells equates to a reduction of the Brillouin zone, the number of reciprocal space sampling points decreases. In most of cases, the sampling decreased to a single k-point, even when accounting for symmetry breaks as a result of the displaced atoms.

This small number of spatial sampling points makes parallelisation extremely challenging for such large calculations. This is due to how computational cost scales with size, despite the inverse correlation in the number of k-points. As a result, k-point parallelisation becomes impossible, while the overall need for parallelisation increases. As a result, it is quite easy to over-parallelise the calculation with respect to G-vectors, to the point of losing calculation speed as opposed to gaining it.

Additionally, the scale of the cells and the impact of symmetry loss can substantially increase the memory requirements of the calculation. In the case of highly correlated materials, this can reach a point at which involving a sufficient number of cores to satisfy memory requirements without relying on access to a hard drive may lead to inappropriately overparallelised calculations. As a result, it may be necessary to depopulate computation nodes, using only a fraction of their cores as primary processors and threading the others, merely so as to unlock the amount of memory required for individual calculations.

Conversely, as these calculations are set up and submitted manually as opposed to by using a set software package, it is feasible to submit multiple at the same time. While this does nothing to counter the cost of the overall work in terms of core-hours, it does reduce the amount of time necessary to perform it.

Supercomputing clusters do impose certain restrictions, however, on the number of nodes that can be utilized by a single user at any one time. They also often utilize an adaptive task queuing system which prioritizes tasks for users with a smaller number of core-hours recently accessed. As a result, there may still be limitations and drawbacks for regarding the cost of these calculations, even when they are submitted in separate simultaneous computational tasks.

3.8 Methodological limitations

3.8.1 Exchange-correlation functionals

The local density approximation functional is simple and has a number of limitations, although these are well known [98][99]. Most commonly, it has a tendency to over-bind atoms, to the point of shortening bond lengths for weakly bonded structures. This is more likely to occur in non-homogeneous systems. It also has a tendency to underestimate electronic bandgaps, although this also occurs when using a generalised gradient approximation functional.

As side effects of its simplicity, the LDA often produces surprisingly accurate and realistic results due to cancellations of errors between its exchange and correlation terms. Additionally, it accidentally reproduces VdW-like forces without the need for an additional empirical scheme to be implemented. However, its combined weaknesses can interact somewhat unpredictably in complex non-homogeneous structures, leading to hard-to-define errors.

A scissor operator solution to its underestimation of the band gap may be of use in certain circumstances. However, it was avoided in the case of this study due to how it may misrepresent the distribution of electron states in and around the band gap when subjected to thermal smearing.

In comparison to the relatively cheap and simple LDA, meta-GGAs such as RSCAN are quite sophisticated, but also a lot more expensive and computationally challenging to implement. On top of the expanded cost, the relative novelty of the functional means that as of the time of this study, semi-empirical dispersion correction schemes to simulate the effect of VdWs forces have not yet been rigorously implemented for RSCAN in CASTEP. As such, variable cell geometry optimizations cannot be reliably performed while using RSCAN on a VdW bonded material.

3.8.2 Anisotropy in materials

Our evaluation methods are directional in nature, and aligned by default with axes normal to and in plane with material layering where appropriate. However, offering fully anisotropic results is challenging, and thus so is by extension accounting for the full directional behaviour of simulated materials as a result of their anisotropy.

As such, while our values for ZT and by extension its components may be accurate along the three axes that have been focused, we can at best offer approximations for their properties beyond those axes as we are not properly accounting for anisotropic direction-specific synergies. We can also perform total averages of our results so as

to offer approximate values for the properties of the average grain of the material when far from the small-grain limit.

These averages would rely on the underlying assumption that thermoelectric behaviour of our materials are likely at their extremes along high symmetry directions either normal to or in plane with their layered configuration.

However, offering some insight on anisotropic behaviour is important, as many structures of thermoelectric interest including ones being studied to this day benefit greatly from their anisotropic nature [100; 101].

3.8.3 Material defects

An underlying assumption of our methodology is that the bulk material is ideally crystalline. While this assumption is often computationally necessary for DFT calculations due their cost, it ignores the high likelihood that a real material would in fact incur defects to its crystalline structure during manufacture, possibly even becoming polycrystalline as a result of multiple nucleation sites. These defects can include point defects, line defects and planar defects, and may often prove beneficial to thermoelectric efficiency due to their impact on the lattice thermal conductivity [102].

3.8.3.1 Point defects

Point defects are either a single or a pair of atomic locations which go against the typical structure of the rest of the lattice. Impurities can appear within the material as point defects, either as elements replacing atoms within the lattice, known as substitutions, or as elements appearing in areas between sites in the lattice, known as interstitial defects. There can also be cases of empty lattice sites, known as vacancies.

Point defect pairs can also exist in the form of antisites, where two different atoms swap position during formation, which is more common in highly ordered materials and alloys. Alternatively, atoms can occasionally move into relatively stable interstitial positions, creating a vacancy. This pair is known as a Frenkel defect.

These impurities can lead to local electronic irregularities impacting transport properties, and collectively impact the overall electronic structure, including the Fermi level and band gap. Additionally, the resulting variations in mass distribution across the lattice can result in phonon scattering, reducing the thermal conductivity.

3.8.3.2 Line defects

Line defects are structural abnormalities in the form of a row of atoms within a lattice which lead to a significant local strain. This can occur in the form of edge dislocations, where a plane of the lattice ends suddenly along a one-dimensional edge, forcing the planes on either side to curve inwards to reconnect. Another form of line defect is the screw dislocation, in which a line within the plane is sheared, connecting one side of each plane along the shearing motion with the opposite side of a neighbouring plane.

Line defects tend to have a substantial impact on the mechanical properties of the material as a result of the strain, and by extension can strongly influence thermal transport. This has already lead to experimental improvements of ZT in bismuth telluride by increasing the occurence of line defects [103].

3.8.3.3 Planar defects

Planar defects include grain boundaries, which are connecting regions between individually grown crystallites. Our Boltzmann transport calculations can produce values for the material at their small grain limits, as these supersede the need for a correcting relaxation time.

However, assuming that the small-grain limit is not reached, our values for the components of ZT do not account for the existence of grain boundaries, and how they might impact both electronic and phononic transport conductivities through additional scattering of particles due to their irregular structure.

Another type of planar defect is the antiphase boundary, which is similar to an antisite defect, except that it involves the reversal of the ordering of lattice planes along a boundary. These may occur as the result of line defects, such as screw dislocations.

Planar defects such as grain boundaries have been used to increase the scattering effect on phonons with minimal impact on electrons or holes. As a result, these defects have also been nanoengineered to improve the efficiency of thermoelectric materials by reducing thermal conductivity [104].

Additionally, it has been found that grain boundaries can be used to scatter certain electron energy ranges, specifically lower energy ones [105]. As a result, it is possible to exacerbate the asymmetry in transport properties across the band gap in favor of a high ZT in n-type thermoelectric semiconductors.

3.8.3.4 Theoretical simulations in the context of defects

Considering the range and variety of defects that can regularly occur during manufacture, our idealised tests of bulk materials may not fully realistically represent the exact

properties that one may find experimentally. However, they can be used as a starting point, from which the impact of these defects, be they purposefully nanoengineered or merely incidental to the manufacturing process, can be added, and potentially adjusted so as to improve the performance of the material.

It is also important to note that while defects are unavoidable in most experimental cases, there are methods of manufacture, such as atomic layer deposition, that allow the creation of bulk materials while avoiding the occurrence of defects. Such methods are typically used to nanoengineer materials such as semiconductors, however the resources and time required for these processes are substantial, heavily impacting the cost of manufacture to the point that it may not be feasible for production in bulk.

3.8.4 Structural variations in manufacture

All of our calculations assume a perfect crystal lattice as defined within our unit cell. As noted in the last few subsections, there are a number of ways in which a real material may deviate from the ones simulated using DFT. As such, it is worth pointing out that a layered material will typically have substantially different formation energies along the directions within and normal to the plane of its layering, typically favouring formation along the plane.

As the growth of grains within the material is determined by the formation energy, they will typically favour expanding along the directions normal to their layers. This means that the grains within a layered material will tend to align according to the layers. As such, while an imperfect layered and anisotropic crystal with grain boundaries may be difficult, slow and expensive to grow in an exact set orientation, it may be possible for cheaper manufacturing methods to allow for the selection of angles that favour either transport within the layer, or normal to the layer.

Chapter 4

As_2Te_3

Considering the criteria discussed in the chapter 3, β-As_2Te_3 was chosen as a good first subject for analysis based on limited prior research and structural similarities to Bi_2Te_3. However, its unusual electron bandstructure necessitated the application of the DOS method discussed in chapter 2. In order to ensure that this approach was consistent with the effective mass method, the electronic properties of α-As_2Te_3 were analysed using both methods for the sake of comparison.

4.1 Material overview

4.1.1 Structure

4.1.1.1 α-phase of As_2Te_3

The α-phase of As_2Te_3 is a pnictide-sesquichalcogenide alloy with interlocking layers within its bulk connected by Van der Waals forces, which has already been the subject of some investigation for thermoelectric properties [106]. This layering is constructed of planes alternating between two orthogonal direction, with layer segments that are two atoms thick and junctions that are one atom thick. As such, this structure resembles 2-ply layering, with a single repeating layer structure, that is following a step-like pattern, see figure 4.1.

It is worth noting the high anisotropy of this material configuration, with an irregular form of layering suggesting irregular phononic interactions across the gaps with regards to the angle of approach. Additionally, the layers align neatly in the Y-direction defined in figure 4.1, but are slightly offset in the Z-direction despite forming a hexagonal structure.

This combination of hexagonal structures and angled layering means that phonons

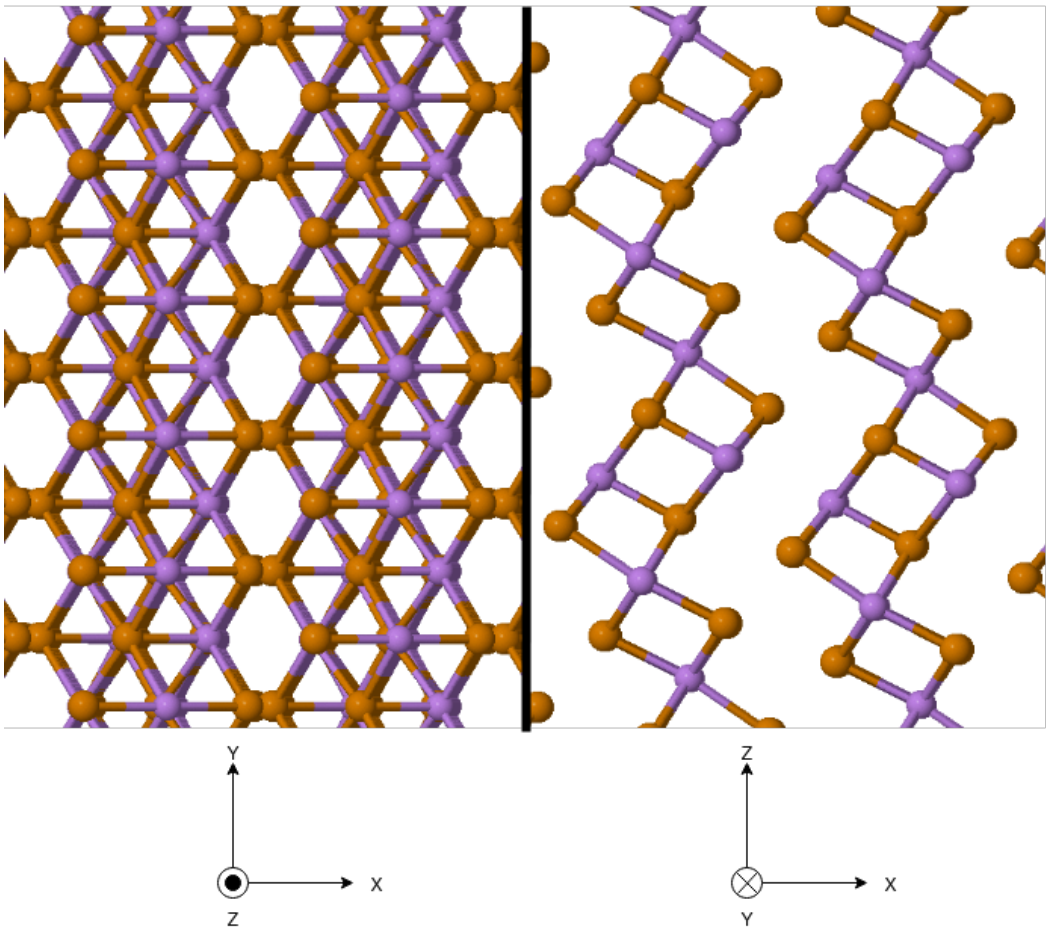

Figure 4.1: Cross sections of the α-phase of As_2Te_3 in the direction of the interlocking layers (left) and along the length of the layers (right). This bulk structure was geometry optimised using a local density approximation. Arsenic atoms are shown in purple, Tellurium atoms are shown in gold, and the X-, Y- and Z- axes are defined such that X is normal to the layers, and Y and Z follow the layers such that Z is the axis along which the layers interlock.

travelling along any covalent bond would have to traverse the spacing between layers, and any phonon travelling within the plane of a layer (the YZ plane) would have to travel at a minimum angle of 30 degree from the most closely aligned covalent bonds. Meanwhile phonons travelling normal to the planes (the X-direction) would traverse layers that are one to two atoms thick at approximately 30 and 60 degree angles to their covalent bonds.

Each one of these directions of phonon transport is significantly different, likely favouring varying phonon modes based on whether they are in or out of plane, or how many covalent bonds they traverse at a time, or at which angle. This disparity in phononic properties would likely result in direction-specific phononic transport properties, and by extension direction specific electron-phonon scattering events. As such it seems reasonable to expect a high anisotropy in both charge carrier and phononic transport properties. Another characteristic of this configuration is that the tellurium atoms are

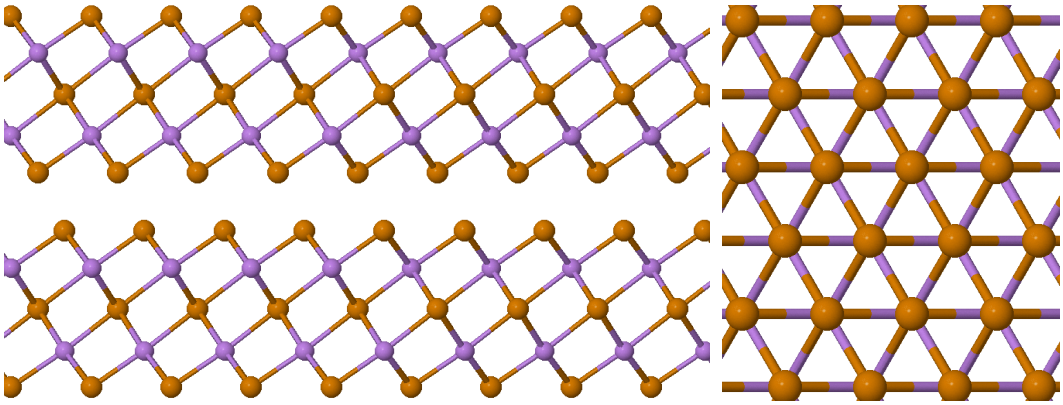

(a) (b)

Figure 4.2: Image of a cross section of the β-phase of As_2Te_3 as seen (a) along the direction of the plane and (b) along the axis normal to the plane, once geometry optimised using a local density approximation. Once again, Arsenic atoms are shown in purple and Tellurium atoms are shown in Gold. We notice a 5-ply layered structure, with a hexagonal structure within the layer.

the primary actors along the Van der Waals interfaces between each layer, shielding the smaller arsenic atoms, which are nearer to the center of each layer.

The material belongs to the space group $C2/m$ (numbered 12), making it a monoclinic system. As such, its geometry optimized primitive cell is an oblique rhombic prism with a base formed of two lattice vectors calculated to both be 7.24 Å long and angled at 32.24°. The length of the third vector was found to be 9.67 Å, set at oblique angles of 96.53°. The 10-atom primitive cell calculated was found to have a volume of 268.60 $Å^3$ once geometry optimized, which is approximately 5% smaller than the experimentally found value of 282.485 $Å^3$ [107].

4.1.1.2 β-phase of As_2Te_3

The β-phase of As_2Te_3 has, as expected, an identical atomic composition to the α-phase, albeit layered more conventionally, see figure 4.2. Once again, the arsenic atoms are shielded from the Van der Waals interfaces by the tellurium atoms. When compared to the α-phase, it appears as if the transformation from the β-phase to the α-phase would be equivalent to the application of multiple line defects to every layer.

This metastable phase was predicted to occur at pressures of around 7 GPa [108], which was then successfully replicated at temperatures of around 423K [109]. In the process, it was found that it could be formed with a purity of approximately 97%, with residual glass impurities, via experimental methods. Additionally, it was also shown to transform back into α-As_2Te_3 at around 480K, and to transform into various allotropes when cooled beneath 210K.

This configuration is nearly identical to that of Bi_2Te_3, as they both have 5-ply layering

with tellurium atoms along the Van der Waals interfaces and through the center of each layer. Combined with the electronic similarity between these compositions, one may expect β-As_2Te_3 to perform well as a thermoelectric. One key difference would be the difference in mass between arsenic and bismuth atoms within their apparently similar configuration, and how that may impact the phonon transport properties.

The β-phase belongs to the space group $R\bar{3}m$ (166), making it a trigonal system. As such, its primitive cell has equal lattice vector lengths of 9.67 Å, set at angles of 24.07° to form an elongated rhombohedral primitive cell. These 5-atom primitive cells contain aligned atoms from each of the 5 ply in the material's layered structure, and have a volume of 132.11 $Å^3$ when geometry optimized using an LDA functional. This result is also approximately 5% smaller than the volume found experimentally [109], most likely due to over-binding as a result of using the LDA functional. This minimalist configuration is relatively computationally efficient despite the complexity of the bulk material.

4.1.2 Composition

The inclusion of arsenic within the material serves as a dominant factor with regards to the k-point sampling due to its highly complex Fermi surface, leading to complex energy isosurfaces within the alloys, see figure 4.3. Additionally, there is a low core electron radius caused by the inclusion of the 3d electron orbitals as part of the valence band in the pseudopotential for arsenic. In order to capture these states along with the strongly localised fine features and sharp band gradients near the band gap, a high number of plane waves is required, leading to a high cut-off energy.

The use of these pseudopotentials was however necessary in order to implement phonon calculations, and was therefore maintained across other calculations for the sake of consistency. As a result, the input parameters would typically resemble those shown in appendix A.

This cut-off energy substantially increased the computational cost of calculations going forward , making them challenging both in terms of computational operations and memory even when parallelised. This is an issue as there is relatively little reference literature on the topic of As_2Te_3 in the context of thermoelectric and related properties, especially regarding the β-phase, for which the few academic sources are mostly exploratory studies, both experimental and DFT-related, in tangentially related properties [110; 111].

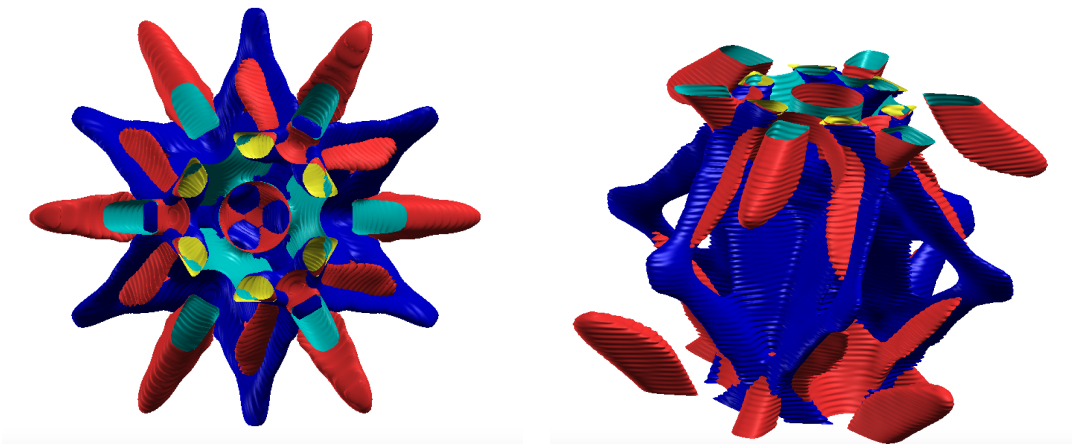

(a) (b)

Figure 4.3: Image of mono-energy surfaces of the valence band in red and cyan, and of the conduction band in dark blue and yellow, for the β-phase of As_2Te_3, produced using xcrysden [112]. Angle (a) shows sharp and narrow fine features which requires high k-point sampling to realistically represent in electronic eigenvalue calculations. From angle (b) we see how the fine structures interlock, but difficulties in sampling the cross sections become apparent. This is due to the layered nature of the structure, combined with the elongation of the primitive cell shape in the direction normal to the layers.

4.2 Electronic properties

4.2.1 Bandstructures

4.2.1.1 α-phase of As_2Te_3

The preliminary band structure of α-As_2Te_3 shows densely distributed band edges across both the valence band and the conduction band when approaching the band gap with many apparent crossing points, see figure 4.4. The optical band gap, when scanned across the bandstructure using the OptaDOS package [94], is found to be 0.38 eV, which appears to be reasonably close to the experimental value of 0.4 eV[113], found via scanning tunneling spectroscopy.

Comparisons to other theoretical values for the indirect band gap are more challenging, both due to their limited availability, and the variability of results in the literature. Deng provides a value of 0.32 eV for the indirect band gap[114], which is inconsistent with our result of 0.026 eV; however, the bandstructure path used in their work does not include the Y symmetry point at which we found our conduction band minima. Were we to sample ours at the M symmetry point instead, as they did, we find over 0.177 eV added to our band gap. This is further highlighted in Deng's density of states for the same material, which does not appear to include a band gap, which is not consistent with their reported bandstructure.

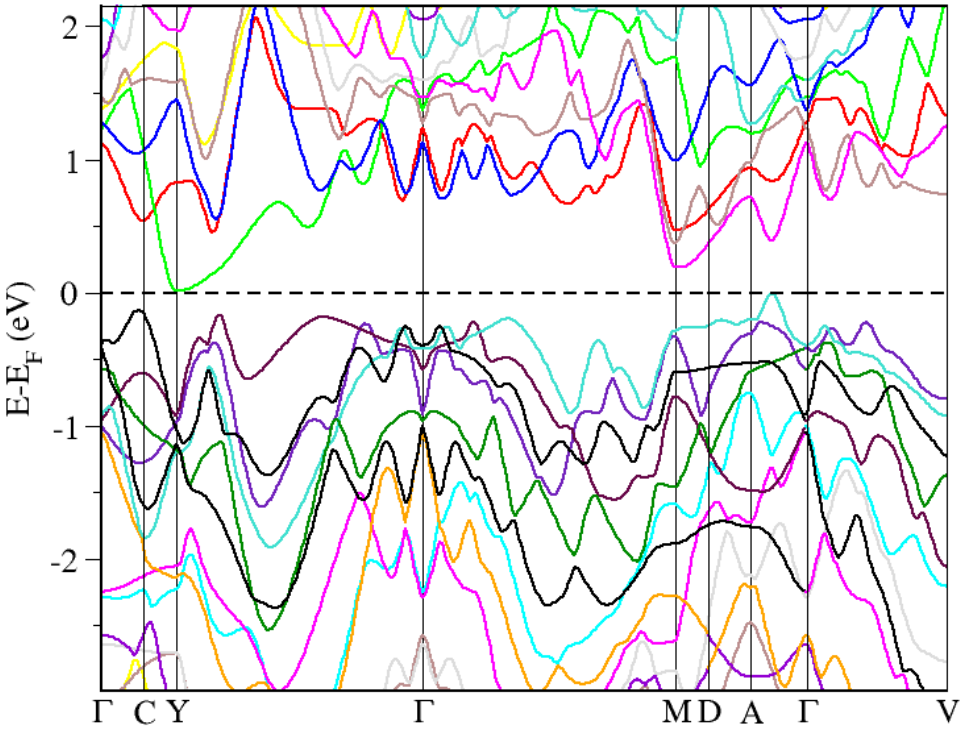

Figure 4.4: Plot of the band structure of the α-phase of As_2Te_3 in eV across high symmetry points.

Another study by Lee *et al* [115] provides a value of 0.38 eV, although its bandstructure uniquely presents a nearly direct gap. It also displays a much higher conduction band value at Y than our bandstructure, and a much higher value at Z than that found by Deng.

Further, a Materials Project result [116] appears to provide a value of 0.581 eV using a generalised gradient approximation functional in DFT, which is unexpected considering the experimental result of 0.4 eV, and the tendency for band gaps to be underestimated using this method. In fact, this appears to be the only result with such a discrepancy in its optical band gap when compared to experiment. It also never samples the path between the Γ-point and the A symmetry point, which is where both the results of Lee *et al* and our own bandstructure find a clear valence band maxima.

The severe inconsistencies between all of the few published DFT results for α-As_2Te_3, along with differences in their convergence parameters, DFT codes and choice of sampling path and high symmetry points make it challenging to identify a reliable reference value for the indirect band gap, for the purposes of comparison to our estimate.

As mentioned earlier, the small size of our bandgap relates to the low CBM at the Y_2 point, exceeding the second largest peak by a difference in electron band energy of 0.177 ± 0.01 eV. The VBM, on the other hand, appears between the A and Γ symmetry points, differing from the nearest value valence peak by a value of 0.121 ± 0.01 eV. As

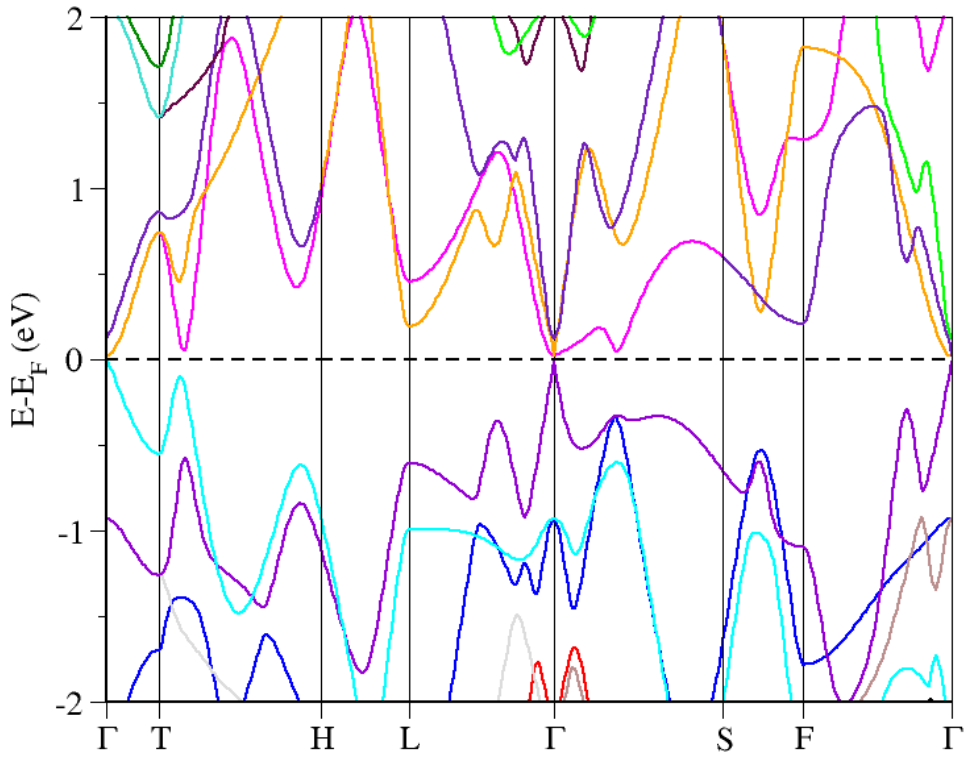

Figure 4.5: Plot of the band structure of the β-phase of As_2Te_3 in eV across high symmetry points.

a result, one would not necessarily expect an inherently high asymmetry across the Fermi energy despite the presence of numerous sharp peaks across both band edges.

The narrow band gap would also suggest a thermally sensitive Seebeck coefficient, as the scale of the band gap is such that the thermal smearing of electrons could be expected to have a significant impact on electron state symmetry across it. For example, the thermal energy of an electron even at room temperature is approximately equal to 0.025 eV, which is close to the value of the band gap. Thus, one could expect significant thermal smearing of electrons across the gap at typical industrial operating temperatures of 400 to 500 kelvin.

4.2.1.2 β-phase of As_2Te_3

The β-phase also shows a small band gap, measuring at 0.033 ± 0.001 eV, which appears to be direct. Additionally, there appear to be multiple bands coalescing near the CBM, leading to the appearance of a shoulder in the density of states. Conversely, the VBM is merely constituted of a lone band with a very narrow parabolic region and steep edges.

These unusual properties are susceptible to variation when evaluated with an over-binding functional, such as an LDA. This results in the narrow parabolic region of

the VBM being reduced to a cone-like shape, which can occur when a band gap is reduced to the point of achieving semi-metallic properties.

We can compare the low band density and variation in slope around the VBM to the relatively higher band density and larger parabolic regions of the CBM. The differences in band density suggest a local asymmetry in the density of states around the band gap, and the differences in slope of the bands would likely result in asymmetric behaviour of these varying densities, which one may expect to impact the Seebeck coefficient.

Thus we can already suspect promising Seebeck coefficient peaks and strongly localised variations in the electron-phonon relaxation time from a qualitative review of our preliminary band structure.

4.2.2 Densities of states

A density of states (DOS) calculation is in effect a discrete sampling of a continuum of densities. As this sampling typically produces results that are difficult to interpret unless extremely fine, a broadening or integration method is typically used to extrapolate a continuum representative of the system.

Additionally, while the results may be correct relative to each other, their absolute value can often be arbitrary depending on the methods of both measurement and broadening. As such, it can be useful to normalise the plot such that the integral of the values beneath the Fermi energy at ground state is equal to the number of electrons in the system. Thus the results to represent a real, if idealised, system.

A linear extrapolation of the DOS contributions can be used to approximate the DOS around each k-point, thus producing a more realistic representation of the overall density [117]. However this approach can lead to some level of uncertainty in accounting for band curvature and finer density of states features due to the first order approximation.

An alternative, mentioned in section 3.4.1.2, involves applying an adaptive Gaussian broadening to the measured state densities [95]. This can effectively maintain sharp features in the DOS while redistributing the densities. However, this can require very high spectral k-point sampling, or the points sampled may produce Gaussian artifacts instead of a continuous distribution. Calculations involving low densities of states or linear distributions are especially susceptible and thus can require very high sampling densities. These phenomena were tested multiple times using both β-As_2Te_3 and graphene as case studies in evaluating the impact of varying sampling densities and broadening methods, see appendix B.

As such, the narrow band gaps and fine features of the arsenic-based compound studied were found to require unfeasible sampling densities to produce continuous density

plots using an adaptive broadening. As such, non-thermally smeared DOS plots offered better results when broadened with the linear extrapolation method. However this comes at the cost of the very narrow bandgap in the β-phase being squeezed out.

It was conjectured that a preemptive adaptive smearing, even if applied to an insufficient sample, would produce better approximations when later subjected to thermal electron smearing when plotting thermal densities of states. This is because the alternatives would involve either no initial broadening, in which case the thermal smearing alone would not necessarily account for the discreet nature of the measurements, or an initial linear smearing, which could potentially result in the loss of fine features in the DOS.

The density of states of both phases of As_2Te_3 shown in figures 4.6 have a steep valley around the band gap, with densely packed states on either side. However, the α-phase appears to have a shallower, nearly linear slope for the first 0.3 eV above the CBM. This causes asymmetry relative to the VBM, where the curve of the DOS grows substantially steeper within 0.1 eV. This behaviour is visible in the bandstructure, where the lower conduction band edge repeatedly dips significantly past the other bands directly above it, while multiple valence band edges converge more densely along the band gap.

The β-phase also shows asymmetry in its DOS valley around the band gap, but as a result of an immediate step-like shoulder above the CBM, which is not reflected at the VBM. This parallels the convergence of bands visible on the band structure, which appear to lead to a cluster of states increasing the gradient at that point. The single isolated band forming the VBM leads to a shallow and nearly linear gradient across the first 0.2 eV beneath the Fermi level, which is appears consistently regardless of the broadening.

The band gap appears to be located within a steep valley, with densely packed states on either side, leading to a rapid smearing as the temperature is increased.

4.2.3 Seebeck coefficient

4.2.3.1 α-phase of As_2Te_3

The Seebeck coefficient was plotted from a calculation of electron energy levels sampled across the system using a dense 25 by 25 by 25 grid, which was plotted in the form of a density of electrons states in figure 4.7.

It was found to have high maxima, measuring $(2.72 \pm 0.04) \times 10^{-4}$ volts per kelvin at the CBM respectively at room temperature, which appears to be in accordance with GGA results [118], but is also a significant overestimate when compared to experimental results [119]. These values suggest that the α-phase is likely to be substantially

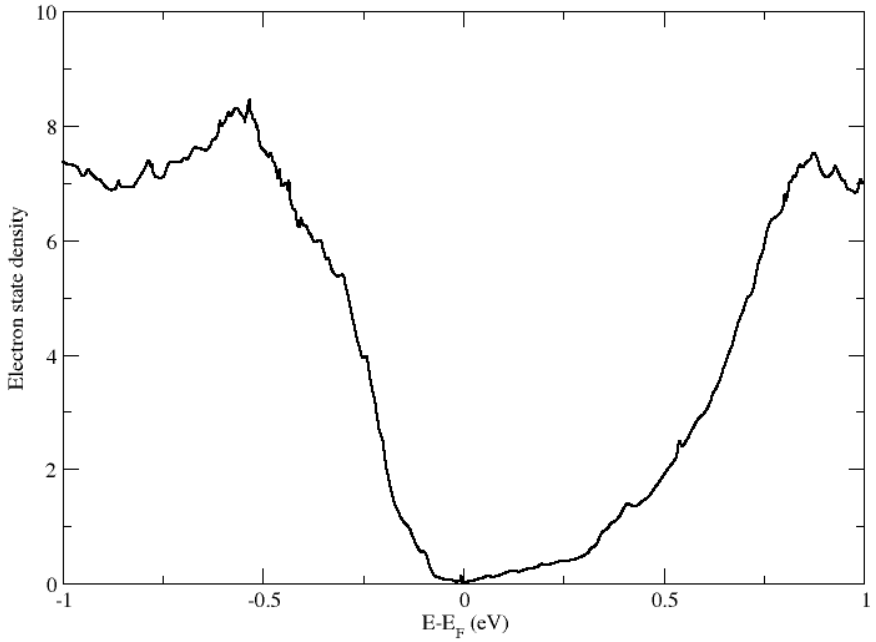

(a)

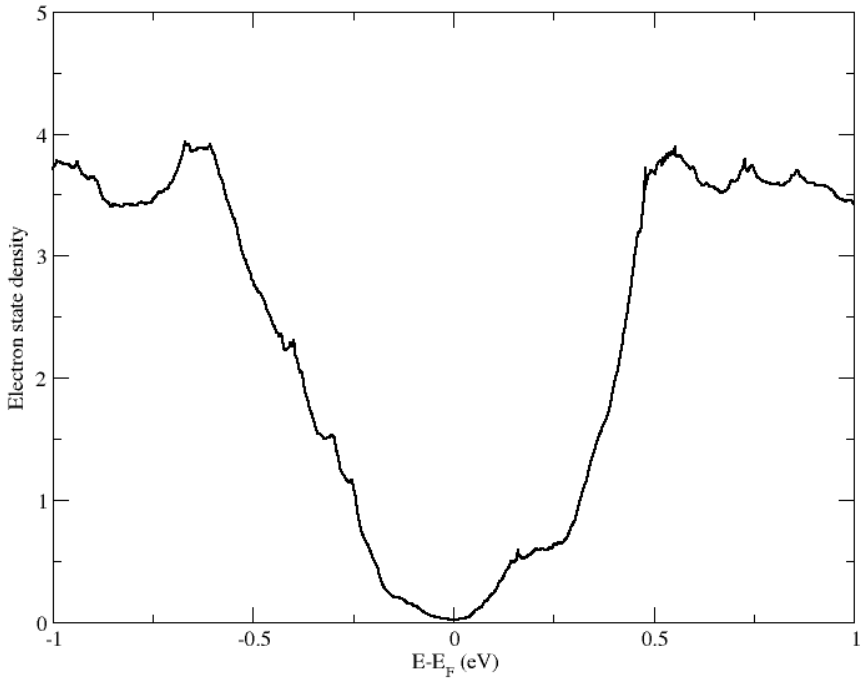

(b)

Figure 4.6: The densities of states of the α-phase (a) and β-phase (b) of As_2Te_3 calculated with a local density approximation functional.

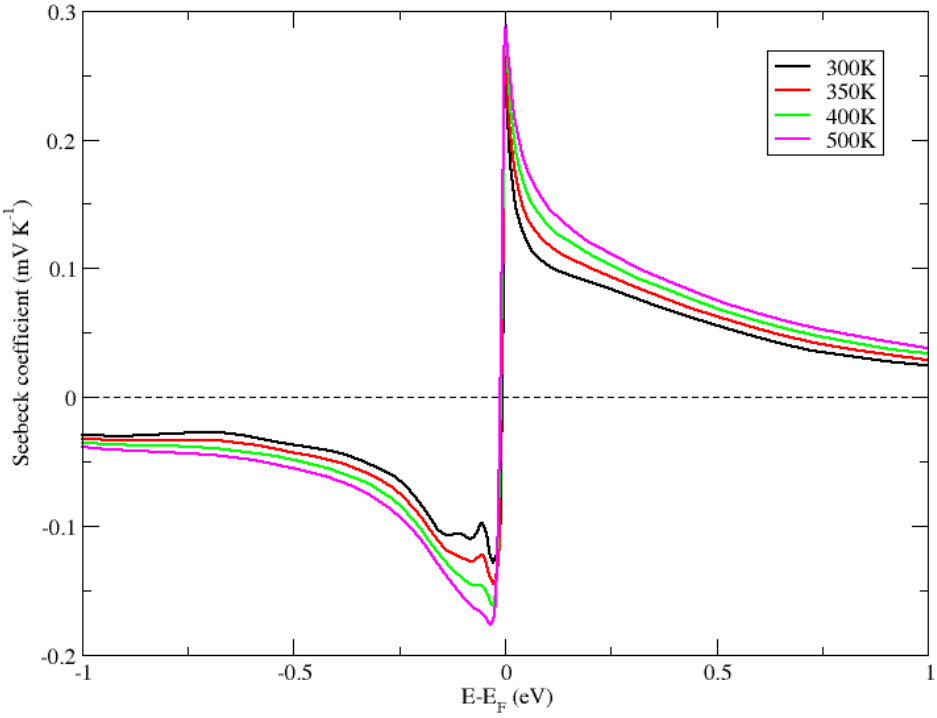

Figure 4.7: Plot of the Seebeck coefficient of the α-phase of As_2Te_3 with respect to band energy at 100 kelvin intervals.

more effective as a p-type thermoelectric device, as the Seebeck coefficient is the only squared term when calculating the figure of merit.

There is relatively little variation in the peak at the CBM with respect to temperature beyond a slight increase, which one would typically expect, which is suggests a promising efficiency at low temperatures. There is also significant asymmetry in the width of the peaks, as the one at the VBM broadens substantially over the span of an approximate 0.1 eV doping range. This could be linked to the increasing asymmetry in the DOS over that range, as the steepening of the gradient below the bandgap is not reflected by the states above it, which increase linearly over that range. It is also worth noting that the peak at the CBM shifts slightly away from the band gap as the temperature increases.

4.2.3.2 β-phase of As_2Te_3

The Seebeck coefficient of the β-phase of As_2Te_3 demonstrates slightly lower values than the α-phase, although the α-phase also appears more sensitive to doping. Its peak at the VBM shows a substantial shift as the temperature increases, likely as a result of the movement of the density of states minimum. The peak at the CBM gives a maximum room temperature value of $(2.30 \pm 0.03) \times 10^{-4}\ VK^{-1}$, which also appears to be

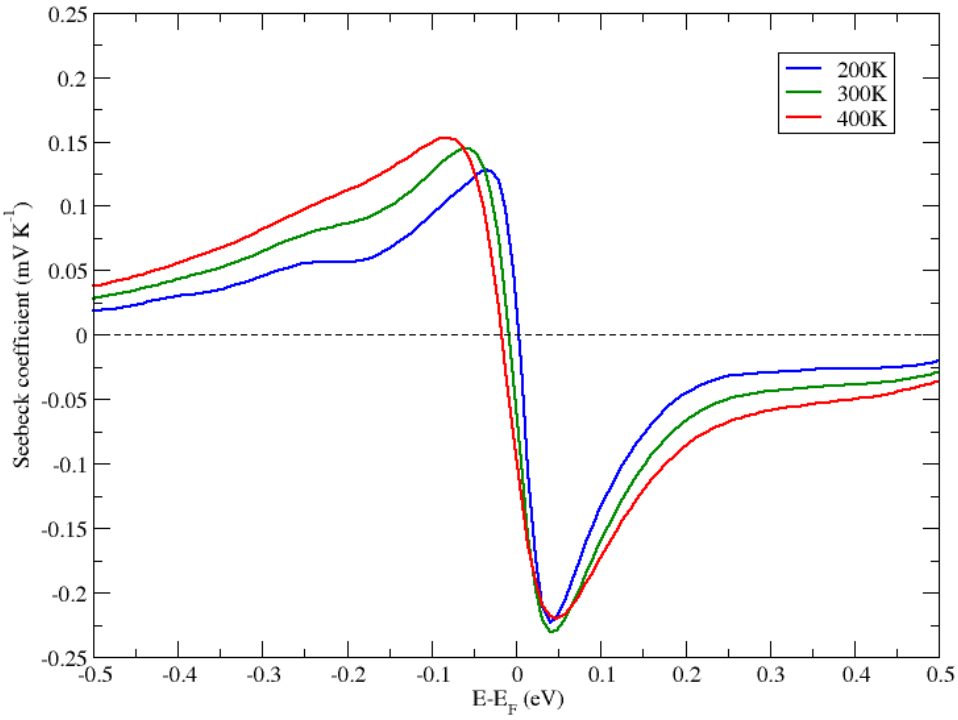

Figure 4.8: Plot of the Seebeck coefficient of the β-phase of As_2Te_3 with respect to band energy at 100 kelvin intervals.

approximately in accordance with GGA results [118], albeit as a slight underestimate.

The values around the CBM cross over, as asymmetry is lost at higher temperatures, causing a maximum at around 300K. This unusual behaviour can be linked to the convergence of states on one side of the Fermi energy, causing a shoulder in the DOS that improves the asymmetry at lower temperatures. Higher temperatures will lead to the reduction of these finer features due to thermal electron smearing.

We expect that such features may have a significant impact on the final thermoelectric efficiency, as the thermal correlation of the Seebeck coefficient is typically a major reason for the inefficiency of thermoelectric devices at lower temperature ranges.

4.3 Phononic properties

The density of phonon states in β-As_2Te_3 was evaluated using a slightly coarse 5 by 5 by 5 sampling grid of phonon energy levels to minimize computational cost, see figure 4.9.

It is dominated along the 0 to 80 cm^{-1} range by its three acoustic phonon modes, with the highest energy mode oriented in the z-axis, normal to the material layers. The two other acoustic modes are found to behave very similarly at each q-point, suggesting

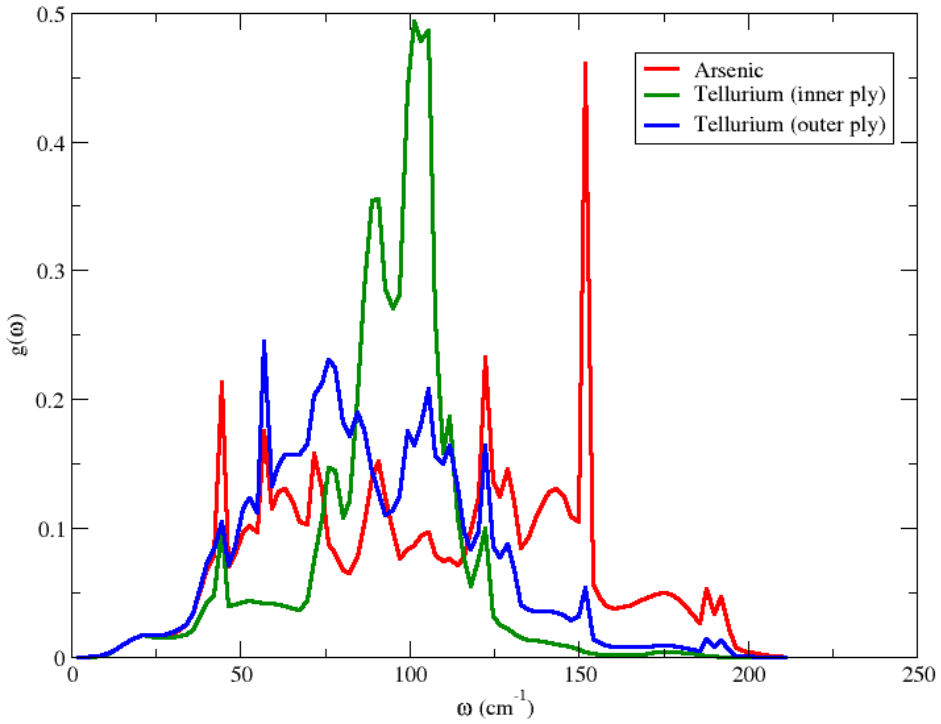

Figure 4.9: The projected phonon DOS of β-phase As_2Te_3.

near-isotropic behaviour by phonons within the layer.

By utilizing a projected DOS plot, we can observe that the acoustic region is impacted approximately evenly by contributions from both tellurium atoms on the outermost ply of the layers, and arsenic atoms. Near the middle of the energy range of the phonon modes, the central ply of tellurium atoms begins to dominate, while the highest energy optical modes appear to become dominated by arsenic.

The phonon sum rule is found to be satisfied within error, with all 3 acoustic modes demonstrating no amplitude at the Γ-point. All 12 of the remaining optical phonons are likely to be active within the effective temperature range, as an ambient temperature of 300K is approximately equivalent to an ω of 201 cm^{-1}.

The calculation of the 3^{rd} order phonon term in order to evaluate phonon-phonon relaxation times was more computationally expensive than that of the 2^{nd} order term. This was the result of having to calculate the third order terms using the finite displacement method, as DFPT calculations of such terms had not been implemented in CASTEP as of the time of this project. However, as there was no publicly available option for DFPT parallelisation over individual q-points, only the finite step calculations of the third order term could be parallelised. This made the third order term easier to produce computationally, with adaptive k-point parallelisation depending on the broken symmetries in each calculation, despite the higher cost..

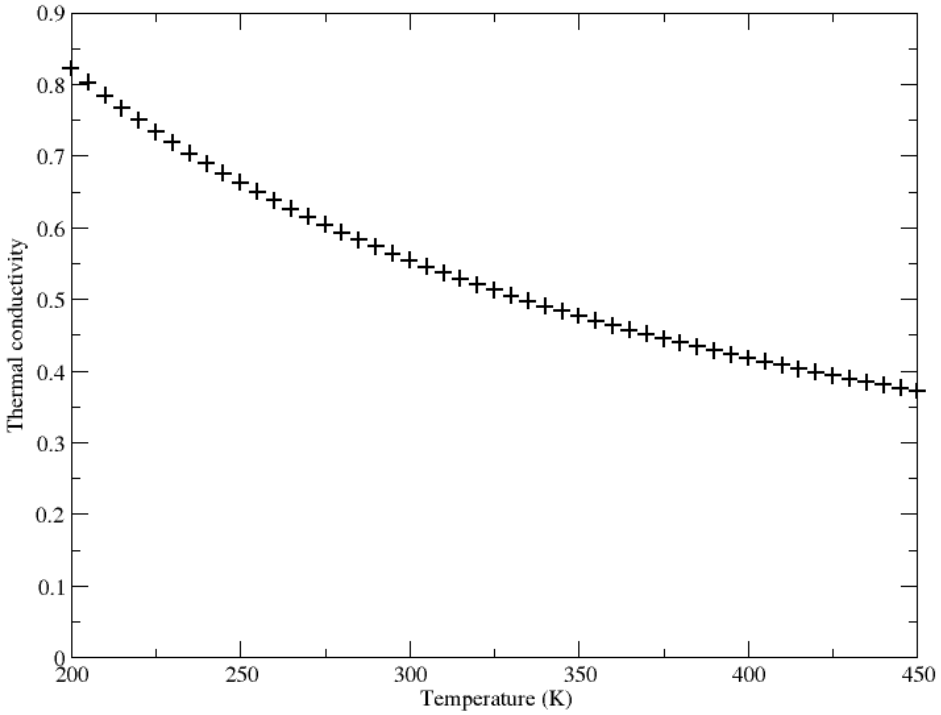

Figure 4.10: The phonon contribution to thermal conductivity with respect to temperature in the xy plane for the β-phase of As_2Te_3.

The result was a relatively standard lattice thermal conductivity, as shown in figure 4.10, whose value in-plane reduces from approximately 0.82 ± 0.08 $Wm^{-1}K^{-1}$ to 0.38 ± 0.04 $Wm^{-1}K^{-1}$ in the 200 to 500 K range, with a value of about 0.55 ± 0.05 $Wm^{-1}K^{-1}$ at room temperature.

Substantial anisotropy appears to have resulted in the lattice thermal conductivity being four times higher in the direction normal to the plane. This may be linked to the weaker Van der Waals forces between layers acting as a weak spring constant in the lattice vibrations in that direction, and thus increasing amplitude in that direction.

As a result, lattice vibrations within the plane would be likely to be scattered into directions nearer the axis normal to the plane, reducing their mean free path and by extension the conductivity along these directions. Such behaviour would then favour both the transport of longitudinal phonons normal to the plane and transverse phonons within the plane with angles of oscillation normal to the plane.

It should be noted that the tendency for the LDA to over-bind systems, as demonstrated in the difference between lattice vectors calculated and those found experimentally, would mean that the energy of the phonon modes is most likely overestimated. This upwards shift of the phonon DOS of our systems has most likely increased the proportional impact of the lower energy phonon modes with respect to the higher energy ones.

4.4 Electron-phonon scattering times

4.4.1 Deformation potentials

The band structure was used to identify the reciprocal-space coordinates of the VBM and CBM.

Their respective band numbers were then determined by cross referencing the energy values from the calculation of electron bands in part 4.2.3.1. These particular eigenvalues were then measured as the unit cell was slightly deformed along three orthogonal axes.

Once the range of deformation along each axis was found to be small enough to offer linear variation in the local bands, deformation potentials were calculated for both phases of As_2Te_3. The linear region was evaluated iteratively after an appropriate cell deformation was identified through convergence of the deformation magnitude, as explained in section 3.5.1, and the resulting deformation potential terms are given in table 4.1. For most materials in this project, a cell deformation of 1% was found to be acceptable, but the β-phase of As_2Te_3 demonstrated a narrower linear region, resulting in a 0.5% deformation being applied.

	CBM (eV)			VBM (eV)		
	x	y	z	x	y	z
x	211±6	53±1	74±1	135±4	41±1	33±1
y	–	315±9	179±5	–	247±7	114±3
z	–	–	65±2	–	–	20±1

Table 4.1: Deformation potential terms in meV, calculated for β-As_2Te_3, set as upper diagonal matrices due to the equivalency between terms such as D_{ij} and D_{ji}, where both describe shifts in eigenvalues along the same linear region.

Additionally, deformations within the plane produced potentials of the same order of magnitude. However, deformations normal to the planes lead to results one order of magnitude smaller, meaning relatively little variation in the local bands when compressing or separating layers separated by Van der Waals forces.

The β-phase produced significantly different results for the CBM and VBM, with lower deformation potentials below the Fermi level. This would suggest a reduced impact of electron phonon scattering at the VBM.

As the α-phase results were to be used for comparing the different methods of calculating the relaxation time, with the effective mass based approach assuming an isotropic material, the results were directionally averaged to a single value, see table 4.3.

4.4.2 Sound velocities

The sound velocities of the α- and β-phases of As_2Te_3 were evaluated based on their phonon dispersion plots. The three acoustic phonon modes were evaluated near the Γ-point of each material, allowing for the measurement of the gradient of their linear regions. The results were found to be similar within the plane, with substantial splitting of transverse acoustic modes.

	x	y	z
α-As_2Te_3	$(1.27\pm0.06)\times10^3$	$(3.37\pm0.16)\times10^3$	$(2.57\pm0.12)\times10^3$
β-As_2Te_3	$(3.05\pm0.14)\times10^3$	$(1.17\pm0.05)\times10^3$	$(2.05\pm0.09)\times10^3$

Table 4.2: Sound velocities of As_2Te_3 in ms^{-1}.

The axes of measurement were defined as normal to or within the structural planes. As a result of this measurement, a single directional average for the sound velocity could be calculated for each material. The different phases demonstrated substantially different velocities, with averages of $(2.40\pm0.13)\times10^3$ ms^{-1} for the α-phase and $(2.09\pm0.09)\times10^3$ ms^{-1} for the β-phase.

4.4.3 Effective mass calculation

The fractional positions of the separate VBM and CBM of α-phase As_2Te_3 were identified from its band structure, and the bands of interest were identified, similar to when calculating deformation potentials.

Iterative parabola fitting led to a convergence of a stencil step-size for each direction and at each point, which was then directionally averaged to 0.008 2πÅ^{-1}, at the CBM, and 0.014 2πÅ^{-1} at the VBM. Additionally, certain extrema involved varying curvatures along their respective axis on either side of the apex. This asymmetry can cause uncertainty in parabolic approximations using a three-stencil approach.

The use of a 5-stencil approach helps improve fitting by eliminating the effects of third and fourth order terms. However, it is necessary to manually review each result to ensure close fitting, and if unsuccessful, to redefine the size of the region over which we place the stencil in order to allow for appropriate fitting of the parabolic region. This can lead to slight variations in stochastic error tolerances between measurements, but is of relatively low impact and eliminates the possibility of systematic errors being introduced due to the evaluation of non-parabolic regions.

Finally, an inherent compromise of this approach is that the harmonic averaging of axial results is a close approximation but not an exact estimate of the overall anisotropic average.

The resulting effective masses were of $0.611m_e$ (or $(5.57 \pm 0.28) \times 10^{-31}$ kg) and $2.07m_e$ (or $(2.07 \pm 0.10) \times 10^{-30}$ kg) at the CBM and VBM respectively. This appeared to match expectations, as the parabolic region at the VBM was substantially broader than any other parabolic region over the two bands, with a lower rate of change in the band gradient along its length.

4.4.4 Thermally smeared DOS

The application of thermal smearing to the DOS of the α-phase of As_2Te_3 calculated using the LDA resulted in a range of results with similar features, including a lack of band gap as a result of thermal smearing. However, the DOS minimum replacing it around the Fermi energy does appear to vary, increasing by a factor of 2.25 when the temperature is increased from 200K to 500K in the α-phase.

This would have a substantial impact on the relaxation time, as it is inversely proportional to the value of the DOS. As a result, we can expect a substantial decrease in the electrical conductivity and electron thermal conductivity once corrected for the band-dependent relaxation time at that band.

The change in shape of the local valley within the DOS is substantial, as density peaks visible in the α-phase at 200k are flattened by thermal smearing as the temperature increases, see figure 4.11a. One side effect is that the shape of the DOS nearest the Fermi energy changes from near-parabolic at lower temperatures to a more irregular curve as the temperature increases. One may expect a slight increase of the Seebeck coefficient with temperature as a result.

The thermal smearing of the β-phase, see figure 4.11b, also demonstrates a significant impact when varying temperature. It also produces an increase in the effective DOS minimum around the Fermi energy, approximately doubling between 200K and 500K. This alone would also result in an effective halving of the relaxation time correction, and by extension a halving of the electrical and electron thermal conductivities, at these specific electron energies.

However, the DOS of the β-phase of As_2Te_3 shows a substantially asymmetric distribution of densities around the Fermi level at low temperatures. This can be linked to the convergence of bands at the CBM visible in the bandstructure, which would be likely to result in an increase of the Seebeck coefficient near the Fermi level. As temperature is increased, the shoulder near the CBM is smeared towards the Fermi energy, reducing its gradient, and the steeper gradient around 0.15 eV below the VBM smears towards the more linear region. The result is a DOS region around the band gap that becomes more smoothly parabolic, and less asymmetric about the Fermi energy.

As transport properties are in part tied to charge carrier density, a reduction in asym-

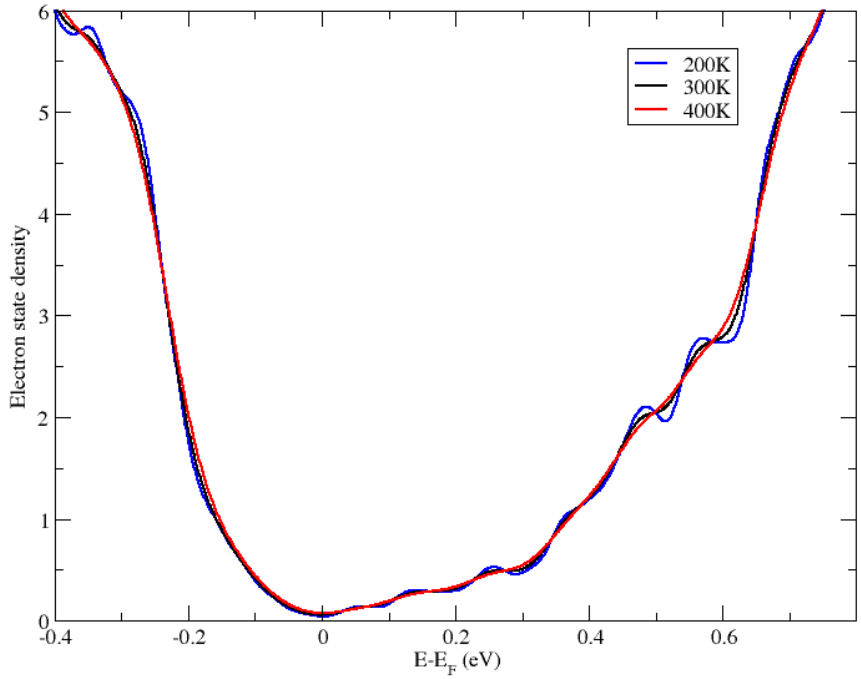

(a) Plots of the thermally smeared DOS of the α-phase of As_2Te_3 with respect to electron band energy. Thermal smearing erases the band gap for the α-phase, and slightly increases the asymmetry on either side of the Fermi energy.

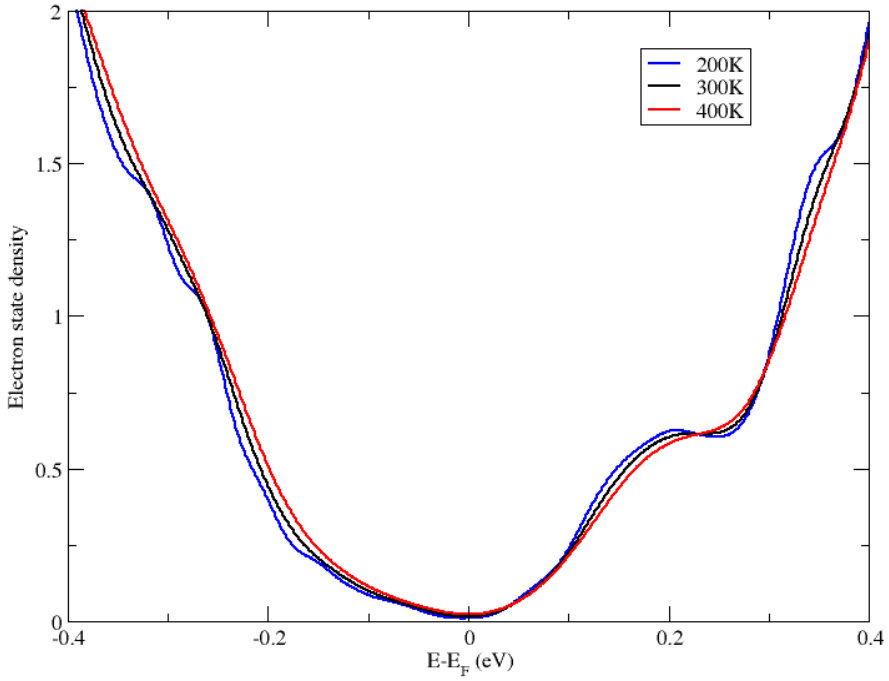

(b) Plots of the thermally smeared DOS of the β-phase of As_2Te_3 with respect to electron band energy. Increasing the temperature increases the DOS minimum.

Figure 4.11: Thermally smeared DOS results for both phases of As_2Te_3.

metry of the latter is likely to decrease the asymmetry in transport properties about the band gap. Considering that the Seebeck coefficient is effectively a measure of the asymmetry in transport properties between carriers that are thermally smeared about the Fermi energy, it seems reasonable to expect that the Seebeck coefficient may decrease as a result of the thermal smearing of the DOS of the β-phase of As_2Te_3.

4.4.5 Electron-phonon relaxation time

We have discussed results relating to two different approaches to calculating the electron-phonon relaxation time. The conventionally used method relies on the deformation potential average D, effective electron mass m^* and elastic constants c_{ii} and, as a reminder, calculates the relaxation time as:

$$\frac{1}{\tau} = \frac{3D^2 m^{3/2} (k_B T)^{3/2}}{2\sqrt{2\pi}\hbar^4 c_{ii}} \tag{4.1}$$

where k_B is the Boltzmann constant, T is temperature and $\hbar$ is the reduced Planck constant. This approach will be referred to by the shorthand the "effective mass method".

The band energy dependent method relies on the use of a thermally smeared density of states $N(E)$, sound velocity $v_{\boldsymbol{q}}$ and displacement specific deformation potential $D_{\boldsymbol{q}}$, and calculates the relaxation times as:

$$\frac{1}{\tau_{\boldsymbol{k}}} = \frac{\pi D_{\boldsymbol{q}}^2 k_B T}{\hbar v_{\boldsymbol{q}}^2 \rho V} N(E) \tag{4.2}$$

which will be referred to henceforth as the "density of states method" or "DOS method".

When comparing the values produced using both methods, as applied to the α-phase of As_2Te_3, we find numbers that match relatively well, within an error margin of under 30%, as shown in table 4.3. Additionally, the VBM results appear remarkably similar, with a difference of approximately 5%, which may be linked to the results in figure 4.11a, where low temperature values above the Fermi energy appear to be subject to significant variation. This may suggest that sharp peaks in the non-smeared DOS increase the likelihood of error in the DOS method as a result of the approximation involved in the combination of methods to broaden sampled points into a continuum, and to thermally smear electron states.

However, when considering the differences in underlying assumptions and dependencies between our methods, the results appear generally consistent. It should be noted, however, that the result found using the DOS method was specifically taken at sampling points located at the VBM and CBM, while the effective mass method merely approximates the directionally averaged behaviour across the parabolic region

Effective mass method		
	VBM	CBM
Elastic constant average (Pa)	$(101.3 \pm 4.7) \times 10^9$	
Effective mass (kg)	$(5.57 \pm 0.28) \times 10^{-31}$	$(2.07 \pm 0.10) \times 10^{-30}$
Deformation potential (J)	$(2.13 \pm 0.06) \times 10^{-18}$	$(1.31 \pm 0.04) \times 10^{-18}$
Relaxation time (s)	$(4.24 \pm 0.82) \times 10^{-14}$	$(1.56 \pm 0.30) \times 10^{-14}$
DOS method		
Density of states (eV^{-1})	0.074 ± 0.001	0.410 ± 0.005
Sound velocity (ms^{-1})	$(2.40 \pm 0.13) \times 10^3$	
Relaxation time (s)	$(4.02 \pm 0.77) \times 10^{-14}$	$(1.91 \pm 0.37) \times 10^{-14}$

Table 4.3: Relaxation time components and results at room temperature for α-As_2Te_3 using the two different methods. The results from the calculations using the DOS method are averaged over all directions for the sake of this comparison, as the effective mass method does not properly account for anisotropic materials.

of the band traversing these points.

As a result of the more targeted sampling region of the DOS method with regards to both band energy and space, one might expect it to yield higher results. The fact that this is not the case at the VBM may be the result of either the effective mass based approximation of relaxation time, or of the broadening of the DOS around the band gap not only filling in the region, but also transferring electron states from the steep gradient from higher densities of states at lower electron energies towards the VBM when combined with the effects of thermal electron smearing.

A benefit of the density of states method is that it allows the plotting of the relaxation time in terms of the distance from the Fermi energy, see figure 4.12. This allows us to identify the range in which we can maintain a high relaxation time, for the sake of engineering materials via doping.

However, our model gives us results in terms of band variance from an approximated Fermi energy, not in terms of doping. This is important, as our broadening methods result in the loss of the band gap in our DOS. As such, based on our equations, we would expect our relaxation time to diverge towards infinity and our electrical conductivity to approach zero as we enter the band gap, as there would be no electron states to conduct or scatter. In order to determine the exact optimal doping levels, it would be necessary to accurately plot the band gap as a discontinuity in our colour maps.

As such, we can both measure the potential efficacy of the material, and predict optimal doping ranges for achieving said efficacy. This is in contrast with the method reliant on the effective mass and elastic constant values, which merely offer an averaged local value for the relaxation time, and by extent for the figure of merit.

The temperature dependence informs us on just how much the thermal smearing near the peak can lead to an increase in available effective electron states, which allow

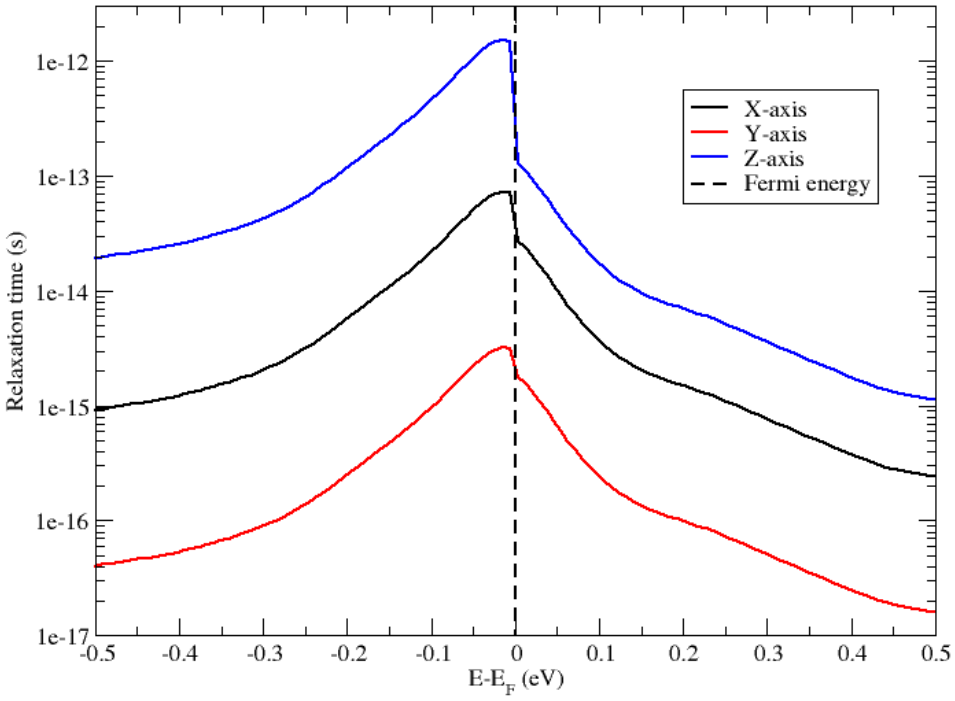

Figure 4.12: Electron-phonon relaxation time plots along the x-, y- and z-axes in real space, for the β-phase of As_2Te_3 with respect to band energy at 300K, produced using the DOS method.The overall values decrease and the peaks narrows with temperature, shifting towards a lower energy. This is due to the inverse dependence on both temperature, and the increasingly thermally smeared asymmetric DOS. The discontinuities at the Fermi energy are due to the change in the deformation potential used between the valence band and the conduction band.

for higher rates of scattering. As the electron-phonon relaxation time, the Seebeck coefficient and the lattice thermal conductivity all decrease as the temperature is increased, one can expect these effects to partially cancel out, as the figure of merit increases with the first two, but decreases with thermal conductivity.

There is also substantial variation in the results based on direction. The asymmetry in the deformation potential and sound velocity depending on the alignment of the covalent bonds in the hexagonal structure of the layer result in a very high relaxation time along the x-axis and a relatively low one along the y axis. Electron-phonon coupling along the z-axis, normal to the layers, is found to be quite weak, but also changes substantially between the valence band and the CBM.

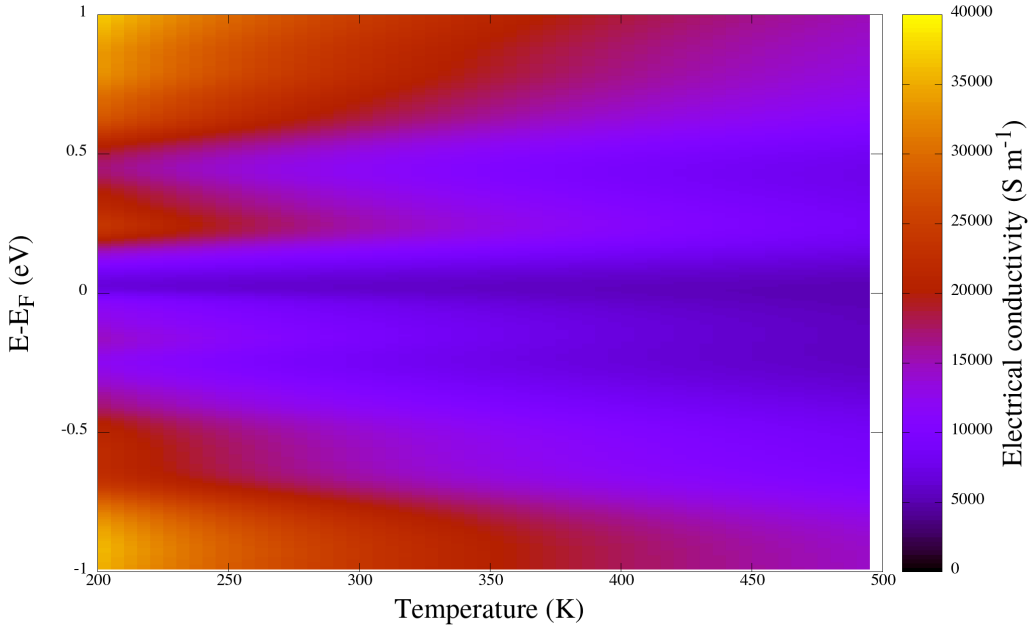

Figure 4.13: Colour map of the electrical conductivity of the β-phase of As_2Te_3 with respect to band energy and temperature, produced using the DOS method.

4.4.6 Electrical conductivity

Once corrected using our relaxation time calculation with respect to both temperature and band energy, we can calculate our electrical conductivity, see figure 4.13. Interestingly, it appears to be at its lowest in the 0 to 0.1 eV range above the Fermi energy, despite this being within the maximal range of the relaxation time correction. One would expect lower electrical conductivity before relaxation time correction at low electron state densities, but this particular subregion is likely also affected by the steep gradients of the parabolic regions of the bands converging around the CBM, leading to low electron mobility in the region. This may result in a direct reduction of the power factor in that region, as well increasing the impact of the phonon thermal relaxation time.

The Lorenz number, defined by the Wiedermann-Franz law as the coefficient of temperature giving the ratio between electron thermal and electrical conductivities, was found to be approximately $(2.42 \pm 0.05) \times 10^{-8}\ V^2K^{-2}$ for β-phase As_2Te_3 at around 300K. This appears to be within error of the expected value of approximately $2.428 \times 10^{-8}\ V^2K^{-2}$, for a degenerate semiconductor [120; 121]. However, this value increases substantially within the ground state band gap due to a numerical quirk in the calculation of the electron thermal conductivity, see Appendix C.

As shown in figure 4.14, the ratio between electron thermal conductivity and the total thermal conductivity across the temperature range between 200K and 500K is around 1 : 4, confirming that the lattice thermal conductivity is the dominant term. This is to

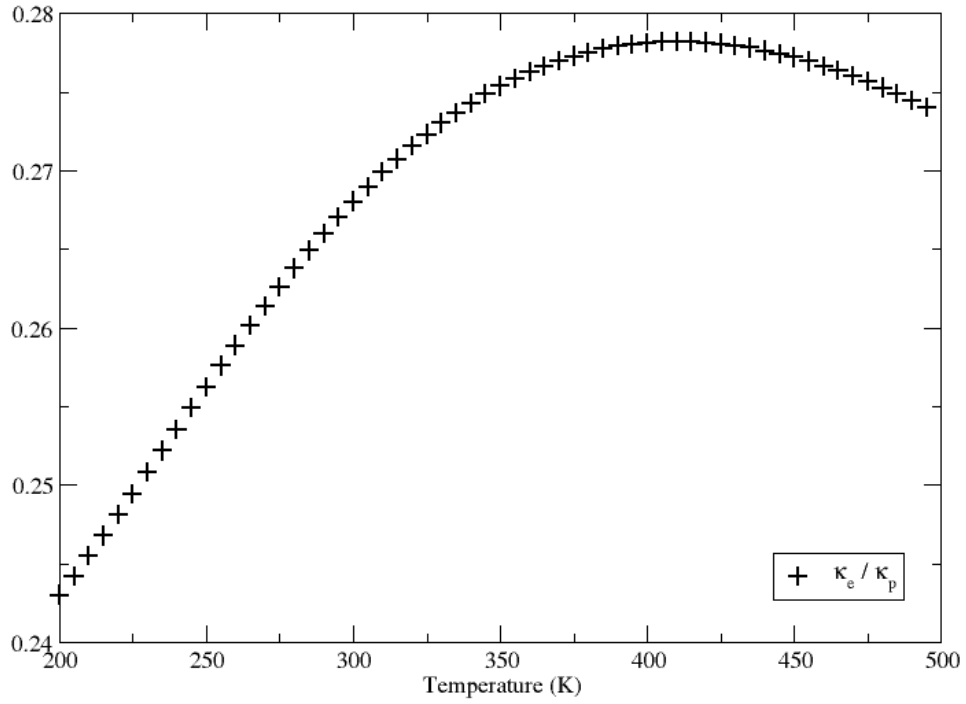

Figure 4.14: Ratio of the electron thermal conductivity κ_e over the lattice thermal conductivity κ_p for the β-phase of As_2Te_3 plotted with respect to temperature.

be expected as both the electron thermal conductivity and lattice thermal conductivity are inversely correlated to temperature.

4.5 Thermoelectric effectiveness of As_2Te_3

The final thermoelectric terms of the materials were combined using the scripts shown in Appendix D. The narrow band gap and asymmetric densities of states of the β-phase of As_2Te_3 appears to have led to promising values of ZT within narrow doping ranges of the Fermi energy.

The electronic components of these results are dominated by the Seebeck coefficient, which peaks sharply at narrow doping ranges, with the opposing peaks at or under 0.1 eV of each other. However there is a slight widening of the maximal range of ZT for any temperature, as the electron-phonon relaxation time approaches its maximum at higher ranges.

As expected, the reduction in phonon thermal conductivity with temperature, combined with the temperature dependence of the figure of merit, have led to ZT values increasing with temperature, see figure 4.15. However, the rate of increase is higher at

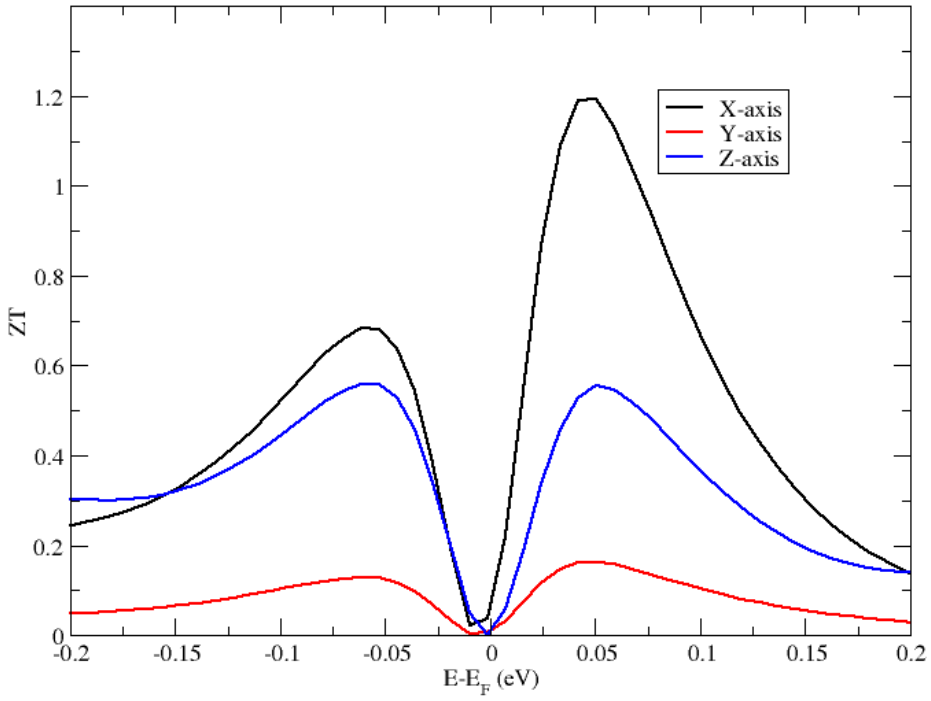

Figure 4.15: Plot of the figures of merit ZT of β-phase As_2Te_3 with respect to band energy at 300K plotted along the x-, y- and z-axes in real space.

lower temperatures for the CBM, due to the Seebeck coefficient reaching its maximum around 300K. As a result, the figure of merit slows its increase and even begins to plateau when exceeding temperatures of over 400 to 450 kelvin. This behaviour is particularly pronounced along the x-axis.

This feature can be linked to the asymmetry between the range of low DOS values beneath the band gap and the shoulder above it. As the temperature increases, the thermal smearing of the electron states into the region fills the effective band gap and shifts the local minimum in the DOS to a lower electron energy, decreasing the asymmetry. This also shifts the maximum ZT values further from the Fermi energy and broadens the peak.

This variability in the optimal doping range with temperature may limit the versatility of the β-phase , while its low temperature ZT values suggest that it may operate effectively, if sub-optimally, as a relatively low temperature thermoelectric device in the 300 to 400K range. The impact of the phonon conductivity is substantial however, at around four times the value of the electron thermal conductivity around 300K. As such, one may expect this material to benefit substantially from doping, nano-engineering or the application of select grain boundaries for phonon-scattering purposes.

As noted when discussing the relaxation time, the distinction between our electron

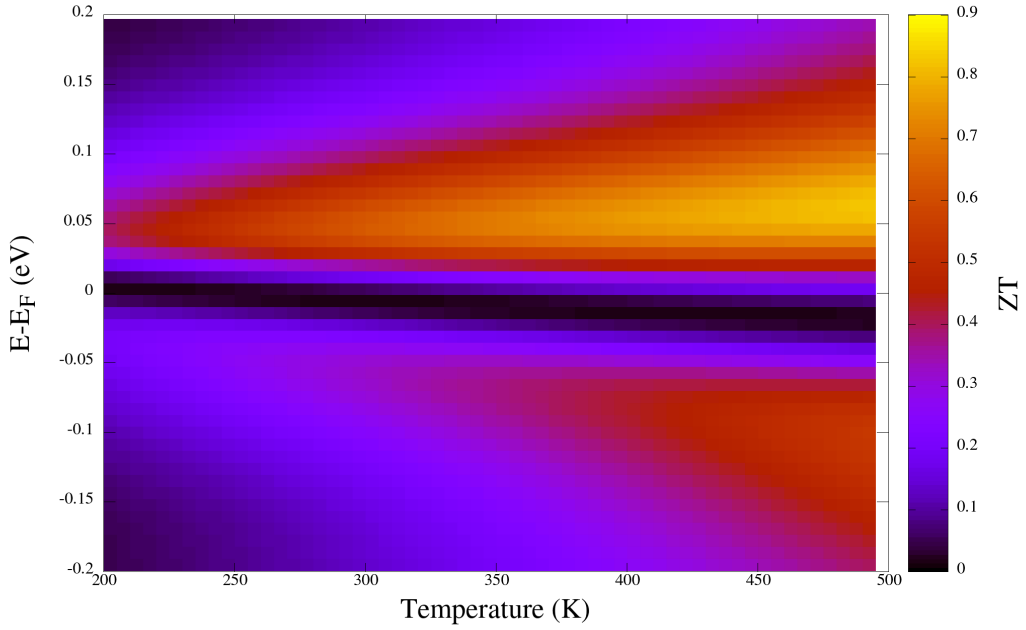

Figure 4.16: Figure of merit of β-phase As_2Te_3 averaged over all directions. While this is a directional average, it appears possible to exceed a ZT value of 1 along the X-axis, as shown in figure 4.15

energy mapping approach and actual doping must be accounted for when considering material engineering problems. This is especially important in our case, as our approach does not allow us to accurately map the impact of the band gap as a result of our DOS broadening and thermal smearing methods.

An alternative method which could improve upon our results would be the tetrahedron method [122], by which instead of smearing and normalising DOS results, the unit cell is instead split into tetrahedra, within which the bandstructure is interpolated via a polynomial. The resulting output for each tetrahedral cell of this constructed polygon is then integrated in order to produce a density of states.

One advantage is that the ground state DOS would no longer need to be broadened, which adds error sources akin to additional thermal smearing. While the tetrahedral method was not explored in this body of work, it has shown promising results when tested on a variety of metallic systems [123]. However, it can also pose the challenge of maintaining a consistent ordering of the bands in order to appropriately track them when they cross each other, so as to integrate over them [124].

The optimal ZT values found exist at over 0.05 eV above and below the Fermi level. As the Fermi level is centered inside a band gap approximated at 0.031 eV, it seems reasonable to assume that the favoured electron energy range does not fall inside of the band gap.

It is worth noting that this material offers promising results when averaging over multiple directions, getting quite close to the Bi_2Te_3 peak in ZT of 1.0 [125]. However, this is merely the averaging of more extreme behaviours that are highly dependent on direction. It is clear that the properties along the x- and y-axis within the plane are highly different as a result of the differences in electron-phonon coupling produced by the relative alignment of covalent bonding in the hexagonal structure.

4.6 RSCAN

The entire set of calculations applied to the β-phase of As_2Te_3 using the LDA functional were subsequently reapplied using the RSCAN functional in order to assess the effect of a higher level of theory on the electronic structure, and consequent effects on ZT.

However, the Van der Waals forces binding the layers of the material together must usually be modelled separately, usually through the implementation of a semi-empirical dispersion correction scheme. As no such scheme was available in CASTEP for the RSCAN functional at the time, a variable cell geometry optimisation using the RSCAN functional would cause the layers to separate. Consequently, the dimensions of a cell geometry optimised using the LDA functional was used instead for all RSCAN unit cells. This allowed for the implementation of a fixed cell geometry optimisation of each structure, with no risk of the layers separating.

The following spectral calculations offered similar results, albeit with the unexpected feature that the band gap has now apparently disappeared completely from even the bandstructure, which presented kissing bands at the Fermi energy instead, see figure 4.18. The apparent semi-metallic behaviour exacerbated the challenge in broadening the density of states near the Fermi energy without losing fine features, resulting in a shorter relaxation time when compared to that calculated using LDA.

Additionally, the bands that converged at the CBM when using LDA were found to be more spread out here, with the Γ-point values of their parabola separating out over a range of about 0.5 eV. This had the effect of softening the shoulder in the DOS above the Fermi energy, decreasing low temperature asymmetry. As a result, the Seebeck coefficient demonstrated a more traditional temperature correlation, and both it and the relaxation time peaks show a reduced tendency to smear into the region beneath the Fermi energy.

The impact of applying RSCAN in this way appears to have shifted our values for the band gap, and by extension its associated terms, even further from experimental results than when using the LDA functional. It may be that merely using LDA to optimise the geometry of this highly correlated material may have led to an underestimation of the lattice vectors, leading to an overestimation of the occupied

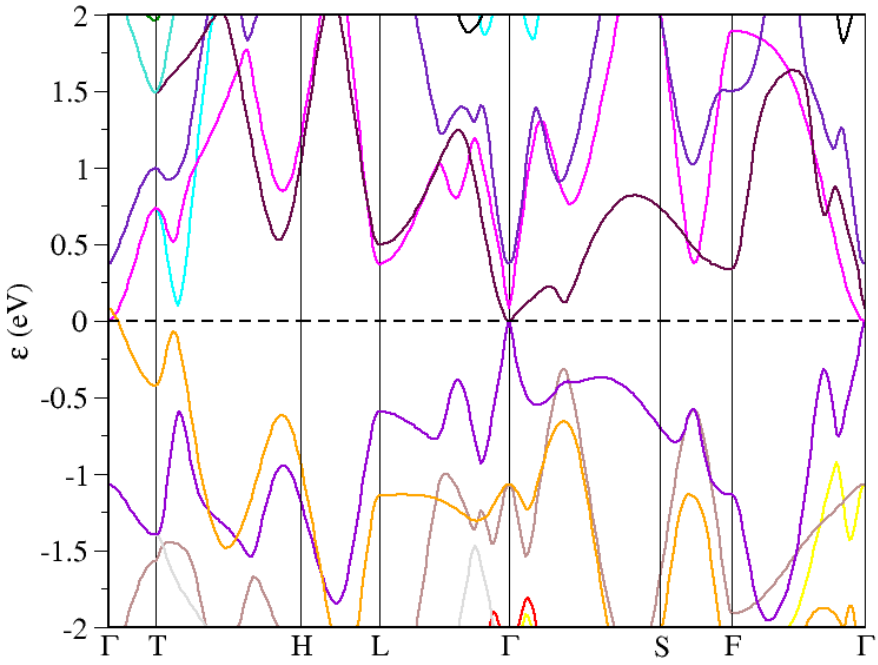

(a) Band structure of β-phase As_2Te_3 calculated using the RSCAN functional. Unlike with the LDA functional calculations, we no longer see a band gap.

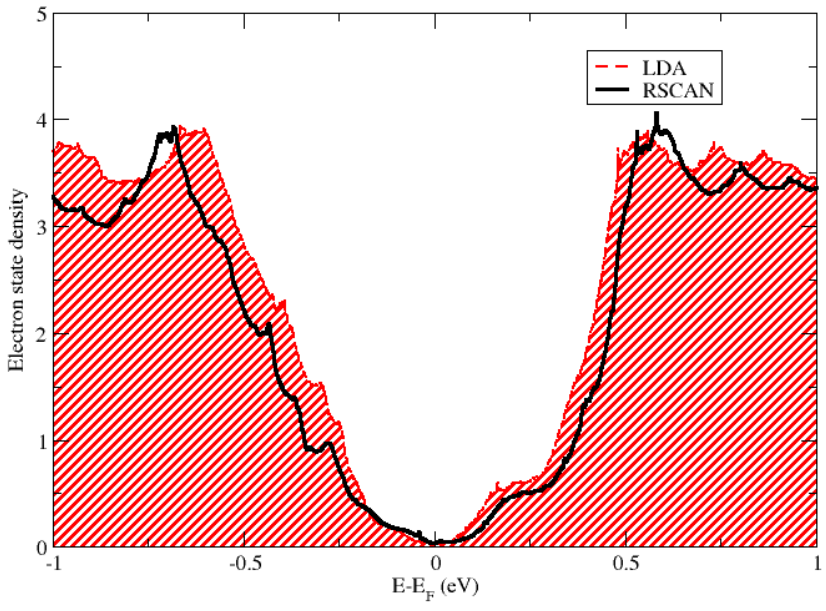

(b) Density of states of β-phase As_2Te_3 calculated using the RSCAN functional, and compared to the LDA DOS in red. We notice a tendency to broaden and separate states across the valley, reducing the gradients on either side.

Figure 4.17: Spectral calculation results for the RSCAN calculation of the β-phase of As_2Te_3.

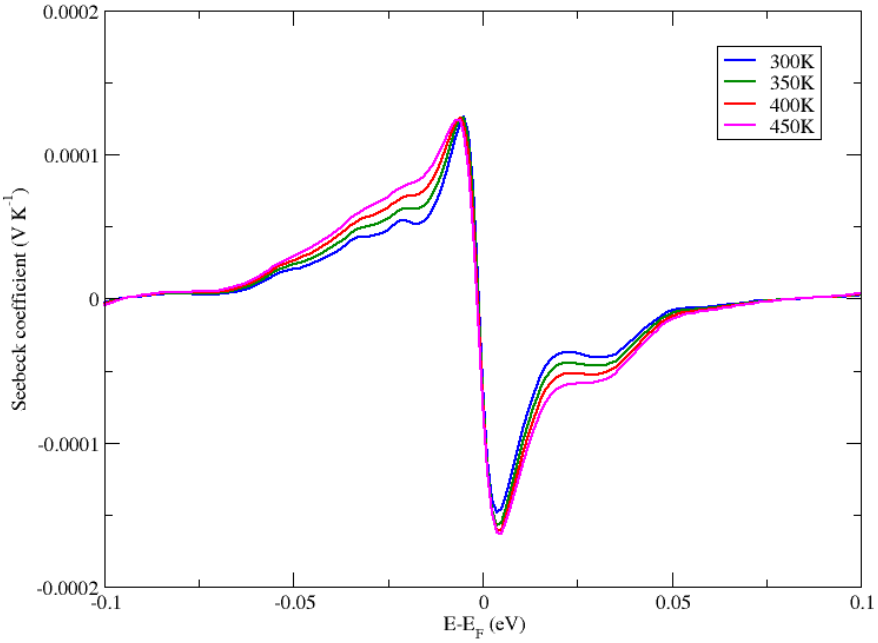

(a) Seebeck coefficient of β-phase As_2Te_3 calculated using the RSCAN functional. We notice that the values are closer to a conventional thermal correlation, as the fine features leading to sharp gradients near the CBM found for using the LDA functional have been softened.

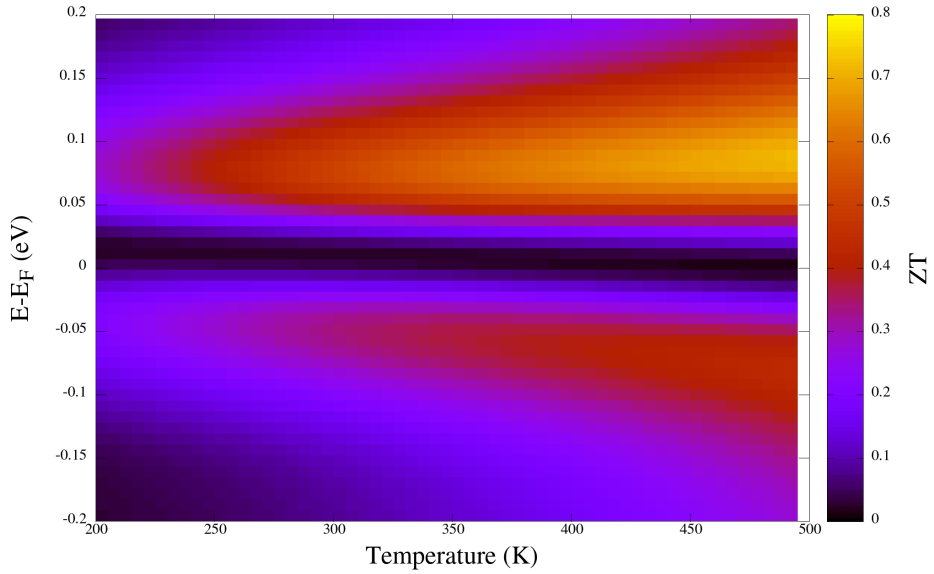

(b) Figure of merit of β-phase As_2Te_3 calculated using the RSCAN functional. The reduction in electrical conductivity combined with the increased thermal correlation of the Seebeck coefficient have led to the figure of merit being more strongly temperature correlated above the Fermi energy when compared to LDA results. However, a local minimum remains at the Fermi level despite the lack of band gap, as it the region over which the Seebeck coefficient swaps sign

Figure 4.18: Key thermoelectric values for the β-phase of As_2Te_3, while using the RSCAN exchange-correlation functional.

electron energies and by extension a further reduction of the band gap which, which might otherwise have been partially cancelled out through the tendency of the LDA functional to underestimate the exchange energy.

Additionally, the individual issues related to the two methods may have compounded the underestimation of the band gap. Indeed, on one hand the LDA tendency to overbind produced a system under pressure, with more localised electron orbitals and deeper electron wells, thus applying an upwards shift to valence bands even when calculated with RSCAN. On another, the use of a semi-local functional to evaluate an already reduced band gap may exacerbate the issue mentioned in section 2.2.5.2 by which a discontinuous derivative function of energy is mapped using continuous derivative fitting, smoothing discontinuities such as the energy gap between the VBM and nearby CBM.

The increased computational expense of using the RSCAN functional made it unfeasible to run second or third order phonon calculations on the material. Instead, the figure of merit was estimated by using the lattice thermal conductivity calculated using the cheaper LDA functional as an approximation.

Unsurprisingly, the values for ZT were found to be lower. While this is in part related to the disappearance of the band gap, it is likely that the separation of the bands near the CBM also had an impact on the Seebeck coefficient. The separation is likely to be a more realistic approximation by the RSCAN functional. While this is detrimental to the figure of merit, it is also worth pointing out that a more exact approach to the band gap with regards to electron state broadening at low DOS values would likely increase asymmetry achieved when doping, meaning that these two errors could partially cancel out.

4.7 Error estimations

There are many terms involved in calculating the thermoelectric figure of merit ZT. This is especially true when including the two different electron-phonon coupling evaluation methods incorporated in this chapter. As such, it is worth underlining and comparing the different sources of uncertainty involved in the process.

First of all, there are errors due to the numerical approximations involved in all DFT calculations when estimating both the total internal energy of the unit cell and the individual electron band energies within it. The former is primarily determined by the level of convergence of the k-point grid density and the cut-off energy used in the calculations, as underlined in our methodology section 3.3, and are converged in all cases within this body of work to an uncertainty in the energy of the unit cell of under 1 meV per atom. The latter is in part dependent on the former, and also on

the tolerance allowed as part of the self-consistent field loops, as described in theory section 2.2.2, which in this case was set to 10^{-6} eV per atom by default.

These stochastic errors directly impact all band-dependent results, including the density of states that is fed into solving the Boltzmann transport equation for determining transport properties such as electrical conductivity, electron thermal conductivity and the Seebeck coefficient. It also impacts the ability to measure the band gap as calculated using LDA, and finite-difference band-related calculations such as those of the deformation potential and the effective electron mass.

The uncertainty in our finite difference band calculations can be evaluated trivially from the stochastic error in band measurements as a ratio between the band tolerance and the magnitude of the smallest finite difference step. However, the very small shifts in the band accommodated by the linear region of the deformation potential or in narrow parabolic band regions meant that the effects of the stochastic errors became amplified to between 1 and 5 % for most related terms, depending on the band and direction.

It is worth noting that these errors were amplified as a result of the very small linear region described by the deformation potential. Thus, in order to minimize error caused by loss of linearity while also limiting the impact of stochastic errors, an iterative deformation potential convergence method was adopted as described in section 3.5.1.

Determining the effect of our meV error margin when solving the Boltzmann transport equation is difficult to resolve analytically. Thus, the impact of stochastic errors in bands was instead estimated by applying and quantitatively propagating the error to account for its impact on our results, as shown in appendix E.1. It was found that the effect of stochastic errors remained relatively small throughout, with a maximal error margin found in ZT for the valence band of the β-phase of As_2Te_3 of approximately 2%.

A similar method was implemented to approximate the impact of a likely systematic underestimate of the band gap as a result of our use of the local density approximation functional, as shown in appendix E.2. This was found to have a much more significant impact, causing the value of ZT to be systematically underestimated by between 10 and 20%, appearing inversely correlated to temperature.

The uncertainty in phonon terms is also challenging to evaluate analytically from electron energy calculations. As an alternative, the range of error was approximated as the correction to the acoustic sum rule within density functional perturbation theory, which states that the sum of the changes within the cell must equal zero. This is not true for our phonon calculations, so a static correction must be applied at each phonon sampling point. As such, the ratio between this correction and the highest phonon mode at each point can act as an approximation of the fractional error. Thus, we took the highest fractional error approximated across our sampling grid, which was in

all cases located at the Γ-point, as the basis for our phonon error tolerance, which lay in the 4 to 5% range for all calculations involving either α- or β-phase of As_2Te_3.

Finally, there are systematic errors that may become as a result of our chosen level of theory. While we have already mentioned the likely impact of LDA on the band gap, it is also likely to have caused additional systematic errors in our calculations when compared to higher levels of theory, like meta-GGAs. For one, it tends to overbind systems, shortening lattice parameters and potentially overestimating responses to deformations and perturbations of the system. Additionally, while it tends to hold layers together, it is not an attempt to accurately simulate the interaction between layers in the way that semi-empirical dispersion schemes are, and may produce slightly different results.

Thus in summary, we found that the effects of stochastic errors in our bands were close to negligible when solving the Boltzmann transport equation, but became significant sources of error when calculating the relaxation time, alongside errors in the phonon calculations. Additionally, the likely underestimation of the bandgap as a systematic error is likely to be the largest source of error in our calculations.

4.8 Chapter summary

Over the course of this chapter, we have analysed the electronic and phononic contributions to the figure of merit in β-As_2Te_3. Our first step after optimizing the geometry of the structure was to perform spectral calculations to identify its bands around the band gap, along with the gradient and asymmetry in its density of states near the Fermi energy. This allowed us to evaluate its Seebeck coefficient over a range of temperatures, which appeared very promising near the CBM, with a room temperature value of $(2.30 \pm 0.03) \times 10^{-1}\ mVK^{-1}$.

Our next step was to calculate the phonon DOS along with the third order scattering terms using a finite displacement approach, in order to produce a plot of the lattice thermal conductivity with a phonon-phonon scattering correction. This left us with the challenge to evaluate the impact of electron-phonon scattering on the electron transport properties.

The band shape of β-As_2Te_3 forced us to rely on an unusual DOS-dependent method to evaluate its electron-phonon relaxation time. In order to verify consistency, we performed both the traditional effective mass method and the DOS method on the α-phase of As_2Te_3, and found that they offered similar results. We then used calculated values for the deformation potential tensor, sound velocities, and the thermally smeared DOS to produce direction dependent terms for the electron-phonon relaxation time of β-phase As_2Te_3 around both the VBM and CBM with respect to both

band energy and temperature.

With all of our terms determined with respect to band energy, temperature and direction, we were finally able to produce maps of ZT values, showing optimal operating ranges for β-As_2Te_3. From this we could determine that the material is indeed capable of functioning as an efficient thermoelectric device by modern standards.

Finally, we reiterated our calculations of β-As_2Te_3 using RSCAN as our exchange correlation functional. In doing so we determined that the previous use of the LDA had most likely caused an increased convergence of states around the CBM, exaggerating some of the properties of the material. However, as we were forced to perform our calculations on a material with lattice parameters defined using an LDA for the sake of accounting for VdW forces, we deemed that the superposition of assumptions associated with performing DFT calculations using one functional on a cell defined using another led to the risk of certain errors compounding. As such, we could not deem the results for the electronic terms to be conclusive.

Chapter 5

$As_2S_xTe_{3-x}$

5.1 Sulphur in β-As_2Te_3

5.1.1 Structures

A first approach at evaluating the impact of replacing one of the chalcogenides in our structures with another was to substitute an atom of sulphur into our β-phase of As_2Te_3. This process resulted in a reduction in symmetry, and by extension an expansion of the irreducible wedge, increasing the computational cost. The unaltered material was already computationally challenging, so it was decided against expanding beyond the primitive cell, as it would likely render some aspects of our method unfeasible. This led to limited options regarding substitution, as any such action would lead to a material of composition As_2STe_2.

As the structure of the β-phase involves 5 repeating rows of atoms within each layer, these will be referred to as the plys of the layer. As the original structure involves tellurium atoms on the center ply and two outer plys of our 5-ply layers, and the two outer plys are symmetrically identical, two different configurations were selected. These were to either replace the center ply with sulphur, or one of the outer plys, see figure 5.1. Neither of these configurations are realistic unless as a result of expensive nano-engineering manufacturing methods, but they allow us to evaluate types of interaction between the sulphur substitutions and the rest of the lattice while keeping our computational costs manageable.

While sulphur and tellurium are somewhat electronically similar, both being chalcogenides, it should be noted that sulphur has approximately one quarter of the atomic mass of tellurium. As a result of their substantial difference in both mass and the range of the effective distribution of their electron orbitals, one may expect them to act as effective phonon scattering elements in compounds containing the other, all the while maintaining a similar general shape for the lattice.

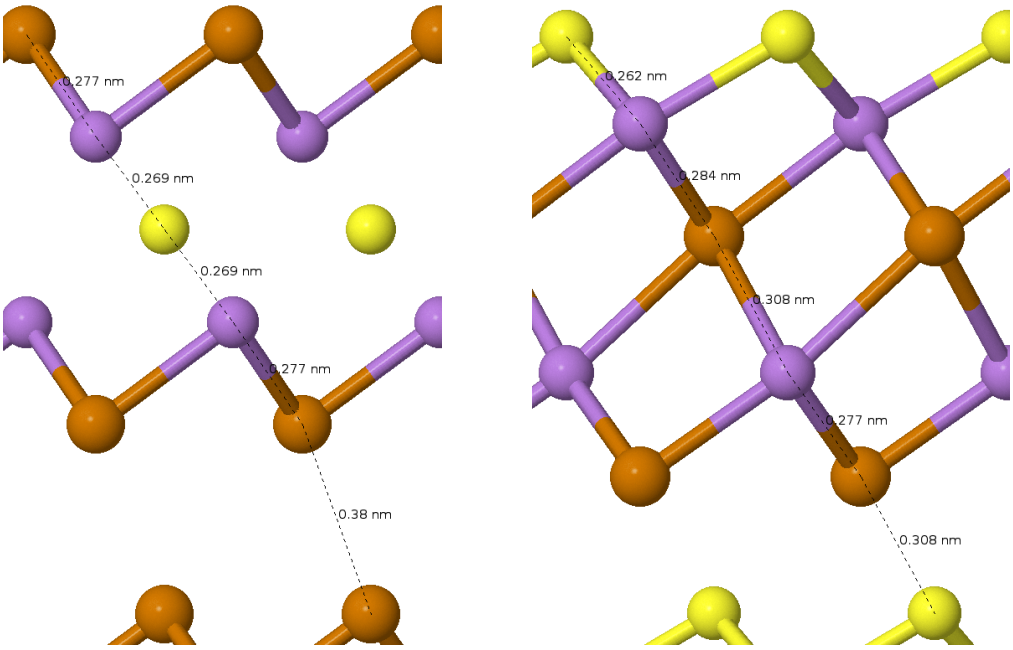

(a) (b)

Figure 5.1: Structures of As_2Te_2S, substituted with sulphur on the central ply for (a) and on the outer ply for (b). The arsenic is in purple, the tellurium is in orange and the sulphur is in yellow. The bonds have a tendency to shorten when in the vicinity of sulphur atoms. As with the undoped structure, the x and y axes are considered within the layering plane, with x being the side-to-side axis in this figure, and z is the axis normal to the plane.

	β-As_2Te_3			Inner doped As_2Te_2S			Outer doped As_2Te_2S		
	a	b	c	a	b	c	a	b	c
Lengths	9.67	9.67	9.67	9.63	9.63	9.63	9.12	9.12	9.12
	α	β	γ	α	β	γ	α	β	γ
Angles	24.07	24.07	24.07	23.10	23.10	23.10	24.75	24.75	24.75

Table 5.1: Lattice parameters of $As_2Te_{3-X}S_X$ structures in Å, both doped and non-doped, shown for comparison.

Sulphur also had a particular effect on the interaction between the plys in the layers. Its smaller size and stronger attracting force resulted in the shortening of atomic bonds in its vicinity, and the lengthening of bonds among the more distant ply. As a result, sulphur atoms, when placed in the central ply, contract and stiffen the layers, widening the VdW bonds between them. Sulphur atoms on the outer ply would attract both the two nearest ply of their own layer and that of the opposite, shortening the VdW bonds between layers and stretching the distances between the ply on the other side of the layer.

As a result, one may expect these two positions to have opposing effects on the material structure. Central ply substitutions reduce the thickness of the layer, strengthening its bonds while weakening VdW forces, effectively enhancing the properties of the material caused by the layering of the structure. Outer ply substitutions bond the layers

together, reducing the asymmetry between VdW and covalent bonds, while breaking symmetry within the layers, likely leading to more varied lattice vibration modes.

We can describe some of the the thermodynamic underpinnings for this substitutive doping of the β-phase of As_2Te_3. For a thermodynamic reaction to occur spontaneously, the change in its Gibbs free energy G must be negative, for:

$$G = U + pV - TS \tag{5.1}$$

where U is the internal energy of the system, p is the pressure applied to the system, V is the volume of the system, T is temperature and S is entropy. Thus for a transformation such as the formation of a defect in a material to occur, the minimum energy required, known as the formation energy, would be the energy required in order for the Gibbs free energy to become negative.

The pV term can be ignored in the case of a material that has been geometry optimized to achieve ground state, assuming no externally applied pressure. Additionally, in order to produce an estimate of the formation energy, we approximate that the defect formation occurs at a sufficiently low temperature and for a sufficiently low change in entropy that the $T\Delta S$ can be ignored.

Thus we find that for a low temperature system, the defect formation energy E can be described as:

$$E \approx U_D - U_{ND} - \Delta\mu \tag{5.2}$$

where the calculated internal energy for the material subject to the defect is U_D, that of the material with no such defect is U_{ND}, and, where applicable, the difference in the chemical potentials of the substituted elements is $\Delta\mu$. However, these chemical potentials are not known, and may vary depending on which element is in excess during the formation. If it is arsenic, then one may approximate the terms in the thermodynamic reaction to all be arsenic alloys such that the reaction takes the form:

$$3As_2Te_3 + As_2S_3 \rightleftharpoons 3As_2Te_2S + As_2Te_3 \tag{5.3}$$

In such a situation, we can then calculate $\Delta\mu$ in terms of a difference in total energies:

$$\Delta\mu = \mu_S^{As\ rich} - \mu_{Te}^{As\ rich} = \frac{1}{3}(U(As_2S_3) - U(As_2Te_3)) \tag{5.4}$$

We have already calculated the total energy of the undoped phase of β-As_2Te_3 to be -7337.274 ± 0.005 eV for 5 atoms, and that of the undoped phase of As_2S_3 studied later in this chapter to be -6549.556 ± 0.001 eV for the same number of atoms. Additionally, we also calculated the total energies of the inner- and outer-doped phases of As_2Te_2S to be -7074.859 ± 0.001 eV and -7074.554 ± 0.005 eV respectively.

From this we can solve equation 5.2, and approximate that the inner-doped phase has a formation energy of -0.158 ± 0.005 eV based on our parameter convergence of 1 meV per atom, and the outer-doped phase has a formation energy of 0.147 ± 0.005 eV. This leaves them with a significant difference in formation energy of 0.305 ± 0.010 eV, favouring the inner-configuration. Moreover, this suggests that the inner-doped configuration is thermodynamically stable, being of lower energy than the undoped configuration, while the outer-doped configuration is not.

Bearing in mind that the thermal energy of an atom is $\frac{3}{2}k_BT$, or approximately 38.7 meV at 300 K, or around 193.5 meV for our 5-atom cell, this suggests that the outer-doped phase is still accessible from an undoped phase, but the inner-doped phase is preferred. As such, this may lead to a mixture of defects at finite temperatures if analyzed using statistical mechanics [126]. It is worth noting however that there are two possible doping sites for the outer-doped phase and only one for the inner-doped phase, doubling the relative likelyhood of such occurances. As a result, it appears sensible to study both phases, despite the significant difference in their formation energies.

As much of this section will discuss and compare the properties of these two materials, we will, for the sake of ease, be using the short hand "inner doped" when referring to the structure containing sulphur in the third ply of its layers, and "outer doped" when referring to the structure with sulphur on the outer ply of its layers. However, while our analysis may hold some relevance to real world doping, the scale of the substitution is such that our structures are more akin to alloys than to doped materials.

5.1.2 Electronic terms

The band structures of the two altered versions of the material also display significant divergence in how their modifications have impacted their electronic properties. The substitution of sulphur on the outer ply appears to to have had relatively little impact on the bands around the band gap beyond a slight expansion of the band gap from approximately 0.031 ± 0.001 eV to 0.052 ± 0.001 eV, see figure 5.2b.

However, the substitution of sulphur in the inner ply substantially impacted the bands near the gap, expanding it to approximately 0.480 ± 0.001 eV, see figure 5.2a. This occurred as a result of the displacement of the highest valence band downwards, broadening and reducing its peak at the Γ-point, and also shifting many conduction bands upwards by approximately 0.2 eV. It is likely that this shifting of bands clustering near the band gap and broadening of peaks will have resulted in a lowering of the effective electron masses and by extension an increase in electron mobility at these respective bands.

The density of states calculations give us matching results, with a very large band gap

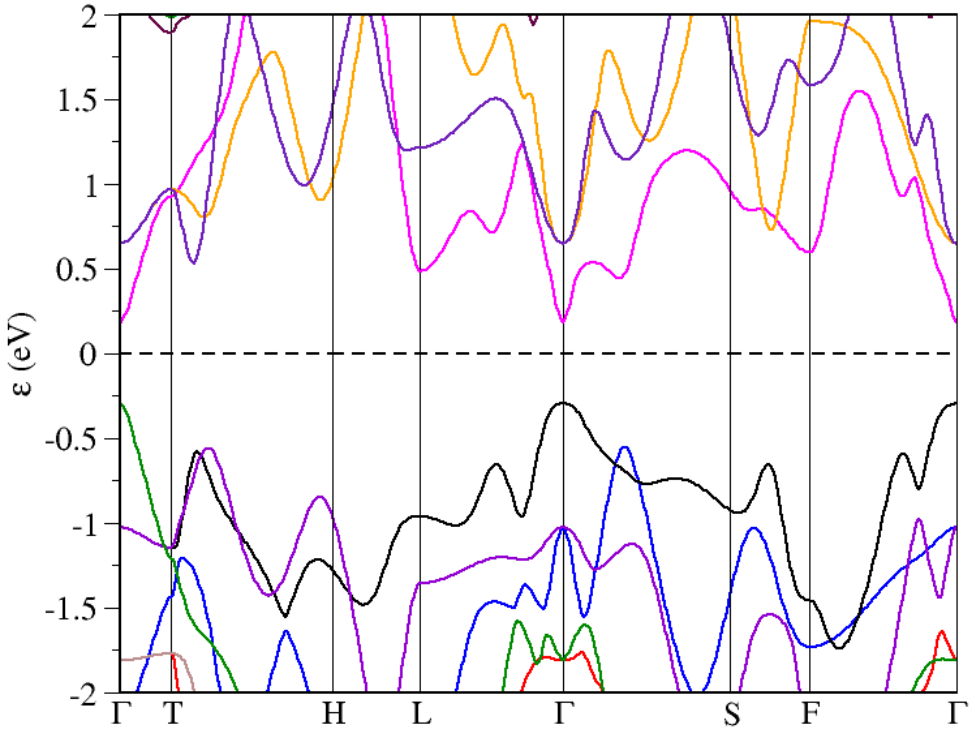

(a)

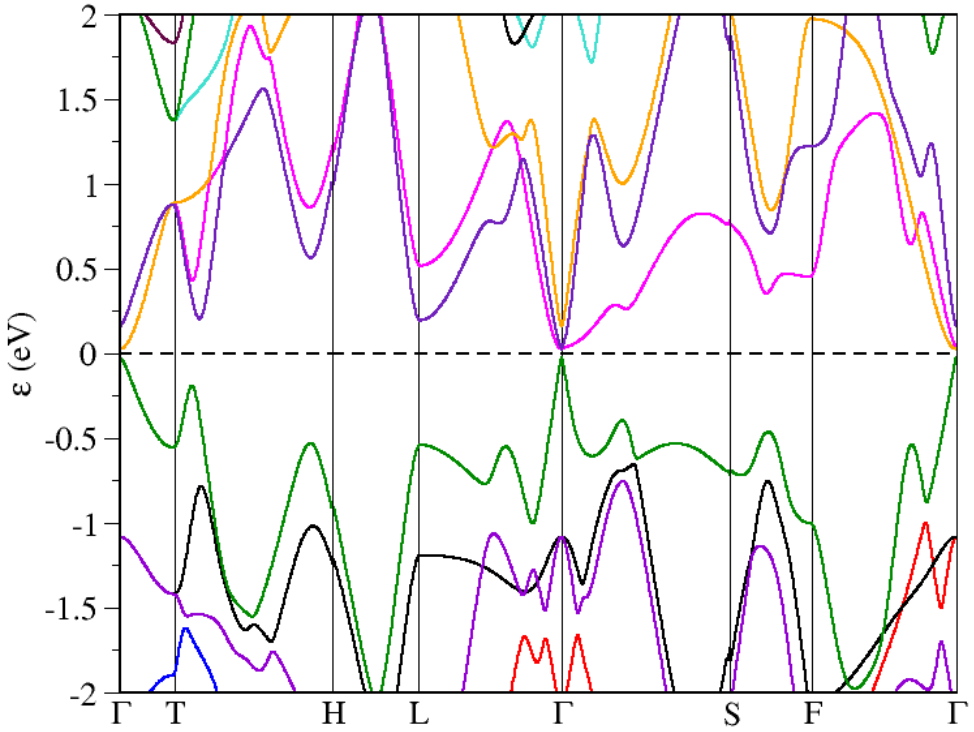

(b)

Figure 5.2: The band structures of As_2Te_2S, substituted with sulphur on the inner ply for (a) and on the outer ply for (b). The latter appears remarkably similar to that of β-As_2Te_3, while (a) displays a much wider band gap.

shown in figure 5.3a and a general similarity to the unaltered material shown in figure 5.3b. The conduction band of the inner doped structure has maintained a rapidly increasing gradient culminating in a local plateau in the DOS, forming a shoulder similar to that of the unaltered material. However, the broadening and reduction of the peak at the valence band maximum has resulted in the disappearance of the low density linear region present in the unaltered phase. Instead, this range of band energies is occupied by the band gap, and the broadened, and by extension flattened, highest band now produces a much steeper gradient in the DOS. As a result, the asymmetry of the system appears to have flipped when compared to the unaltered phase, with a shallow gradient in the DOS at the CBM than at the VBM.

The outer-doped phase remains more similar to the unaltered one, with a long, nearly linear DOS region around the valence band maximum and a steeper distribution in the conduction band, all separated by a narrow band gap. However, a slight separation in the three lowest conduction bands has led to a slight reduction of the local gradient, and the erasure of the shoulder visible in both the unaltered material and the inner-doped one. This suggests that some electronic asymmetry has been lost, rendering this material less electronically efficient for n-type doping.

The resulting Seebeck coefficients of these two electronic densities of states are markably different, see figures 5.4. Specifically, the inner doped phase appears to produce a Seebeck coefficient that is nearly an order of magnitude greater than that of either the unaltered or outer doped phases. This is primarily tied to the scale of its expanded band gap, as we are measuring the coefficient across said band gap, which is being partially thermally smeared. As a result, the apparent asymmetry across a point in the band gap with no states available on one side, and a small number of allowed states as a result of thermal smearing on the other, offers a numerically high value. This does not necessarily reflect the actual asymmetry present at the ground state VBM and CBM.

As such, while we observe significant peaks approximately 0.10 eV away from each other in our Seebeck coefficient plot, this does not match up with our non-smeared DOS, which shows the ground state VBM and CBM being separated by an approximated 0.480 eV gap. Thus, the more realistically applicable ranges of Seebeck values exist at and around the cross over points between the different temperatures, in the 0.2 to 0.3 $mV\ K^{-1}$ range. Values that delve further into the band gap measured for our ground state are likely to be countered in our evaluation for ZT by a decrease in our electrical conductivity. In other terms, while we theoretically do have the ability to apply a high potential to states deep within the ground state band gap, there will be so few of them that they will produce very little current.

The Seebeck coefficient of the outer doped phase is more akin to that of the unaltered material, albeit with generally more similar values above and below the Fermi energy at higher temperatures, likely as a result of the reduced intrinsic asymmetry across the

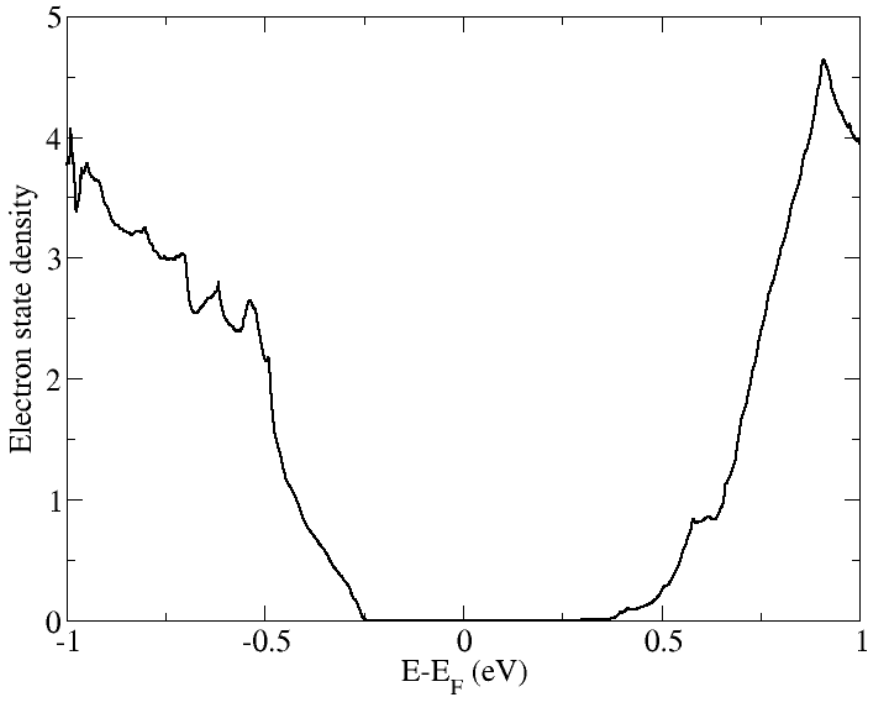

(a)

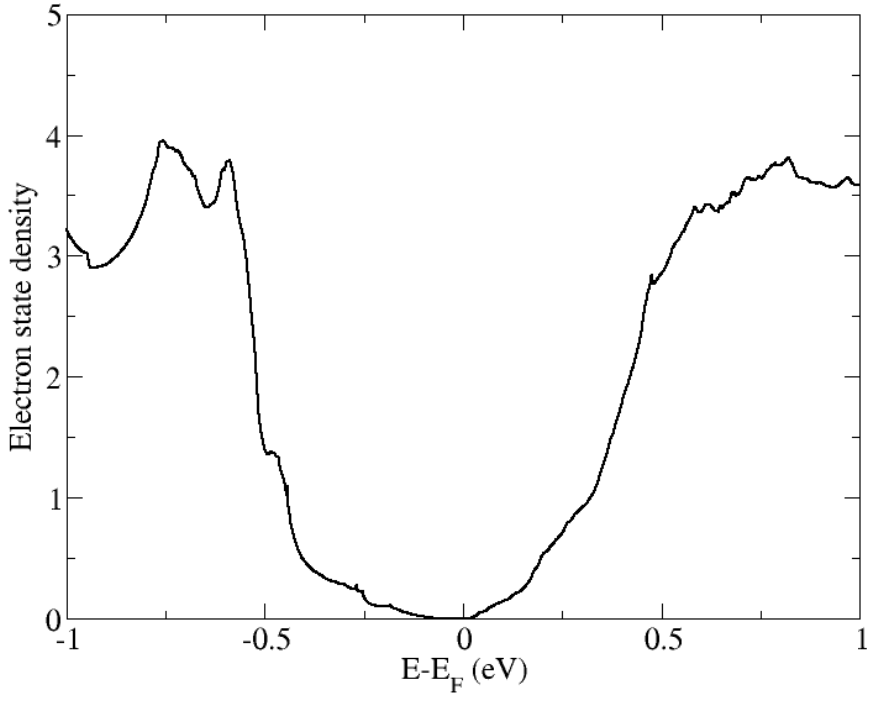

(b)

Figure 5.3: The densities of states of As_2Te_2S. These reflect the broadening of band gaps shown in the band structures. We also find that (a) has maintained some of the fine features of the unaltered material despite the increase in the band gap, while (b) appears to have lost a some of the asymmetric features.

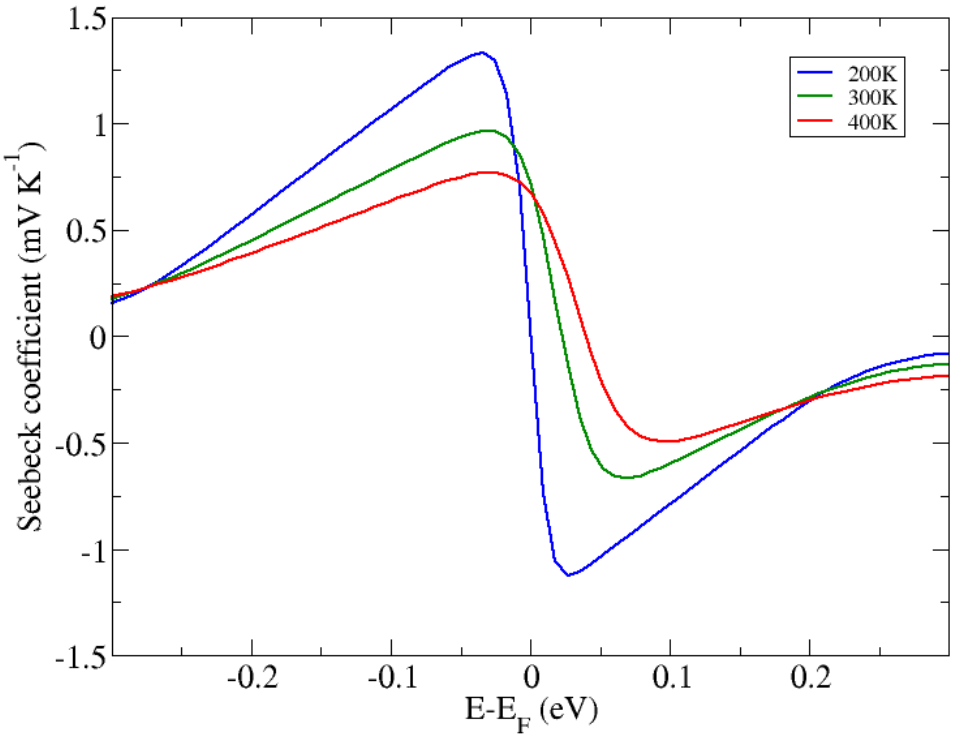

(a)

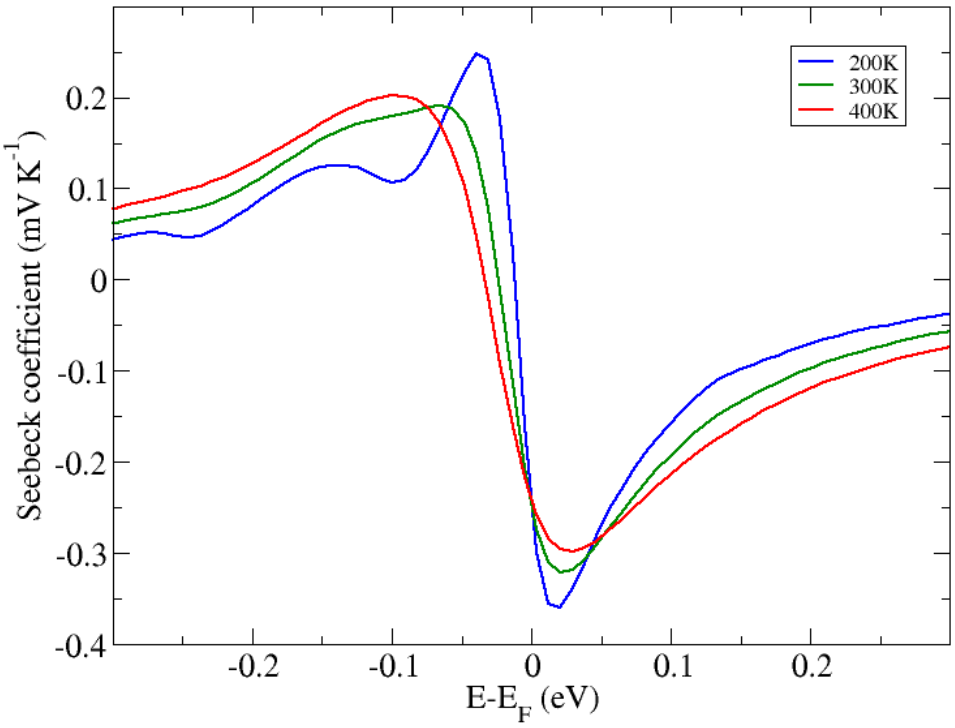

(b)

Figure 5.4: The Seebeck coefficients of the of As_2Te_2S, both inner-doped (a) and outer-doped (b).

band gap. At lower temperatures, we observe some oscillations in the coefficient below the VBM, which are likely to be linked to the sudden shifts in gradient in the DOS. Thermal smearing erases these fine features beyond 300K, thus the disappearance of this behaviour in the Seebeck coefficient.

5.1.3 Phonon transport properties

The phonon DOS of the inner doped phase of As_2Te_2S (see figure 5.5a) shows that its higher frequency optical region is dominated by sulphur, whereas the heavier elements are primarily responsible for lower frequency phonon modes, including acoustic modes. One may expect that this redistribution of phonon modes to higher frequencies may benefit our electron-phonon coupling terms, assuming that they are typically primarily impacted by acoustic phonon scattering.

We also find that from the second order terms we can derive a value for lattice thermal conductivity in the small grain limit, at around $(3.43 \pm 0.10) \times 10^{-1}\ Wm^{-1}K^{-1}$ in both directions within the plane, and $(3.27 \pm 0.09) \times 10^{-1}\ Wm^{-1}K^{-1}$ in the axis normal to the plane. These compare favourably to the values of $(3.83 \pm 0.17) \times 10^{-1}$ and $(4.44 \pm 0.20) \times 10^{-1}\ Wm^{-1}K^{-1}$ respectively for the unaltered material.

However, when applying the phonon-phonon relaxation time correction, we find very similar results for the inner doped cell when compared to the unaltered material. Once again it descends smoothly down the 0.8 to 0.4 $W\ m^{-1}\ K^{-1}$ range in the x and y directions, see figure 5.6, with a substantially higher conductivity achievable in the z direction.

It is worth pointing out that while the outer doped phase of As_2Te_2S offered similar results in terms of conductivity, its phonon DOS (see figure 5.5b) displayed a significant redistribution of the phonon modes, with a split in the sulphur peak and a smearing of arsenic and tellurium states around the acoustic and low optical regions.

5.1.4 Electron-phonon coupling

5.1.4.1 Deformation potential

The deformation potential terms calculated for both of our doped compounds appear substantially higher in all three axial directions when compared to our unaltered material, meaning that they are subject to substantially more electron-phonon coupling. This is particularly noticeable when comparing uni-axial directions within the plane for the VBM, or the CBM values for the inner doped configuration, see table 5.2.

By the nature of the deformation potential, variations may be linked both to structural

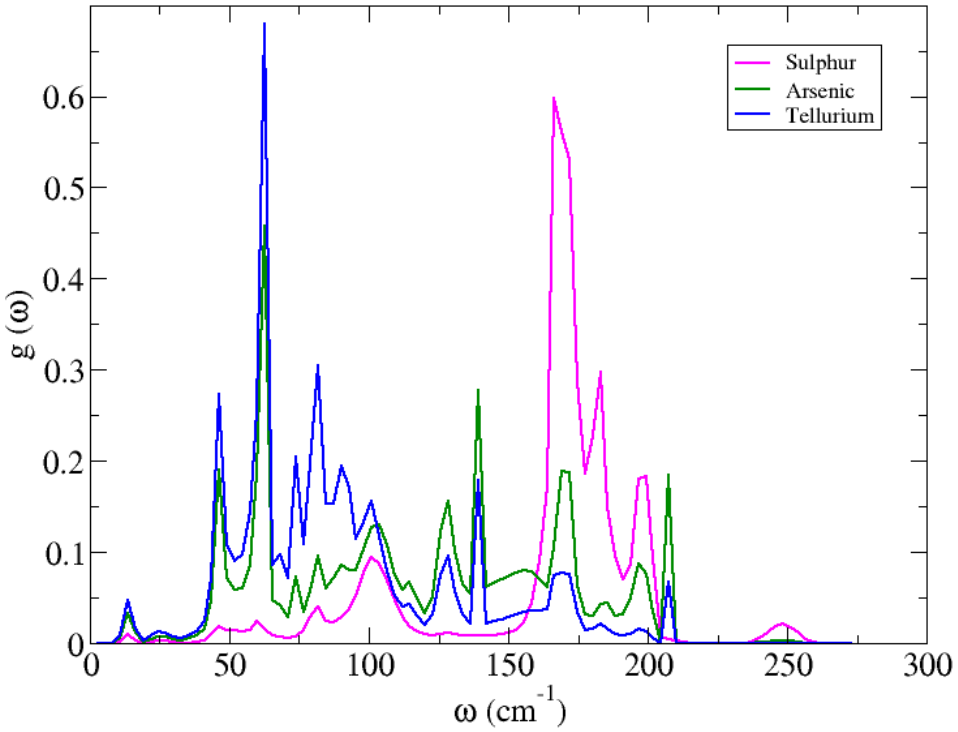

(a)

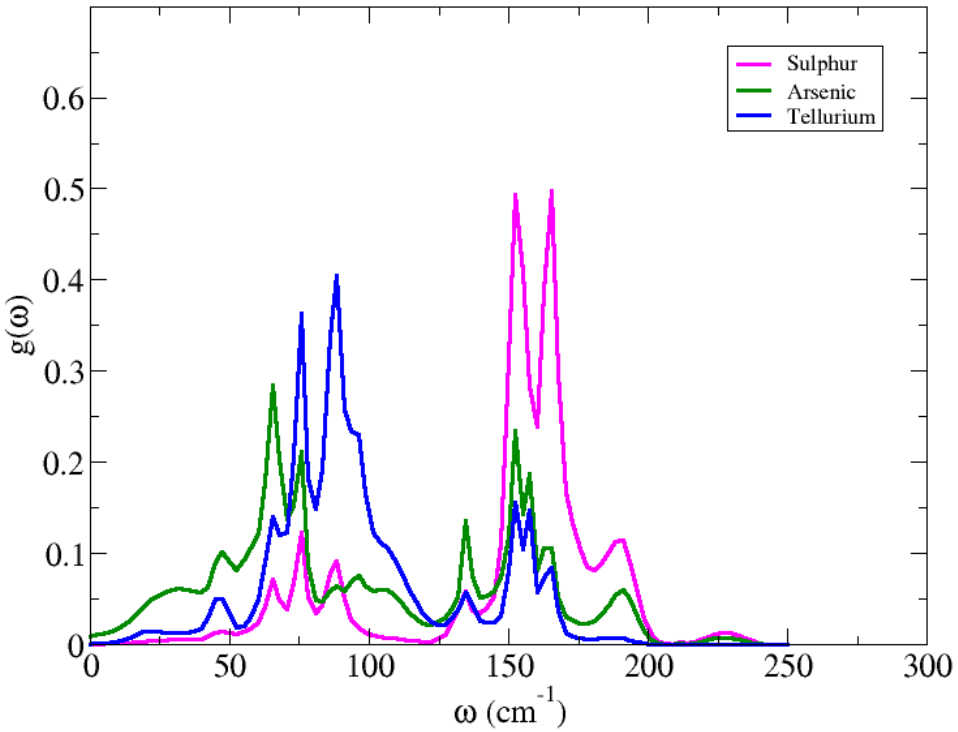

(b)

Figure 5.5: Projected phonon density of states of As_2Te_2S, both inner doped (a) and outer doped (b).

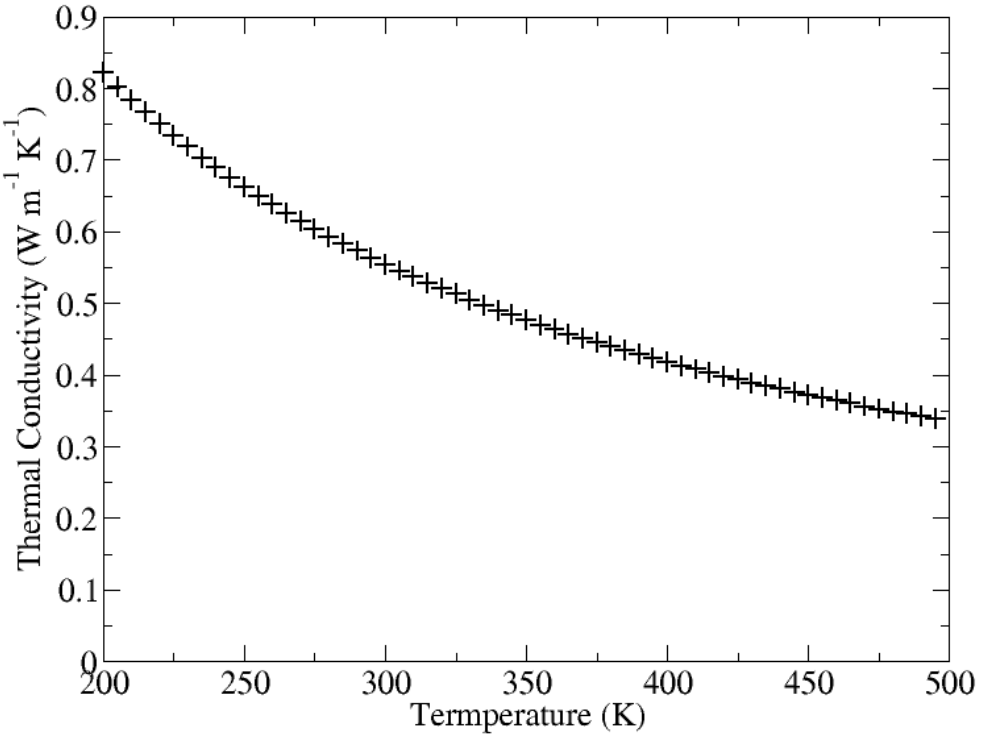

Figure 5.6: Lattice thermal conductivity of inner doped As_2Te_2S

	Inner doped					
	CBM			VBM		
	x	y	z	x	y	z
x	0.39±0.02	0.06±0.01	0.13±0.01	0.30±0.02	0.05±0.01	0.06±0.01
y	–	0.39±0.02	0.26±0.01	–	0.30±0.02	0.17±0.01
z	–	–	0.20±0.01	–	–	0.04±0.01
	Outer doped					
	CBM			VBM		
	x	y	z	x	y	z
x	0.41±0.04	0.07±0.01	0.06±0.01	0.29±0.03	0.05±0.01	0.06±0.01
y	–	0.36±0.03	0.19±0.02	–	0.29±0.03	0.15±0.01
z	–	–	0.08±0.01	–	–	0.16±0.02

Table 5.2: Deformation potential terms in eV, calculated for both phases of As_2Te_2S, set as upper diagonal matrices due to symmetry.

lattice alterations, and variations in the electrical properties. As such, it is unsurprising that the deformation potential would be at its highest along the x axis, which happens to be aligned with the bonds within the plane.

Additionally, the highest deformation potentials normal to the plane (along the z axis) occurs for each material on the side of the band gap for which their extremum occurs in a sharp peak. This is because the direct band gap is located at the Γ-point, which itself is mapped on the outer surface of the 5-ply layering. As such, varying

the inter-layer distance in the region where the electron states define the band gap minima, is likely to produce a substantially greater response if the bands form narrow extrema and whose values, as a result, are highly sensitive to atomic motion.

This fits with the expansion of the band gap in the inner doped phase, as it has the most impacted layer surfaces, both in terms of electrical properties and in terms of atomic positions. This is due to the presence of the sulphur atoms on the third ply of the layer, pulling in nearby atoms within the layer, and applying a strong potential on the electron bands of atoms on the outer ply.

5.1.4.2 Sound Velocity

The sound velocities of both doped versions of our material appear to be effectively isotropic within the plane of their layers, see table 5.3, in which x and y are in-plane axes, and z is the axis normal to the plane, differing significantly from the undoped phase which was highly anisotropic in-plane. Additionally, while the average sound velocity within the plane of the inner doped material is similar to that of the unaltered phase, that of the outer doped has reduced markedly. Finally, both doped phases appear to have significantly higher sound velocities in the direction normal to the plane, with the inner doped phase having a maximum at 3378.80 m/s.

	inner doped	outer doped	undoped
x	$(2.43\pm0.06)\times10^3$	$(1.97\pm0.05)\times10^3$	$(3.05\pm0.14)\times10^3$
y	$(2.44\pm0.06)\times10^3$	$(1.97\pm0.05)\times10^3$	$(1.17\pm0.05)\times10^3$
z	$(3.38\pm0.08)\times10^3$	$(2.88\pm0.07)\times10^3$	$(2.05\pm0.09)\times10^3$

Table 5.3: Sound velocity terms in metres per second, calculated for As_2Te_2S, with the results for the undoped phase included for comparison.

These factors relate to the elastic characteristics of any material, which related the average speed of sound v to the bulk modulus B and the mass density ρ :

$$v = \sqrt{\frac{B}{\rho}} \tag{5.5}$$

By altering these phases, we reduced the mass density from 4.03 AMU/A^3 to 3.61 AMU/A^3 for the inner doped material, and 3.73 AMU/A^3 for the outer doped material. This increased their sound velocities by a factor of 1.06 and 1.04 respectively.

The resulting bulk modulus calculated from equation 5.5 was thus even more affected. The inner doped structure incurred more compact layers with higher internal stresses, resulting in higher elastic constants and thus a further increase to the sound velocity. Meanwhile, the outer doped structure has unevenly stretched layers, decreasing the bulk modulus and by extension the sound velocity.

It should be noted that were the sulphur substitutions occurring evenly in the same material, these two opposing effects would partially cancel out. However, this would be unlikely, as the inner-doped phase has a significantly lower formation energy, even though there are twice as many atoms on the outer doping position than on the inner doping position, with one on each side of the layer for each inner-doped position.

5.1.4.3 Electron-phonon relaxation time

The presence of a substantial band gap in the inner doped phase poses a challenge to our methodology. Thermal smearing and broadening terms compound to produce an exaggerated smearing of our electron states into the band gap. The electron-phonon relaxation time is calculated as a function of the number of states that are smeared, and as a result converges towards infinity as the number of states to be scattered converges towards zero. Under ideal circumstances, this would be cancelled out when correcting the electrical conductivity, as the uncorrected term for conductivity converges towards zero along with the number of states.

However, the operations applied to our DOS when calculating the relaxation time increase its value disproportionately to the $\frac{\sigma}{\kappa}$ term output by BoltzTraP. This numerical discrepancy leads to a non-physical increase in the resulting σ term inside the ground state bandgap, which can be seen in figure 5.7.

In order to fix this, a regularization term γ is applied to the relaxation time in order to force it to converge in the direction of a finite value instead, as defined by equation 5.6. By adding a term that is significantly larger than τ^{-1} in the relevant region, we are able to minimize the hyperbolic behaviour that it causes in σ while maintaining realistic values for τ.

$$\tau_r = \frac{1}{\gamma + \frac{1}{\tau_u}} \tag{5.6}$$

where τ_r is the regularized value of the relaxation time τ, τ_u is the non-regularized value, and γ is the regularization term. By iteratively decreasing the regularization term and plotting the electrical conductivity σ with respect to band energy, it is possible to converge towards a point in which the conductivity stops displaying hyperbolic behaviour.

While this method does appear to work, as shown in figure 5.7, an ideal value for the regularization term is not known, and so it is necessary to use boundary conditions to constrain its range. The resulting impact on ZT was found to be within an acceptable error range when compared across the allowed values of γ, see appendix F.

These effects did not occur in the outer doped phase, as its band gap was small, resulting in the combined smearing and broadening effects covering its full range at

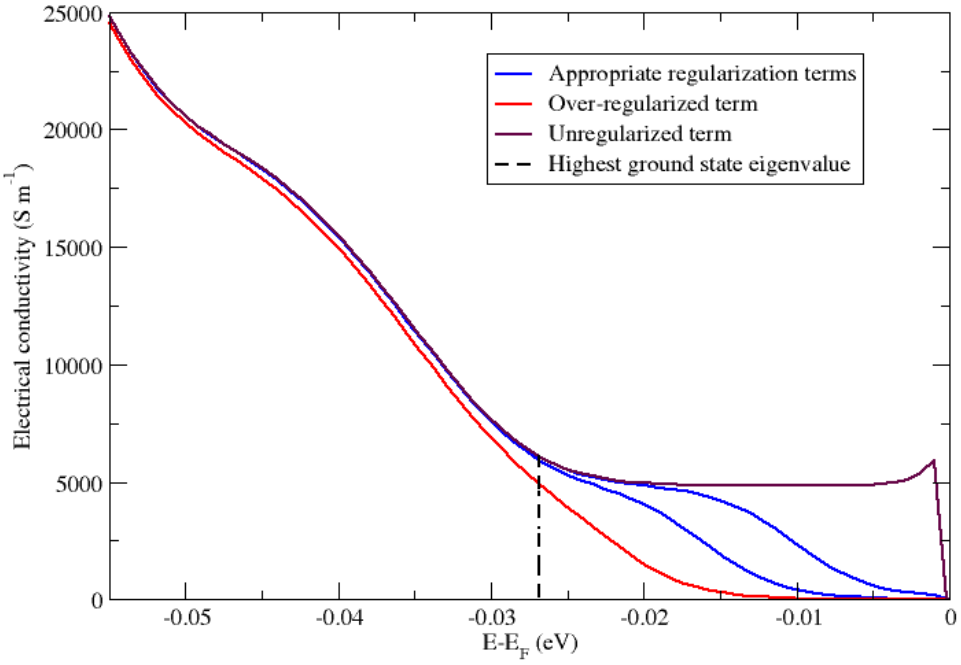

Figure 5.7: The electrical conductivity in the valence band of the inner doped phase of As_2Te_2S when corrected with the relaxation time, calculated as per appendix F. The brown line shows the result produced without a regularization term, leading to non-physical behaviour as a result of a numerical discrepancy caused by compounding smearing methods. The blue lines show regularized values using valid regularization terms. The red line shows over-regularized behaviour, in which the regularization term has significantly over-corrected the electrical conductivity.

our lowest sampled temperature of 200K. While this also meant that it was evaluated at over-estimated DOS values, reducing the relaxation time, this was counter balanced by its smaller deformation potential at the VBM, resulting in promising relaxation time values as a p-type semiconductor, see figure 5.8.

5.1.5 Thermoelectric figure of merit

The thermoelectric figure of merit of the inner doped phase of As_2Te_2S proved to offer promising values of ZT, but only at higher temperatures than the unaltered or outer doped phases. This behaviour appears to be linked to the necessity for uneven electron state distributions to be produced via thermal smearing into the band gap, which combined with substantial electron phonon coupling has resulted in this material being highly thermally dependent, see figure 5.9.

These results make it clear that efficient thermoelectric function at low temperatures

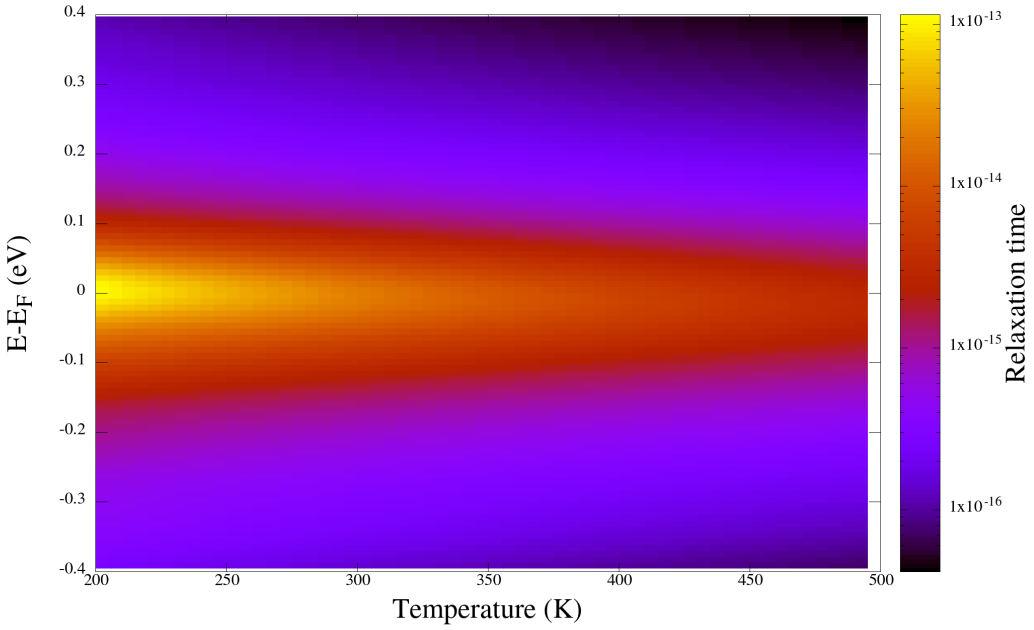

Figure 5.8: Relaxation time of the outer doped phase along the x direction.

can be dependent on the ability to effectively smear thermal electrons across the band gap. As a result, a band gap narrow enough to be substantially impacted by thermal smearing at a select temperature is preferable when optimizing thermoelectric efficiency for said temperature.

Considering that the thermal energy of an electron defines its range within a Fermi-Dirac distribution, and that the Seebeck coefficient is effectively a measure of asymmetry in the DOS over a range around a point as defined by a Fermi Dirac distribution, one may conjecture that an ideal band gap for any operating temperature would preferably be no more than approximately four times the thermal energy of an electron for that temperature.

5.1.6 Error estimations

The process for evaluating errors in the case of the both phases of As_2Te_2S is nearly identical to that used for the β-As_2Te_3. However, the wider band gap apparent in the inner doped phase has had some significant impacts.

For one, the linear region of the deformation potential in the VBM and CBM in the inner doped phase appears to be broader, effectively halving the error margins of nearly 5% that is apparent in both the outer doped phase and the unaltered material.

Additionally, the use of a constrained regularization term as described in appendix F has added a source of error that dominates the relaxation time of the inner doped

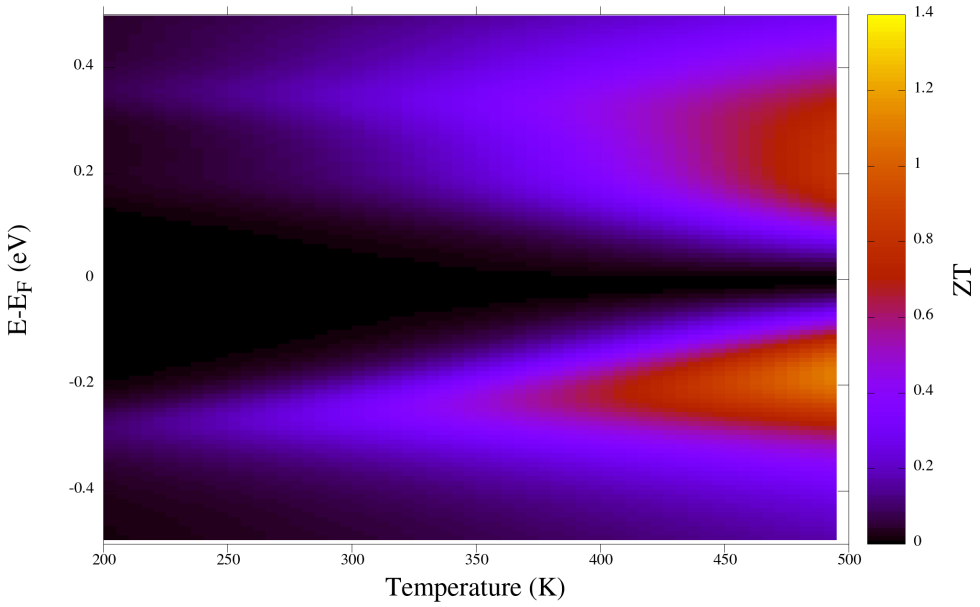

(a)

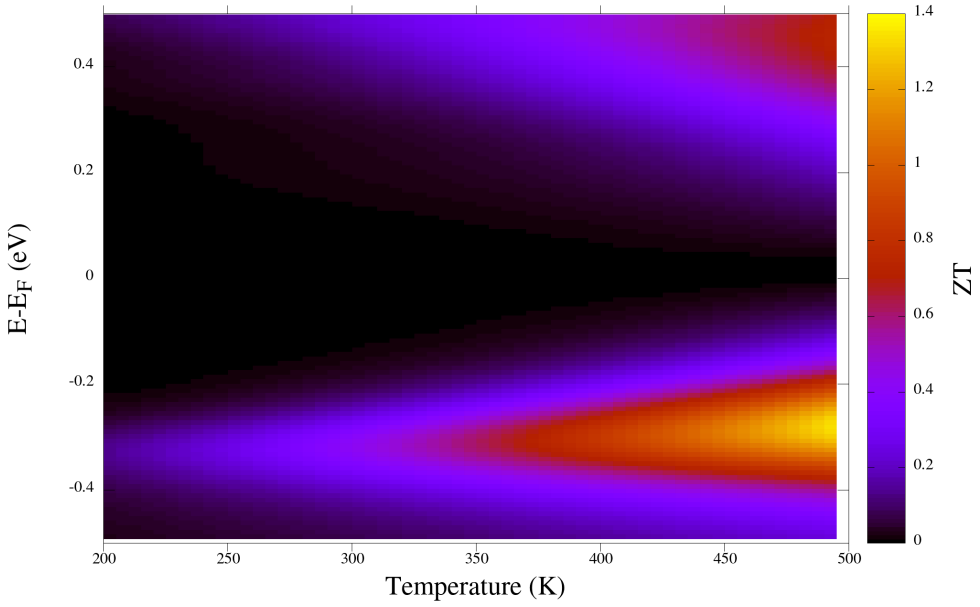

(b)

Figure 5.9: Thermoelectric figure of merit of inner doped As_2Te_2S in (a) the x direction and (b) the z direction. When accounting for all terms, the ZT averages out as being approximately isotropic with respect to the x and y directions, while the z direction provides higher values in only the VBM due to the exceptionally low local deformation potential and high sound velocity, these are mostly countered by a high lattice thermal conductivity.

phase, with error margins of between 9 and 15% at the conduction band, and between 7 and 10% at the valence band.

Meanwhile, electron transport terms calculated from solving the Boltzmann transport equation appear mostly unaffected. They show small tolerances resulting from stochastic errors in band calculations within under 2% for both phases.

Phonon calculations involving these doped phases appear to result in lower relative acoustic sum rule corrections. As a result, the approximated error from phonon terms appears to be equal to 2.78% and 2.79% for the inner and outer doped phases respectively.

As a result, it would appear that the error tolerance in our estimations of ZT in both phases are dominated by the electron-phonon relaxation time estimation. In the case of the outer-doped system with its narrow band gap, strongly resembling the electronic of the unaltered material, the squared component of the deformation potential combined with its 5% error appears to dominate. However, in the case of the inner-doped system, the deformation potential appears easier to converge, while its need for a regularization term in order to maintain numerical stability when applying the relaxation time correction to the electrical transport properties leads to an uncertainty that is dominant, especially at the conduction band.

With these terms accounted for, we can now compare the highest ZT values for each of the configurations studied of $As_2Te_{3-X}S_X$, both doped and undoped. We find that once errors are accounted for, the ZT results for both the outer doped and undoped configurations appear to be almost entirely within error of each other, both in the optimal direction, and when averaging over direction, although the doped configuration has slightly higher ZT values at a higher temperature of 500K.

Meanwhile, the inner-doped phase appears to be significantly impacted at lower temperatures, with ZT values of less than half those of the other configurations at room temperature. However, it becomes significantly more thermoelectric at higher temperatures, to the point of displaying the highest total ZT when averaged over all directions at 500K. Though it should be pointed out that it also has the largest error margins due to the uncertainty involved in estimating the regularization term.

	ZT					
	β-As_2Te_3		inner doped		outer doped	
	300K	500K	300K	500K	300K	500K
Optimal	1.19±0.12	1.32±0.14	0.42±0.11	1.35±0.34	1.11±0.11	1.48±0.15
Total	0.63±0.06	0.83±0.09	0.28±0.07	1.19±0.30	0.66±0.07	0.95±0.09

Table 5.4: Highest ZT terms calculated with respect to $(E - E_F)$ for all 3 phases of $As_2Te_{3-X}S_X$ at 300K and 500K, both in the optimal direction for that material, and as an average over all directions.

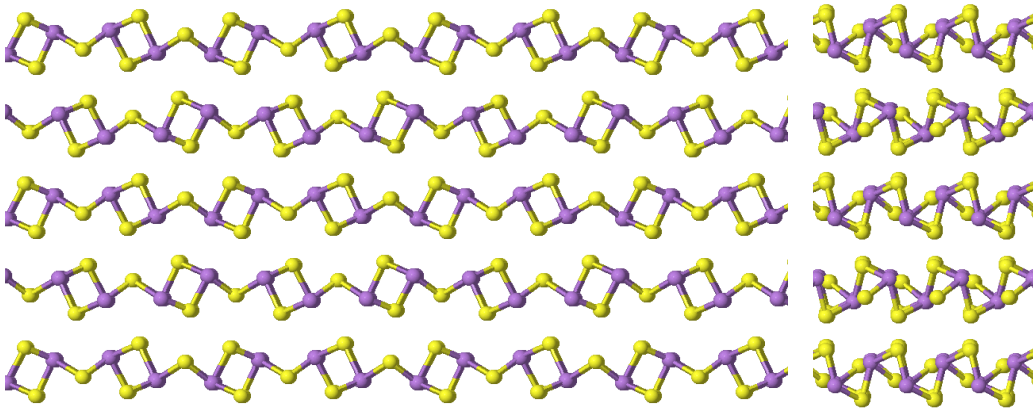

(a) (b)

Figure 5.10: Unaltered configurations of As_2S_3, seen from two orthogonal directions along the layer. We will refer to the x-axis as that along the side-to-side direction in (a), and the y-axis as that in (b). The arsenic is in purple and the sulphur is in yellow.

5.2 As_2S_3

5.2.1 Structures

Like both phases of As_2Te_3, As_2S_3 is a pnictide-chalcogenide alloy, and it also has a layered structure separated by VdW forces. Specifically, it is made of uneven layers, one to two atoms thick, which alternate, such that each layer sits between two layers that are rotated by 180 degrees relative to itself and offset by half the distance of periodicity along one in-plane direction, which we refer to as the x axis. As with the β-phase of As_2Te_3, we define the z axis as being that normal to the plane, and the y axis as being orthogonal to both the x and z axes.

This structure allows for all atoms in the system to maintain close to tetrahedral configurations, with each bond angle existing in a range between 85 and 105 degrees. The result is that each arsenic atom is configured in such a way that its lone electron pair is aligned with that of a sulphur atom in an opposing layer, allowing for a hydrogen-bond-like Coulomb coupling between layers. This complementary behaviour differs to that of β-phase As_2Te_3, in which the inter-layer spacing is defined by chalcogenide to chalcogenide VdW interactions. One might expect that as a result As_2S_3 may demonstrate higher spring constants along the VdW forces connecting its layers.

As a consequence of this more complex interaction between layers, the primitive cell of the unaltered system is substantially larger, consisting of 20 atoms. This increases the computational cost of our system, to the point that certain large supercell or q-point calculations became practically unfeasible. The latter is related to the $3N$ number of perturbations that need to be calculated at each q-point, where N is the number of atoms in the cell.

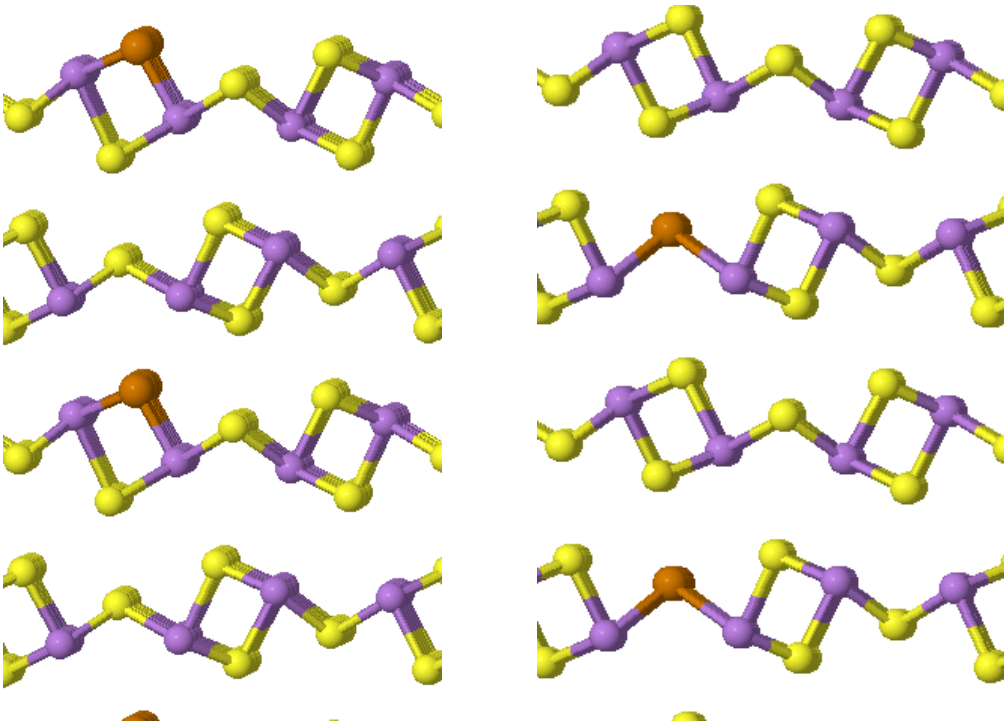

(a) (b)

Figure 5.11: Configurations of As_2S_2Te, substituted with tellurium on an arsenic bonded sulphur site (a) and a non-bonded site (b). The arsenic is in purple, the tellurium is in orange and the sulphur is in yellow.

Just as with the β-phase of As_2Te_3, we also performed calculations on two altered versions of As_2S_3, each defined by the substitution of one chalcogenide atom with another, making As_2S_2Te. In this case, we substituted sulphur atoms with tellurium ones in two sites, one that is aligned with an arsenic atom in a neighbouring layer, and one that is not, as shown in figure 5.11. As a short hand, we will refer to these two configurations as the "bonded" and "non-bonded" doped structures respectively.

The formation energies of these structures was calculated using the same method as in section 5.1.1, wherein the arsenic-bonded configuration had a calculated total energy for a 20-atom cell of -26460.70 ± 0.02 eV and the non-bonded configuration and a total energy of -26460.39 ± 0.02 eV, while the unaltered structure had a total energy for a 20-atom cell of -26198.224 ± 0.02 eV.

Additionally, the difference in chemical potentials was found to be the opposite value to that for As_2Te_3. Thus by using the same approximations, assuming that there is no internal pressure due to the geometry optimised state, ignoring the impact of temperature and entropy on the Gibbs free energy, and assuming an arsenic-rich system, we find a formation energy of 0.41 ± 0.02 eV and 0.10 ± 0.02 eV, per cell, for the arsenic-bonded and non-arsenic bonded systems respectively.

These As_2S_2Te defect formation energies are not that much higher than those calculated of As_2Te_2S phase, being 0.024 eV and 0.101 eV higher per formula unit

respectively, which is within 0.2 meV per formula unit, making these thermally accessible. Thus we may expect spontaneous occurrences of these doped configurations within the temperature range studied. Additionally, it is worth noting that the size of the cell studied is also larger, with 8 possible sites for the arsenic-bonded doping configuration, and 4 possible sites for the non-bonded doping configuration.

As a result, it seems likely that conventional doping would favor some combined usage of both sites, and thus neither of our systems are exactly representative of experiment. Additionally, by substituting doping agents into our systems, we further broke symmetry. As a result, we found that on average, both doped configurations required approximately twice as many k-point calculations as the unaltered one.

5.2.2 Electronic terms

The electronic band structure of As_2S_3 shows an indirect band gap measuring 1.333 ± 0.001 eV, see figure 5.12a with the VBM region flattened around the Γ-point along the direction normal to the plane, or z axis. As we obtain a parabolic region in the x and y axis within the plane, we can infer a much higher electron mobility along the direction normal to said plane.

We also notice two band regions competing for the VBM, one along the x-direction and another along the y-direction. The band along the x-axis (left to right in figure 5.12a) is slightly higher, albeit by a difference of only 0.026 ± 0.001 eV. It also appears quite broad along the direction leading away from the Γ-point, also suggesting increased electron mobility.

The band structures of both of our doped configurations offer very similar features, with a general upwards shift of the highest valence band, and a measured global maximum along the y-axis, propagating from the Γ-point, see figure 5.12b. The conduction band is less impacted, although a slight shift has led to a new CBM along the y-axis, albeit within the inter-layer spacing neighbouring that of the Γ-point. The overall band gap of our doped configurations has shrunk to about 0.95 eV, with an overall flattening of the valence band suggesting higher electron mobility than in the unaltered structure.

The DOS of As_2S_3 matches our observations of the band structure, see figure 5.13a. displaying a substantial band gap and a peak in the number of states at around 0.7 eV above the Fermi energy matching the flattening of the conduction band in the band structure. The valence band offers a slightly shallower gradient in the DOS than the conduction band.

Our DOS plot for the non-bonded configuration also displays a narrower band gap than for the unaltered structure, see figure 5.13b. The shifting and flattening of the highest conduction band into the band gap has resulted in the appearance of a peak

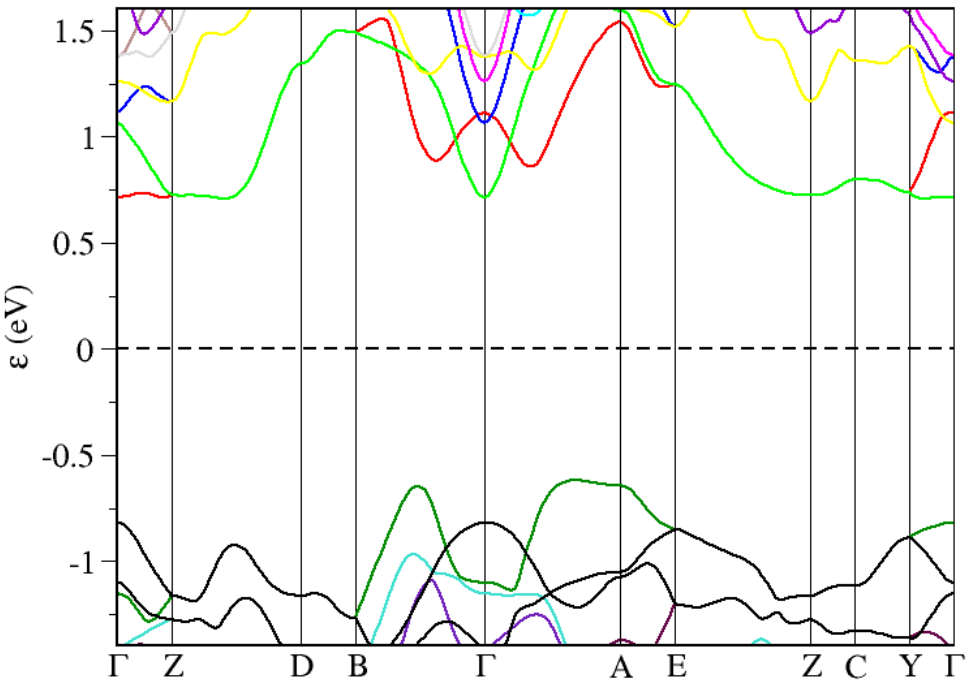

(a)

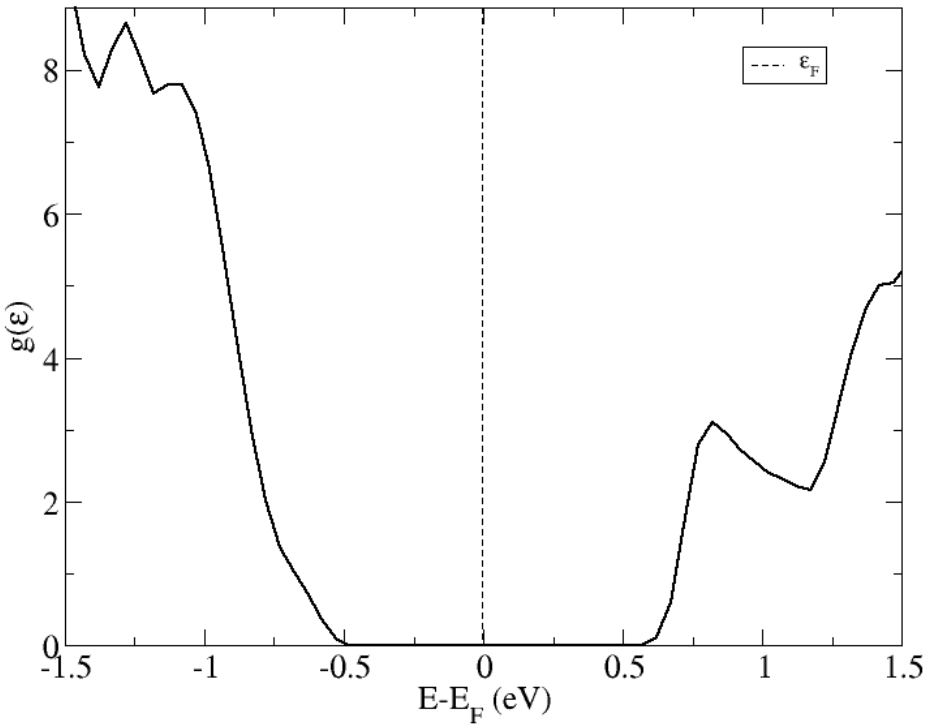

(b)

Figure 5.12: Band structure (a) and density of states (b) of As_2S_3.

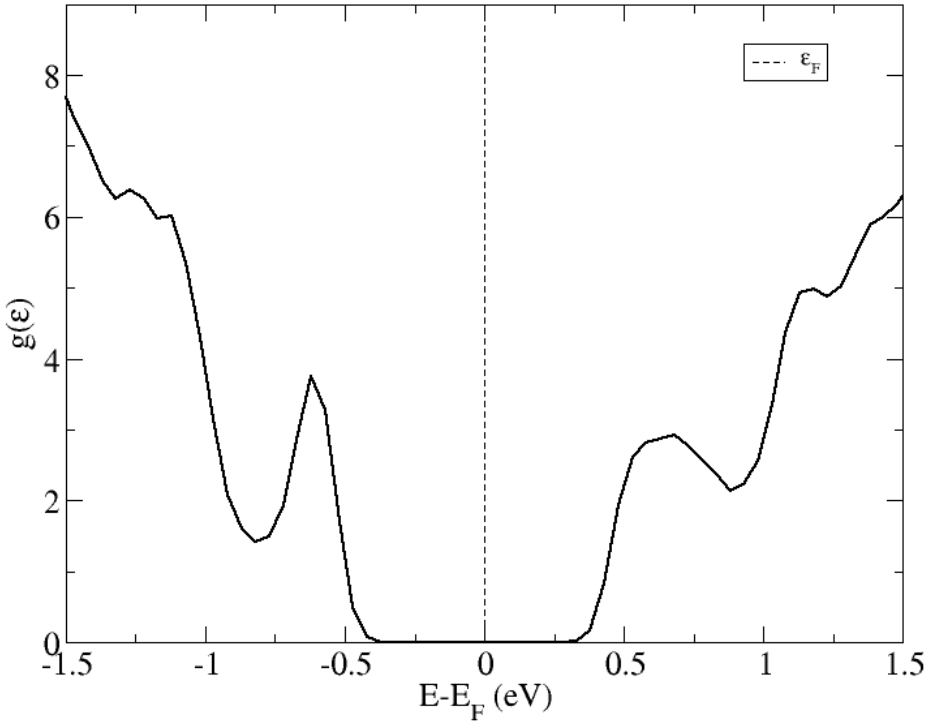

(a)

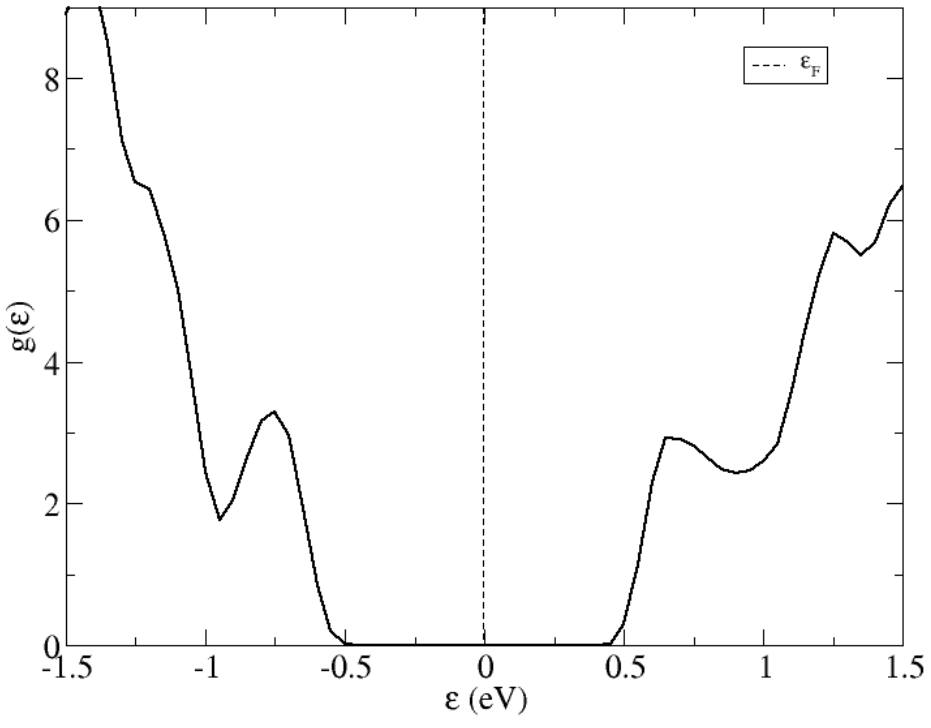

(b)

Figure 5.13: Densities of states of As_2S_2Te, with (a) an arsenic-bonded sulphur site configuration, and (b) a non-arsenic bonded sulphur site configuration. The DOS of both doped configurations are close to identical.

just under the gap in our DOS, mirroring that above the DOS and producing a steeper gradient than that of the valence band in the unaltered material.

When evaluating the resulting Seebeck coefficients, it was found that the larger band gap offered by As_2S_3 resulted in a similar effect as with the inner-doped As_2Te_2S. Specifically, the Seebeck coefficient evaluated over regions of the ground state band gap populated by small amounts of thermally smeared electrons would result in very high values, see figure 5.14.

In the case of As_2S_3, this effect becomes increasingly pronounced for each point further and further into the band gap, until we reach a point at which our Fermi Dirac smearing does not promulgate sufficiently to be included as part of the Seebeck effect being calculated. This results in a step-like reduction of the coefficient to zero, thus the unusual behaviour in our graphs.

This can only occur when the band gap is significantly larger than the range of our Fermi Dirac smearing and DOS broadening terms combined. Increasing the temperature to the point that the step behaviour stops also leads to the gradual decrease of the coefficient, as the smearing terms on either side of the gap begin to cancel out and converge towards a more realistic distribution.

As such, the reduction of the band gap in our doped phases has also diminished the impact of our smearing problem, leading to our extreme Seebeck coefficient values being reduced at lower temperatures, see figure 5.14b.

5.2.3 Phonons transport properties

Due to the expanded computational costs of As_2S_3 when compared to As_2Te_3, multiple calculations relating to phonon terms were found to be unfeasible for a variety of reasons. DFPT calculations could not be parallelised consistently and were found to be extremely slow, to the point that certain individual q-points could not be evaluated for the doped compounds.

Finite displacement supercell calculations had large memory requirements and few sampling points over which to distribute tasks between computer cores. This had the effect of making hundreds of simultaneous calculations of this type impractical for even the unaltered compound.

As a result of these problems, our analysis of the lattice thermal properties of As_2S_3 is unfortunately more limited than for the β-phase of As_2Te_3. We were able to evaluate its 2nd order phonon terms for the unaltered phase, as well as a coarse dispersion plot for all phases, allowing us to estimate sound velocities. The projected phonon DOS could then be plotted, see figure 5.15, and the Boltzmann transport equation applied while using the small grain limit as the scattering term.

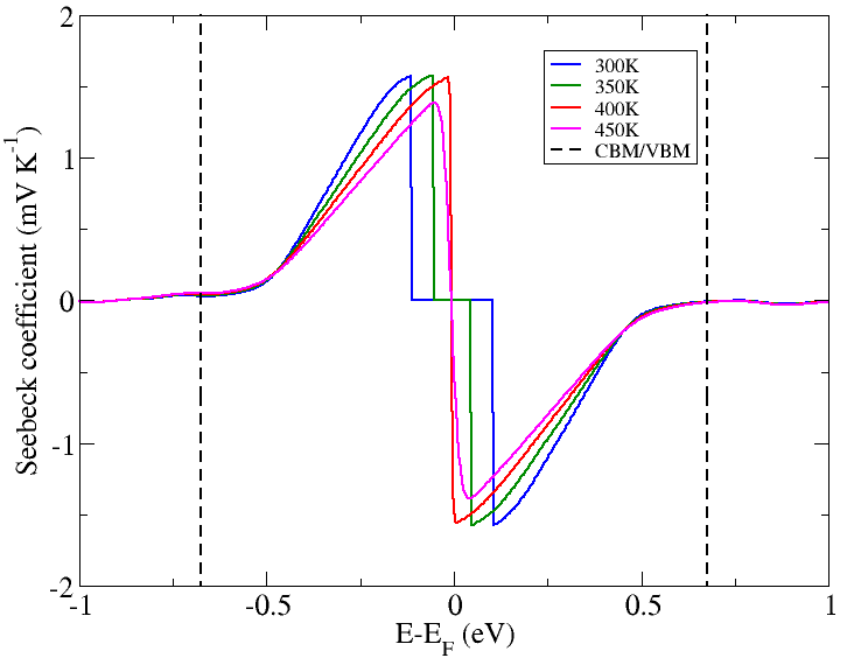

(a)

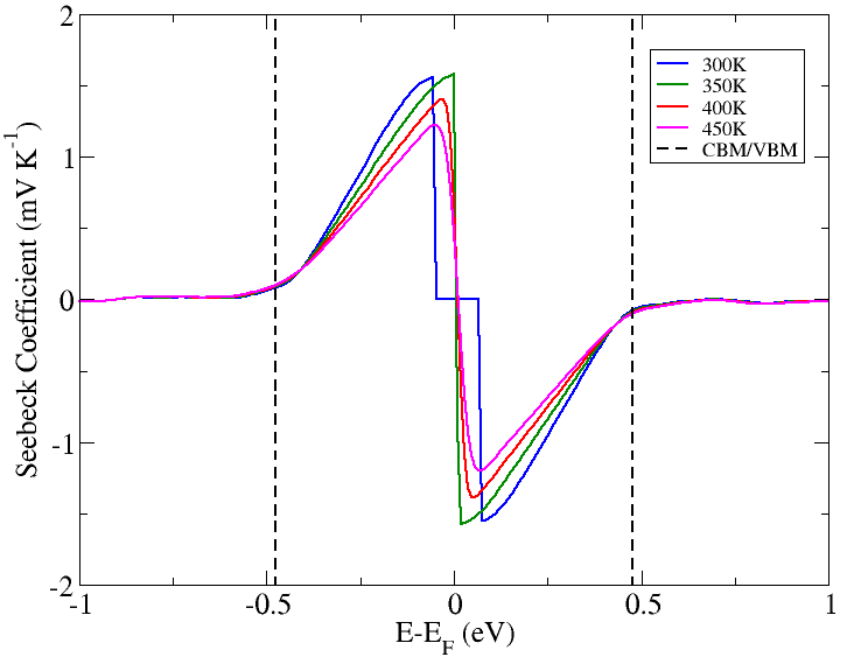

(b)

Figure 5.14: The Seebeck coefficient plots for $As_2S_{3-X}Te_X$, with (a) an unaltered configuration and (b) a doped, non-arsenic bonded sulphur site configuration. BoltzTraP's attempt at DOS broadening leads to very small non-zero values occurring in the band gap, and by extension to the extremely large Seebeck coefficient values demonstrated in these graphs. Only values that are *outside* the band gap region, delimited here by the dotted lines for the VBM and CBM, were used to provide the values used in our calculations of ZT. This allows us to avoid these numerical artefacts, inherent to BoltzTraP calculations across larger bandgaps.

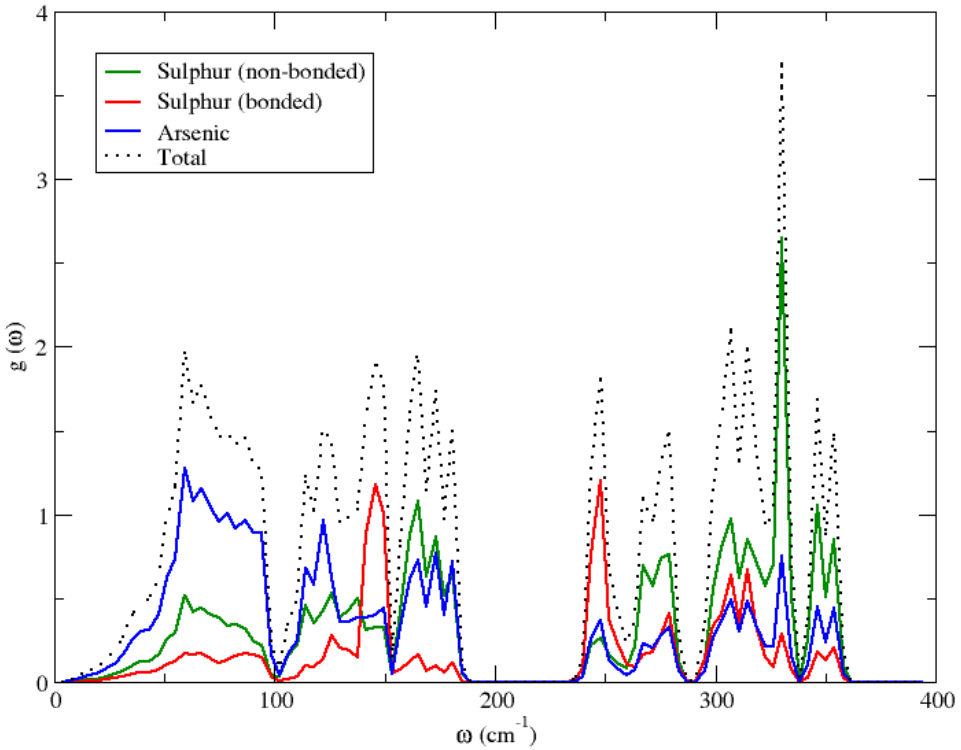

Figure 5.15: Projected phonon density of states of As_2S_3. It shows how the arsenic atoms dominate the low-energy acoustic phonon modes, as well as a clear distinction between the phonon modes of the bonded and non-bonded sulphur atoms within the optical range.

The projected DOS demonstrates how the lighter sulphur atoms dominate the high frequency optical modes, while the arsenic atoms dominate the acoustic modes. The actual lattice contribution to the thermal conductivity appears highly anisotropic, with values at 300K of $(5.35\pm0.12)\times10^{-1}$ and $(3.94\pm0.09)\times10^{-1}$ $W\ m^{-1}\ s^{-1}$ in the plane along the x and y axes, and a substantially lower value of $(1.34\pm0.03)\times10^{-1}$ $W\ m^{-1}\ s^{-1}$ along the z-axis normal to the plane.

5.2.4 Electron-phonon coupling

5.2.4.1 Sound velocity

The sound velocity of As_2S_3 was found to be relatively high and isotropic within the xy plane, see table 5.5, suggesting that the layers are quite brittle with a high bulk modulus. The sound velocity normal to the plane is substantially lower, most likely due to the weaker VdW forces.

Doping the structure in either of our two selected sites leads to a sharp reduction in all values of the sound velocity, along with the appearance of significant anisotropy

between the x- and y- directions within the plane. The highest values in the doped structures occur in both cases along the x-direction, which is aligned with the bonds (left to right direction in figures 5.11).

	As_2S_3	arsenic bonded As_2S_2Te	non-arsenic bonded As_2S_2Te
x	$(5.79\pm0.13)\times10^3$	$(4.83\pm0.11)\times10^3$	$(4.75\pm0.11)\times10^3$
y	$(5.79\pm0.13)\times10^3$	$(2.80\pm0.06)\times10^3$	$(3.38\pm0.07)\times10^3$
z	$(2.55\pm0.06)\times10^3$	$(1.70\pm0.04)\times10^3$	$(1.43\pm0.03)\times10^3$

Table 5.5: Sound velocity terms in metres per second, calculated for all three configurations (tellurium-doped and unaltered) of $As_2S_{3-X}Te_X$.

Once again, we can explain one of the impacts of doping using Hooke's law, as the addition of mass is inversely proportional to the rate of propagation of lattice vibrations. The loss in isotropy within the layer is related to the shape of the primitive cell. Specifically, the cell is set up as being 3 times longer in the planar direction following the bonds (see figure 5.10a) than in the one orthogonal to it (see figure 5.10b). As a result, we end up with our doping being much higher in one dimension than in the other. Furthermore, the configuration of our cell means that the tellurium doping agents are in direct proximity with each other, leading to direct interactions between larger, heavier elements during sound propagation.

It may also be noted that the arsenic-bonded configuration also offers a slightly higher sound velocity normal to the plane than the non-arsenic bonded one, most likely related to stronger VdW interactions between planes being applied to the mass of the tellurium atoms. However, offering qualitative analysis of the differences in sound velocity within the plane between the two doped structures is more challenging.

5.2.4.2 Deformation potential

The deformation potential was evaluated for all three materials, and was found to be almost exclusively significant within the uni-axial directions. As a result, we find that As_2S_3 presents generally stronger electron-phonon coupling than our previous materials, especially along the direction normal to the plane. In fact, it appears to be the direction with the strongest electron phonon coupling in the unaltered material, and for the VBM of non-arsenic bonded As_2S_2Te.

However, the arsenic-bonded doped configuration appears to present a substantially decreased electron-phonon coupling in the z-axis, especially in the CBM, while generally increasing it in the y-axis, favouring conductivity normal to the plane as opposed to that within the plane.

	As_2S_3					
	CBM			VBM		
	x	y	z	x	y	z
x	0.28±0.01	0.00±0.01	0.00±0.01	0.37±0.02	0.00±0.01	0.00±0.01
y	–	0.41±0.02	0.00±0.01	–	0.26±0.02	0.00±0.01
z	–	–	0.42±0.02	–	–	0.35±0.02
	arsenic bonded As_2S_2Te					
	CBM			VBM		
	x	y	z	x	y	z
x	0.31±0.02	0.07±0.01	0.06±0.01	0.27±0.02	0.00±0.01	0.00±0.01
y	–	0.43±0.03	0.19±0.02	–	0.39±0.03	0.00±0.01
z	–	–	0.13±0.01	–	–	0.21±0.02
	non-arsenic bonded As_2S_2Te					
	CBM			VBM		
	x	y	z	x	y	z
x	0.29±0.02	0.01±0.01	0.00±0.01	0.24±0.01	0.01±0.01	0.00±0.01
y	–	0.40±0.01	0.00±0.01	–	0.36±0.01	0.00±0.01
z	–	–	0.38±0.02	–	–	0.44±0.02

Table 5.6: Deformation potential terms in eV, calculated for As_2S_3 and the arsenic bonded and non-bonded phases of As_2S_2Te, set as upper diagonal matrices due to symmetry.

5.2.5 Thermoelectric properties

5.2.5.1 Electrical conductivity

As our As_2S_3-based compounds all demonstrate substantially larger band gaps than for any of our previous materials, we find ourselves with a similar challenge as with the inner-doped phase of β-As_2Te_3. As such, the excess smearing of electron states into the band gap has also resulted in an excessively increasing relaxation time as we approach the Fermi energy. Once again we have applied a regularisation term iteratively to our relaxation time, using the same procedure shown in appendix F, in order to remove hyperbolic behaviour from our electrical conductivity to obtain a more realistic gradient in the term, see figures 5.16.

From this, we find that the impact of the lower sound velocity and high deformation potentials along the x-axis, combined with the conductivity terms evaluated using the BTE, have resulted in an electrical conductivity that is an order of magnitude smaller in the direction normal to the plane than in the directions along it. This is in part reversed in the arsenic bonded As_2S_2Te, in which the significantly lower deformation potentials in the z axis are reflected with higher values along x, particularly in the CBM.

However, the conductivity along x is further increased despite the reduction in sound

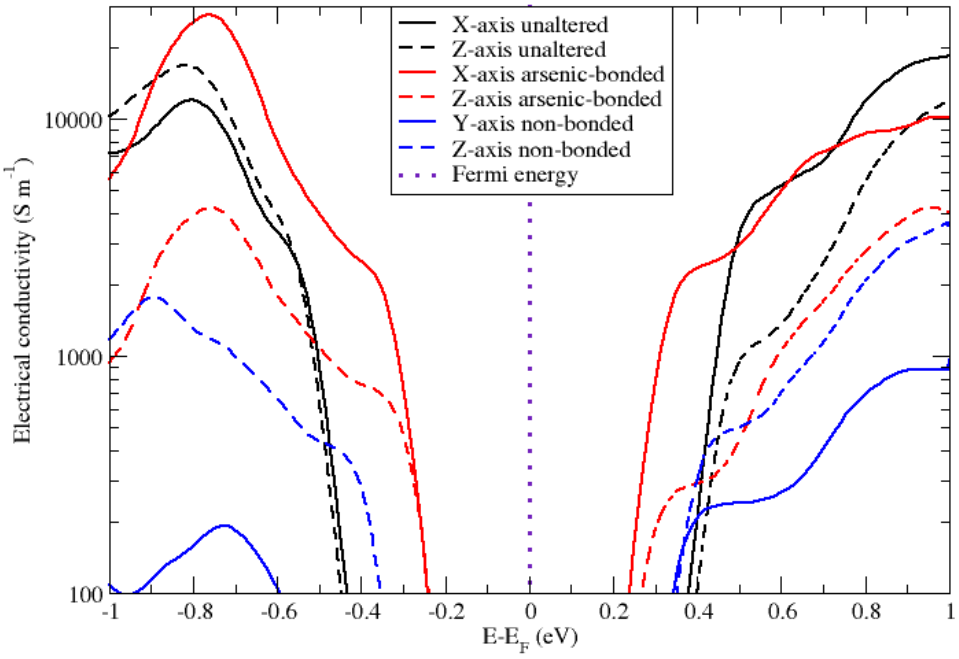

Figure 5.16: Electrical conductivities plotted for As_2S_3, for the As_2S_3 along the x-axis and the z-axis, for arsenic bonded As_2S_2Te along the x-axis and the z-axis, and for non-bonded As_2S_2Te along the y-axis and the z-axis. We find that the plot along the z-axis for the unaltered and bonded configurations are generally similar to those in x, but favour the VBM over the CBM.

velocity in that direction, mostly as a result of the further reduction in the deformation potential in the VBM along that axis. While this is also true for non-arsenic bonded As_2S_2Te, it also suffers from an even lower electrical conductivity in the z-axis than the unaltered structure along with a significantly negatively impacted value in the y direction.

5.2.5.2 Approximating the thermoelectric figure of merit

While we may not be able to thoroughly evaluate the figure of merit of our As_2S_3 compounds, as we lack the third order phonon terms for all three structures, and the second order phonon DOS for the doped phases, we can still make a first order approximation. We do so by evaluating ZT in a limited context, within the small grain limit, such that phonon scattering is dominated by grain boundaries as opposed to phonon-phonon interaction.

While this is likely to result in an overestimate when compared to a perfect lattice, it can at least be applicable for some more realistically achievable materials with rela-

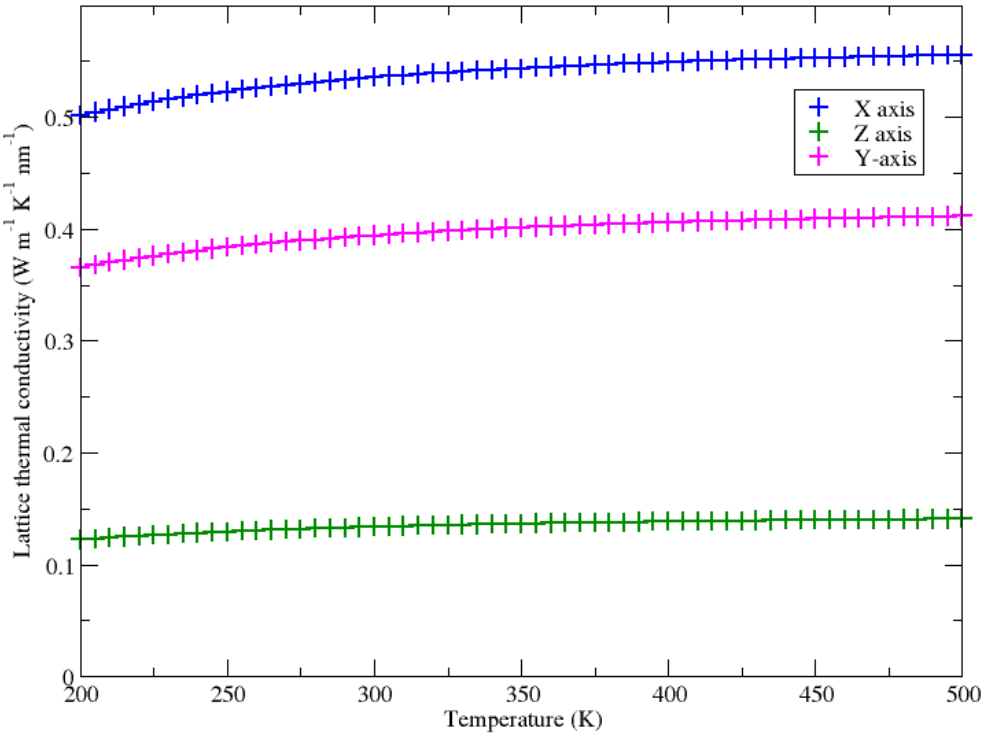

Figure 5.17: The lattice thermal conductivity of unaltered As_2S_3 within the small grain limit, calculated as a proportionality term with respect to the size of the grain in nm.

tively small grain sizes. It should be noted, however, that beyond just underestimating ZT, the value of the lattice thermal conductivity does not descend with temperature, see figure 5.17, as it does when computing it with the third order phonon term as our scattering term. Additionally, we are assuming as a broad approximation that the doped variants of As_2S_3 share the same lattice thermal conductivity, as running appropriately sampled phonon density of states calculations on the doped materials was found to be too computationally challenging.

	unaltered		bonded		non-bonded	
	VBM	CBM	VBM	CBM	VBM	CBM
x	0.37±0.05	0.47±0.07	0.37±0.05	0.30±0.04	0.55±0.08	0.40±0.06
y	0.22±0.03	0.57±0.06	0.08±0.01	1.09±0.15	0.07±0.01	0.23±0.03
z	0.49±0.07	0.22±0.03	0.19±0.03	0.08±0.01	0.11±0.01	0.13±0.01

Table 5.7: ZT values at room temperature (approximated as 300K), calculated for As_2S_3, as well as bonded and non-bonded phases of As_2S_2Te, using a lattice thermal conductivity as calculated assuming a mean free path of 1 nm within the small grain limit.

As a result of applying this approximate set of values for lattice thermal conductivity, we are able to plot ZT values for our As_2S_3 compounds, which we can then tabulate in terms of the peak values at room temperature, see table 5.7. Thus we can see that while

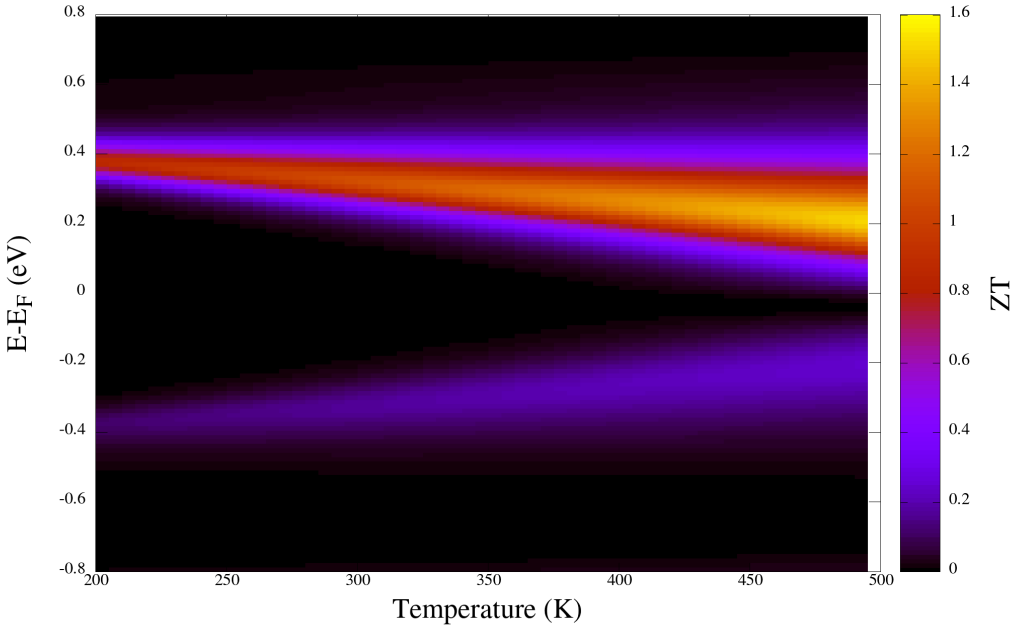

Figure 5.18: The highest value of ZT calculated for As_2S_3, found by evaluating it over the y direction in the arsenic-bonded doped structure. Achieving this maximum requires n-type doping.

the arsenic-bonded As_2S_2Te offers the highest possible ZT, at 1.09 ± 0.15 along the y-axis when n-type doped, the value found when averaging over directions is 0.49 ± 0.07. The highest value when p-type doped is along the x-axis of the non-bonded doped compound, but the best value when averaging over directions for p-type doping is actually offered by the unaltered As_2S_3 cell, with a value of 0.36 ± 0.07.

While many of these values are not that competitive when comparing to record values of ZT at room temperature, it should be noted that even despite the inverted behaviour of the lattice thermal conductivity, the ZT of As_2S_3 appears to be strongly correlated to temperature when compared to As_2Te_3. This is to be expected for a material with a larger band gap, leading to some impressively high values when selecting for optimal doping and direction of the thermal gradient, see figure 5.18. However, it should also be noted that this value is highly direction dependent, offering a maximal value along the z axis of 0.3, and only when n-type doped.

As such, while we have produced some specialised, targeted and promising results, we must account for systematic error sources that might increase our values. These include our use of the small grain limit, which likely reduces the impact of the lattice thermal conductivity on our ZT values. Additionally, any error associated with our regularization of electron-phonon relaxation time values around the band gap is greater the further we move into the ground state band gap from either the ground state VBM or CBM. Then we must account for the dependencies of our results on exact directional

function and doping, which may be challenging and expensive to synthesise around.

5.2.6 Error estimations

Evaluating the errors produced using our previously established methodology is the same for phases of As_2S_3 as it is for phases of As_2Te_3. Errors caused by numerical approximations in band calculations had a significant impact on the calculation of deformation potential due to the need for fine levels of convergence in these structures, remaining within a 4 to 5% range throughout. The acoustic sum rule correction appears to be relatively small for all phases, leading to apparent errors of around 2.8%, similar to the sulphur-doped phases of As_2Te_3 studied earlier in this chapter.

5.2.7 Chapter summary

This second and final results chapter focused on reiterating the method tested in the previous chapter on a larger number of materials, including doped and alloyed structures. These were deemed likely to have interesting thermoelectric properties, as well as to be highly anisotropic and computationally challenging, allowing us to test the versatility of our method.

The first two were variations on β-As_2Te_3, which involved substitutions of tellurium for sulphur atoms. This had a substantial impact on the distribution of electron states for the inner doped configuration, expanding its band gap and exposing a susceptibility for numerical error in our method, requiring correction via a regularisation term. It also demonstrated the impact of the DOS shape on a materials ability to retain thermoelectric efficiency at low temperatures.

The difference in location between these two substitutions, when considering the differences between tellurium and sulphur, resulted in very different behaviour in electron-phonon coupling. As a result, we observed a substantial increase in the electron-phonon relaxation time of the outer doped configuration. As a result, our modified materials both delineate nano-engineering mechanisms by which the figure of merit of β-As_2Te_3 may be improved.

The next materials analysed were variants upon an As_2S_3 structure with interesting inter-layer interactions. These were examples of larger band gap semiconductors, which limited the applicability of their electronic properties at lower temperatures. Their high anisotropy and inter-layer interactions also lead to markedly different results with respect to direction, which allowed the method used to identify optimal parameters.

However, a combination of a larger primitive cell and fewer symmetries led to a sub-

stantial increase in overall computational cost when compared to previous materials. This made rigorous phonon calculations impractical or unfeasible, and as a result only allowed for lattice thermal transport properties to be evaluated within the small grain limit.

Chapter 6

Conclusions

6.1 Current progression

6.1.1 Properties of arsenic, tellurium and sulphur based compounds

Our analysis has helped underline the capacity of the β-phase of As_2Te_3 for a promising room temperature thermoelectric figure of merit. While maximal values can only be found within specific directions within the plane which may be challenging to optimize for in experiment, the overall average over directions offers ZT values approaching those of bismuth telluride when appropriately doped.

While this does not directly account for the impact of grain boundaries on individual transport properties, it seems reasonable to expect the performance to remain competitive within a range of grain sizes when considering the scattering impact of such boundaries on not only electrons, but also phonons.

The impact of sulphur doping β-As_2Te_3 appears to have a range of effects. Both doping configurations tested appear to have generally decreased the anisotropic behaviour of the figure of merit within the plane and increased its average value it, but at the cost of slightly reducing the maximal term. They also both appear to have substantially improved performance along the direction normal to the plane, to the point of making it favourable if one can select for it during manufacture.

However, while the inner-doped configurations are thermodynamically favourable, they also substantially increase the size of the band gap, and by extension the optimal energy at which to obtain a maximal ZT. Additionally, it displayed substantially different behaviour above and below the band gap, strongly favouring the VBM and by extension usage in a p-type semiconductor. Its electron thermal behaviour also suggests greater thermal dependence of both its optimal ZT and matching energy when the band gap is widened.

Thus, whilst some amount of sulphur doping of β-As_2Te_3 may help improve performance, it is important to account for the greater need for optimization with regards to doping, grain alignment and preferred temperature ranges for optimal performance.

Our analysis of As_2S_3 suggests some capacity for thermoelectric function with the appropriate optimisation when evaluated within the small grain limit, but the efficiency when averaged over directions may not be quite as competitive when compared to bismuth telluride. We have obtained some high values both within and normal to the plane, however, leading to an average efficiency that may still be useful if used in bulk when considering the comparative cheapness of the structure, as sulphur is currently approximately 400 times cheaper than tellurium per kilogram.

It should be noted, however, that As_2S_3 is at its most efficient as a p-type doped semiconductor along the direction normal to the plane, and as an n-type doped semiconductor along directions within the plane. It should also be pointed out that, as with one of the doped configurations of β-As_2Te_3, its larger band gap renders it more temperature dependent, and as a result means that it would function best at temperatures significantly higher than room temperature.

The doped variants of As_2S_3 appear to show less promise, however, as their figure of merit within the plane becomes substantially stunted. They also appear to become more direction dependent within the plane, with a very promising value offered along one of these directions for the material in which the doping agent is aligned with arsenic atoms in neighbouring layers.

However, the non-bonded configuration tested presents an opposite behaviour, restricting efficiency in that direction, which on average means that our doping attempts do not appear to reflect a general positive relationship between the addition of tellurium to the As_2S_3 system and the improvement of the figure of merit.

6.1.2 Methodological limits and assumptions

While we have produced a substantial amount of data through our calculations, it should be noted that much of it relies on some underlying assumptions and approximations despite the ab-initio roots. For example, the use of a local density approximation functional, while computationally effective and powerful in the case of VdW bonded materials, lacks some sophistication and accuracy that could be offered by other functionals. One of the primary effects of this decision is the tendency to over-bind atoms, reducing lattice parameters, and often increasing valence band energy values to the point of shrinking the band gap.

This has a significant impact on our calculations, mostly due to the potential for causing shifts in the gradient of the DOS. In principle, one could attempt to replace

it with various improved approaches, such as a meta-GGA or a hybrid functional. While one of these was used to complement our analysis of β-As_2Te_3, these were mostly avoided due to limitations in DFT implementation and substantial increases in computational cost that could not be afforded.

An important theoretical assumption that is fundamentally merely approximate lies in the use of simple unilateral deformations to evaluate deformation potentials on exact, localised bands. While this is efficient, it does not properly account for electron-phonon scattering from optical phonon modes, nor for the distributed behaviour of neighbouring bands when subjected to thermal smearing.

Additionally, the mismatch between the rate of change of our calculated electrical conductivity and relaxation times with energy when entering the band gap requires the use of a regularisation term, which can only be approximated iteratively. As such, results produced near the band gap at high temperatures undergo increasing uncertainty as they approach the center of the ground state band gap.

The deformation potential approximation, while computationally efficient, is limited in its ability to account for flattened, overlapping or kissing bands, which may partially interact with and impact electron-phonon scattering around the conduction band minimum and valence band maximum.

6.1.3 Computational challenges and opportunities

This body of work has focused on the simulation and thermoelectric evaluation of multiple materials using a low-throughput approach with some focus on detail. While much of this process has already been applied on other materials, this study has encountered the computational costs and limitations of certain analytical methods. Additionally, it recommends the use of an adaptive, direction dependent approach that is not typically used in the literature, referred in this thesis by the shorthand "the DOS method".

Arsenic is a highly correlated element with a complex Fermi surface and thus requiring a high cut-off energy and dense k-point sampling. When included in highly anisotropic alloys including symmetry-breaking dopants, we find materials that are multiple orders of magnitude more computationally expensive to analyze than structures like bulk silicon or graphene.

By combining it with circumstances where k-point parallelisation is inconsistent, such as in perturbed cells with broken symmetries, or where computational cost goes up while numbers of k-points are reduced, such as with supercells produced for finite step third order phonon calculations, we have determined that certain calculations are highly impractical and in some cases unfeasible. This is true even when using a simple

and efficient exchange-correlation functionals like the local density approximation.

As such, performing a rigorous first principles analysis of all thermoelectric properties of a material can be computationally challenging to the point of being impractical for the sake of high-throughput research. That being said, forgoing lattice transport properties in order to focus on electronic components can still allow us some powerful insight on a material, even if it forces us to rely on first order approximations of the thermal conductivity.

If doing so, a traditional effective mass based approximation can become the dominant computational cost due to the underlying calculation of the elastic constants, which involves numerous broken symmetry geometry optimization calculations. Additionally, its use is limited in a highly anisotropic system.

As such, a DOS based method seems computationally optimal. The only DFT calculations it requires once one has a geometry optimized cell at one's disposal are one density of states calculation, one phonon dispersion calculation that can rely on as little as two sampling points to find the sound velocity and a set of single k-point calculations of deformed cells so as to evaluate the deformation potentials. All of these calculations combined are typically computationally cheaper than even a single set of elastic constant or phonon calculations.

Once processed through DOS broadening scripts, a software package for solving the Boltzmann transport equation to derive transport properties, and a script for subsequently solving individual ZT terms, these results can give us a detailed, energy, temperature and direction specific description of all key electronic terms of ZT.

6.1.4 Key factors in thermoelectric efficiency

From the sum of our work, we can identify some key features in our materials that improve our thermoelectric figure of merit for specific temperature ranges and are generally easy to identify through preliminary analysis.

Starting with the theory, the relaxation time has an inverse correlation to the electron mobility, meaning that one would expect favourable electron mobility from broader parabolic features in bands around the CBM or VBM. Similarly, one may generally expect higher values for the Seebeck coefficient between bands with significantly different shapes, and along segments of DOS plots with steep gradients near a band gap, as these suggest asymmetry in relative transport properties across short distances.

Selecting materials with large potential differences between atoms may also be effective at stiffening the bulk modulus and thus increasing the sound velocity. This will lead to a reduction in the impact of electron-phonon coupling on electrical conductivity, improving the figure of merit. The inclusion of some elements with lower atomic

masses into a system that is otherwise quite heavy will also provide phonon-phonon scattering, as well as split more phonon modes into high energy optical regions, where they may be less likely to scatter electrons.

It is also worth nothing the importance of layering and other types of VdW bonding within bulk structures, as these can allow for phonon-phonon scattering and the appearance of flattened electron bands near the band gap, reflecting homogeneous energy regions being produced in either one or two dimensions within the interlayer spacing. Furthermore, weak VdW interactions are unlikely to lead to substantial deformation potentials, meaning that they can be used to reduce electron-phonon coupling in the direction normal to the plane. Alternatively, our deformation potentials also appear to be weak along directions that align well with covalent bonding, as these allow for a more direct route for electron transport that varies little as a result of uni-axial deformation.

When evaluating semiconductors, it is generally preferable for the band gap to be between a range of around one to four times the smearing energy at the targeted temperature. If it is too narrow, states will smear into it at lower temperatures, to the point of reducing relative gradients and by extension Seebeck coefficient values. If it is too large, ZT values will become increasingly temperature dependent, requiring higher and higher temperatures to achieve competitive efficiencies. Fine features in the DOS, especially in the form of converging bands or otherwise localised peaks in the DOS near a band gap can lead to a Seebeck coefficient that favours thermoelectric properties at a lower range of temperatures.

6.2 Final summary

We began this project with the goal of analysing a set of materials that have not been the subject of much research despite their obvious parallels to famously efficient thermoelectrics. In doing so, we hoped to identify promising thermoelectric properties and streamline our process, although we had to do so with a detail-oriented, low-throughput approach due to computational cost.

Along the way, we successfully managed to develop an alternative to traditional methods for evaluating thermoelectric properties in temperature, energy and direction dependent terms. This has also helped us decrease the substantial computational costs of some of our calculations, to the point that we could implement automation to some parts of the process. We have however encountered some properties that can prove too computationally expensive or impractical to calculate rigorously, forcing us to make some additional assumptions and approximations.

Despite this, we have been able to evaluate a number of key features in our materials that are specific to their highly anisotropic and VdW force dependent structures.

We now have a detailed analysis of their transport properties, including parameter specific extrema which may allow for further optimization. In doing so, we have also been able to underline useful structural and electronic trends which may be of use when performing cheaper, preliminary evaluations of materials.

Along the way, we have found some interesting values for the ZT of our unaltered compounds. As_2Te_3 offered some highly anisotropic results with an average room temperature ZT value of 0.63, but a theoretical maximum along the optimal direction going as high as 1.19. As_2S_3 presented an average room temperature ZT value of around 0.39, but with the ability to reach 0.57 when operating at an appropriate doping level and along an optimal direction. While these results are not as competitive when compared to Bi_2Te_3, it is worth noting that As_2S_3 is a much cheaper material and may still therefore offer some utility.

6.3 Future work

While a lot of research has been done in the field of implementing nano-engineered structures in materials for the sake of scattering phonons and improving overall thermoelectric efficiency, this may not be computationally practical in the case of arsenic based compounds. Future computational work on these compounds may be beneficial, but only if it remains viable. As a result, evaluations of deformed, perturbed, doped or alloyed versions of bulk arsenic-based semiconductors may currently be the limit of our computational ability. More complex structures would likely be easier to study experimentally for the moment.

That being said, our methodology itself may prove useful for a high-throughput analysis of thermoelectric materials. If, like much of the literature, we decide to focus on the electrical components of ZT for the sake of minimizing computational cost, it may be possible to substantially reduce the number of DFT calculations required, which tend to make up the bulk of our computational cost. In fact, in order to evaluate the Seebeck coefficient, the electrical conductivity and the electron thermal conductivity, we only need to perform three sets of DFT calculations.

The first and most important is an electron DOS calculation. While it is the most important calculation and requires a relatively high sampling density, it is also quite easy to parallelise. The second is a phonon dispersion plot, which need only sample the linear region near the Γ-point of the cell in order to identify the sound velocity. As such, it can be made extremely cheap when compared to a conventional phonon DOS calculation. And finally, we need a set of single k-point DFT calculations of deformed versions of the cell. These are extremely cheap and can be automated via scripting, although it may also be possible to evaluate the deformation potential through one

single q-point phonon calculation.

Considering that all of these calculations combined can prove to be orders of magnitude cheaper and faster than rigorous calculations of phononic properties or the bulk modulus, they lend themselves well to a higher throughput analysis of a larger number of compounds. Alternatively, one may use them in an attempt to evaluate larger, more complex and more expensive cells than are usually considered for DFT analysis. It should be noted, however, that cells containing very large numbers of atoms do not necessarily lend themselves well to DFPT calculations, as the number of perturbations calculated per q-point is equal to three times the number of atoms.

If one wants to opt for an even cheaper, higher throughput approach so as to perform a preliminary analysis of a large number of thermoelectric as part of a screening for example, it may be possible to rely on as a little as a single spectral calculation. By evaluating the geometry of the cell, the approximate distribution of electron states near the Fermi energy as shown in a band structure, the width of the band gap and the rate of change in the gradient of the bands near the VBM or CBM, it may be possible to identify many of the key features that have been underlined in this body of work with as a little as a geometry optimized band structure calculation.

By evaluating the properties just listed and using various weighting factors to reflect their respective impact on the material, these may be used as the parameters by which to train a machine learning model to identify thermoelectric properties. While interest has already been expressed in exploring thermoelectric materials using a machine learning approach [127], to the point that such a project has already been developed to varying levels [88], it relied on the use of preexisting databases to predict whether more complex transport properties, such as electrical conductivity, were likely to offer promising results. Our suggestion relies on the use of simpler, directly relevant properties, which can be easily and cheaply generated, most likely in a partially automated manner.

Appendix A

Examples of CASTEP input files

A.1 Parameter file

```
TASK                    :       geometry optimization
opt_strategy            :       Speed
cut_off_energy          :       1500.0 eV
xc_functional           :       LDA
grid_scale              :       2.0
max_scf_cycles          :       120
mix_charge_amp          :       0.9
nextra_bands            :       60
elec_method             :       dm
CONTINUATION            :       default
```

Listing A.1: An example of a basic parameter file set up to iteratively optimise the geometry of the primitive cell of β-As_2Te_3.

A.2 Cell file

```
%BLOCK LATTICE_CART
ang
 2.3313889    -0.0000000     9.3515067
-1.1656944     2.0190419     9.3515067
-1.1656944    -2.0190419     9.3515067
%ENDBLOCK LATTICE_CART

%BLOCK POSITIONS_FRAC
As     0.397703   0.397703   0.397703
As     0.602297   0.602297   0.602297
Te     0.000000   0.000000   0.000000
Te     0.212218   0.212218   0.212218
Te     0.787782   0.787782   0.787782
```

```
%ENDBLOCK POSITIONS_FRAC

%BLOCK SPECIES_POT
NCP
%ENDBLOCK SPECIES_POT

KPOINTS_MP_GRID 5 5 5

PHONON_KPOINT_MP_GRID 3 3 3

spectral_kpoints_mp_grid 25 25 25

fix_all_cell    false

symmetry_generate
```

Listing A.2: An example of a the .cell file set up alongside the parameter file shown, to iteratively optimise the geometry of the primitive cell of β-As_2Te_3. Additional parameters have been included as examples, such as a phonon k-point grid (or q-point grid) and a spectral k-point grid for a phonon and electron DOS respectively.

Appendix B

Graphene reference calculations

We performed a set of cheap DOS calculation in order to evaluate the impact of different broadening approaches on the fine features and linear regions of a material with an extremely small band gap, or in this case, no band gap at all. Different spectral k-point samplings were used so as to determine the impact of our broadening in various cases.

Graphene was chosen as a test material for its well known features, such as having linear regions in its DOS as a result of its Dirac cones, which would converge towards 0 at the Fermi energy. These would be difficult to maintain for broadening schemes which rely on extrapolating techniques or Gaussians, and would parallel the fine features in some of our arsenic based compounds. Additionally, graphene is relatively cheap to evaluate using DFT and only needs to be sampled in two dimensions, resulting in a shallower scaling of its k-point sampling than for three-dimensional materials.

Our results showed that adaptive broadening methods were quite effective when applied with an appropriate width ratio. If set too low, it would result in Gaussian artefacts, and setting it too high would smooth out substantial amounts of the region around the Fermi level, as shown in an exaggerated manner in figure B.1. A linear extrapolation method was relatively consistent for all sampling levels, compromising between realistic exploration of the Dirac cone regions and noise, see figure B.2. However, at higher sampling densities, a carefully widened adaptive method became more consistent at ensuring minimal noise near the Fermi energy while coming very near to a 0 DOS point, see figure B.3. Of course, if one can afford to sufficiently increase the level of sampling, the final results of all methods converge to extremely similar results B.4.

As the sampling density in figure B.3 is approximately the same as the grid density sampling used for the β-phase of As_2Te_3 when accounting for lattice parameters, an adaptive broadening method was chosen as the default. However, to verify these observations, a further test was performed on the β-phase of As_2Te_3 itself using a 25 by 25 by 25 grid, see figure B.5. This confirmed the result, as a carefully selected adaptive broadening width (of about 0.4) was able to substantially reduce the noise from

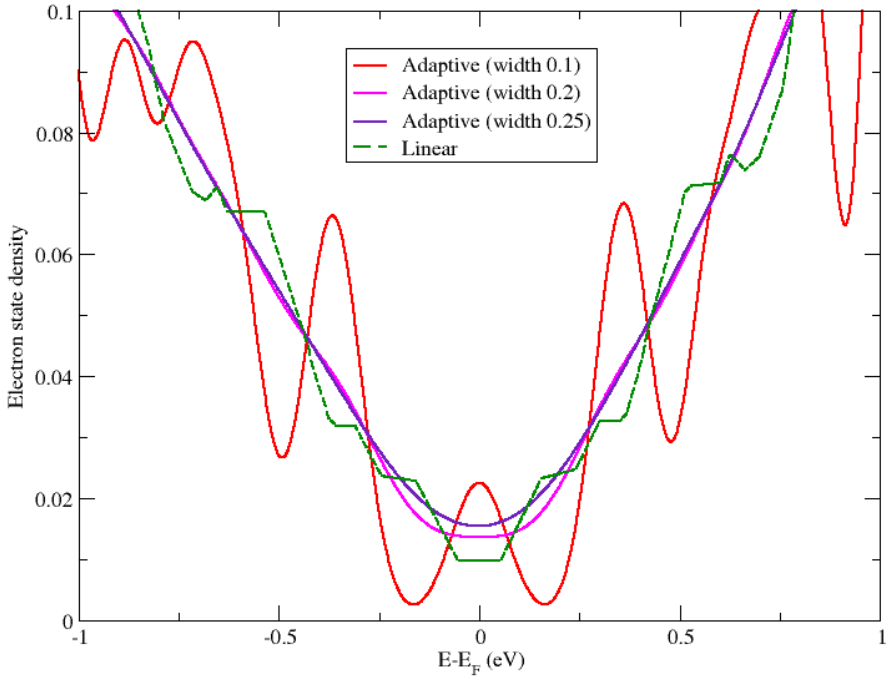

Figure B.1: A 45 by 45 grid DOS sampling of graphene. Insufficiently wide broadening parameters result in Gaussian noise for the adaptive method. The linear method adds substantial noise too, but explores more of the well at the Fermi energy

Gaussian artifacts while maintaining reasonably low values around the Fermi energy.

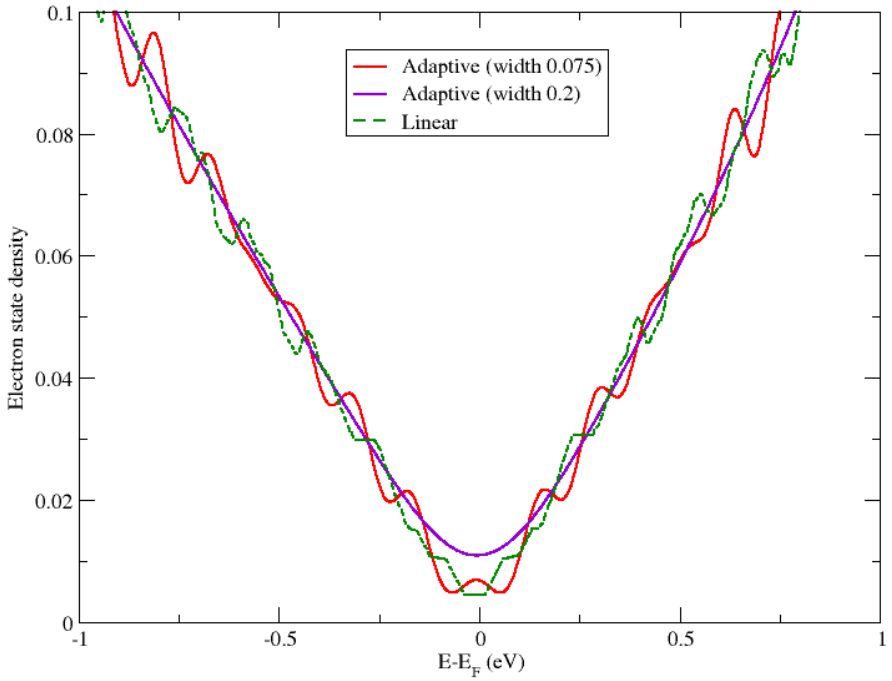

Figure B.2: A 99 by 99 grid DOS sampling of graphene. Narrow adaptive broadening and linear extrapolation methods are beginning to offer similar results.

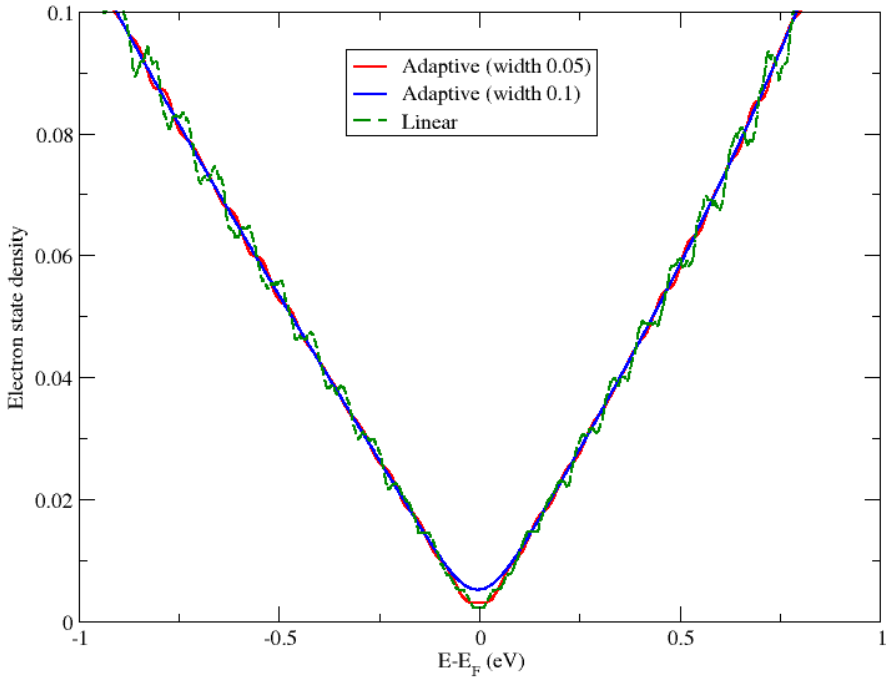

Figure B.3: A 201 by 201 grid DOS sampling of graphene. The linear and appropriately defined adaptive methods are now equally capable of exploring the DOS well, but the linear method is now producing the most noise. The spectral grid density is now similar to a 50 by 50 by 50 grid in each direction of the β-As_2Te_3 cell.

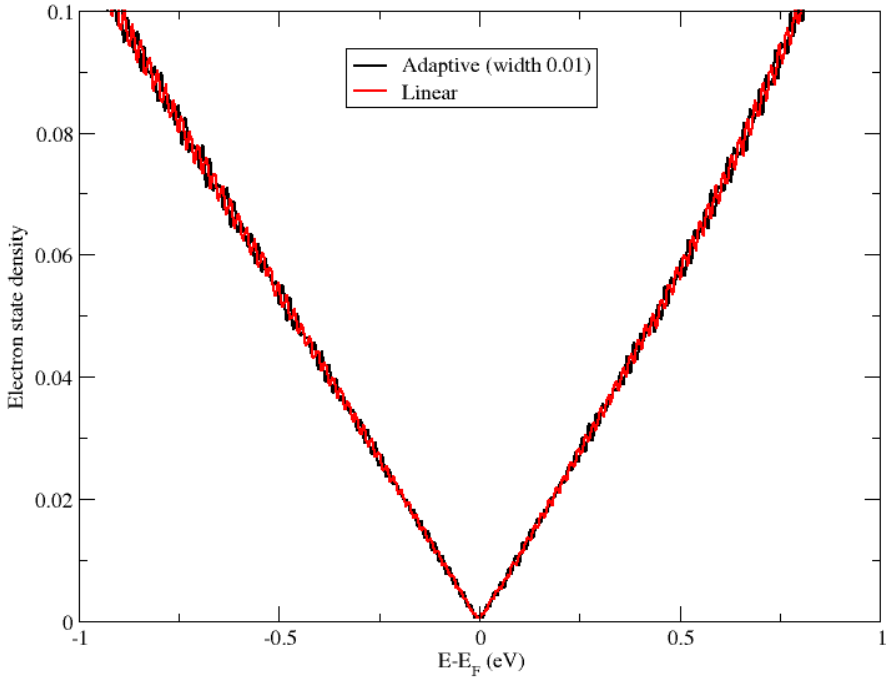

Figure B.4: A 801 by 801 grid DOS sampling of graphene. This system is overly converged, yet the linear method still produces the most noise.

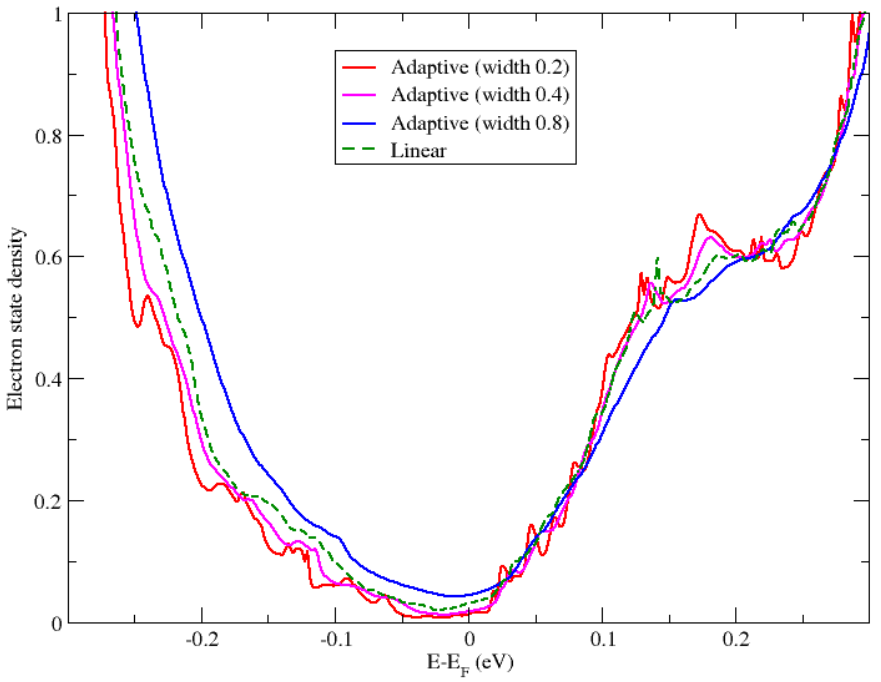

Figure B.5: A 25 by 25 by 25 grid DOS sampling β-phase As_2Te_3. At this grid density, the more irregular DOS shape makes it unclear how much of the variations in the narrow width adaptive method broadening is noise, and how much is due to fine features which are being lost through the other methods. A 50 by 50 by 50 grid was therefore found preferable when possible.

Appendix C

κ_e behaviour in β-As_2Te_3

The Lorenz number does not appear constant near the Fermi energy for β-As_2Te_3 as the electron thermal conductivity in that region increases substantially and the electrical conductivity does not. The reason comes from the fact that Boltztrap calculates the electron thermal conductivity in terms of electron entropy S_{el} such that:

$$\kappa_{el} = T\left(\frac{\delta S_{el}}{\delta f}\right)_N \alpha_{el} \tag{C.1}$$

where α_{el} is the thermal diffusivity of electrons, N is the non-smeared density of electron states and f is the Fermi distribution such that:

$$f = \frac{1}{e^{\frac{E-E_f}{k_B T}} + 1} \tag{C.2}$$

where E_f is the Fermi energy and T is temperature. Boltztrap then defines electron entropy as:

$$S_{el} = -k_B \int [f \ln(f) + (1-f)\ln(1-f)] N(E) dE \tag{C.3}$$

where k_B is the Boltzmann constant and E is energy. As such, we find that when E tends towards E_f, the derivative of $[f \ln(f) + (1-f)\ln(1-f)]$ tends towards $-\infty$. In practice, this produces a peak in κ_e which is not found in σ, and occurs only around the Fermi energy in regions defined by band gaps that are filled with thermally smeared states, see figure C.1. As a result, we find a substantial localised peak when mapping the Lorenz number with respect to energy.

While this effect in one of our results is likely to have a substantial negative impact on the figure of merit, it should be pointed out that it is localised in such a way as to coincide with a trough in the absolute value of the Seebeck coefficient, see figure C.2. As the Seebeck coefficient is the only squared term in ZT, and therefore the dominant term, its localised trough has a very substantial impact on the figure of

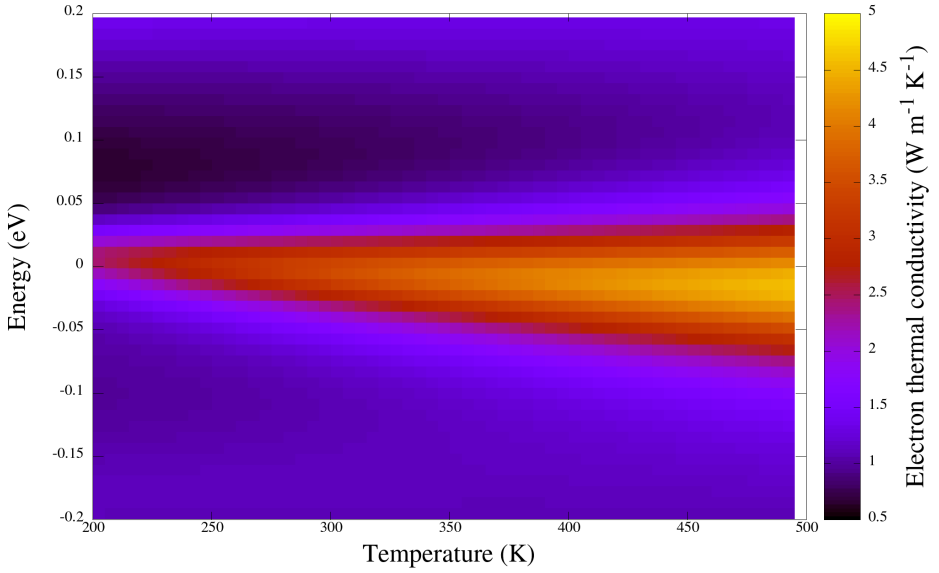

Figure C.1: Electron thermal conductivity with respect to temperature and energy. We notice a substantial peak near the Fermi energy.

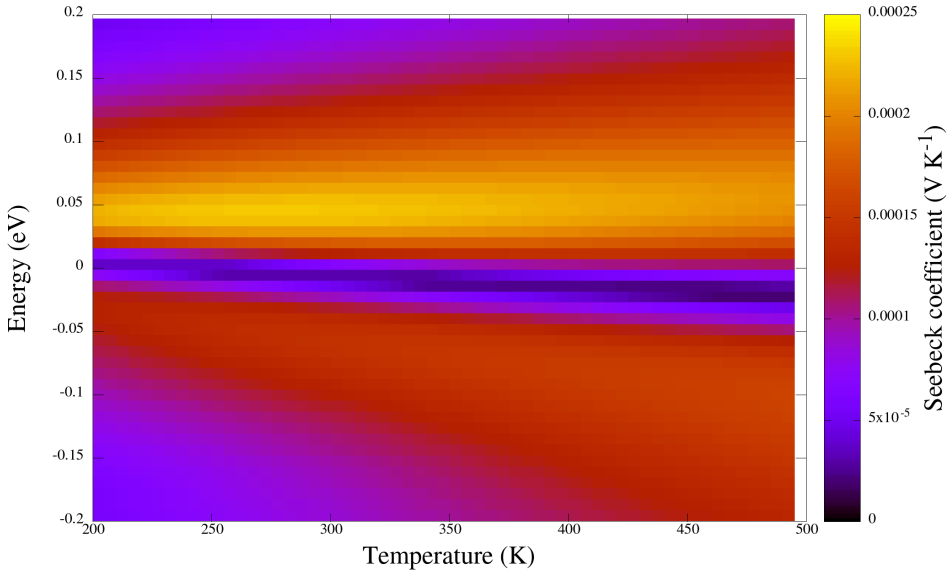

Figure C.2: Colour map of the absolute value of the Seebeck coefficient of β-As_2Te_3 with respect to temperature and energy. We notice a substantial peak near the Fermi energy.

merit regardless of the divergent behaviour of the calculated electrical conductivity and electron thermal conductivity.

Appendix D

Examples of code

D.1 Program for calculating ZT

```
program Calc_ZT
  implicit none
  integer, parameter :: dp = selected_real_kind(15,300)
  real(kind=dp), allocatable,
      dimension(:) :: Seebeck, temperature, doping, phonon, DOSfinal
  real(kind=dp), dimension(4) :: total
  real(kind=dp) :: constants
     , pi, electron, Planck, Boltzmann, mass, variab, reg_term
  integer ::
     line, i, istat, shift, energytotal, temp_samples, total_samples
  real(kind=dp
     ), allocatable, dimension(:,:) :: Seebeck_matrix, Sigma_matrix
     , kappae_matrix, tau_matrix, phonon_matrix, ZT_matrix
  real(kind=dp), dimension(9,200) :: phonon_list
  real(kind=dp), dimension(9) :: deformation_matrix, sound_matrix



  !Checking the
      number of temperature values for which the values are samples
  open(unit=10, file='temp_samples.dat', iostat=istat)
  if (istat/=0) stop 'could not open temperature samples file'

  read(unit=10, fmt=*, iostat=istat) variab
  temp_samples = int(variab)

  close(unit=10, iostat=istat)
  if (istat/=0) stop 'could not close temperature samples file'
```

```
!Checking the number of doping values
    (in eV above and below the Fermi level) the values are samples
open(unit=11, file='eV_list.dat', iostat=istat)
if (istat/=0) stop 'could not open energy list file'

energytotal = 0

do
   read(unit=11, fmt=*, iostat=istat)
   if (istat/=0) exit
   energytotal = energytotal + 1
end do

close(unit=11, iostat=istat)
if (istat/=0) stop 'could not close energy list file'



!Calculating
    and announcing the number of samples in our 2D sampling space
total_samples = energytotal*temp_samples

print *, energytotal, "doping values times",  temp_samples
   , "temperatures gives a total of", total_samples, "samples."



!Allocating doping energy, phonon, relaxation
    time, conductivity, Seebeck coefficient and ZT arrays
allocate (doping(total_samples), stat=istat)
if (istat/=0) stop 'could not allocate doping array'

allocate (phonon(total_samples), stat=istat)
if (istat/=0) stop 'could not allocate phonon array'

allocate (result(total_samples), stat=istat)
if (istat/=0) stop 'could not allocate result array'

allocate (Seebeck(total_samples), stat=istat)
if (istat/=0) stop 'could not allocate Seebeck array'

allocate (temperature(total_samples), stat=istat)
if (istat/=0) stop 'could not allocate temperature array'



!Matrix array allocation
```

```
allocate (Seebeck_matrix(9, total_samples), stat=istat)
if (istat/=0) stop 'could not allocate Seebeck matrix'

allocate (Sigma_matrix(9, total_samples), stat=istat)
if (istat/=0) stop 'could not allocate Sigma matrix'

allocate (Kappae_matrix(9, total_samples), stat=istat)
if (istat/=0) stop 'could not allocate Kappae matrix'

!Opening the matrix output files taken from BoltzTraP
open(unit=12, file='Seebeck_matrix.dat', iostat=istat)
if(istat/=0) stop 'could not open input seebeck matrix file'

open(unit=13, file='Sigma_matrix.dat', iostat=istat)
if(istat/=0) stop 'could not open input sigma matrix file'

open(unit=14, file='Kappae_matrix.dat', iostat=istat)
if(istat/=0) stop 'could not open input kappae matrix file'

!A simple loop over all Boltztrap data (on Seebeck
   , electrical conductivity and electron thermal conductivity)
!so as to collect all that data into our 3
   arrays (9 in length in one dimension for all matrix components)
!These
    columns are set up in the order: xx xy xz yx yy yz zx zy zz.
do line = 1, (total_samples)
   total(1) = line
   read(unit=(12), fmt=*, iostat=istat) Seebeck_matrix(1,
       line), Seebeck_matrix(2, line), Seebeck_matrix(3, line), &
        Seebeck_matrix(4, line), Seebeck_matrix(5, line
           ), Seebeck_matrix(6, line), Seebeck_matrix(7, line), &
        Seebeck_matrix(8, line), Seebeck_matrix(9, line)
   read(unit=(13), fmt=*, iostat=istat) Sigma_matrix
      (1, line), Sigma_matrix(2, line), Sigma_matrix(3, line), &
        Sigma_matrix(4, line), Sigma_matrix(5,
            line), Sigma_matrix(6, line), Sigma_matrix(7, line), &
        Sigma_matrix(8, line), Sigma_matrix(9, line)
   read(unit=(14), fmt=*, iostat=istat) Kappae_matrix
      (1, line), Kappae_matrix(2, line), Kappae_matrix(3, line), &
        Kappae_matrix(4, line), Kappae_matrix(5, line
           ), Kappae_matrix(6, line), Kappae_matrix(7, line), &
        Kappae_matrix(8, line), Kappae_matrix(9, line)
end do

!Closing the BoltzTraP files we just read
close(unit=12, iostat=istat)
if (istat/=0) stop 'could not close Seebeck matrix file'
```

```
close(unit=13, iostat=istat)
if (istat/=0) stop 'could not close Sigma matrix file'

close(unit=14, iostat=istat)
if (istat/=0) stop 'could not close Kappae matrix file'



!Temperatures are listed at 5 kelvin increments
    from 200K to max temp for every doping value combination
!This is done by assigning a temperature
    value for every temperature-doping value combination
!As we cycle through these values, temperatures
    are listed in ascending order until they reach the max
!Everytime the list of temperatures reaches
    max value, it is reset to 200K until the cycle completes
i = 0
do line = 1, (total_samples)
   temperature(line) = 200 + (5*i)
   if (i == (temp_samples-1)) then
      i = -1
   end if
   i = i + 1
end do

print *,
    "printed list of temperatures for each energy value in range"



!Defining the terms necessary for the relaxation time calculation
pi = 3.14159265359_dp
electron = 1.60217662_dp*10.0_dp**(-19)
planck = 1.054571817_dp*10.0_dp**(-34)
Boltzmann = 1.38064852_dp*10.0**(-23)
constants = (electron*planck)/(pi*Boltzmann)



!Reading the mass term for our cell
open(unit=15, file='mass.dat', iostat=istat)
if(istat/=0) stop 'could not open mass file'

read(unit=10, fmt=*, iostat=istat) mass

close(unit=15, iostat=istat)
if(istat/=0) stop 'could not close mass file'
```

```
!Reading deformation potential matrix
open(unit=16, file='deformation.dat', iostat=istat)
if(istat/=0) stop 'could not open deformation file'

read(unit=(16), fmt=*, iostat=istat) deformation_matrix
    (1), deformation_matrix(2), deformation_matrix(3), &
     deformation_matrix(4), deformation_matrix
        (5), deformation_matrix(6), deformation_matrix(7), &
     deformation_matrix(8), deformation_matrix(9)
if (istat/=0) stop 'Could not read deformation file'

close(unit=16, iostat=istat)
if(istat/=0) stop 'could not close deformation file'



!Reading sound velocity matrix
open(unit=17, file='sound.dat', iostat=istat)
if(istat/=0) stop 'could not open sound file'

read(unit=17, fmt=*, iostat=istat) sound_matrix
    (1), sound_matrix(2), sound_matrix(3), sound_matrix(4), &
     sound_matrix(5), sound_matrix
        (6), sound_matrix(7), sound_matrix(8), sound_matrix(9)
if (istat/=0) stop 'Could not read sound velocity file'

close(unit=17, iostat=istat)
if(istat/=0) stop 'could not close sound file'



!converting
    hartree to joules in the deformation potential calculation
!Feel free to comment this out if done previously
do i = 1, 9
   deformation_matrix
      (i) =(deformation_matrix(i) * (27.2_dp) * electron)
end do



!Defining DOSfinal based on the thermal DOS produced via BoltzTraP
!This is a 1D array as DOS is not directionally dependent
allocate (DOSfinal(total_samples), stat=istat)
if(istat/=0) stop 'could not allocate DOSfinal array'
```

```
open(unit=18, file='DOS_thermal.dat', iostat=istat)
if(istat/=0) stop 'could not open DOS_thermal file'

do line = 0, (energytotal-1)
   do i = 1, temp_samples
      read(unit
         =17, fmt=*, iostat=istat) DOSfinal((line*temp_samples)+i)
      if(istat
         /=0) stop 'could not read thermally smeared DOS data'
   end do
end do

close(unit=18, iostat=istat)
if(istat/=0) stop 'could not close DOS_thermal file'



!looping through energies
   and temperatures, calculating tau for each when DOS is non-zero
!In cases where electron DOS values
    are zero, values for sigma and tau do not make physical sense
!As such, we stick to a convention
   that sigma is corrected to 0 when there are no electron states.
!We regularize the denominator
    by adding a small value if keep a more realistic progression
!The regularisation term
    is hardcoded here by default for the sake of this example code
allocate (tau_matrix(9, total_samples), stat=istat)
if(istat/=0) stop 'could not allocate tau matrix array'

reg_term= 1E+012

do line = 0, (energytotal-1)
   do shift = 1, temp_samples
      do i = 1, 9
         if (DOSfinal((line*temp_samples)+shift) .gt. 0.0001) then
            tau_matrix
                (i, (line*temp_samples)+shift) = 1/ ( reg_term + (
                 1/ ( (constants * (sound_matrix(i)**2) * mass) / &
                  (temperature((line*temp_samples
                     )+shift) * (deformation_matrix(i)**2.0_dp) * &
                   DOSfinal((line*temp_samples)+shift)) ) ) )
         else
            tau_matrix(i, (line*temp_samples)+shift) = 0
         end if
      end do
   end do
end do
```

```
print *, "Finished calculating relaxation time"



!Element wise multiplication of sigma and tau matrices
!This is effectively
    our relaxation time correction now that we have tau calculated
do line = 1, (total_samples)
   do i = 1, 9
      sigma_matrix
          (i, line) = sigma_matrix(i, line)*tau_matrix(i, line)
      kappae_matrix
          (i, line) = kappae_matrix(i, line)*tau_matrix(i, line)
   end do
end do
print *, "Finished correcting kappa and sigma"



!Reading the
    phonon conductivities in all directions (so a 2D 9 by X array)
!phonon_list may have
    been hardcoded its allocation at the beginning of this script
open(unit=19, file='kappa_phonon.dat', iostat=istat)
if (istat/=0) stop 'could not open kappa_phonon file'

do line = 1, temp_samples
   read(unit=19, fmt=*, iostat=istat) phonon_list
      (1, line), phonon_list(2, line), phonon_list(3, line), &
       phonon_list(4, line), phonon_list(5,
            line), phonon_list(6, line), phonon_list(7, line), &
       phonon_list(8, line), phonon_list(9, line)
   if (istat/=0) stop 'could not read kappa_phonon file'
end do

close(unit=19, iostat=istat)
if (istat/=0) stop 'could not close kappa_phonon file'



!Duplicating
   the number of phonon data points by the number of energy values
!This will allow
    us to easily match the arrays for electron and phonon terms
allocate (phonon_matrix(9, total_samples), stat=istat)
if (istat/=0) stop 'could not allocate phonon matrix array'
```

```
do line = 1, energytotal
   do shift = 1, temp_samples
      do i = 1, 9
         phonon_matrix(
            i, shift+(line-1)*temp_samples)= phonon_list(i, shift)
      end do
   end do
end do

print *, "Just finished reading and arranging phonon values"



!Reading "doping" energy values
     from BoltzTraP calculation to define energy sampling points
!These are then converted over from Rydberg to eV
open(unit=20, file='doping.dat', iostat=istat)
if (istat/=0) stop 'could not open doping file'

do line = 1, (total_samples)
   read(unit=20, fmt=*, iostat=istat) doping(line)
   doping(line) = (13.605684959 * doping(line))
end do

close(unit=20, iostat=istat)
if (istat/=0) stop 'could not close doping file'

print *, "Just finished
     reading and redefining BoltzTraP energy sampling values"



!Time to calculate our final result: ZT
!We do this with a temperature loop, within
     which we map each sigma, kappae, phonon result and seebeck
!The temperature
     loop resets every time we have covered every temperature
!This allows us to keep calculating
     for each temperature until we have covered every energy value
!We maintain matching
     positions in the 3 by 3 directional matrix (thus 9 terms)
allocate (ZT_matrix(9, total_samples), stat=istat)
if (istat/=0) stop 'could not allocate ZT matrix array'

shift = 0
do line = 1, (total_samples)
   temperature(line) = 200 + 5*shift
   do i = 1, 9
```

```
      ZT_matrix(i, line) = sigma_matrix(i, line)
           * temperature(line) * (Seebeck_matrix(i, line) ** 2) / &
            (kappae_matrix(i, line) + (phonon_matrix(i, line)))
   end do
   if (shift == (temp_samples-1)) then
      shift = -1
   end if
   shift = shift + 1
end do

print
    *, "ZT terms calculated, printing to files about to commence."



!To print out all our results, we first need to open up our files
!The results
    we want are: DOS values, tau, kappaE, sigma, Seebeck and ZT
!We want to be
   printing all of these (in directional columns where appropriate
!We also want each of these lines to
    be preceded with temperature and energy for plotting purposes.
open(unit=26, file='ZT.dat', iostat=istat)
if (istat/=0) stop 'could not open ZT file'

open(unit=21, file
   ='Seebeck.dat',action='write', status='replace', iostat=istat)
if (istat/=0) stop 'could not reopen Seebeck file'

open(unit=22, file='sigma_matrix
   .dat', action='write', status='replace', iostat=istat)
if (istat/=0) stop 'could not reopen sigma corrected file'

open(unit=23, file='kappa_matrix
   .dat', action='write', status='replace', iostat=istat)
if (istat/=0) stop 'could not reopen kappa corrected file'

open(unit=24, file='tau_matrix.dat', iostat=istat)
if (istat/=0) stop 'could not open tau file'

open(unit=25, file='DOS_map.dat', iostat=istat)
if (istat/=0) stop 'could not open DOS file'



!We use
    the same temperature loop for printing as when calculating ZT
shift = 0
```

```
do line = 1, (total_samples)
   temperature(line) = 200 + 5*shift
   write(unit=26, fmt=*, iostat=istat) temperature(line
      ), doping(line), ZT_matrix(1, line), ZT_matrix(2, line), &
        ZT_matrix(3, line), ZT_matrix(4, line), ZT_matrix
           (5, line), ZT_matrix(6, line), ZT_matrix(7, line), &
        ZT_matrix(8, line), ZT_matrix(9, line)

   write(unit=21, fmt=*, iostat=istat) temperature(line), doping
      (line), Seebeck_matrix(1, line), Seebeck_matrix(2, line), &
        Seebeck_matrix(3, line), Seebeck_matrix(4, line
           ), Seebeck_matrix(5, line), Seebeck_matrix(6, line), &
        Seebeck_matrix(7,
           line), Seebeck_matrix(8, line), Seebeck_matrix(9, line)

   write(unit=22, fmt=*, iostat=istat) temperature(line), doping
      (line), sigma_matrix(1, line), sigma_matrix(2, line), &
        sigma_matrix
           (3, line), sigma_matrix(4, line), sigma_matrix(5,
            line), sigma_matrix(6, line), sigma_matrix(7, line), &
        sigma_matrix(8, line), sigma_matrix(9, line)

   write(unit=23, fmt=*, iostat=istat) temperature(line), doping
      (line), kappae_matrix(1, line), kappae_matrix(2, line), &
        kappae_matrix(3,
            line), kappae_matrix(4, line), kappae_matrix(5, line
           ), kappae_matrix(6, line), kappae_matrix(7, line), &
        kappae_matrix(8, line), kappae_matrix(9, line)

   write(unit=24, fmt=*, iostat=istat) temperature(line
      ), doping(line), tau_matrix(1, line), tau_matrix(2, line), &
        tau_matrix(3, line), tau_matrix(4, line), tau_matrix
           (5, line), tau_matrix(6, line), tau_matrix(7, line), &
        tau_matrix(8, line), tau_matrix(9, line)

   write(unit=25, fmt=*, iostat
      =istat) temperature(line), doping(line), DOSfinal(line)

   if (shift == temp_samples-1) then
      shift = -1
      write(unit=26, fmt=*, iostat=istat)
      write(unit=21, fmt=*, iostat=istat)
      write(unit=22, fmt=*, iostat=istat)
      write(unit=23, fmt=*, iostat=istat)
      write(unit=24, fmt=*, iostat=istat)
      write(unit=25, fmt=*, iostat=istat)
   end if
```

```
    shift = shift + 1
  end do

  print *, 'Just finished writing to final data files'



  !And now we close our files
  close(unit=25, iostat=istat)
  if (istat/=0) stop 'could not close DOS map file'

  close(unit=24, iostat=istat)
  if (istat/=0) stop 'could not close tau file'

  close(unit=21, iostat=istat)
  if (istat/=0) stop 'could not close Seebeck file'

  close(unit=22, iostat=istat)
  if (istat/=0) stop 'could not close sigma_corrected file'

  close(unit=23, iostat=istat)
  if (istat/=0) stop 'could not close kappa_corrected file'

  close(unit=26, iostat=istat)
  if (istat/=0) stop 'could not close ZT file'


end program Calc_ZT
```

Listing D.1: An example of the core program, written in Fortran 90 for the sake of efficiency, used to parse through the data output of the different elements in the workflow (see figure3.1). It combines all of the terms for ZT and outputs its matrix components with respect to energy and temperature.

D.2 Matching and reorganisation of DOS and BoltzTraP data

```
program Match
  implicit none
  integer, parameter :: dp = selected_real_kind(15,300)
  real(kind=dp),
      allocatable, dimension(:) :: DOSeV, DOS, DOSfinal, energyvalue
  real(kind=dp) :: difference, last, variab
  real(kind=dp), allocatable, dimension(:,:) :: matrix_initial
```

```
integer :: line, i, istat, shift,
   energytotal, DOSvalues, DOS_E_size, temp_samples, total_samples
integer, allocatable, dimension(:) :: match



!Checking the
    number of temperature values for which the values are samples
open(unit=30, file='temp_samples.dat', iostat=istat)
if (istat/=0) stop 'could not open temperature samples file'

read(unit=30, fmt=*, iostat=istat) variab
temp_samples = int(variab)

close(unit=30, iostat=istat)
if (istat/=0) stop 'could not close temperature samples file'



!Checking the number of doping values
    (in eV above and below the Fermi level) the values are samples
open(unit=31, file='eV_list.dat', iostat=istat)
if (istat/=0) stop 'could not open energy list file'

energytotal = 0

do
   read(unit=31, fmt=*, iostat=istat)
   if (istat/=0) exit
   energytotal = energytotal + 1
end do

total_samples = energytotal*temp_samples

close(unit=31, iostat=istat)
if (istat/=0) stop 'could not close energy list file'



!Reading
    the number of DOS values in our array by cycling through them
DOSvalues = 0
open(unit=32, file="DOS.dat", iostat=istat)
if (istat/=0) stop 'Could not open DOS file'
do
   read(unit=32, fmt=*, iostat=istat)
   if (istat/=0) exit
   DOSvalues = DOSvalues + 1
```

```
end do
close(unit=32, iostat=istat)
if (istat/=0) stop 'Could not close DOS file'

print
    *, "Read the number of DOS values in the array as", DOSvalues

open(unit=33, file="DOS_eV.dat", iostat=istat)
if (istat/=0) stop 'Could not open DOS energy file'

DOS_E_size = 0
do
   read(unit=33, fmt=*, iostat=istat)
   if (istat/=0) exit
   DOS_E_size = DOS_E_size + 1
end do
print *, "We have", DOS_E_size, "DOS values for each temperature"

close(unit=33, iostat=istat)
if (istat/=0) stop 'Could not close DOS energy file'



!Allocating the DOS and DOS energy arrays
    based on the number of DOS and DOS energy values respectively
!Then storing
    the DOS values and their respective energies in their arrays
allocate (DOS(DOSvalues), stat=istat)
if (istat/=0) stop 'Could not allocate DOS array'
allocate (DOSeV(DOS_E_size), stat=istat)
if (istat/=0) stop 'Could not allocate DOS energy array'
open(unit=34, file="DOS.dat", iostat=istat)
if (istat/=0) stop 'Could not open DOS file'
open(unit=35, file="DOS_eV.dat", iostat=istat)
if (istat/=0) stop 'Could not open DOS energy file'

do line = 1, (DOS_E_size)
   read(unit=24, fmt=*, iostat=istat) DOSeV(line)
end do

close(unit=35, iostat=istat)
if (istat/=0) stop 'Could not close DOS energy file'

do line = 1, DOSvalues
   read(unit=34, fmt=*, iostat=istat) DOS(line)
end do

close(unit=34, iostat=istat)
```

```
if (istat/=0) stop 'Could not close DOS file'
close(unit=35, iostat=istat)
if (istat/=0) stop 'Could not close eV list file'

print *, "Stored the DOS values and respective energies in arrays"



!finding the nearest DOS energy value to each
    Boltztrap energy value and isolating corresponding DOS value
!Reading the Boltztrap energy values to be approximated
open(unit=36, file='eV_list.dat', iostat=istat)
if (istat/=0) stop 'Could not open energy list'
allocate (DOSfinal(total_samples), stat=istat)
if (istat/=0) stop 'Could not allocate final DOS array'
allocate (energyvalue(energytotal), stat=istat)
if (istat/=0) stop 'Could not allocate energy values to fit'

do line = 1, energytotal
   read(unit=36, fmt=*, iostat=istat) energyvalue(line)
   if (istat/=0) stop 'could not read ev_list'
end do

print *, "Read the boltztrap energy values to be approximated"

close(unit=36, iostat=istat)
if (istat/=0) stop 'Could not close energy list'



!Approximating Boltztrap values with DOS
    sampling energy values and isolating corresponding DOS value
!The order in which DOS values are listed also
    needs to go from temperature(energies) to energy(temperatures)

!We do this by taking every single energy in ascending order
!Then we take each temperature in turn for that energy
!Then we cycle through all DOS energies at that temperature,
    saving the DOS of the one with the lowest difference each time
!Once this cycle is complete
   , we move on to the next energy until we have done all 880
!Then
   rince and repeat on next temperature, until we have done all 60
allocate (match(energytotal), stat=istat)
if (istat/=0) stop 'Could not allocate matching energy values'

print *, "Number of BoltzTraP energy values is", energytotal
print *, "Number of DOS energy values is", DOS_E_size
```

```
print *, "Number of temperature samples is", temp_samples

do line = 1, energytotal
   last = 10000
   do i = 1, (DOS_E_size)
      difference
          = abs(DOSev(i) - (13.605684959 * energyvalue(line)))
      if (difference .lt. last) then
         match(line) = i
         last = difference
      end if
   end do
end do

print *, "plotted match"



!Our DOS results are organised
    as a list of values for each energy at each temperature
!But our Boltztrap values are organised
    as a list of values for each temperature at each energy
!It is therefore preferable
    to reorganise our DOS values to conform with Boltztrap
!We do this by writing our DOS values to
    a 2D matrix, then outputting its content in the correct order
allocate (matrix_initial(temp_samples, energytotal), stat=istat)
if (istat/=0) stop 'Could not allocate initial matrix'

print *, "matrix allocated"

do line = 1, energytotal
   do  shift = 1, temp_samples
      matrix_initial(shift
          , line) = DOS(match(line) + ((shift-1) * DOS_E_size))
   end do
end do

print *,"matrix defined"

do line = 1, energytotal
   do shift = 1, temp_samples
      DOSfinal(shift  +
           ((line-1) * temp_samples)) = matrix_initial(shift, line)
   end do
end do

print *, "final DOS listed"
```

```
  deallocate (matrix_initial, stat=istat)

  print *, "Approximated boltztrap
      values with DOS energies, stored and rearranged DOS values"

  deallocate (DOSeV, stat=istat)
  if (istat/=0) stop 'Could not deallocate DOS energy array'
  deallocate (energyvalue, stat=istat)
  if (istat/=0) stop 'Could not deallocate energy values to fit'
  deallocate (DOS, stat=istat)
  if (istat/=0) stop 'Could not deallocate DOS array'

  !This is where we can then
      output our final DOS values (listed as DOSfinal) into a file
  !Alternatively this
     program can be used as an early module in the "Calc_ZT" program

end program Match
```

Listing D.2: An additional Fortran 90 script which can be used to complement the ZT calculator shown above, this following segment of code was used to match the data from the different thermally smeared DOS plots with the terms outputted by BoltzTraP2.

D.3 Transfer from BoltzTraP/ShengBTE outputs to ZT calculator

```
#!/bin/bash

#Grep the list of doping energies
    for an arbitrary temperature, and count how many there are
grep
   " 400 " ./interpolation.condtens | awk '{print $1}' > eV_list.dat
eV_values=$(wc -l eV_list.dat | awk '{print $1}')
echo 'There
    are' ${eV_values} 'doping values being sampled by Boltztrap'



#Statement of
    the upper temperature bound (minimum as hardcoded below is 200K)
max_temp=500
echo 'The thermal sampling range is 200 to' ${max_temp} 'Kelvin.'
```

```
g=$(echo "${max_temp}-5" | bc -l)

#Calculation of the number
    of temperature values being used (5K steps between each value)
temp_samples=$(echo "(${max_temp}-200)/5" | bc -l)
echo ${temp_samples} > temp_samples.dat
echo 'Number
    of temperature samples calculated to be' ${temp_samples} '.'



#Grep the values of Seebeck
   , E conductivity and E phonon conductivity for all temperatures
#at each doping energy listed above
for i in $(seq 1 1 ${eV_values}); do
    b=$(cat eV_list.dat | sed -n "$i p")
    grep -iE "^\s*$b " ./interpolation.condtens | awk '{print
        $4, $5, $6, $7, $8, $9, $10, $11, $12}' >> Sigma_matrix.dat
    grep
       -iE "^\s*$b " ./interpolation.condtens | awk '{print $13, $14
       , $15, $16, $17, $18, $19, $20, $21}' >> Seebeck_matrix.dat
    grep -iE "^\s*$b " ./interpolation.condtens | awk '{print $22,
       $23, $24, $25, $26, $27, $28, $29, $30}' >> Kappae_matrix.dat
    grep -iE "^\s*$b
        " ./interpolation.condtens | awk '{print $1}' >> doping.dat
    grep -iE "^\s*$b
       " ./interpolation.trace | awk '{print $4}' >> DOS_thermal.dat
done
echo 'Seebeck coefficient, electronic
    conductivity and electron phonon conductivity results extracted'



#BTE values for phonon conductivity in all 3
   axis (xx yy and zz) at each temperature gathered from output file
#The values from each axis are
    in the process being averaged to obtain a single isotropic value

cat ./BTE.KappaTensorVsT_sg | awk '{print $2 " " $3 " " $4
    " " $5 " " $6 " " $7 " " $8 " " $9 " " $10}' >> kappa_phonon.dat
```

Listing D.3: A short bash script used to extract the data from BoltzTraP and ShengBTE and implement a basic format so as to make it compatible with the Fortran scripts.

Appendix E

Quantitative error propagation analyses

E.1 Numerical error propagation

In order to identify the impact of the numerical uncertainty in our DFT calculations on our final results, one can implement an error propagation analysis. However, doing so analytically is quite challenging due to the dimensional convolutions involved in solving the Boltzmann transport equation.

In the case of the electron transport terms calculated using the Boltzmann transport equation, it may therefore be preferable to implement a quantitative approach. This involves implementing a shift in our eigenvalues by a set amount representing their uncertainty range, and subsequently calculating the resulting values for ZT in order to determine the impact.

In order to ensure that we had accounted for the highest possible uncertainty effect in our relevant data, we opted for an eigenvalue shift of 1 meV, which is an order of magnitude higher than our eigenvalue energy tolerance and equal to our atomic energy convergence. This would likely overestimate the uncertainty, ensuring that it is not under-represented.

The shift was implemented iteratively to every single eigenvalue of the valence and conduction bands, and in each case the full energy landscape was searched in order to find the highest value of ZT across both bands, and calculate how much it had varied from the original estimate. The highest possible variation produced across all eigenvalues and resulting ZT values available in both bands was then recorded as the maximal possible variation for each specified temperature.

The resulting propagated impact of our potential numerical errors on ZT was then plotted with respect to temperature, as shown in figure E.1. From this data we find that even in our overestimation of our numerical error, the highest uncertainty in our maximal ZT is approximately 0.008 and 0.002 in the valence and conduction bands

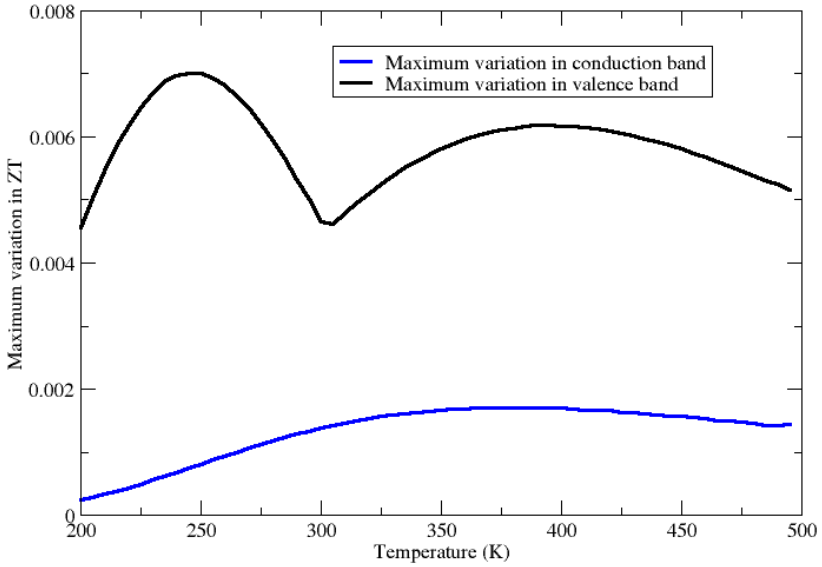

Figure E.1: Maximal variation in the highest values of ZT in β-phase As_2Te_3 across temperature as a result of a 1 meV shift in the eigenvalues, plotted separately for the valence and conduction band.

respectively, translating to approximately 2% and 0.3% error margins. Considering the relative magnitude of some of our other errors, both random and systematic, it would appear reasonable to state that the impact of our numerical error on our results is effectively negligible.

E.2 Band gap error propagation

We know that the use of the LDA exchange-correlation functional is likely to have led to an underestimation of the bandgap. While the magnitude of this systematic error is unknown, we can use a similar method to that mentioned in appendix E.1 to approximate how our results would vary were the real bandgap to be significantly wider than that calculated for our material.

This involves implementing a scissor operator to artificially increase the size of the bandgap in our ground state density of states, and then using this as the basis for calculating new values for ZT in order to detect how the error propagates through our different electronic terms. For the sake of this test, we arbitrarily chose to double the bandgap as this would account for quite a severe but plausible [58] LDA-related error.

We found that the resulting percentage variation in our ZT term existed within a 10 to 20% error range, see figure E.2. Additionally, the magnitude of the error grew smaller

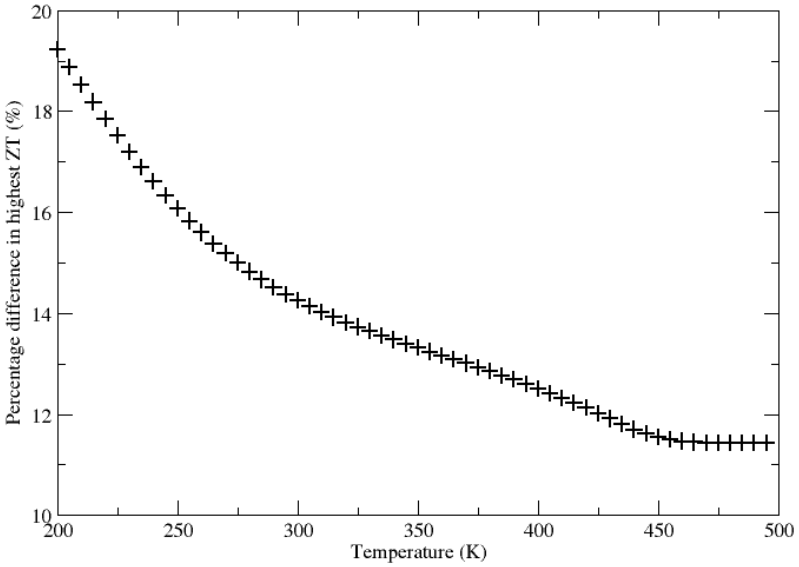

Figure E.2: Proportional increase in the highest values of ZT in β-phase As_2Te_3 with respect to temperature as a result of a doubling the width of the band gap through the use of a scissor operator.

with increasing temperature, and demonstrated two significant shifts in gradient as temperature increased.

It is worth noting that the two primary shifts in gradient occurred around temperature values for which the k_BT term would be equal to approximately 0.5 and 1.0 times the bandgap width. This suggests that the presence or lack thereof of thermally smeared electron states within the ground state bandgap at non-zero temperatures when varying its width makes up a significant part of our error when using a poorly approximated bandgap width.

Additionally, when evaluating the impact of this systematic error by widening the bandgap, we find that the resulting impact on ZT appears to be entirely positive. This suggests that our current method may be slightly underestimating the figure of merit as a result by underestimating the bandgap width.

Appendix F

Constraining the regularization term

The electrical transport properties of the inner-doped phase of β-As_2Te_3 were found to be numerically unstable near the bandgap when corrected by the electron-phonon relaxation time τ. While the implementation of a regularisation term γ can resolve the parabolic behaviour observed, it is not known what value for γ would be appropriate to best describe the system. However, it is possible to define key boundary conditions in order to constrain its order of magnitude.

This is because an insufficiently constrained τ produces spikes in the electrical transport properties and by extension in ZT for density of electron state values that lie within the ground state bandgap as a result of thermal smearing. Inversely, an overly regularised τ will apply an unrealistic reduction to all corrected electrical conduction terms within proximity of the bandgap.

Hence, we apply the following constraints:

- Constraint 1: All electron transport values that exist within the bandgap and are more than k_BT away from the nearest eigenvalue representing either the valence band maximum (VBM) or conduction band minimum (CBM) must be zeroed. This is necessary as there are no electrons within a bandgap beyond the smearing range described by k_BT. The smearing methods used by the BoltzTraP software package do not do this, leading to the correction of a very small but non-zero value for the electrical conductivity σ with a τ that diverges to infinity, which produces a sharp local spike.
- Constraint 2: The value of a corrected σ term cannot at any point increase along the path connecting the ground state band edges at the band gap to the center of said gap. This is due the nature of Fermi-Dirac smearing, which decreases progressively in magnitude when moving away from the band. This reduction in charge carriers should realistically lead to a decrease in the transport properties that depend on them.
- Constraint 3: The value of the transport properties at the nearest eigenvalues (in

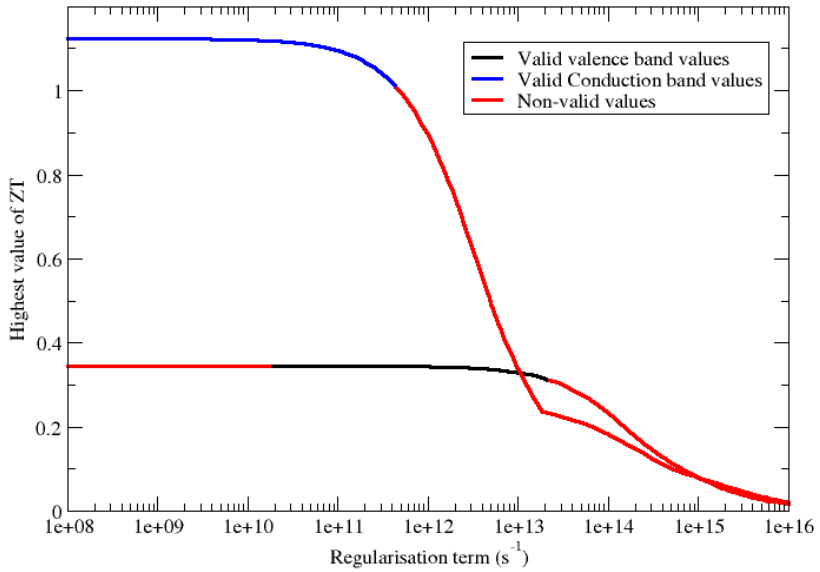

Figure F.1: Variation in the maximal value of ZT at room temperature, for a range of regularisation terms across multiple orders of magnitude. The black and blue data points represent values in the VBM and CBM respectively, which also meet the requirements of all three constraints. The red points failed to meet the requirements of either constraint 1 or 2.

this case the VBM and CBM) must not be significantly affected. They are located on ground state band edges, and thus corrections to numerical artifacts in thermal smearing should not significantly affect them.

The first constraint allows us to define the energy range in which the implementation of our regularisation term is appropriate. The second constraint gives us a potential lower bound to the value of γ, as insufficient regularisation may lead to spikes in σ. The third constraint provides a hard upper bound to γ, as a substantial shift in σ at the ground state eigenvalues would signify that our numerical correction is producing physically unrealistic effects. As a base line, we constrained our γ term such that it may not change by more than a set uncertainty range of 5%.

By implementing a broad range of values for γ while calculating our results for ZT, we were able to plot the variation in the highest available value of ZT near the bandgap for any set temperature, as shown for the example case of 300K in figure F.1. The values of σ did not spike near the CBM, even without the implementation of a regularisation term, limiting the effectiveness of constraint 2 and thus allowing for a broader allowable range for γ.

The highest value of ZT in both the valence and conduction bands was identified at each value of γ and temperature via an iterative analysis of the energy range near

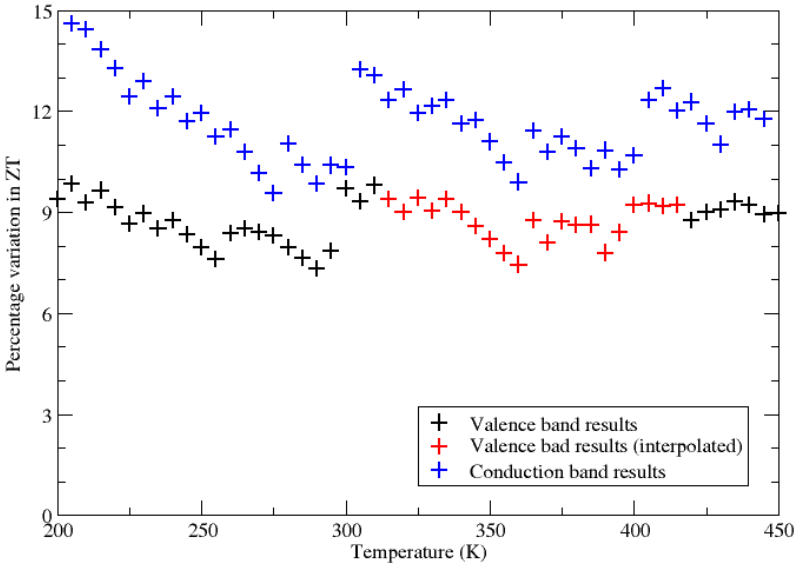

Figure F.2: Percentage variation in the highest value of ZT across the range of allowed values of γ according to our constraints. The red region uses an interpolated lower bound for the allowable regularisation term based on surrounding data.

the band gap. This procedure allowed for the range of allowable values for γ to be propagated such that one could define the range of resulting values for the maximum value of ZT across a range of temperatures, as plotted in figure F.2.

The resulting plots show noise as a result of regularisation term samples transferring from forbidden to allowed ranges as the temperature changes. Thus the magnitude of the noise is inversely proportional to the regularisation sample density, which in our case is 24 samples per order of magnitude on a logarithmic scale.

From these results, we can approximate that the highest error that can be produced in ZT through the usage of a reasonably constrained regularisation term fluctuates with temperature between 9% and 15% in the conduction band, and between 7% and 10% in the valence band. This discrepancy is to be expected when the gradient of the DOS in the conduction band is so steep and thus more sensitive to regularisation. Additionally, it cannot be given a lower bound by constraint 2, further widening the range of variation permitted to our ZT values. It may be worth considering an alternative stronger constraint as the basis for a lower bound to regularization.

It may also be worth noting that as γ limits the growth of κ near the band gap, the only impact that it can have on our results is to reduce the electrical conductivity and electron thermal conductivity. As this reduces ZT, we can state that our margin of error within our allowable regularisation range exists solely in the negative direction.

Bibliography

[1] L. V. Brugnatelli. *Annali di chimica e storia naturale: ovvero raccolta di memorie sulle scienze, arti, e manifatture ad esse relative*. Eredi di Pietro Galeazzi, v. 5 edition, 1794.

[2] M. V. Laue. *Geschichte Der Physik*. Athenaumverlag Bonn, 1950.

[3] Deutsche Akademie der Wissenschaften zu Berlin. *Abhandlungen der Königlichen Akademie der Wissenschaften zu Berlin.*, volume 1822-1823. Berlin :Realschul-Buchhandlung,, 1822.

[4] T. J. Seebeck. Deflection of the magnetic needle. *The London Mechanics' register*, 1:406–411, April 1824.

[5] C. Oersted. Nouvelles experiences de m. seebeck sur les actions èlectromagnetiques. *Annales de Chimie et de Physique*, pages 199–201, 1823.

[6] T. J. Seebeck. Ueber die magnetische polarisation der metalle und erze durch temperaturdifferenz. *Annalen der Physik*, 82(3):253–286, 1826.

[7] W. Haken. *Annalen der Physik*. Wiley-Blackwell, 1910.

[8] G. Magnus. *Annalen der Physik*. Wiley-Blackwell, 1851.

[9] J. C. Peltier. Nouvelles expériences sur la caloricité des courants électrique. *Annales de Chimie et de Physique*, 56:371–386, 1834.

[10] W. Thomson. On a mechanical theory of thermo-electric currents. *Proceedings of the Royal Society of Edinburgh*, 3:91–98, 1857.

[11] W. Thomson. On a dynamical theory of heat. part v. thermo-electric currents. *Transactions of the Royal Society of Edinburgh*, v.21 (1853-1857):782, 1853.

[12] C. Yu and K. T. Chau. Thermoelectric automotive waste heat energy recovery using maximum power point tracking. *Energy Conversion and Management*, 50(6):1506–1512, 2009.

[13] V. Vijayenthiran. BMW showcases thermoelectric technology in 5-series. Motor Authority, August 2011.

[14] J. LaGrandeur, D. Crane, S. Hung, B. Mazar, and A. Eder. Automotive waste heat conversion to electric power using skutterudite, TAGS, PbTe and BiTe. In *2006 25th International Conference on Thermoelectrics*, pages 343–348, 2006.

[15] M. Mori, T. Yamagami, M. Sorazawa, T. Miyabe, S. Takahashi, and T. Haraguchi. Simulation of fuel economy effectiveness of exhaust heat recovery system using thermoelectric generator in a series hybrid. *SAE International Journal of Materials and Manufacturing*, 4(1):1268–1276, apr 2011.

[16] Q. E. Hussain, D. R. Brigham, and C. W. Maranville. Thermoelectric exhaust heat recovery for hybrid vehicles. *SAE International Journal of Engines*, 2(1):1132–1142, apr 2009.

[17] B. Orr, A. Akbarzadeh, M. Mochizuki, and R. Singh. A review of car waste heat recovery systems utilising thermoelectric generators and heat pipes. *Applied Thermal Engineering*, 101:490–495, 2016.

[18] J. Lagrandeur, D. Crane, BSST LLC, Andreas Eder, and BMW. Vehicle fuel economy improvement through thermoelectric waste heat recovery. *2005 Diesel Engine Emissions Reduction (DEER) Conference*, 2005.

[19] W. Bou Nader. Thermoelectric generator optimization for hybrid electric vehicles. *Applied Thermal Engineering*, 167:114761, 2020.

[20] S. Lan, Z. Yang, R. Chen, and R. Stobart. A dynamic model for thermoelectric generator applied to vehicle waste heat recovery. *Applied Energy*, 210:327–338, 2018.

[21] C. C. Sousa, J. Martins, and O Carvalho. Assessment of an exhaust thermoelectric generator incorporating thermal control applied to a heavy duty vehicle. *Energies*, 2022.

[22] A. B. Amar, A. B. Kouki, and H. Cao. Power approaches for implantable medical devices. *Sensors*, 15(11):28889–28914, 2015.

[23] M. Wahbah, M. Alhawari, B. Mohammad, H. Saleh, and M. Ismail. Characterization of human body-based thermal and vibration energy harvesting for wearable devices. *IEEE Journal on Emerging and Selected Topics in Circuits and Systems*, 4(3):354–363, 2014.

[24] D. K. Bhatia, S. Bairagi, S. Goel, and M. Jangra. Pacemakers charging using body energy. *Journal of Pharmacy and Bioallied Sciences*, 2:51 – 54, 2010.

[25] D. Malathi and K. C. Sabitha. Battery less thermo electric energy harvesting generator for implantable medical electronic devices. *Biomedical Research-tokyo*, 27:150–155, 2018.

[26] K. D. Lind. Understanding the market for implantable medical devices. *Public Policy Inst. (Amer. Assoc. Retired Pers.)*, page 1 – 15, 2017. Cited by: 12.

[27] R. L. Heacock. The voyager spacecraft. *Proceedings of the Institution of Mechanical Engineers*, 194:211–224, 1980.

[28] G. Bennett. Space nuclear power: Opening the final frontier. *Proc 4th Int Energy Conversion Engineering Conf Exhibit (IECEC), AIAA, 4191*, 2, 06 2006.

[29] A. Sarris, B. Bhatti, and F. Ciampa. Thermoelectric energy harvesting using vapour chamber coolers for aerospace applications. *Journal of Intelligent Material Systems and Structures*, 33(12):1602–1612, 2022.

[30] T. Becker, A. Elefsiniotis, and M. E. Kiziroglou. *Thermoelectric Energy Harvesting in Aircraft*, chapter 20, pages 415–434. John Wiley & Sons, Ltd, 2015.

[31] Z. Slanina, M. Uhlik, and V. Sladecek. Cooling device with peltier element for medical applications. *IFAC-PapersOnLine*, 51(6):54–59, 2018. 15th IFAC Conference on Programmable Devices and Embedded Systems PDeS 2018.

[32] P. E. Kramer. Thermoelectric applications as related to biomedical engineering for NASA johnson space center. *MRS online proceedings library*, 478:309–314, 1997.

[33] R. A. Taylor and G. L. Solbrekken. Comprehensive system-level optimization of thermoelectric devices for electronic cooling applications. *Transactions on components and packaging technologies*, 31:23–31, 2008.

[34] D. A. Tikhomirov, S. S. Trunov, A. V. Kuzmichev, S. A. Rastimeshin, and O. V. Shepovalova. Energy-efficient thermoelectric unit for microclimate control on cattlebreeding premises. *Energy Reports*, 6:293–305, 2020. Technologies and Materials for Renewable Energy, Environment and Sustainability.

[35] I. Sarbu and A. Dorca. A comprehensive review of solar thermoelectric cooling systems. *International Journal of Energy Research*, 42(2):395–415, 2018.

[36] H. Dehra. Building-integrated thermoelectric cooling-photovoltaic (tec-pv) devices. In *Bringing Thermoelectricity into Reality*, chapter 15. IntechOpen, Rijeka, 2018.

[37] J. A. Esfahani, N. Rahbar, and M. Lavvaf. Utilization of thermoelectric cooling in a portable active solar still — an experimental study on winter days. *Desalination*, 269(1):198–205, 2011.

[38] D. Pollock. *Thermocouples: Theory and Properties*. CRC Press, 1991. ISBN: 9780849342431.

[39] T. W. Kerlin. *Practical Thermocouple Thermometry*. ISA, 1999. ISBN: 9781556176449.

[40] M. H. Hablanian. *High-vacuum technology*. CRC Press, 1990. ISBN = 9780824798345.

[41] D. R. Clarke. Materials selection guidelines for low thermal conductivity thermal barrier coatings. *Surface and Coatings Technology*, 163-164:67 – 74, 2003. Proceedings of the 29th International conference on Metallurgical Coatings and Thin Films.

[42] N. W. Ashcroft and N. D. Mermin. *Solid State Physics*. Saunders College Publishing, 1976.

[43] P. Ehrhart, W. Sander, and W. Schilling. Properties and interactions of atomic defects in metals and alloys. In *Landolt-Börnstein*, volume volume 25 of *New Series III*, 1991.

[44] D. Bastien. Preismonitor. *Federal Institute for Geosciences and Natural Resources*, pages 13–14, 2020.

[45] P. Hohenberg and W. Kohn. Inhomogeneous electron gas. *Phys. Rev.*, 136:B864–B871, Nov 1964.

[46] M. Born and R. Oppenheimer. Zur quantentheorie der molekeln. *Annalen der Physik*, 389(20):457–484, 1927.

[47] S. J. Clark, M. D. Segall, C. J. Pickard, P. J. Hasnip, M. I. J. Probert, K. Refson, and M. C. Payne. First principles methods using CASTEP. *Zeitschrift für Kristallographie - Crystalline Materials*, 220(5-6):567–570, 2005.

[48] J. Hafner. Ab-initio simulations of materials using VASP: Density-functional theory and beyond. *Journal of Computational Chemistry*, 29(13):2044–2078, 2008.

[49] P. Giannozzi and Baroni et al. Quantum espresso: a modular and open-source software project for quantum simulations of materials. *Journal of Physics: Condensed Matter*, 21(39):395502, Sep 2009.

[50] F. Bloch. über die quantenmechanik der elektronen in kristallgittern. *Zeitschrift für Physik*, pages 555–600, 1928.

[51] M. C. Payne, M. P. Teter, D. C. Allan, T. A. Arias, and J. D. Joannopoulos. Iterative minimization techniques for ab initio total-energy calculations: molecular dynamics and conjugate gradients. *Rev. Mod. Phys.*, 64:1045–1097, Oct 1992.

[52] G. P. Francis and M. C. Payne. Finite basis set corrections to total energy pseudopotential calculations. *Journal of Physics: Condensed Matter*, 2(19):4395, may 1990.

[53] W. C. Topp and J. J. Hopfield. Chemically motivated pseudopotential for sodium. *Phys. Rev. B*, 7:1295–1303, Feb 1973.

[54] M. I. J. Probert. Lecture notes in first principles material modelling. `https://www-users.york.ac.uk/~mijp1/teaching/grad_FPMM/lecture_notes/lec2_electronic_structure.pdf`, September 2018.

[55] W. Kohn and L. J. Sham. Self-consistent equations including exchange and correlation effects. *Phys. Rev.*, 140:A1133–A1138, Nov 1965.

[56] M. D. Segall, Philip J. D. Lindan, M. J. Probert, C. J. Pickard, P. J. Hasnip, S. J. Clark, and M. C. Payne. First-principles simulation: ideas, illustrations and the CASTEP code. *Journal of Physics Condensed Matter*, 14(11):2717–2744, March 2002.

[57] J. P. Perdew. Density functional theory and the band gap problem. *International Journal of Quantum Chemistry*, 28(S19):497–523, 1985.

[58] T. Hollins. *Local Exchange Potentials in density functional theory*. PhD thesis, Durham University, 2014.

[59] J. P. Perdew. Generalized gradient approximations for exchange and correlation: A look backward and forward. *Physica B: Condensed Matter*, 172(1):1–6, 1991.

[60] J. P. Perdew, R. G. Parr, M. Levy, and J. L. Balduz. Density-functional theory for fractional particle number: Derivative discontinuities of the energy. *Phys. Rev. Lett.*, 49:1691–1694, Dec 1982.

[61] A. Görling. Exchange-correlation potentials with proper discontinuities for physically meaningful Kohn-Sham eigenvalues and band structures. *Phys. Rev. B*, 91:245120, Jun 2015.

[62] J. Sun, A. Ruzsinszky, and J. P. Perdew. Strongly constrained and appropriately normed semilocal density functional. *Phys. Rev. Lett.*, 115:036402, Jul 2015.

[63] A. P. Bartók and J. R. Yates. Regularized SCAN functional. *The Journal of Chemical Physics*, 150(16):161101, 2019.

[64] J. P. Perdew and L. A. Constantin. Laplacian-level density functionals for the kinetic energy density and exchange-correlation energy. *Phys. Rev. B*, 75:155109, Apr 2007.

[65] J. Sun, R. Remsing, Y. Zhang, et al. Accurate first-principles structures and energies of diversely bonded systems from an efficient density functional. *Nature Chem*, 8:831–836, 2016.

[66] D. R. Hartree and W. Hartree. Self-consistent field, with exchange, for beryllium. *Proceedings of the Royal Society of London. Series A - Mathematical and Physical Sciences*, 150(869):9–33, 1935.

[67] A. D. Becke. A new mixing of Hartree-Fock and local density-functional theories. *J Chem. Phys.*, 98(2):1372–1377, January 1993.

[68] G. P. Srivastava. *The physics of phonons*. Routledge, 1990. ISBN: 0852741537.

[69] K. Parlinski, Z. Q. Li, and Y. Kawazoe. First-principles determination of the soft mode in cubic ZrO_2. *Phys. Rev. Lett.*, 78:4063–4066, May 1997.

[70] J. H. Lloyd-Williams and B. Monserrat. Lattice dynamics and electron-phonon coupling calculations using nondiagonal supercells. *Phys. Rev. B*, 92:184301, Nov 2015.

[71] S. Baroni, P. Giannozzi, and A. Testa. Green's-function approach to linear response in solids. *Phys. Rev. Lett.*, 58:1861–1864, May 1987.

[72] S. Baroni, S. de Gironcoli, A. Dal Corso, and P. Giannozzi. Phonons and related crystal properties from density-functional perturbation theory. *Rev. Mod. Phys.*, 73:515–562, Jul 2001.

[73] S. P. Parker. *Mcgraw Hill encyclopedia of Physics Second edition*. McGraw Hill inc., 1993.

[74] G. K. H. Madsen and D. J. Singh. Boltztrap. a code for calculating band-structure dependent quantities. *Computer Physics Communications*, 175(1):67–71, 2006.

[75] Y. Wang, Y. J. Hu, B. Bocklund, S. L. Shang, B. C. Zhou, Z. K. Liu, and L. Q. Chen. First-principles thermodynamic theory of seebeck coefficients. *Phys. Rev. B*, 98:224101, Dec 2018.

[76] Y. Wang, J. P. S. Palma, S. Shang, L. Q. Chen, and Z. k. Liu. Lorenz number and electronic thermoelectric figure of merit: Thermodynamics and direct dft calculations. *arXiv: Materials Science*, 2020.

[77] J. P. Mckelvey. *Solid state and semiconductor physics*. Harper & Row and John Weatherhill, inc., 1982.

[78] M. Jarrel. Lectures notes on "electronic transport". `https://www.phys.lsu.edu/~jarrell/COURSES/SOLID_STATE/Chap9/chap9.pdf`, 2017. Accessed 05-05-2024.

[79] G. K. H. Madsen, J. Carrete, and M. J. Verstraete. BoltzTraP2, a program for interpolating band structures and calculating semi-classical transport coefficients. *Computer Physics Communications*, 231:140–145, 2018.

[80] T. J. Scheidemantel, C. Ambrosch-Draxl, T. Thonhauser, J. V. Badding, and J. O. Sofo. Transport coefficients from first-principles calculations. *Phys. Rev. B*, 68:125210, Sep 2003.

[81] W. Li, J. Carrete, N. A. Katcho, and N Mingo. ShengBTE: A solver of the Boltzmann transport equation for phonons. *Computer Physics Communications*, 185(6):1747–1758, 2014.

[82] J. Bardeen and W. Shockley. Deformation potentials and mobilities in non-polar crystals. *Phys. Rev.*, 80:72–80, Oct 1950.

[83] C. Herring and E. Vogt. Transport and deformation-potential theory for many-valley semiconductors with anisotropic scattering. *Phys. Rev.*, 101:944–961, Feb 1956.

[84] J. Y. Kim and J. C. Grossman. High-efficiency thermoelectrics with functionalized graphene. *Nano letters*, 15:2830–2835, 2015.

[85] C. Kittel. *Introduction to solid state physics*. John Wiley & Sons, 5 edition, 1976.

[86] V. I. Lebedev. Quadratures on a sphere. *USSR Computational Mathematics and Mathematical Physics*, 16(2):10–24, 1976.

[87] Inorganic crystal structure database. `https://www.psds.ac.uk/`, 2019-2022.

[88] M. W. Gaultois, A. O. Oliynyk, A. Mar, T. D. Sparks, G. J. Mulholland, and B. Meredig. Perspective: Web-based machine learning models for real-time screening of thermoelectric materials properties. *APL Materials*, 4(5):053213, 2016.

[89] W. H. Chen, P. H. Wu, and Y. L. Lin. Performance optimization of thermoelectric generators designed by multi-objective genetic algorithm. *Applied Energy*, 209:211 – 223, 2018.

[90] D. Y. Chung, T. Hogan, J. Schindler, L. Iordarridis, P. Brazis, C. R. Kannewurf, Baoxing Chen, C. Uher, and M. G. Kanatzidis. Complex bismuth chalcogenides as thermoelectrics. In *XVI ICT '97. Proceedings ICT'97. 16th International Conference on Thermoelectrics (Cat. No.97TH8291)*, pages 459–462, 1997.

[91] R. H. Byrd, J. Nocedal, and R. B. Schnabel. Representations of quasi-newton matrices and their use in limited memory methods. *Mathematical Programming*, 63:129–156, 1994.

[92] B. G. Pfrommer, M. Côté, S. G. Louie, and M. L. Cohen. Relaxation of crystals with the quasi-Newton method. *Journal of Computational Physics*, 131(1):233–240, 1997.

[93] Y. Hinuma, G. Pizzi, Y. Kumagai, F. Oba, and I. Tanaka. Band structure diagram paths based on crystallography. *Computational Materials Science*, 128:140–184, 2017.

[94] A. J. Morris, R. J. Nicholls, C. J. Pickard, and J. R. Yates. OptaDOS: A tool for obtaining density of states, core-level and optical spectra from electronic structure codes. *Computer Physics Communications*, 185(5):1477–1485, 2014.

[95] J. R. Yates, X. Wang, D. Vanderbilt, and I. Souza. Spectral and Fermi surface properties from Wannier interpolation. *Phys. Rev. B*, 75:195121, May 2007.

[96] A. Fonari and C. Sutton. Effective mass calculator. `https://github.com/afonari/emc`, 2012.

[97] D. Wilson and A. Walker. Elastic constants calculator. `https://github.com/andreww/elastic-constants`, 2010.

[98] V. Brazdova and D. R. Bowler. *Atomistic computer simulations: A practical guide*. Wiley-VCH, 2013.

[99] M. Rahaman, S. Ganguly, P. Samal, M. K. Harbola, T. Saha-Dasgupta, and A. Mookerjee. A local-density approximation for the exchange energy functional for excited states: The band-gap problem. *Physica B: Condensed Matter*, 404(8-11):1137–1142, may 2009.

[100] C. Chang and L.D. Zhao. Anharmoncity and low thermal conductivity in thermoelectrics. *Materials Today Physics*, 4, March 2018.

[101] Y. Wu, W. Li, A. Faghaninia, Z. Chen, J. Li, X. Zhang, B. Gao, S. Lin, B. Zhou, A. Jain, and Y. Pei. Promising thermoelectric performance in van der waals layered snse2. *Materials Today Physics*, 3:127 – 136, 2017.

[102] T. Takabatake, K. Suekuni, T. Nakayama, and E. Kaneshita. Phonon-glass electron-crystal thermoelectric clathrates: Experiments and theory. *Rev. Mod. Phys.*, 86:669–716, Jun 2014.

[103] S. I. Kim, K. H. Lee, H. A Mun, H. S. Kim, S. W. Hwang, J. W. Roh, D. J. Yang, W. H. Shin, X. S. Li, Y. H. Lee, G. J. Snyder, and S. W. Kim. Dense dislocation arrays embedded in grain boundaries for high-performance bulk thermoelectrics. *Science*, 348(6230):109–114, 2015.

[104] P. Puneet, R. Podila, M. Karakaya, et al. Preferential scattering by interfacial charged defects for enhanced thermoelectric performance in few-layered n-type Bi2Te3. *Scientific Reports*, 3:3212, 2013.

[105] A. Shakouri. Recent developments in semiconductor thermoelectric physics and materials. *Annual Review of Materials Research*, 41(1):399–431, 2011.

[106] J. B. Vaney, J. Carreaud, G. Delaizir, A. Piarristeguy, A. Pradel, E. Alleno, J. Monnier, E. B. Lopes, A. P. Gonçalves, A. Dauscher, C. Candolfi, and B. Lenoir. High thermoelectric performance in sn-substituted α-As2Te3. *J. Mater. Chem. C*, 4:2329–2338, 2016.

[107] G. J. Carron. The crystal structure and powder data for arsenic telluride. *Acta Crystallographica*, 16(5):338–343, May 1963.

[108] T. J. Scheidemantel, J.F. Meng, and J.V. Badding. Thermoelectric power and phase transition of polycrystalline as2te3 under pressure. *Journal of Physics and Chemistry of Solids*, 66(10):1744–1747, 2005.

[109] C. Morin. Polymorphism in Thermoelectric As2Te3. *Inorganic Chemistry*, 54, October 2015.

[110] S. Li, Q. Zheng, Y. Lv, X. Liu, X. Wang, P. Y. Huang, D. G. Cahill, and B. Lv. High thermal conductivity in cubic boron arsenide crystals. *Science*, 361(6402):579–581, 2018.

[111] F. Tian, B. Song, B. Lv, J. Sun, S. Huyan, Q. Wu, J. Mao, Y. Ni, Z. Ding, S. Huberman, T.H. Liu, G. Chen, S. Chen, C.W. Chu, and Z. Ren. Seeded growth of boron arsenide single crystals with high thermal conductivity. *Applied Physics Letters*, 112(3):031903, 2018.

[112] A. Kokalj. Xcrysden—a new program for displaying crystalline structures and electron densities. *Journal of Molecular Graphics and Modelling*, 17(3):176–179, 1999.

[113] L. Khalil and J.-C. et. al. Girard. Electronic band gap of van der Waals α-As2Te3 crystals. *Applied Physics Letters*, 119(4):043103, 07 2021.

[114] H. Deng. Theoretical prediction of the structural, electronic, mechanical and thermodynamic properties of the binary α-as2te3 and β-as2te3. *Journal of Alloys and Compounds*, 656:695–701, 2016.

[115] J. Lee, Y. Jhon, K. Lee, Y. M. Jhon, and J. Lee. Nonlinear optical properties of arsenic telluride and its use in ultrafast fiber lasers. *Scientific reports*, 10:15305, 09 2020.

[116] A. Jain, S. P. Ong, G. Hautier, W. Chen, W. D. Richards, S. Dacek, S. Cholia, D. Gunter, D. Skinner, G. Ceder, and K. A. Persson. Commentary: The Materials Project: A materials genome approach to accelerating materials innovation. *APL Materials*, 1(1):011002, 2013.

[117] J. E. Müller and J. W. Wilkins. Band-structure approach to the x-ray spectra of metals. *Phys. Rev. B*, 29:4331–4348, Apr 1984.

[118] Y. Sharma and P. Srivastava. First principles investigation of electronic, optical and transport properties of α- and β-phase of arsenic telluride. *Optical Materials*, 33(6):899–904, 2011.

[119] J. B. Vaney, J. Carreaud, G. Delaizir, C. Morin, J. Monnier, E. Alleno, A. Piarristeguy, A. Pradel, A.P. Gonçalves, E.B. Lopes, C. Candolfi, A. Dauscher, and B. Lenoir. Thermoelectric properties of the α-As2Te3 crystalline phase. *Journal of Electronic Materials*, 45(3):1447–1452, Mar 2016.

[120] P. J. Price. The Lorenz number. *IBM Journal of Research and Development*, 1(2):147–157, 1957.

[121] M. Thesberg, H. Kosina, and N. Neophytou. On the Lorenz number of multiband materials. *Phys. Rev. B*, 95:125206, Mar 2017.

[122] P. E. Blöchl, O. Jepsen, and O. K. Andersen. Improved tetrahedron method for brillouin-zone integrations. *Phys. Rev. B*, 49:16223–16233, Jun 1994.

[123] J. J. Jorgensen and G. L. W. Hart. Effectiveness of smearing and tetrahedron methods: best practices in DFT codes. *Modelling and Simulation in Materials Science and Engineering*, 29(6):065014, July 2021.

[124] C. J. Pickard and M. C. Payne. Extrapolative approaches to brillouin-zone integration. *Phys. Rev. B*, 59:4685–4693, Feb 1999.

[125] H. Julian Goldsmid. Bismuth telluride and its alloys as materials for thermoelectric generation. *Materials*, 7(4):2577–2592, 2014.

[126] T. Guenault. *Statistical Physics*. Springer, 2007. ISBN: 9781402059742.

[127] T. D. Sparks, M. W. Gaultois, A. Oliynyk, J. Brgoch, and B. Meredig. Data mining our way to the next generation of thermoelectrics. *Scripta Materialia*, 111:10 – 15, 2016.